

# Boundary layers and wind in turbulent thermal convection

## Dissertation

zur Erlangung des mathematisch-naturwissenschaftlichen Doktorgrades  
„Doctor rerum naturalium“  
der Georg-August-Universität Göttingen  
im Promotionsprogramm ProPhys  
der Georg-August University School of Science (GAUSS)

vorgelegt von

**Sebastian Wagner**  
aus Göttingen

Göttingen, 2014

## Betreuungsausschuss

### **Prof. Dr. Andreas Dillmann**

Institut für Aerodynamik und Strömungstechnik, Deutsches Zentrum für Luft- und Raumfahrt (DLR)  
Drittes Physikalisches Institut, Georg-August-Universität Göttingen

### **Prof. Dr. Andreas Tilgner**

Institut für Geophysik, Georg-August-Universität Göttingen

## Mitglieder der Prüfungskommission

### **Referent: Prof. Dr. Andreas Dillmann**

Institut für Aerodynamik und Strömungstechnik, Deutsches Zentrum für Luft- und Raumfahrt (DLR)  
Drittes Physikalisches Institut, Georg-August-Universität Göttingen

### **Korreferent: Prof. Dr. Andreas Tilgner**

Institut für Geophysik, Georg-August-Universität Göttingen

## Weitere Mitglieder der Prüfungskommission

### **Prof. Dr. Hans Hofsäss**

Zweites Physikalisches Institut, Georg-August-Universität Göttingen

### **Prof. Dr. Ulrich Parlitz**

Max-Planck-Institut für Dynamik und Selbstorganisation  
Institut für Nichtlineare Dynamik, Georg-August-Universität Göttingen

### **Prof. Dr. Martin Rein**

Institut für Aerodynamik und Strömungstechnik, Deutsches Zentrum für Luft- und Raumfahrt (DLR)  
Drittes Physikalisches Institut, Georg-August-Universität Göttingen

### **Prof. Dr. Jürgen Vollmer**

Max-Planck-Institut für Dynamik und Selbstorganisation  
Institut für Nichtlineare Dynamik, Georg-August-Universität Göttingen

## Weiterer Korreferent

### **Prof. Dr. Jörg Schumacher**

Institut für Thermo- und Fluidodynamik, Technische Universität Ilmenau

**Tag der mündlichen Prüfung:** 26. Juni 2014

# Danksagung

In den letzten Jahren habe ich die Möglichkeit gehabt innerhalb von zwei Projekten der Deutschen Forschungsgemeinschaft eigenverantwortlich zu forschen, meine Ergebnisse in Zeitschriften zu publizieren und auf zahlreichen Konferenzen einem Fachpublikum vorzustellen. Am vorläufigen Ende dieser Forschung steht die hier vorliegende Dissertation. Dies war natürlich nur durch Unterstützung auf vielseitige Art möglich, für die ich mich an dieser Stelle herzlich bedanken möchte.

Zunächst einmal möchte ich meinem Doktorvater Professor Dillmann, dem Korreferenten Professor Tilgner und allen weiteren Mitgliedern der Prüfungskommission danken, dass sie diese Aufgabe übernommen und mich beratend unterstützt haben.

Desweiteren gebührt größter Dank Olga Shishkina, die mich während meiner Promotionszeit hervorragend betreut hat und mich in die Welt der wissenschaftlichen Arbeitens mit all seinen Facetten eingeführt hat. Ohne die von ihr beantragten Projekte der Deutschen Forschungsgemeinschaft (DFG), wäre die Promotion in dieser Form nicht möglich gewesen. Daher möchte ich natürlich an dieser Stelle auch der DFG für die Finanzierung meiner Arbeit innerhalb der Projekte SH405/2 und SH405/3 danken.

Bei meiner Arbeit konnte ich auf ein bestehendes numerisches Verfahren zurückgreifen. Für dessen Weiterentwicklung möchte ich mich bei Matthias Kaczorowski, Tomasz Czarnota und Susanne Horn bedanken. Natürlich bedarf es auch hinreichend Rechenzeit um die numerischen Simulationen durchzuführen. Zu diesem Zweck stand mir stets der abteilungsinterne Rechencluster SCART zur Verfügung, wofür ich mich gerne bei Claus Wagner bedanken möchte.

Für Diskussion rund um meine erste Zeitschriftenveröffentlichung möchte ich Jörg Schumacher und Guenter Ahlers danken. Zudem danke ich Xiaozhou He für Diskussionen rund um moderne Rayleigh–Bénard Experimente.

Für eine angenehme Arbeit bedarf es einem gute Betriebsklima für das ich mich bei allen Mitarbeitern der Abteilung Fluidsysteme bedanken möchte. Besonders hervorheben möchte ich dabei (zusätzlich zu den bereits oben genannten) meinen Bürokollegen Daniel Schmeling, sowie Klaus Ehrenfried und Daniel Feldmann. Insbesondere die zahlreichen Diskussionen und Gespräche zu den verschiedensten Themen hatten einen großen Anteil an der stets angenehmen Atmosphäre.

Schlussendlich möchte ich Annika Hennies und Lena sowie meiner Familie danken, die mich während der letzten Jahr stets unterstützt und für den nötigen Ausgleich gesorgt haben.



# Abstract

This cumulative thesis is based on seven publications and is devoted to the investigation of turbulent thermal convection by means of Direct Numerical Simulations (DNSs). Special focus is placed on the boundary layers and the global flow in the generic setup of Rayleigh–Bénard convection (RBC), i.e. a fluid, which is confined between a heated bottom and a cooled top plate as well as thermally insulating sidewalls. Under consideration of the Oberbeck–Boussinesq approximation, the RBC flow is characterized by two dimensionless parameters: the Rayleigh number and the Prandtl number. In all the publications a large amount of instantaneous temperature and velocity fields is used for a posteriori analysis.

At first, the local and instantaneous boundary layer structure appearing in RBC in a cylindrical container close to the bottom plate is studied. For this purpose a method for the extraction of the large-scale circulation (wind) is introduced, to circumvent azimuthal reorientations occurring in cylindrical containers. The study reveals strong deviations from the theoretical approach of Prandtl–Blasius–Pohlhausen (PBP) for the description of laminar boundary layers. The latter approach is commonly used for the characterization of the boundary layers in RBC at moderate Rayleigh numbers and for modelling purposes.

This approach is also used to estimate the Kolmogorov and Batchelor microscales at the boundary layer edge and, hence, the required spatial resolution of the boundary layers in a DNS. The theoretical PBP estimates are compared with corresponding numerical results, revealing that the estimates are not restrictive enough and therefore their improvement is desirable. This is achieved by extending the PBP approach to a non-vanishing pressure gradient parallel to the heated/cooled plates. The pressure gradient depends on the angle of attack at which the flow approaches the plates. The resulting velocity boundary layer equation is of the Falkner–Skan type and leads to a better agreement with the DNS results with respect to the ratio of the thicknesses of the thermal and viscous boundary layers. The value for the latter ratio is derived analytically for arbitrary angles of attack and infinitesimal or infinite Prandtl numbers. This leads to improved estimates for the required spatial resolution of the boundary layers in the DNS.

Furthermore, the influence of the container geometry on RBC is studied. The mean heat fluxes and the global flow structures are evaluated for different Rayleigh numbers and different shapes of the container. First of all, the results obtained in a cubic enclosure are compared with the results obtained in the cylindrical container. The comparison reveals changes of the global

flow, the mean heat flux and the mean kinetic energy with increasing Rayleigh number for the cubic container, which are not present in the cylinder.

In addition, like in some experimental studies, quasi two-dimensional RBC is investigated, i.e. RBC in a container of equal height and length and rather short depth. The aspect ratio of depth per height is varied and the influence on the global flow structure, the mean heat flux and the mean kinetic energy are evaluated. The study reveals a strong influence of the latter quantities on the aspect ratio. For the aspect ratio of one fourth, a similar flow structure as in the experiments is obtained, even though the considered Rayleigh numbers in the DNS are much smaller. Additionally, the mean heat flux is found to be equal to that in a cylindrical container.

Finally, this quasi two-dimensional geometry is extended by adding heated and cooled obstacles, which are attached to the bottom and top plates, respectively. These obstacles represent regular surface roughness, which is often used in technical applications to achieve an increased heat flux. The heat flux and the velocity magnitude for varying height and width of the obstacles is investigated. It can be well described by a presented empirical relation, reflecting the result that, for constant covering area of the surface, slender obstacles can lead to the largest heat flux increase.

# Contents

I	Introduction	1
1	Thermal convection in nature and technology	3
2	The classical Rayleigh–Bénard problem	5
3	Turbulent Rayleigh–Bénard convection	11
4	Numerical investigation of turbulent RBC	17
5	Recent questions and recurrent thread	21
II	Results	25
6	Boundary layer structure analysis	27
7	Spatial resolution requirements	61
8	Falkner-Skan boundary layer structure	69
9	Further evaluation of the Falkner-Skan ansatz	95
10	Influence of the shape of the domain	109
11	Aspect-ratio dependency for box-shaped containers	117
12	Heat flux increase due to rough heating and cooling plates	139
III	Conclusions	163
13	Summary	165
14	Outlook	169
	Bibliography	173





## Part I

# Introduction



# 1 Thermal convection in nature and technology

*Convection due to nonuniform heating is, without overstatement, the most widespread type of fluid motion in the Universe.*

– Getling [48]

The basic mechanism behind this type of fluid flow, characterized here by Getling [48], goes back to Archimedes of Syracuse [7]. His principle indicates that bodies (or fluid particles) encounter a buoyant force as soon as their density differs from the density of the surrounding medium. If such differences in the density are caused by spatial temperature variations and if this is the only driving mechanism of a flow, it is called *natural convection* or *thermal convection*. As nicely described by Normand *et al.* [92], these termini go back to the nineteenth century to describe the heat transport in apple pies. Already in the eighteenth century thermal convection has been accounted for the global circulation of the Earth’s lower atmosphere (cf. figure 1.1) by Hadley [58] and, according to Ostroumov [94], independently by the Russian scientist Lomonosov at around the same time.

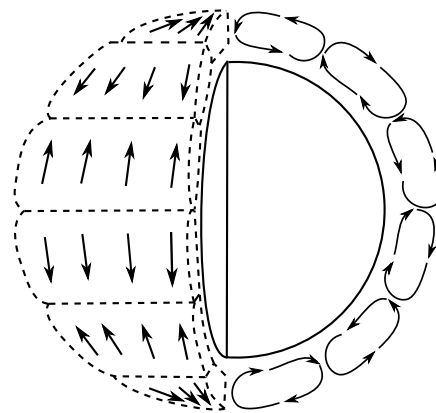


FIGURE 1.1: Large scale motion of the Earth’s lower atmosphere (*Hadley cells*) with rising air at the equator and falling air at the poles, leading in combination with the Earth’s rotation to the so-called *trade winds*. (Sketch according to [92].)

But thermal convection is not limited to the Earth’s atmosphere. Together with density changes by varying salt concentration, it drives the large-scale circulation of the oceans [86], which is also known as *thermohaline circulation*. Further, in the Earth’s core and mantle thermal convection takes place and is supposed to be connected to the maintenance of the Earth’s magnetic field

## 1 THERMAL CONVECTION IN NATURE AND TECHNOLOGY

(see e.g. [38] for an overview) and plate tectonics [13], respectively. Of course such phenomena are not limited to Earth but can take place also in other planets and in stars [130].

Apart from such geo- and astrophysical phenomena, thermal convection is important also locally in nature and technology. Examples from daily life are heating of water in a pot, air conditioning (e.g. in aircraft cabins as in figure 1.2), exhaust transport in chimneys, the local upwind zones used by birds of prey and gliders to gain height above the ground and further meteorological phenomena. Furthermore, in many technical applications heat exchangers play an important role (e.g. in nuclear power plants), which benefit from large heat fluxes caused by thermal convection.

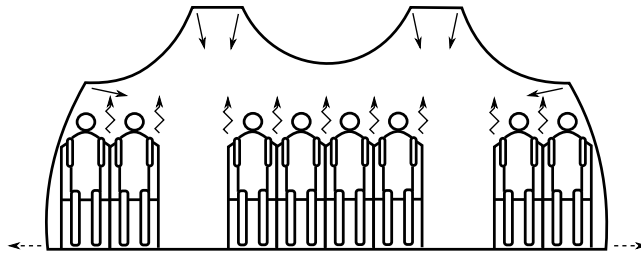


FIGURE 1.2: Schematic of the air conditioning in an aircraft cabin according to Kühn *et al.* [78]. The warm air rises above the warm passengers (squiggly arrows), mixes with the cold air entering the cabin through air inlets (solid straight arrows) and leaves the cabin through outlets close to the passengers' feet (dashed arrows).

What all these examples have in common is their complexity. Not only the geometry is rather complicated in many technical applications (e.g. aircraft cabin, figure 1.2), but also effects apart from thermal convection play an important role. These additional effects range from rotation of the system (e.g. in the Earth's atmosphere), interaction with an electromagnetic field (as in the Earth's core), moisture (important for meteorology, as e.g. in [131]), superposed pressure gradients, which additionally drive the flow (cf. ventilation) and many more. Furthermore the considered fluids might be non-Newtonian and may further have strongly temperature and pressure dependent material properties.

Since for such systems and fluids fundamental research becomes very difficult due to the large amount of free parameters, a simplified system is desirable for studying pure thermal convection. One possibility of such a simplified system is the so-called *Rayleigh–Bénard convection* (RBC). As described in the next chapters, RBC is usually studied in generic geometries under the consideration of generic fluids, which leads to simple (approximated) conservation laws of mass, momentum and energy, and allows to study the fundamentals of this *wide-spread type of fluid motion*.

## 2 The classical Rayleigh–Bénard problem

A generic system in which thermal convection has been widely studied is Rayleigh–Bénard convection (RBC). It is named after Henri Bénard [11] being the first to conduct quantitative measurements, with a thin fluid layer heated from below and a colder free upper surface. Bénard found for sufficient temperature difference, that the fluid layer becomes unstable, thermal convection takes place and structures of finite size develop. Original sketches by Bénard showing the typical hexagonal structure are depicted in figure 2.1.

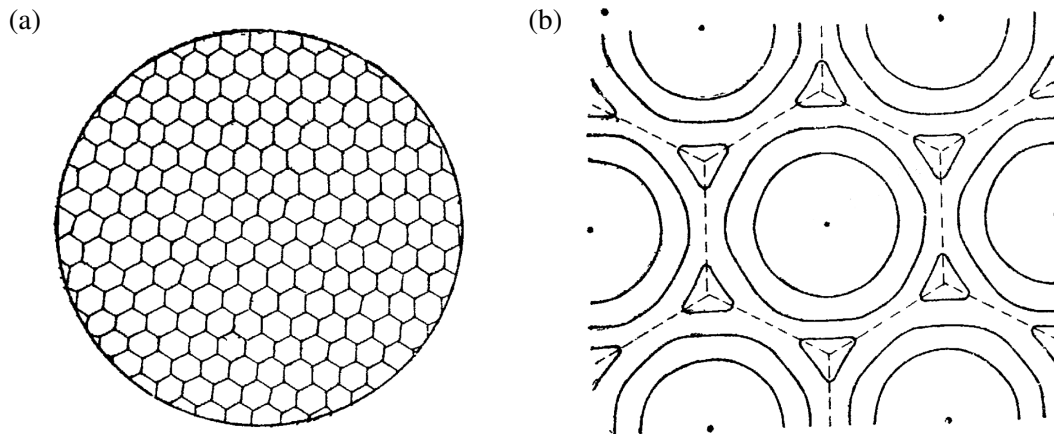


FIGURE 2.1: Sketches from the original paper by Bénard [12]. (a) Hexagonal cells developing in a thin fluid layer viewed from above. (b) Close up view on a single cell and its neighbors (dashed lines). The solid circles represent roughly the deformation of the free surface in the experiments, while the black dots indicate the points of largest depression.

The second person giving RBC its name was Lord Rayleigh [85]. He described Benard's result as follows:

*The layer rapidly resolves itself into a number of cells, the motion being an ascension in the middle of a cell and a descension at the common boundary between a cell and its neighbours.*

– Lord Rayleigh [85]

Rayleigh theoretically investigated the onset of thermal convection in an infinite fluid layer between heated bottom and cooled top plates, which are assumed to be solid and stress-free. He derived that there is a critical temperature difference  $\Delta$  for the onset of convection. This

## 2 THE CLASSICAL RAYLEIGH–BÉNARD PROBLEM

critical  $\Delta$  depends on the distance  $H$  between the plates and the physical properties of the fluid. It should be noted that the result derived by Rayleigh disagrees with the experimental results by Bénard, as Rayleigh neglected the free upper surface and the corresponding effects caused by the surface tension, which were present in Bénard experiments. Already Bénard himself suspected, that inhomogeneities of the surface tension by its temperature dependence may be crucial for the onset of convection [92]. The experiments by Block [15] and the theoretical description by Pearson [95] confirmed that the patterns observed by Bénard can be caused only by gradients of the surface tension. To distinguish between the effect of surface tension and the purely buoyancy driven flow, the surface tension affected flow is known today as Bénard–Marangoni or thermocapillary convection [48].

In his derivations Rayleigh simplified the equations describing the conservation of mass, momentum and energy by assuming a Newtonian fluid with constant viscosity  $\mu$ , thermal conductivity  $\Lambda$  and specific heat capacity at constant pressure  $c_p$ . The buoyancy force is assumed to be proportional to the temperature, by linearizing the temperature dependence of the density and introducing the isobaric thermal expansion coefficient  $\alpha$ . Additional compressibility effects are neglected. For thermal convection in laboratories (in contrast to e.g. convection in the Earth’s core) it is reasonable to further use a constant gravitational acceleration  $g$ . Effects like heat radiation or additional external forces (e.g. electromagnetic ones) are neglected.

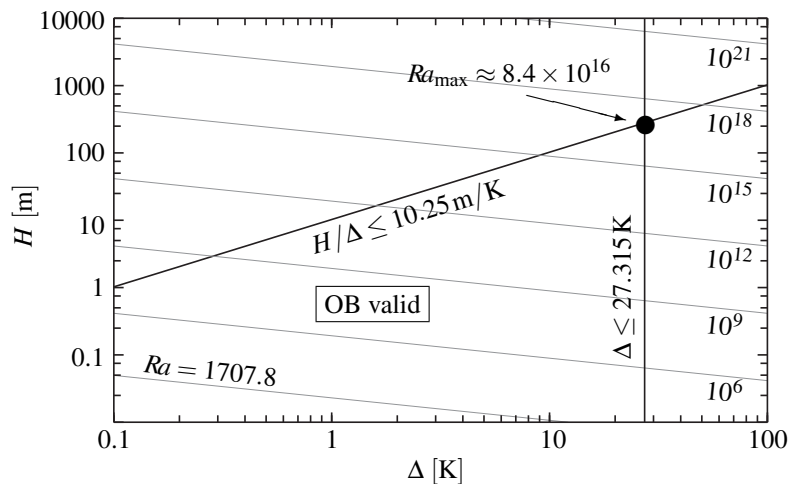


FIGURE 2.2: Limits of the Oberbeck–Boussinesq approximation (OB) in terms of the temperature difference  $\Delta$  and the distance  $H$  between the bottom and top plates, respectively. The limits are calculated for air at standard conditions ( $T = 273.15\text{ K}$ ,  $P = 1013.25\text{ hPa}$ ) according to Gray & Giorgini [49] and based on material properties given in [148]. Lines of constant Rayleigh number ( $H \sim \Delta^{-1/3}$ ) are depicted in grey.

This set of assumptions is known as Oberbeck–Boussinesq (OB) approximation [17, 93]. Deviations from this approximation may occur in case of large temperature or static pressure differences. What exactly *large* means in this case, was elaborated by Gray & Giorgini [49]. They derived the regions of validity of the OB approximation in terms of residual errors for

general Newtonian fluids. They assumed that the OB approximation holds, if all residual errors, which are associated with the temperature- and pressure-dependencies of the material properties, are less than ten percent. This results in limitations of the temperature difference and the height of the fluid layer (i.e. differences of the static pressure). For example in the case of air at ambient conditions, the temperature difference  $\Delta$  is limited to about 30 K, while the height of the fluid layer  $H$  shall not be larger than about  $10 \text{ m/K}\Delta$  (see figure 2.2). If this requirement is fulfilled, the equations describing the conservation of mass, momentum and energy are reduced to the following set of equations:

$$\begin{aligned}\frac{\partial \vec{u}}{\partial t} + \vec{\nabla} \cdot (\vec{u} \otimes \vec{u}) &= -\frac{1}{\rho} \vec{\nabla} p + \nu \underline{\Delta} \vec{u} + \alpha g (T - T_M) \hat{e}_z, \\ \frac{\partial T}{\partial t} + \vec{\nabla} \cdot (\vec{u} T) &= \kappa \underline{\Delta} T, \\ \vec{\nabla} \cdot \vec{u} &= 0.\end{aligned}\tag{2.1}$$

Here  $\vec{u}$  is the velocity,  $t$  is time,  $p$  is the pressure reduced by the (constant) static pressure at mid height,  $T$  is the temperature,  $T_M$  is the system's mean temperature and  $\hat{e}_z$  is the unit vector in vertical direction. Further,  $\kappa = \Lambda / (\rho c_p)$  is the thermal diffusivity and  $\nu$  is the kinematic viscosity (i.e. the momentum diffusivity).

By applying Buckingham's  $\Pi$ -theorem [21, 22], under the assumption that the OB approximation is valid and  $g$  is constant, one obtains that two dimensionless parameters are sufficient for dynamic similarity (i.e. the system is described by the same dimensionless equations). These are by convenience the Rayleigh number  $Ra = \alpha g \Delta H^3 / (\nu \kappa)$ , which is roughly spoken the ratio of the convective timescale by buoyant motion and the diffusive time scale, and the Prandtl number  $Pr = \nu / \kappa$ , which characterizes the fluid as the ratio of diffusion of momentum and of thermal energy.

Besides dynamic similarity, also geometric similarity is required to obtain similar results in different realizations of an experiment or a simulation. Geometric similarity is connected to the boundary conditions for equations (2.1). In case of the temperature, Dirichlet boundary conditions at the horizontal heating and cooling plates are chosen, such that temperature levels  $T_{\text{top}}$  and  $T_{\text{bottom}}$  are fixed at these surfaces with  $T_{\text{top}} < T_{\text{bottom}}$ . In addition, temperature boundary conditions at the vertical walls are required if in contrast to Rayleigh's calculations the horizontal extend of the fluid layer is limited. The generic choice is adiabatic sidewalls, i.e. von Neumann boundary conditions with a vanishing temperature gradient in the wall-normal direction. Solid walls are usually assumed to be impermeable, i.e. the wall-normal velocity component vanishes at the walls. Further, either a no-slip condition, i.e. the velocity component tangential to the wall vanishes at the wall, or a free-slip condition is set at the wall, which means that the wall-shear stress vanishes at the walls.

## 2 THE CLASSICAL RAYLEIGH–BÉNARD PROBLEM

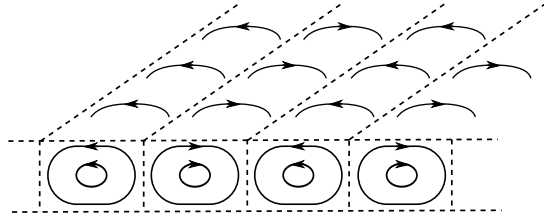


FIGURE 2.3: Sketch of two-dimensional rolls as the flow state at the onset of convection in a fluid layer with large lateral extent according to Getling [48].

The latter choice results in different critical Rayleigh numbers  $Ra_c$  for the onset of motion in an infinite layer of fluid. For stress-free boundaries (free-slip condition), Rayleigh's critical temperature difference mentioned above results in  $Ra_c = 27\pi^4/4 \approx 657.5$ , while for rigid walls (no-slip)  $Ra_c = 1707.8$  is obtained [48]. These results are independent of the Prandtl number  $Pr$ . As soon as the fluid layer's lateral extent is limited,  $Ra_c$  increases depending on the aspect ratio, which is the ratio of lateral extent and height of the fluid layer, and the shape of the container. For example, in a rigid cylindrical container with equal diameter and height the onset of motion takes place at  $Ra_c \approx 4000$  [23].

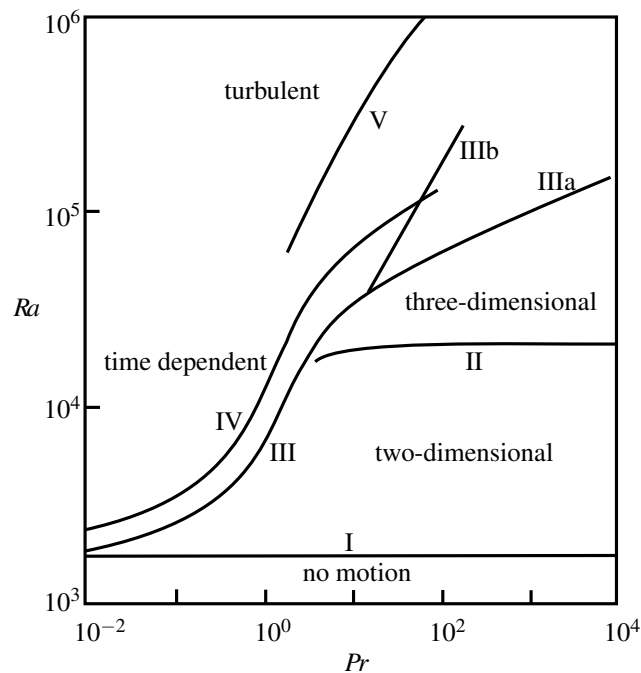


FIGURE 2.4: Sketch of a regime diagram according to Busse [24] and Krishnamurti [75],[76],[77] based on experimental results for large aspect ratio. The lines indicate the onset of two-dimensional steady rolls (I), steady three-dimensional flow (II), time dependent flow with a single frequency (III) at single spots (IIIa), in the whole fluid layer (IIIb) and with the doubled frequency in addition (IV). For sufficiently large  $Ra$  (V) the time-dependence becomes chaotic and may be considered as turbulent.



When the Rayleigh number (and the aspect ratio) is sufficiently large, motion takes place in form of quasi two-dimensional steady rolls (c.f. figure 2.3). If  $Ra$  is further increased, this steady flow structure undergoes transitions to more complex three-dimensional and even time-dependent flow structures depending on the Prandtl number  $Pr$  and the geometry of the container [24, 75, 76, 77]. A regime diagram showing roughly the transition to time-dependent flow is depicted in figure 2.4. The time-dependence of the flow, which can be represented at first by a single frequency, becomes for certain higher  $Ra$  more complicated and even chaotic. This chaotic state does not show the characteristics of a turbulent flow and can thus be considered to a certain extent as a laminar one [1]. Only for even higher  $Ra$  above a threshold  $Ra_t$  the laminar flow structure breaks up into small scale fluctuations and the bulk flow can be considered as turbulent [5].

By all this, RBC is a system in which a variety of physical phenomena can be studied under controlled conditions. Besides hydrodynamic stability [30], pattern formation [37] and the onset of chaotic motion and turbulence [16], RBC is as mentioned above a generic system for investigating turbulent thermal convection. The latter is connected to more fluid-mechanical questions, such as the convective heat transfer and the interaction of boundary layers with the bulk flow. In the present thesis, the focus is placed on RBC as a (turbulent) buoyancy-driven interior flow as elaborated in the next chapter.



### 3 Turbulent Rayleigh–Bénard convection

In 1978 Friedrich Busse described in his review paper on Rayleigh–Bénard convection the turbulent state as follows:

*At moderate Prandtl numbers, turbulent convection at Rayleigh numbers of the order of  $10^5$ – $10^7$  exhibits the typical structure of relatively steady large-scale cells in which highly fluctuating (both in space and in time) small-scale convection elements are imbedded.*

– Busse [24]

Even though more than 75 years of research had passed after Bénard’s experiments, he concluded that

*Little is known about this form of convection which seems to combine random processes with the permanence of a large-scale organizing structure.*

– Busse [24]

Since then, the investigation of RBC have been focused more and more on the turbulent state, such that in the last few decades a wide knowledge has been gained as it is collected in the review papers by Siggia [129], Ahlers *et al.* [5] and Lohse & Xia [84].

For the investigation of the turbulent state, sufficiently large Rayleigh numbers are required. Since in practice the limitations of the Oberbeck–Boussinesq approximation restrict the experimentalists to small temperature differences  $\Delta$ , large  $Ra$  can be achieved by large heights  $H$  of the fluid layer. To retain the feasibility of laboratory experiments, small aspect ratios (i.e. lateral extent per height) are usually considered. Otherwise, the experiments become too large and providing constant temperatures of the heating and cooling plates is difficult. Thus, in the last years usually aspect ratios of order one have been investigated. Nevertheless, for air or water at ambient conditions as working fluids  $Ra$  not larger than about  $10^{12}$  can be reached in practice. In air such high  $Ra$  can be only achieved in large-scale experiments like the so-called *Barrel of Ilmenau*, which is a cylindrical container with a height of more than six meters [104]. To obtain even larger  $Ra$ , fluids with extreme material properties, as they occur e.g. close to the critical point, are used. Today, in the *U-Boot of Göttingen* Rayleigh numbers up to  $10^{15}$  can be achieved. This is realized by using sulfur hexafluoride ( $SF_6$ ) at room temperature and pressurized up to 19 bar in a high-pressure vessel which contains Rayleigh–Bénard experiments of height 2.24 m

### 3 TURBULENT RAYLEIGH–BÉNARD CONVECTION

(aspect ratio 1/2) [6] and 1.12 m (aspect ratio 1) [61]. A different approach was first made by Threlfall [144], being the first who studied RBC of gaseous helium at a low mean temperature of about 4 K. By changing the pressure, eleven orders of magnitude in  $Ra$  can be investigated, but there  $Pr$  varies as well [31, 64].

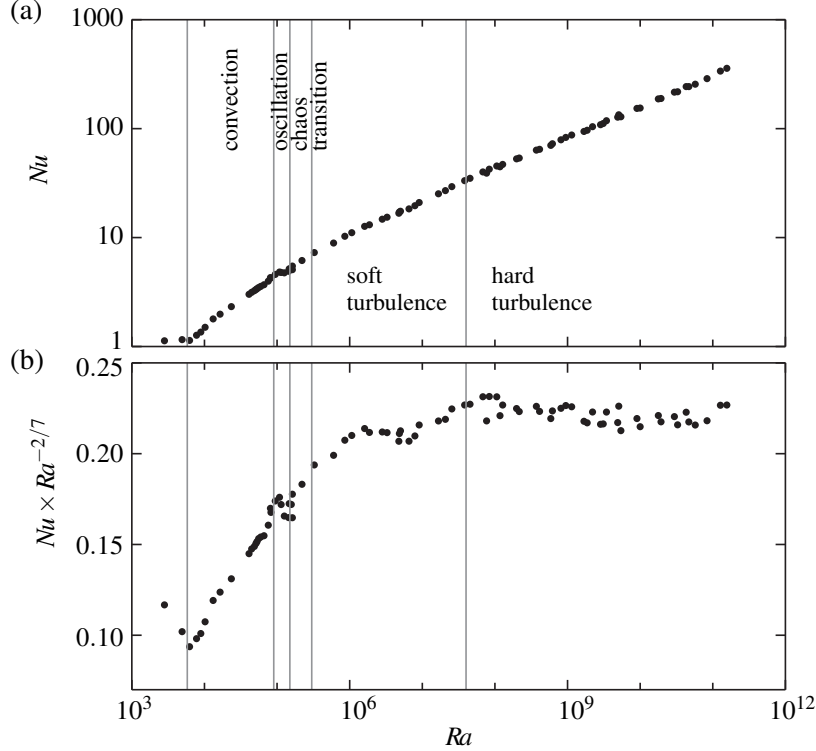


FIGURE 3.1: Experimental results for the the Nusselt number  $Nu$  in dependence of the Rayleigh number  $Ra$ , obtained in a cylindrical container with equal diameter and height filled with helium at temperature 4 K and for different working pressures. The  $Ra$  range is divided into several regimes of convection by vertical lines. (a) on double logarithmic axes, and (b)  $Nu$  reduced by  $Ra^{2/7}$  to highlight the differences between soft and hard turbulence. Both the experimental results and the regimes are according to Heslot *et al.* [64].

When  $Ra$  is sufficiently high, the fluid reacts with an onset of motion causing an increase of the heat flux from the bottom to the top plate. The time- and spatially averaged heat flux can be expressed by the Nusselt number  $Nu$ , which is the ratio of this heat flux to the heat flux in a solid body with the same heat conductivity  $\Lambda$ . Further, the strength of the motion can be expressed by the Reynolds number  $Re$  based on the distance between the plates and a characteristic velocity. Since there is no prescribed mean flow in RBC, several choices of the characteristic velocity are possible as discussed for example by Ahlers *et al.* [5]. In the last few decades the dependence of these two quantities  $Nu$  and  $Re$  on  $Ra$  and  $Pr$  (and the geometry of the container) have been studied extensively [5]. It has been obtained, that there is no universal scaling law describing for example  $Nu(Ra)$ , since the scaling changes due to different regimes of convection. These changes do not occur only due to the onset of turbulence, but even the turbulent regime can

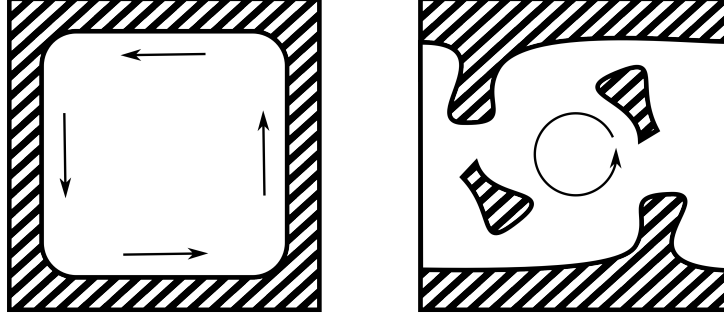


FIGURE 3.2: Sketch of the structure of (a) the velocity and (b) the temperature field in a closed Rayleigh–Bénard sample at sufficiently large  $Ra$  according to Grossmann & Lohse [50]. (a) A turbulent bulk flow (white) causes laminar boundary layers attached to all rigid walls (striped). (b) Thermal plumes detach from the thermal boundary layers at the heating and cooling plates, and are treated (from the modelling point of view) as part of these boundary layers. (Sketch similar to Ahlers *et al.* [5].)

be splitted up as it is indicated in figure 3.1 showing  $Nu$  obtained in the helium experiments mentioned above. The transition from a so-called *soft turbulent* regime to a *hard turbulent* regime is visible in  $Nu(Ra)$  [27] (when considering the reduced Nusselt number  $Nu \times Ra^{-2/7}$  as in figure 3.1b). It is further characterized by changes of the temperature statistics in the center of the container [64].

There are several theoretical predictions for the scaling of  $Ra$  and  $Nu$  (for a detailed overview see [5]). Perhaps the most established ansatz so far is the theory by Grossmann & Lohse [5, 50, 51, 52, 53, 54, 55, 134]. It is based on the assumption, that the flow can be decomposed into a turbulent bulk flow, with large coherent structures consisting of packages of hot and cold fluid (so-called *thermal plumes*) and viscous and thermal boundary layers attached to the solid walls (see figure 3.2). Further, analytical relations for the temporal and spatial averages of the viscous dissipation rate  $\varepsilon_u \equiv \nu(\Delta \vec{u}^2/2 - \vec{u} \cdot \Delta \vec{u})$  and the thermal dissipation rate  $\varepsilon_T \equiv \kappa(\vec{\nabla} T)^2$  are used [128]. The latter ones are splitted into contributions of the boundary layers and the bulk flow. These contributions are modelled separately by using the assumption of homogeneous isotropic turbulence [101] in the bulk region and by assuming laminar boundary layers of the Prandtl–Blasius–Pohlhausen type [14, 99, 102] caused by a mean wind. Several extreme cases (e.g. large  $Pr$ ) are considered and connected via certain crossover functions  $f$  and  $g$ . This all leads to the two coupled equations

$$\begin{aligned}
 (Nu - 1)RaPr^{-2} &= c_1 \frac{Re^2}{g(\sqrt{Re_L}/Re)} + c_2 Re^2 \\
 Nu - 1 &= c_3 \sqrt{RePrf \left[ \frac{2aNu}{\sqrt{Re_L}} g \left( \sqrt{\frac{Re_L}{Re}} \right) \right]} + c_4 PrRef \left[ \frac{2aNu}{\sqrt{Re_L}} g \left( \sqrt{\frac{Re_L}{Re}} \right) \right]
 \end{aligned} \tag{3.1}$$

### 3 TURBULENT RAYLEIGH–BÉNARD CONVECTION

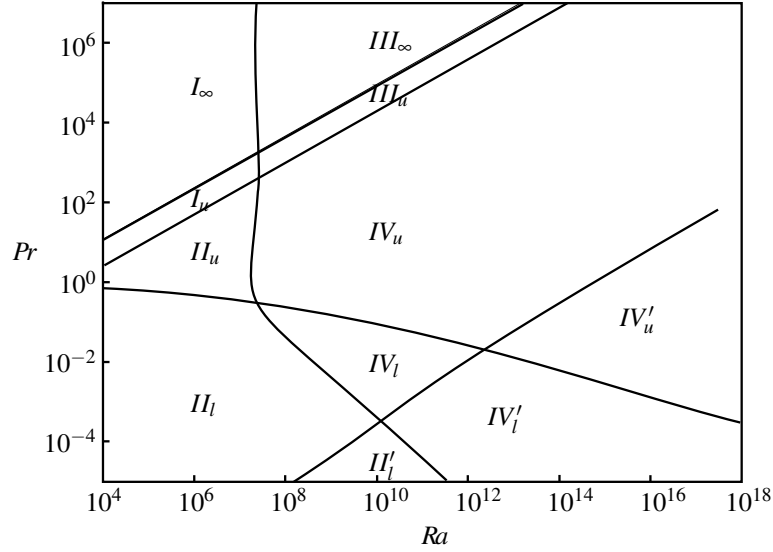


FIGURE 3.3: Regimes in the  $Ra - Pr$  plane according to the theory by Grossmann & Lohse [50][134]. The numbers indicate whether the boundary layers ( $I$ ), the bulk flow ( $IV$ ) or a mixture of them ( $II$ ,  $III$ ) dominate the flow. Further the indices separate with respect to the ratio of the thicknesses of thermal and viscous boundary layers. The regimes denoted with an additional prime, are supposed to be *ultimate*, i.e. turbulent boundary layers dominate the flow [55].

for  $Nu$  and  $Re$  with  $f(x) = (1 + x^4)^{-1/4}$  and  $g(x) = x(1 + x^4)^{-1/4} = xf(x)$ . The six free parameters  $a$ ,  $Re_L$ ,  $c_1$ ,  $c_2$ ,  $c_3$ ,  $c_4$  are fixed by fitting the theory to experimental (and numerical [134]) data. From the theory, regimes in the  $Pr$ - $Ra$  space can be obtained, in which either the boundary layers or the bulk flow dominate the volume- and time-averaged dissipation rates. These regimes are depicted in figure 3.3.

The boundary layers occurring in turbulent RBC, which are assumed to be laminar in the original theory by Grossmann and Lohse, may become turbulent like the bulk flow, as it was already discussed by Kraichnan [74] and later Spiegel [130]. Such a transition is expected to take place at sufficiently high  $Ra$ . It would cause changes in the scalings of  $Nu$  and  $Re$ , such that an additional regime of convection, which is often called as *ultimate*, might be present. The scalings in this regime would be of large importance, as for example in stars the Rayleigh numbers exceed values of  $10^{20}$  [130], which can not be studied in laboratory experiments so far. Within their theory Grossmann & Lohse [55] predicted that the onset of this ultimate regime is Prandtl number dependent (see also figure 3.3) and characterize it further in terms of scaling exponents.

The experimental evidence for the transition is thereby rather controversial (as discussed e.g. by Ahlers *et al.* [6]). At present only the experiments with helium at around 4 K and with pressurized  $SF_6$  can reach the required  $Ra$  (see the discussion above). Figure 3.4 depicts a collection of experimental results for the reduced Nusselt number by several groups. They

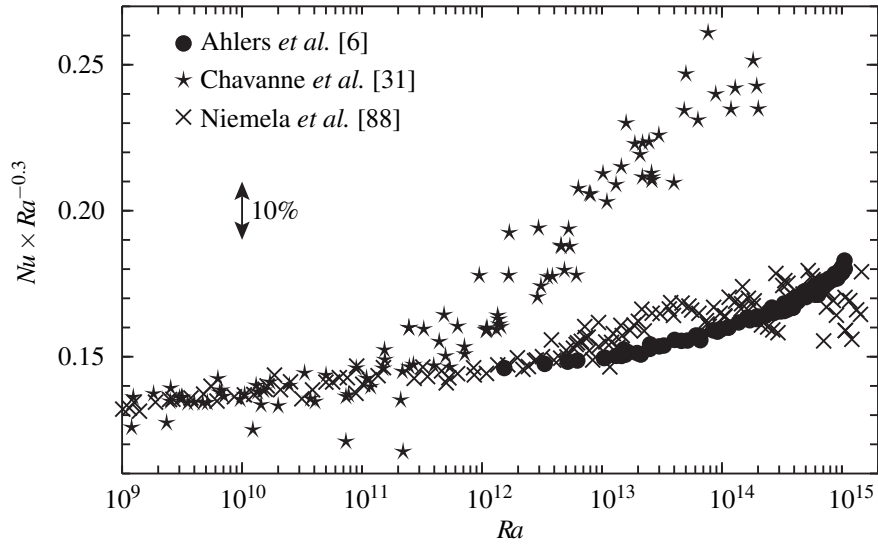


FIGURE 3.4: Experimental results for the Nusselt number at high  $Ra$  showing strong deviations for  $Ra \gtrsim 10^{11}$ . Experiments by Niemela *et al.* [88] and Chavanne *et al.* [31] were conducted in helium at temperature around 4 K, while in the experiments by Ahlers *et al.* [6] sulfur hexafluoride at ambient temperature and under high pressure was used. The container in all this experiments was a cylinder with a height of twice the diameter.

indicate large differences for  $Ra \gtrsim 10^{11}$  large differences. This makes an interpretation in terms of scaling exponents difficult. Furthermore, due to the required shielding of the whole experiment to suppress heat losses, a detailed analysis of the boundary layers and the bulk flow is almost impossible. Therefore, it is difficult to use the experiments for testing the fundamentals of the theory, and only predictions like scaling exponents can be checked.

Thus, in the next section a different approach for the study of turbulent RBC is described, which consists in the usage of so called Direct Numerical Simulations (DNSs). Also the feasibility of studying large  $Ra$  by means of DNSs is discussed.





## 4 Numerical investigation of turbulent Rayleigh–Bénard convection

Apart from experiments, turbulent Rayleigh–Bénard convection (RBC) can be investigated by solving the set of equations (2.1) for given boundary and initial conditions. In contrast to the case of a laminar flow, the non-linearities in the equations become important for turbulent RBC, such that solving these equations analytically is hardly possible. Therefore, the partial differential equations (PDEs) can be discretized and the discrete equations can be solved numerically. For the numerical solving of partial differential equations as (2.1) a broad spectrum of methods exists in the literature, cf. the book by Ferziger & Perić [43].

Like any other turbulent flows, turbulent RBC is thereby a multiscale problem, i.e. spatial and temporal scales of various size are present and cannot be neglected as the non-linearities lead to a mixing of different wavelengths and frequencies in contrast to linear PDEs like e.g. the wave equation [142]. Therefore, either all relevant scales are considered, which is an approach called as *Direct Numerical Simulation* (DNS), or (some) small scales are modelled by empirical turbulence models. In the following only DNSs are further discussed.

If the computational domain is bounded in horizontal direction by solid walls, the domain's extent limits the spatial scales from above. In contrast, if an infinite layer of fluid is considered, which is realized in numerical simulations by choosing a certain periodicity length, this length (together with the height  $H$ ) determines the physics of the flow. As pointed out by Hartlep *et al.* [60], for periodicity lengths up to five times the height, the heat flux and connected to this also the global flow is still affected by the periodicity of the domain.

The lower limit of the spatial and temporal scales is given (up to a multiplicative constant) by the Kolmogorov [73] scales (for  $Pr \leq 1$ ) and the Batchelor [10] scales (for  $Pr > 1$ ), respectively. Smaller scales are not present due to dissipation. To resolve also the smallest scales in the DNSs a sufficient spatial resolution and time-step size is required.

To determine whether a single simulation (i.e. for a set of parameters  $Ra$ ,  $Pr$ ) is sufficiently resolved, a posteriori checks are required. These can be realized by comparison of the numerical results calculated on different computational meshes, by comparison of the numerical results with experimental ones or by comparison of the spatial resolution with realized Kolmogorov (or Batchelor) scales (see [110] for an overview). Since repeating simulations because of insufficient resolution is expensive and time-consuming, estimates for the proper computational

## 4 NUMERICAL INVESTIGATION OF TURBULENT RBC

mesh resolution are required.

Usually, there are different estimates for the boundary layer region and for the bulk flow region. The latter is commonly assumed to be (local) homogeneous and isotropic [101], while in the boundary layers the flow is highly anisotropic. In the following, we only discuss the case  $Pr \leq 1$ , which is most important in the present thesis. The Batchelor scales, which become more restrictive for  $Pr > 1$ , are connected to the Kolmogorov scales here discussed by a factor  $\sqrt{Pr}$  [121]. When assuming homogenous and isotropic turbulence in the bulk region, the Kolmogorov length scale  $\eta_K$  is given (up to a constant factor) by  $\eta_K = \nu^{3/4} \varepsilon_u^{-1/4}$ , with  $\varepsilon_u$  being the viscous dissipation rates as defined in chapter 3. For the volume- and time-averaged viscous dissipation rates  $\langle \varepsilon_u \rangle_{V,t}$  occurring in turbulent RBC the analytical relation

$$\langle \varepsilon_u \rangle_{V,t} = \frac{\nu^3}{H^4} (Nu - 1) \frac{Ra}{Pr^2} \quad (4.1)$$

holds [128]. Based on these averaged dissipation rates, a mean Kolmogorov length scale

$$\frac{\eta_K}{H} = \frac{\sqrt{Pr}}{(Nu - 1)^{1/4} Ra^{1/4}} \quad (4.2)$$

is obtained, which serves commonly as an estimate for the bulk resolution by requiring that the mesh spacing is smaller than this length scale [121]. It should be noted, that in the literature further other requirements exist [57, 110], which connect the required mesh spacing and the mean Kolmogorov scales in different ways.

Finding an appropriate estimate for the resolution of the boundary layers is more difficult, since details of the boundary layer structure are required. Shishkina *et al.* [121] derived estimates under the assumption of boundary layers of the Prandtl–Blasius–Pohlhausen type, with the result (for  $3 \times 10^{-4} \leq Pr \leq 1$ )

$$\frac{\eta_K}{H} = \frac{Pr^{0.5355 - 0.033 \log_{10} Pr}}{2^{3/2} a Nu^{3/2}} \quad (4.3)$$

and  $a$  is a constant of order one, which can be determined from experiments. (Estimates for other  $Pr$  are also given in their paper.)

When assuming, that  $Nu \sim Ra^{3/10}$ , which is roughly fulfilled in the hard turbulent regime but below  $Ra = 10^{11}$  for  $Pr \approx 1$  (see figure 3.4), it is obtained from equation (4.2) that in the bulk  $\frac{\eta_K}{H} \sim Ra^{-13/40}$  and in the boundary layer region from equation (4.3) that  $\frac{\eta_K}{H} \sim Ra^{-9/20}$ . Thus, the computational effort, which is connected to the spatial resolution, grows with increasing  $Ra$  quite rapidly. Therefore, the largest  $Ra$ , for which properly resolved three-dimensional DNSs can be performed today, are still far from the ultimate regime of convection as proposed on the basis of experimental results.

Thus, for very large  $Ra$  at which the ultimate regime is expected, numerical simulations cannot

replace the experiments. But at lower  $Ra$  between about  $10^7$  and  $10^{12}$ , for which experiments with optical access are feasible, the latter can be complemented by DNSs, which in contrast to the experiments provide full information at any point of the flow field. In the experiments the temperature boundary conditions (i.e. fixed temperature on the horizontal and vanishing temperature gradient at the vertical walls) cannot be realized perfectly due to the finite heat conductivity of the used materials. Furthermore, effects like heat radiation or Coriolis forces by the Earth's rotation are always present in experiments. The latter insufficiencies are not present in DNSs. In addition the instantaneous and fully resolved temperature and velocity fields, which are available from DNSs in the whole domain, can, to my best knowledge, not be obtained today from experiments by any existing measurement technique. On the other hand, the physical time simulated in DNSs is strongly limited due to the large computational effort, such that slow transients, as they occur in turbulent RBC [5], are difficult to investigate by means of DNSs.

Nevertheless, nowadays, DNSs are the most reliable tool to study turbulent RBC in detail on time scales of a few ten to hundred turnover times for Rayleigh numbers up to  $10^{12}$ .



## 5 Recent questions and recurrent thread

As discussed already in chapter 3, the occurrence of the ultimate regime of thermal convection is closely related to the transition of the boundary layers (BLs) from the laminar to the turbulent state. To identify such a transition, first of all the laminar state must be well-investigated. Thus, over the last years a large effort has been made to study the viscous and thermal boundary layers in experiments and in numerical simulations (see [32] for an overview) and to compare the results with existing theoretical descriptions. In the case of laminar BLs the theoretical descriptions by Prandtl, Blasius and Pohlhausen (PBP) (cf. [112]) is usually used to estimate the heat flux, the kinetic energy and the required spatial resolution in Direct Numerical Simulations (DNSs) as described in chapters 3 and 4. Such comparisons are often made with respect to temporally (and sometimes even spatially) averaged temperature and velocity profiles, resulting in visible disagreement with the PBP theory (except of the cases of  $Pr > 1$  and moderate  $Ra$ , when a sophisticated rescaling of the data is applied [32]). This is not surprising, as in this theory, the thermal and viscous BLs are assumed to be laminar and pressure gradients as well as buoyancy are neglected. Since RBC is a purely buoyancy driven flow and due to the complicated flow structure pressure gradients are expected to be important, some of the assumptions of the PBP theory are not valid. Thus it can not be expected that the PBP theory can precisely describe the BLs in turbulent RBC.

To obtain a better description of the BLs in turbulent RBC, it is insufficient to study averaged temperature and velocity profiles, as the spatial and temporal evolution of the BLs is a major issue of a BL theory. Therefore the idea was to evaluate from DNS data local and instantaneous BL characteristics like the wall shear stress, the wind velocity and related quantities. The computational domain is chosen to be a cylinder with equal diameter and height, since such a container is used in many experiments. In RBC there is no prescribed mean flow and thus no preferential direction of the flow. Thus the flow's azimuthal orientation in a cylindrical container is not fixed and reorientations (and similar processes) may occur from time to time [5]. Therefore, if a comparison with two-dimensional theories as the one by PBP is desired, an extraction of the large-scale circulation from instantaneous flow fields is required before in a second step the boundary layer characteristics can be evaluated and compared to theory. In chapter 6 (published in the Journal of Fluid Mechanics [155]), such an extraction method is introduced and applied to DNS data for  $Pr = 0.786$  and  $Ra$  between  $10^5$  and  $10^9$ . Further, an analysis technique of the BL characteristics is developed and tested in detail for fixed  $Ra$  and

## 5 RECENT QUESTIONS AND RECURRENT THREAD

then applied to different  $Ra$ . It reveals, besides others, that the wind is not constant along the bottom plate of the container. Therefore it is not surprising to find that e.g. the growth of the thickness of the BLs does not follow the predictions of the PBP theory. Furthermore, the ratio of the thicknesses of the thermal and viscous BL is found to be almost twice larger than predicted by the PBP theory.

Since this ratio is one of the main ingredients of the estimates for the required spatial resolution of the BLs, it is reasonable to compare these estimates with the DNS results as it is done in chapter 7 (published as a conference proceeding in a book by Springer [157]). The main result is, that the estimates are not restrictive enough. Finding better estimates based on an improved BL theory is therefore an additional motivation for the BL study.

A first step in finding a better description of the BLs in turbulent RBC is made in chapter 8 (published in the Journal of Fluid Mechanics [119]), in which the PBP theory is extended to a non-vanishing pressure gradient, while buoyancy remains neglected. The resulting BL equations are of the Falkner & Skan [42] type (see also [112]). The pressure gradient is connected to an angle of attack of the global flow (wind) approaching the horizontal plates, which is caused by the lateral walls. The predictions of the new theory are compared with DNS results for  $Pr = 0.786$  and  $Pr = 4.38$  for  $Ra$  between  $10^7$  and  $10^9$  and show much better agreement with respect to the ratio of the BL thicknesses.

A further step is then made in chapter 9 (published in Physical Review E [127]), where analytical relations for the ratio of the BL thicknesses for infinitesimal and infinite  $Pr$  at arbitrary angle of attack are derived. A comparison with DNS results for  $Pr$  between 0.1 and 10 and  $Ra$  between  $10^7$  and  $10^9$ , reveals that in this parameter range the angle of attack can be assumed as constant and that the resulting prediction of the ratio of the BL thicknesses fits much better than the PBP theory, which is a special case of the developed theory for a vanishing angle of attack. Further, the consequences for the estimates of the spatial resolution are analyzed, and the estimates are found to be more restrictive those based on the PBP theory [121].

Besides studying the boundary layer structure below the ultimate regime, there are attempts to use rough heating and cooling plates to reach the ultimate regime at lower  $Ra$ , which can be analyzed easier in experiments and also by DNSs. Isothermal rough surfaces, as considered in RBC, are difficult to realize in experiments due to the finite conductivity of the heating and cooling plates (cf. [105]). Further, the construction of plates with different roughness configurations to study their influence is quite expensive. Therefore, DNS is an attractive tool to study the influence of rough surfaces on turbulent RBC. To avoid the above mentioned difficulties because of the azimuthal symmetry of a cylindrical container, for further studies box-shaped containers are used. In chapter 10 (published as a conference proceeding in a book by Springer [156]), the mean heat flux (which is related to the thickness of the thermal BL), the mean kinetic energy and the global flow in a cubic container and in a cylindrical one are evaluated and compared for  $Pr = 0.786$  and  $Ra$  between  $10^5$  and  $10^7$ .

Since it is found that in a cubic domain the global flow structure changes at  $Ra \approx 10^6$  to a complicated diagonal flow, in a further study the ansatz of *quasi two-dimensional RBC*, known from experiments in water at  $Ra \gtrsim 10^{10}$  [167], is pursued. In these experiments a container of equal length and height and a depth of one fourth of the height is used. The resulting global flow structure is a single roll oriented orthogonal to the short direction of the container. In chapter 11 (published in *Physics of Fluids* [152]), the results of the DNSs for different aspect ratios of depth per height between 0.1 and 1 are analyzed, while  $Pr$  is fixed to 0.786 and  $Ra$  is varied between  $10^5$  and  $10^9$ . It is obtained that the global flow structure is strongly affected by the aspect ratio of the container. Nevertheless, for the aspect ratio of one fourth a comparable flow structure as in the experiments is found even though  $Ra$  is some decades smaller.

Within this geometry, the influence of different roughness configurations, represented by regularly distributed obstacles, are studied by means of DNSs in chapter 12 (under review by the *Journal of Fluid Mechanics* [154]). Apart from a two-dimensional study [125] and a study with modeled roughness [138], this is the first DNS study of three-dimensional RBC for different roughness configurations. Not only the influence of the obstacle height and width on the heat flux and the wind velocity is investigated, but also the heat flux increase due to the roughness is connected to single parts of the obstacles and an empirical description of this heat flux increase is given.





Part II

Results



## 6 Boundary layer structure analysis

**Citation and credit:** This chapter consists of a paper published in the Journal of Fluid Mechanics 697, pages 336–366, April 2012.

It is available online at <http://dx.doi.org/10.1017/jfm.2012.69>. With permission of Oxford University Press the authors' version of the paper is posted here.

©Cambridge University Press 2012

**Title:** Boundary layers and wind in cylindrical Rayleigh–Bénard cells

**Authors:** Sebastian Wagner, Olga Shishkina & Claus Wagner [155]

**Contribution:** I performed the numerical simulations, developed the analysis techniques, created all the figures and wrote the first version of the manuscript, which structure is preserved.

### Abstract

We analyse the wind and boundary layer properties of turbulent Rayleigh–Bénard convection in a cylindrical container with aspect ratio one for Prandtl number  $Pr = 0.786$  and Rayleigh numbers ( $Ra$ ) up to  $10^9$  by means of highly resolved direct numerical simulations. We identify time periods in which the orientation of the large-scale circulation (LSC) is nearly constant in order to perform a statistical analysis of the LSC. The analysis is then reduced to two dimensions by considering only the plane of the LSC. Within this plane the LSC is treated as a wind with thermal and viscous boundary layers developing close to the horizontal plates. Special focus is on the spatial development of the wind magnitude and the boundary layer thicknesses along the bottom plate. A method for the local analysis of the instantaneous boundary layer thicknesses is introduced which shows a dramatically changing wind magnitude along the wind path. Furthermore a linear increase of the viscous and thermal boundary layer thickness along the wind direction is observed for all  $Ra$  considered while their ratio is spatially constant but depends weakly on  $Ra$ . A possible explanation is a strong spatial variation of the wind magnitude and fluctuations in the boundary layer region.

## 6.1 Introduction

One of the classical problems in fluid dynamics is the flow driven by the temperature difference between a heated bottom and a cooled top plate. This is a simplified model for many convective flow phenomena occurring on the Earth, e.g. in the atmosphere, as well as extraterrestrial such as the convection in stars. Named after its first two investigators, Rayleigh–Bénard convection (RBC) has been studied for more than hundred years. Nevertheless it is still under extensive investigation, since many aspects are not yet well understood.

Over recent decades the scaling of two important system responses, the Nusselt number  $Nu$  and the Reynolds number  $Re$ , with the governing dimensionless parameters, the Rayleigh number  $Ra$  and the Prandtl number  $Pr$ , has been studied theoretically, experimentally and numerically. For recent reviews we refer to [5] and [84].

The flow typically found in Rayleigh–Bénard cells with aspect ratios (diameter/height) of order unity is characterized by the boundary layers (BLs) close to the rigid walls and the large-scale flow motion. Their interaction is a key point in understanding the system’s responses to the temperature difference and is the subject of several theoretical studies, among which [27, 50, 65, 74, 128] should be mentioned here. The theoretical models developed are in most cases based upon assumptions on the structure of the BLs and their interaction with the bulk region.

Besides checking whether the theories give accurate predictions of the convection system’s responses it is also necessary to verify the assumptions they are based on. In the Grossmann–Lohse (GL) theory the BLs are assumed to be of Prandtl–Blasius (PB) type [55] (up to a shear Reynolds number of  $Re_s \approx 420$ ). Prandtl–Blasius BL theory [113] is a successful approach to approximate the BLs occurring when a laminar and stationary wind of constant magnitude flows over a flat plate of semi-infinite length and infinite width. It not only gives an analytical solution (within a set of approximations) for the BL profile but also for the development of its width and other characteristics along the plate. In a confined Rayleigh–Bénard cell the situation is very different from a semi-infinite plate and a constant wind velocity. This might have a negligible influence on the mean heat flux (Nusselt number) scaling with the Rayleigh number, but can lead to deviations of other local quantities from the PB predictions.

The usual check for whether PB BLs occur is through the analysis of the time and spatially averaged vertical profiles of temperature and velocity [65, 103, 122, 135, 140, 145]. In some cases strong deviations from PB profiles are found. This is partially explained by recent studies of Zhou & Xia [173] and Zhou *et al.* [169] which show that an instantaneous analysis and a more complex rescaling lead to better agreement. These studies are focused on profiles averaged spatially over a small region around the vertical centreline of the cell, which make it impossible to compare them with predictions of the PB theory on the spatial development of certain BL characteristics like its thickness along the wind direction. In a recent paper by Zhou *et al.* [170],

in which the horizontal dependence of BL profiles is investigated by means of two-dimensional numerical simulations, it was found that the BL thickness develops in a complicated way along the wind direction. In the present paper we develop a method to analyse the spatial behaviour of instantaneous as well as time-averaged local profiles and BL characteristics.

To ensure that the results are not influenced by the two-dimensionality of the flow [114] as in quasi-two-dimensional experiments [167] and two-dimensional numerical simulations [139], we perform three-dimensional direct numerical simulations (DNS) of the turbulent flow within a cylindrical container with aspect ratio one. This geometry is used in many experiments because of its symmetry and certain experimental advantages. On the other hand this also introduces the disadvantage of the lack of asymmetries, which stabilise the large-scale circulation (LSC) for sufficiently large  $Ra$  and can simplify the analysis. Azimuthal re-orientations of the large-scale motion may occur in cylindrical containers as found in experiments [19, 36, 106] and numerical simulations [87, 132] as well.

To analyse the azimuthal orientations and to find a time period without major reorientations we use the method by Brown & Ahlers [19]. For such time periods the analysis of the flow is reduced to a plane in which the LSC is mainly located. Therefore the analysed fields are two-dimensional while they still contain threedimensional physics. A further analysis using different diagnostic functions shows that additional more complex modes like twisting [44, 45] and sloshing [20, 164, 165, 171] vanish statistically and do not disturb the time-averaged fields. To reduce the complexity of the wind analysis, the main focus is further on BLs occurring next to the heated bottom plate, namely along one line which is the wind direction. Besides its simplicity, this approach allows the comparison of the results with those of the two-dimensional PB theory.

The paper is organised as follows. In section 6.2 the numerical method and the simulation parameters are presented. Numerical results with respect to the Nusselt number are compared to experimental ones in section 6.3. Distributions of the local heat flux and the corresponding flow fields are also analysed there. In section 6.4 different procedures to determine the LSC plane within the cylindrical geometry and the proper timeaveraging period are described and compared. To perform the BL analysis a method to investigate local instantaneous profiles is suggested and validated in section 6.5. Here the main focus is on how to determine the BL thickness and the corresponding quantities in detail. In section 6.6 this method is applied to flow fields for different  $Ra$  and mean characteristics of the wind and BLs are studied. In particular the scalings of the mean quantities with  $Ra$  are investigated. The results obtained are compared in section 6.7 with existing theoretical approaches. Finally the results are summarized in section 6.8.

## 6.2 Numerical method and setup

Direct numerical simulations (DNS) of turbulent Rayleigh–Bénard convection have been performed using a fourth-order-accurate finite-volume code in cylindrical coordinates  $(r, \phi, z)$  together with semi-implicit time-integration as described in detail by Shishkina & Wagner [123]. The method was originally developed by Schmitt *et al.* [115] and is based on the volume-balance procedure by Schumann [116], staggered grids and uses the Chorin ansatz for pressure–velocity coupling.

The dimensionless conservation laws of momentum, energy and mass in the Oberbeck–Boussinesq approximation with gravitational acceleration in the  $z$ -direction read:

$$\begin{aligned}\partial_t \vec{u} + \vec{u} \cdot \vec{\nabla} \vec{u} &= -\vec{\nabla} p + \nu_1 \vec{\nabla}^2 \vec{u} + T \vec{e}_z, \\ \partial_t T + \vec{u} \cdot \vec{\nabla} T &= \nu_2 \vec{\nabla}^2 T, \quad \vec{\nabla} \cdot \vec{u} = 0.\end{aligned}\tag{6.1}$$

Here  $\partial_t$  stands for the partial derivative with respect to time  $t$  and  $\vec{u}, T, p, \vec{e}_z$  denote the dimensionless velocity, temperature, dynamic pressure and unit vector in  $z$ -direction, respectively. The computational domain is a cylindrical container with aspect ratio  $\Gamma = \widehat{D}/\widehat{H} = 1$  where  $\widehat{D}$  stands for the diameter and  $\widehat{H}$  for the height of the container, where the hat denotes a dimensional quantity. The equations are closed by the following set of boundary conditions: fixed temperatures on bottom and top plates, an adiabatic vertical wall and no-slip condition on all walls. If the cylinder diameter  $\widehat{D}$  and the free-fall velocity  $(\widehat{\alpha}\widehat{D}\widehat{g}\widehat{\Delta})^{1/2}$  are used as references for distance and velocity (while their ratio is the reference for the time), and the temperature is made dimensionless by  $T = (\widehat{T} - \widehat{T}_M)/\widehat{\Delta}$ , this yields parameters  $\nu_1 = Pr^{1/2}Ra^{-1/2}\Gamma^{-3/2}$  and  $\nu_2 = Ra^{-1/2}Pr^{-1/2}\Gamma^{-3/2}$ . ( $\widehat{\Delta}$  denotes the difference between the temperatures of the bottom and top plates and  $\widehat{T}_M$  their arithmetical mean value.) Therefore only the Rayleigh number  $Ra = \widehat{\alpha}\widehat{g}\widehat{H}^3\widehat{\Delta}/\widehat{\nu}\widehat{\kappa}$ , the Prandtl number  $Pr = \widehat{\nu}/\widehat{\kappa}$  and the aspect ratio  $\Gamma$  occur as parameters fixing the set of equations. Note that in the Oberbeck–Boussinesq approximation material properties like the kinematic viscosity  $\widehat{\nu}$ , the thermal diffusivity  $\widehat{\kappa}$ , the thermal volume expansion coefficient  $\widehat{\alpha}$  and the gravitational acceleration  $\widehat{g}$  are constant and therefore their reference values are formally set to some value. (In the following the hat for dimensional quantities is omitted for simplicity.)

In order to perform a proper DNS, Kolmogorov and Batchelor scales need to be resolved, which requires a large number of computational nodes. For the globally averaged Kolmogorov length scale  $\eta_k$  the exact relation  $\eta_k = Pr^{1/2}[Ra(Nu - 1)]^{-1/4}$  holds and the Batchelor length scale  $\eta_T$  can be estimated via  $\eta_T = \eta_k Pr^{-1/2}$ . Since  $Pr = 0.786 < 1$  in all our simulations, resolving the Kolmogorov length scale is the stronger requirement. As shown for example by Kunnen *et al.* [79] the local Kolmogorov length scale  $\eta_k^{local}$  close to the rigid walls is much smaller than its spatial average  $\eta_k$ . Therefore the boundary layer region requires finer spatial resolution than the bulk region. Neglecting this might lead to wrong results even for integral quantities like the

### 6.3 LOCAL HEAT FLUX AND NUSSELT NUMBER

Nusselt number as was shown by Stevens *et al.* [135]. The required number of grid points in the boundary layers has been estimated by Shishkina *et al.* [121]. It is displayed in table 6.1 together with the actual number of nodes in the DNS. The spatially averaged Kolmogorov scale is used as the resolution requirement for the bulk region in every direction. Note that in this case the bulk resolution in our DNS is finer than is needed due to the inhomogeneous distribution of  $\eta_k^{local}$ .

TABLE 6.1: Simulation parameters for  $Pr = 0.786, \Gamma = 1$ : number of mesh nodes in the  $i$ -direction  $N_i$  ( $i = r, \phi, z$ ), number of nodes in the thermal/viscous BL as used in DNS ( $n_T/n_u$ ) and as required by theory [121] ( $\check{n}_T/\check{n}_u$ ), the Nusselt number  $Nu$  with its maximal deviation and the number of dimensionless time units  $\tau$  used for the averaging.

$Ra$	$N_r$	$N_\phi$	$N_z$	$n_T$	$\check{n}_T$	$n_u$	$\check{n}_u$	$Nu$	$\tau$
$10^5$	24	128	48	8	2	7	2	3.85( $\pm 0.02$ )	3776
$3 \times 10^5$	48	256	96	10	2	10	2	5.82( $\pm 0.03$ )	682
$10^6$	48	256	96	8	3	7	3	8.6 ( $\pm 0.1$ )	690
$3 \times 10^6$	96	256	192	11	3	10	3	11.95( $\pm 0.08$ )	993
$7 \times 10^6$	96	256	192	9	3	9	3	15.2 ( $\pm 0.1$ )	1635
$10^7$	96	256	192	8	4	8	3	16.9 ( $\pm 0.2$ )	3775
$3 \times 10^7$	192	512	384	16	4	14	4	22.8 ( $\pm 0.2$ )	515
$7 \times 10^7$	192	512	384	12	5	11	4	29.0 ( $\pm 0.1$ )	586
$10^8$	192	512	384	11	5	11	5	31.9 ( $\pm 0.2$ )	1240
$10^9$	384	1024	768	13	7	12	6	63.1 ( $\pm 0.4$ )	318

To enable a statistical analysis, the flow motion is saved in two different ways. On the one hand an a priori time-averaging is performed. This means that for the whole domain time-averaged temperature and velocity fields together with higher moments and correlations are collected by sampling every  $1.8 \times 10^{-3}$  to  $3.5 \times 10^{-3}$  time units (depending on  $Ra$ ). On the other hand, to allow a posteriori time-averaging of different complex flow characteristics as well as an analysis of time histories, a complete instantaneous flow field (temperature and velocity) is saved about three times each dimensionless time unit.

As an example instantaneous temperature iso-surfaces obtained for three different  $Ra$  are shown in figure 6.1. Even though the mean flow is similar in all three cases (upflow on the left and downflow on the right) the shape of the iso-surfaces changes dramatically with  $Ra$ . Roughly speaking the size of the structures decreases rapidly with increasing  $Ra$ .

### 6.3 Local heat flux and Nusselt number

The heat flux  $\vec{\Omega} = \vec{u}T - \kappa\vec{\nabla}T$  is the system's response to an imposed temperature gradient. Since the main interest lies in the heat transport from the hot bottom plate to the cold top plate, the vertical ( $z$ ) component of the heat flux  $\Omega_z$  is considered. It is made dimensionless with the vertical heat flux which would occur in a solid body with the same properties, resulting

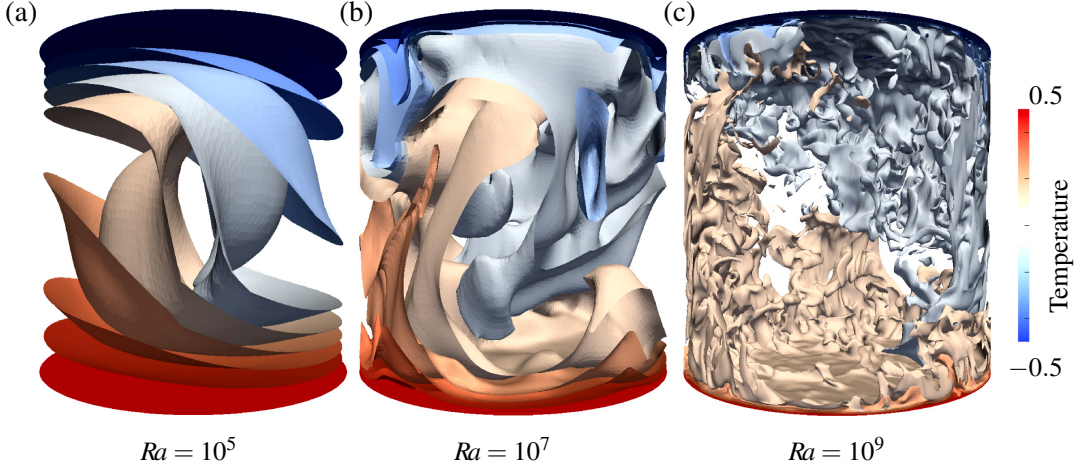


FIGURE 6.1: Instantaneous temperature iso-surfaces for (a)  $Ra = 10^5$ , (b)  $Ra = 10^7$ , and (c)  $Ra = 10^9$ ;  $Pr = 0.786$ ,  $\Gamma = 1$ .

in  $\Omega_z = \sqrt{\Gamma Pr Ra} u_z T - \Gamma^{-1} \partial_z T$ . For comparison e.g. with experiments, an integral quantity, namely the Nusselt number  $Nu = \langle \Omega_z \rangle_{t,\phi,r}$  is used. (Here  $\langle Q \rangle_\xi$  denotes the average of the quantity  $Q$  with respect to the variable  $\xi$ .) It can be shown analytically and is well-known that  $Nu$  is independent of  $z$ . Thus the deviations of  $Nu$  for different heights can be used as a measure for reaching a statistically steady state. In table 6.1 the Nusselt numbers obtained are presented together with their maximal deviation from the  $z$ -averaged  $Nu$ .

In figure 6.2 the reduced Nusselt numbers  $Nu/Ra^{0.3}$  from our DNS are compared to DNS and experiments from the literature. First of all it should be noted that our results cannot be expressed with a universal scaling exponent for the whole  $Ra$ -range considered, but there exist different regimes with a smooth transition:  $Ra \lesssim 10^6$ ,  $10^6 \lesssim Ra \lesssim 10^8$  and  $Ra \gtrsim 10^8$ . The latter observation is especially well supported by DNS results from the literature and the measurements by Ahlers *et al.* [4], with which a good agreement is found. The existence of the different regimes has already been reported in the literature [see 5, 51]. The apparent differences in the results obtained by different authors can be partly explained by the variations in aspect ratios and Prandtl numbers. The remaining deviations to the measurements might be due to the different experimental setups and conditions, but this issue is one of the open problems in RBC [5] and goes beyond the scope of the present paper.

Besides the integral vertical heat flux  $Nu$ , the spatial distribution of the local heat flux  $\Omega_z$  is also worth investigating, since it is related to large-scale flow structures. In figure 6.3 the time-averaged distribution of the local heat flux (in units of the volume-averaged Nusselt number) on the top and bottom plates is presented. Due to the no-slip conditions this is just a multiple of the vertical temperature gradient. From figure 6.3 it is obvious that there is one preferred direction marked with a black line labelled  $l_{LSC}$ , which is an axis of symmetry and which can be interpreted as the direction of the large-scale circulation.



### 6.3 LOCAL HEAT FLUX AND NUSSELT NUMBER

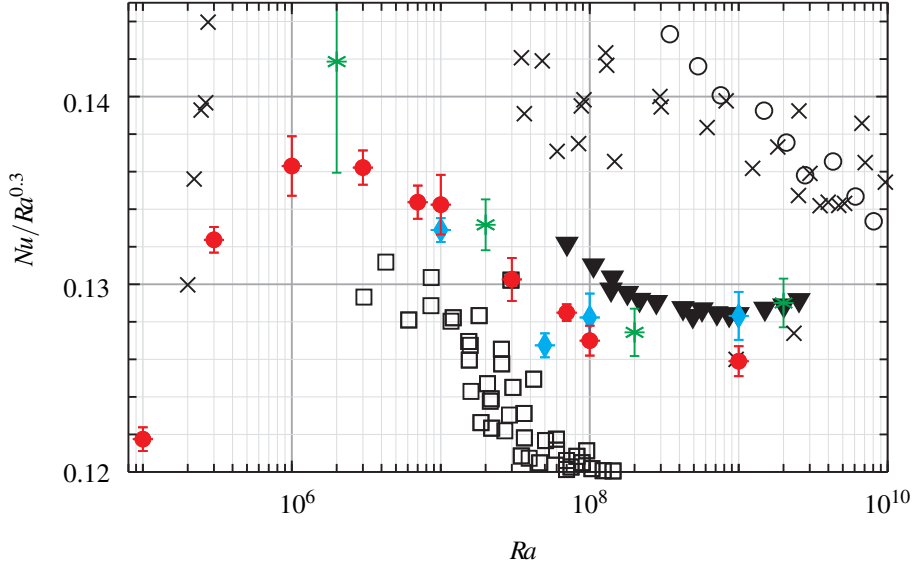


FIGURE 6.2: Comparison of reduced Nusselt numbers for different  $Ra$  from our DNS (red filled circles,  $Pr = 0.786$ ,  $\Gamma = 1$ ) with DNS results by Stevens *et al.* [135] (green stars,  $Pr = 0.7$ ,  $\Gamma = 1/2$ ) and Bailon-Cuba *et al.* [8] (blue diamonds,  $Pr = 0.7$ ,  $\Gamma = 1$ ) as well as experimental results by Ahlers *et al.* [4] (black triangles,  $Pr = 0.67$ ,  $\Gamma = 1/2$ ), Roche *et al.* [107] (black squares,  $Pr = 0.82 - 0.84$ ,  $\Gamma = 1/2$ ), Niemela & Sreenivasan [89] (black open circles,  $Pr = 0.68 - 0.69$ ,  $\Gamma = 1/2$ ) and Chavanne *et al.* [31] (black crosses,  $Pr = 0.65 - 0.76$ ,  $\Gamma = 1/2$ ).

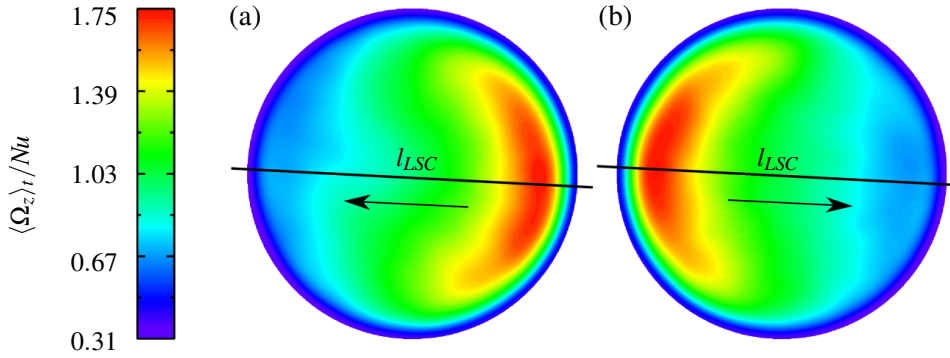


FIGURE 6.3: Time-averaged local heat flux  $\langle \Omega_z \rangle_t$  in units of  $Nu$  on (a) the bottom and (b) the top plate. The plane of the large-scale circulation is marked with a solid black line  $l_{LSC}$  while the arrows point in the direction of the wind.  $Ra = 10^7$ ,  $Pr = 0.786$ ,  $\Gamma = 1$ .

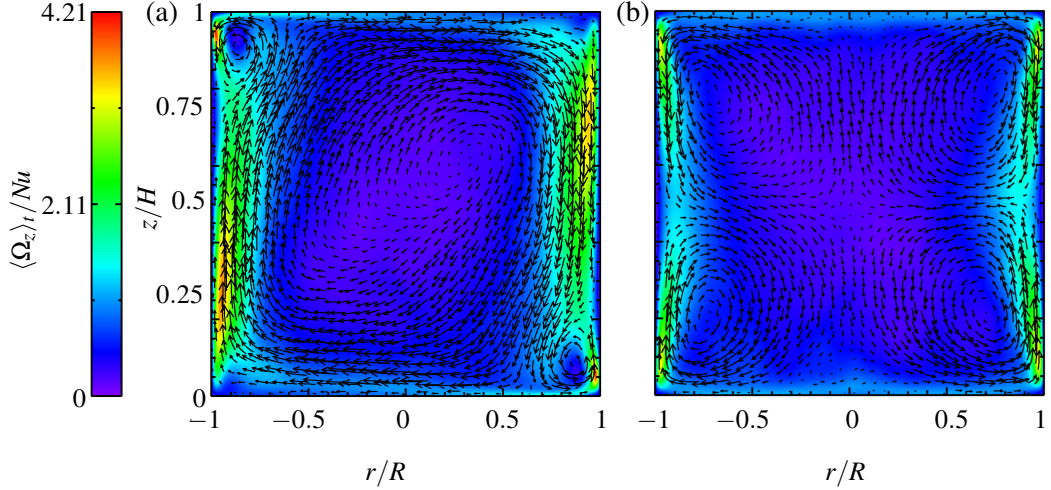


FIGURE 6.4: Time-averaged local heat flux (colour) in units of the Nusselt number and velocity (vectors) in the plane of (a) the LSC and (b) orthogonal to it,  $Ra = 10^7$ ,  $Pr = 0.786$ ,  $\Gamma = 1$ .

If we select the vertical cross-section of the flow field through  $l_{LSC}$ , i.e. what we interpret as the plane of the large-scale circulation, we obtain figure 6.4a in which  $\Omega_z$  (colour) together with the velocity vectors are shown for  $Ra = 10^7$ . In addition the flow field in the plane orthogonal to the LSC is visualized (figure 6.4b). For details regarding the averaging procedure and the extraction of the LSC plane see section 6.4. In the LSC plane the LSC itself represents a huge vortex structure with a diagonal adjustment and two smaller counter-rotating vortices in the upper left and lower right corner. The local heat flux increases in the vicinity of the vertical wall. This has also been reported by Shishkina & Wagner [124]. Within this region the heat flux is largest close to the smaller vortices. We assume therefore that these small structures are essential for the global heat transport. This argument is also supported by figure 6.3 in which the largest vertical heat flux on the bottom plate is again located in the region of the counter-rotating vortex.

In the central vertical cross-section orthogonal to the LSC (see figure 6.4b) there are four vortices of almost the same size rotating in different directions. In the horizontal direction at half-height the fluid moves towards the centre and at the cylinder axis the flow divides into an upward and downward motion. These observations agree well with the four-roll structure experimentally measured by Sun *et al.* [141]. Again the strongest vertical heat flux is located close to the vertical wall. It is surprising that even though the velocity field shows a completely different behaviour in the two orthogonal planes, the resulting heat flux distribution in both planes is quite similar, whereas there is an up-down symmetry which cannot be found in the LSC plane.

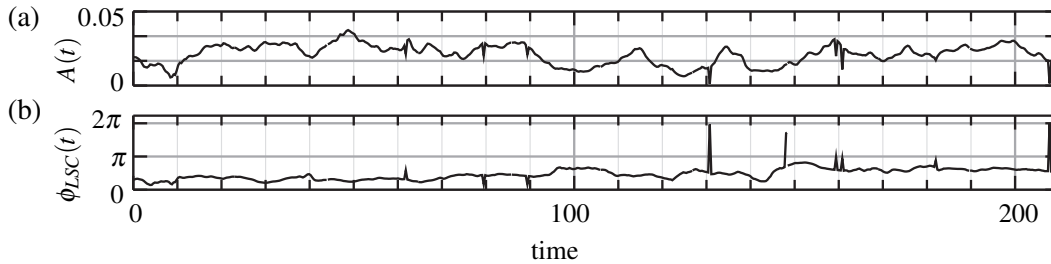


FIGURE 6.5: Time history of the fitting parameters: (a) amplitude  $A(t)$  and (b) phase shift  $\phi_{LSC}(t)$  for  $Ra = 10^9$ ,  $Pr = 0.786$ ,  $\Gamma = 1$  in a time interval without reorientations, i.e. within the interval  $\langle \phi_{LSC} \rangle_t \pm \pi/6$ .

TABLE 6.2: Length of time intervals ( $t_{max}$ ) without reorientations for different  $Ra$  as used for analysis of the LSC.

$Ra$	$3 \cdot 10^6$	$10^7$	$10^8$	$10^9$
time $t_{max}$	602	634	682	210

## 6.4 Extraction of the LSC-plane

In a cylindrical domain the LSC can perform azimuthal reorientations up to complete reversals. This means that in order to study the LSC in a cylindrical container in detail, a time interval without reorientations of the LSC must be identified. It is obtained by following the method proposed by Brown & Ahlers [19] which has also been used to analyse DNS data by Mishra *et al.* [87] and Stevens *et al.* [132].

The temperature on the vertical wall at half the cylinder height is fitted with the (discrete) function  $\psi(x_i) = A \cos(\frac{2\pi i}{N_\phi} + \phi_{LSC})$  using all  $N_\phi$  azimuthal nodes at the positions  $x_i$ . This is done for all samples saved during the runtime (three per time unit as described above). One obtains the time histories of the amplitudes  $A$  and the phase shifts  $\phi_{LSC}$ , shown in figure 6.5 as an example for  $Ra = 10^9$ .

If a certain time period is characterized by a phase shift  $\phi_{LSC}$  which varies within the interval  $\langle \phi_{LSC} \rangle_t \pm \pi/6$ , we consider it as a time period without reorientations. Note that even in such time periods spikes of  $\phi_{LSC}(t)$  can occur. It was shown by Stevens *et al.* [132] that these spikes are caused by single plumes and can be avoided in the time series by averaging over a small number of samples. Since we are not interested in the time series of  $\phi_{LSC}$  at this point but just want to determine proper time intervals without reorientations, we simply neglect these spikes. For the time periods obtained it is possible to analyse the LSC from time-averaged fields. The advantage of this method is its simplicity since the analysis uses two-dimensional fields but still represents the nature of three-dimensional physics.

In table 6.2 the time interval lengths  $t_{max}$  without reorientations, used in the LSC analysis, are presented for different  $Ra$ . Optimal time intervals might be longer than those used in our

## 6 BOUNDARY LAYER STRUCTURE ANALYSIS

analysis and are to be investigated in the future. Note that for  $Ra$  below  $3 \times 10^6$  either the flow is stationary or no proper period could be found as many reorientations occur. The latter leads to very short time intervals between reorientations, so that it is impossible to obtain converged statistics. Throughout the paper (except for the  $Nu$  analysis) the fields are averaged over the described time periods without reorientations. The plane of the LSC is thereby fixed by the angle  $\langle \phi_{LSC} \rangle_t$  which we call  $\phi_{LSC}$  for simplicity in the following. Note that our LSC plane does not coincide with the time average of the instantaneous LSC planes obtained by using the method of Brown & Ahlers [19]. The latter approach to extract the LSC is more sensitive to disturbances due to the appearance of strong single plumes [see e.g. 132] as it is illustrated for example by the spikes in figure 6.5b.

Besides the reorientations, the LSC can perform much more complex movements. These include off-centre (sloshing) modes [20, 164, 165, 171] as well as twisting [44, 45], which cannot be fully detected by the method of Brown & Ahlers [19]. Therefore we perform an additional analysis to determine whether these modes influence the time-averaged fields. For this purpose we consider five functions  $f_i(\phi)$  to determine  $\phi_{LSC}$  from time-averaged fields in five different ways. These functions reflect the flow dynamics in different regions of the domain. If additional modes (like sloshing or twisting) influence the dynamics in that region, it should lead to a different azimuthal behaviour of these functions.

We have already seen in figure 6.3 that  $\phi_{LSC}$  can be determined from the local heat flux on the bottom plate. More quantitative we analyse its rescaled radial average

$$f_{\Omega_z}(\phi) = \frac{2\langle \Omega_z \rangle_{t,r,z=0} - (\max(\langle \Omega_z \rangle_{t,r,z=0}) + \min(\langle \Omega_z \rangle_{t,r,z=0}))}{\max(\langle \Omega_z \rangle_{t,r,z=0}) - \min(\langle \Omega_z \rangle_{t,r,z=0})}, \quad (6.2)$$

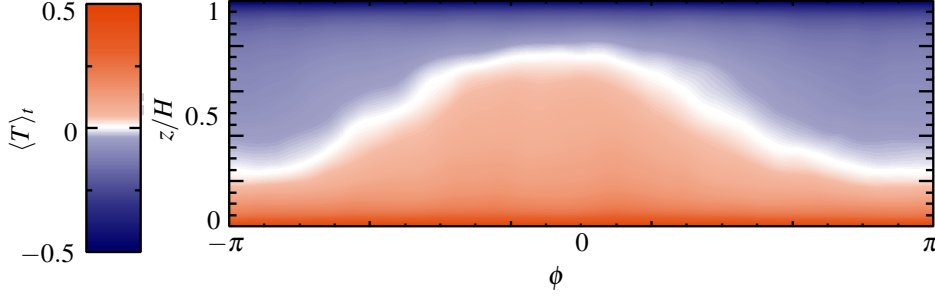
which is a function with values within  $[-1 : 1]$ . A maximum is expected for  $\phi_{LSC}$  and a minimum for  $\phi_{LSC} + \pi$ . In between we expect a smooth crossover to end up with a continuous graph.

Besides the heat flux, the  $\phi$ -component of the vorticity, i.e.  $\omega_\phi = (\vec{\nabla} \times \vec{u}) \cdot \vec{e}_\phi$  seems to be a characteristic quantity as figure 6.4 suggests. By averaging in radial and vertical directions this is reduced to a function  $f_\omega(\phi)$ , namely

$$f_\omega(\phi) = \frac{2\langle \omega_\phi \rangle_{t,r,z} - (\max(\langle \omega_\phi \rangle_{t,r,z}) + \min(\langle \omega_\phi \rangle_{t,r,z}))}{\max(\langle \omega_\phi \rangle_{t,r,z}) - \min(\langle \omega_\phi \rangle_{t,r,z})}. \quad (6.3)$$

For  $\phi_{LSC}$  we expect a high absolute value of the integral vorticity component  $\langle \omega_\phi \rangle_{t,r,z}$  while for  $\phi_{LSC} + \pi/2$  the counterrotating vortices cause an integral vorticity close to zero.

An interesting feature of the LSC is its footprint on the vertical wall. First we consider the temperature on the vertical wall shown in figure 6.6. We are interested in the vertical position  $z_0$


 FIGURE 6.6: Time averaged temperature on the vertical wall.  $Ra = 10^7$ ,  $Pr = 0.786$ ,  $\Gamma = 1$ 

at which the mean temperature is reached. This results in a rescaled function

$$f_T(\phi) = \frac{2z_0 - (\max(z_0) + \min(z_0))}{\max(z_0) - \min(z_0)}. \quad (6.4)$$

Due to rising/falling of warm/cold plumes, which constitute in organised form the LSC, the mean temperature can be found closer to the top plate for  $\phi_{LSC}$  and closer to the bottom plate for  $\phi_{LSC} + \pi$ . In figure 6.6 a cosine-like behaviour of  $z_0(\phi)$  is visible.

Besides the temperature footprint the LSC induces the wall shear stress on the vertical wall shown in figure 6.7. The absolute wall shear stress  $\tau_w^{total} = \sqrt{\langle \partial_r u_z \rangle_t^2 + \langle \partial_r u_\phi \rangle_t^2}$  is displayed by colours and its components due to vertical motion  $\langle -\partial_r u_z \rangle_t$  and azimuthal motion  $\langle -\partial_r u_\phi \rangle_t$  as vectors. Again a cosine-like (blue) curve is obtained. This time the curve reflects the vertical position of the stagnation point  $z_s$  as a function of the angle  $\phi$  and therefore we define the next indicating function as

$$f_\tau(\phi) = \frac{2z_s - (\max(z_s) + \min(z_s))}{\max(z_s) - \min(z_s)}. \quad (6.5)$$

Finally, we consider the temperature distribution on the vertical wall at half height in the fitting procedure described at the beginning of this section. We expect to find a cosine function in the time averaged fields, since it was already used as a fitting function for instantaneous fields. Thus the fifth function reads

$$f_{T_c}(\phi) = \frac{2\langle T \rangle_{t,r=R,z=H/2} - (\max(\langle T \rangle_{t,r=R,z=H/2}) + \min(\langle T \rangle_{t,r=R,z=H/2}))}{\max(\langle T \rangle_{t,r=R,z=H/2}) - \min(\langle T \rangle_{t,r=R,z=H/2})}. \quad (6.6)$$

To complete the analysis of the different functions indicating the angle  $\phi_{LSC}$ , we present them together in figure 6.8. One can see that the five functions based on flow footprints on the bottom plate ( $f_{\Omega_z}$ ), on the vertical walls ( $f_\tau$ ,  $f_T$ ,  $f_{T_c}$ ) and integral characteristics ( $f_\omega$ ) almost coincide. Therefore a characteristic  $\phi$ -behaviour of these quantities exists and reflects almost the same  $\phi_{LSC}$ . Such a collapse of different quantities in a turbulent flow can be present only if any additional modes like sloshing or twisting vanish statistically for the considered  $Ra$ ,  $Pr$ ,  $\Gamma$ .

## 6 BOUNDARY LAYER STRUCTURE ANALYSIS

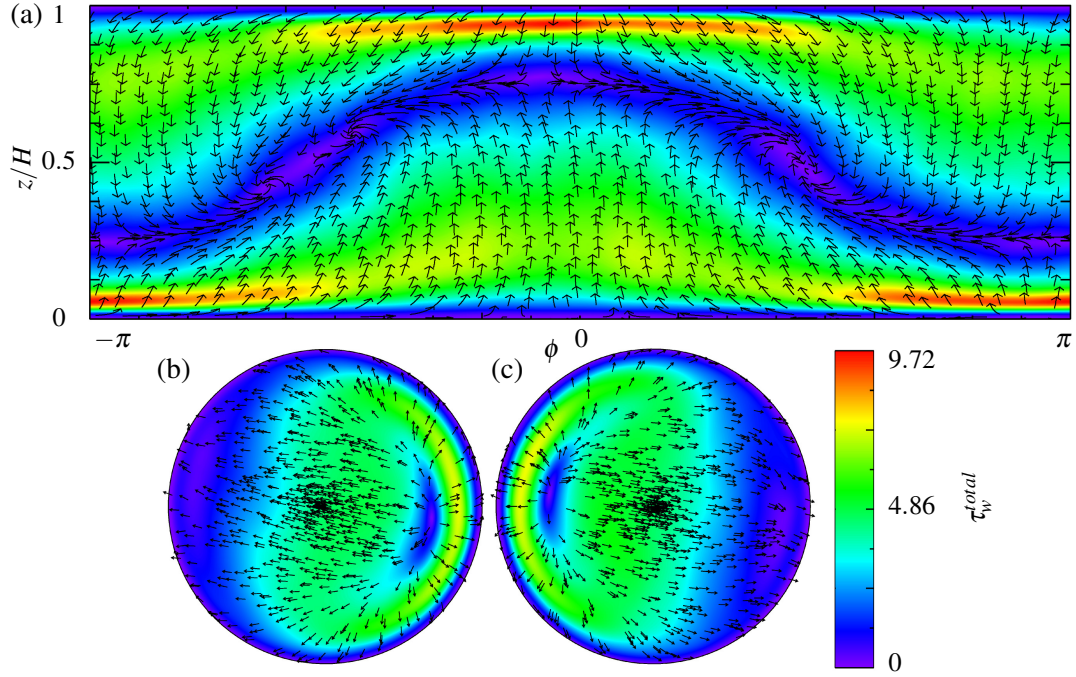


FIGURE 6.7: Absolute (colour)  $\tau_w^{total}$  and contributions of different directions of movement (vectors) of the time-averaged wall shear stress on the (a) vertical wall, (b) bottom plate and (c) top plate.  $Ra = 10^7$ ,  $Pr = 0.786$ ,  $\Gamma = 1$ .

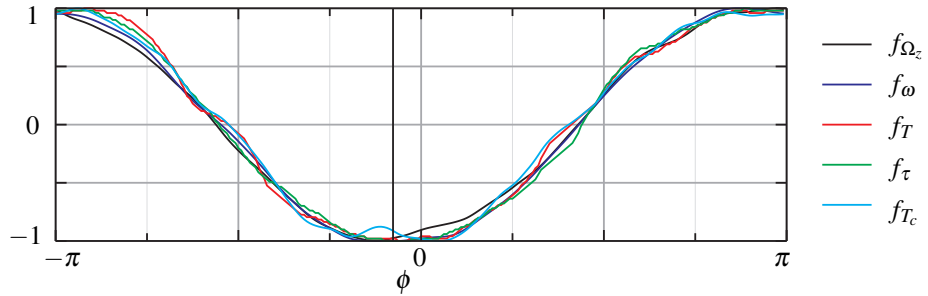


FIGURE 6.8: Different functions indicating the LSC based on:  $f_{\Omega_z}$ , the local heat flux on the bottom plate (6.2);  $f_{\omega}$ , azimuthal component of the vorticity (6.3) in central vertical cross-sections;  $f_T$ , the height at which arithmetical mean temperature on the vertical wall is reached (6.4);  $f_{\tau}$ , height of the stagnation point (6.5) at the vertical wall; and  $f_{T_c}$ , the temperature on the vertical wall at  $z = H/2$  (6.6),  $Ra = 10^7$ ,  $Pr = 0.786$ ,  $\Gamma = 1$ .

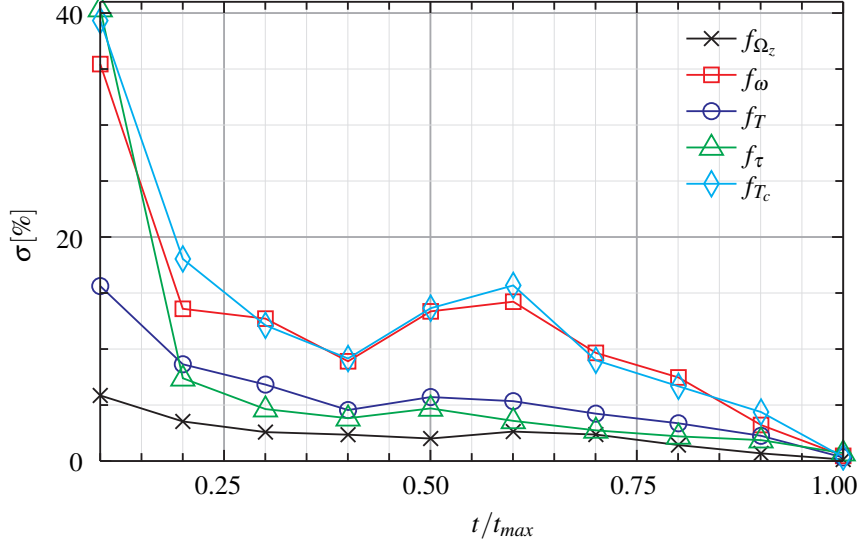


FIGURE 6.9: Convergence of different quantities with increasing averaging period.  $Ra = 10^7$ ,  $Pr = 0.786$ ,  $\Gamma = 1$ .

If only a short time period is available (for example due to frequent reorientations of the LSC or high computational costs for DNS) it is interesting to investigate, which of the considered  $\phi$ -functions that indicate  $\phi_{LSC}$  converges faster. In figure 6.9 the relative deviation in the  $L^2$ -norm from the final curve is shown as a function of the length of the averaging period. The relative deviation  $\sigma$  of a quantity  $Q$  depending on a variable  $\xi$  from a reference  $Q_{ref}$  is calculated via

$$\sigma = \sqrt{\frac{\int [Q(\xi) - Q_{ref}(\xi)]^2 d\xi}{\int [Q_{ref}(\xi)]^2 d\xi}} \quad (6.7)$$

and can be interpreted as a prediction error with respect to an insufficient averaging time. Note that even for the maximal averaging time  $t_{max}$  zero is not necessarily reached as the reference is calculated from time-averaged fields with a higher sampling rate (as described at the end of section 6.2). From figure 6.9 it is concluded that the function  $f_{\Omega_z}$  based on the local heat flux on the bottom plate provides almost immediately the direction of the LSC with an error of  $\sim 6\%$  while the method by Brown & Ahlers [19] ( $f_{T_c}$ ) predicts  $\phi_{LSC}$  at that time with an error of  $\sim 40\%$ . From the latter we conclude that if only a short time interval or a set of few samples is available for determining  $\phi_{LSC}$  (for the above-mentioned reasons), the heat flux criterion should be favoured. It is of course applicable only to numerical data as measuring the local heat flux on the whole plate in experiments is not yet possible. In measurements the available time for averaging is often much larger than that in numerical simulations, and therefore the method by Brown & Ahlers [19] is preferable in this case.

From figure 6.9 it is obvious that within the time interval considered additional dynamics occur

## 6 BOUNDARY LAYER STRUCTURE ANALYSIS

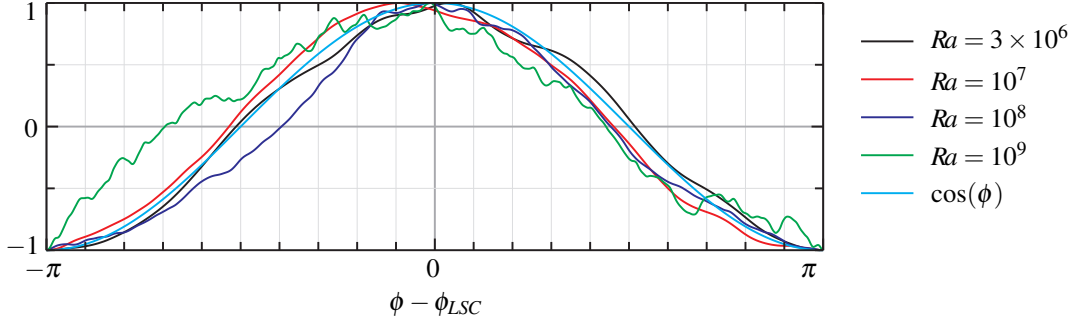


FIGURE 6.10: Function  $f_{\Omega_z}$  (local heat flux on the bottom plate, averaged in time and radial direction) shifted in  $\phi$ -direction for different  $Ra$  and  $\cos$ -function for comparison.

around  $t/t_{max} = 0.6$ . This leads to a disturbance of the functions  $f_{T_c}$  and  $f_{\omega}$  near  $t/t_{max} = 0.6$ , which only influences the speed of convergence but not the time-averaged field as shown in figure 6.8. To check whether the  $\phi$ -dependence of the time-averaged field is universal within a certain interval of  $Ra$  (and fixed  $Pr$ ,  $\Gamma$ ), we consider the heat flux criterion mentioned above. In figure 6.10 the comparison of the function  $f_{\Omega_z}$  (of course shifted in  $\phi$  to offset different orientations of the LSC in the different simulations) with a cosine function reveals a good agreement for different  $Ra$ . This shows that there is a universal behaviour of time-averaged fields if no LSC reorientation takes place within the averaging period. Moreover the similarity obtained with the cosine function is an indirect justification for the fitting procedure described at the beginning of the section.

In addition to the above-mentioned quantities the LSC of course also causes wall shear stress on the top/bottom plate, which is presented in figures 6.7b and 6.7c. Colours display the absolute wall shear stress

$$\tau_w^{total} = \sqrt{\langle \partial_z u_r \rangle_t^2 + \langle \partial_z u_\phi \rangle_t^2}$$

and vectors its components due to radial motion  $\langle \pm \partial_z u_r \rangle_t$  and azimuthal motion  $\langle \pm \partial_z u_\phi \rangle_t$ . Comparing this with the wall shear stress on the vertical wall, we conclude that the LSC is formed mainly by the radial and vertical motion at the top/bottom and vertical walls, respectively.

If we reduce our analysis to the plane of the LSC, we consider the specific case where one velocity component is responsible for the wall shear stress and the viscous BL. Even more interesting are the distributions on the horizontal walls, since there a thermal BL develops in addition to the viscous one. We concentrate our analysis on the region close to the bottom plate knowing that the situation is similar on the top plate due to symmetry.

### 6.5 Boundary layer (BL) analysis

In the following a step-by-step method to extract and analyse the local boundary layer thickness from instantaneous flow fields is introduced and discussed.



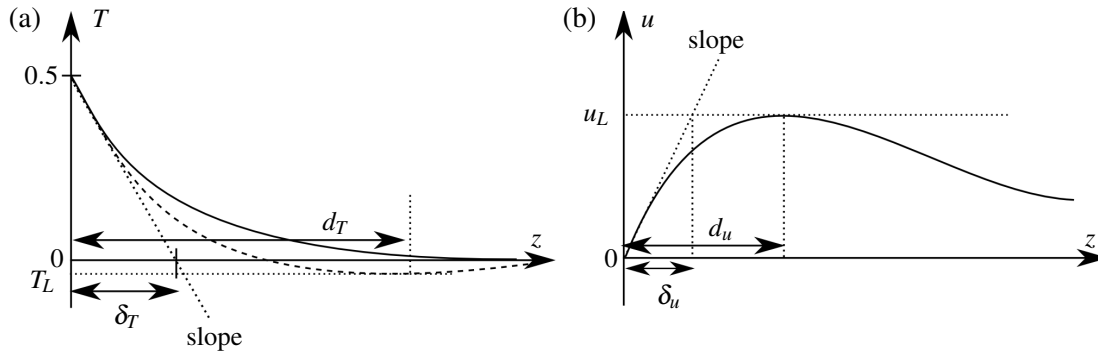


FIGURE 6.11: Definition and nomenclature for BL thicknesses and associated quantities for the cases of (a) thermal and (b) viscous boundary layers.

### 6.5.1 Definition

To evaluate the boundary layer thickness close to the heated bottom plate, it is necessary to deal with instantaneous flow fields. Time-averaged fields do not provide the correlations which are required for our BL analysis. One can use different definitions of the BL thickness, such as the fluctuation criterion (boundary layer thickness is defined as the position of the maximum of the temperature/velocity fluctuations), which lead in general to different results. We use the well-known and often applied [e.g. 121] slope criterion defined in figure 6.11 because it is also applicable locally to instantaneous flow fields.

To apply this criterion the slope of the temperature or (radial) wind velocity is evaluated at the wall. The thermal or viscous boundary layer thickness is then defined as the height  $z$  at which the slope straight line crosses a temperature or velocity level  $T_L$  or  $u_L$ , respectively. The levels of the quantities correspond to the dotted horizontal lines in figure 6.11.

As demonstrated in figure 6.11, the analysis of the thermal BL is similar but not identical to that of the viscous BL. The reason for this is the different boundary conditions for the two quantities. Since the temperature is always maximal at the bottom, the slope at this wall is always negative. On the contrary the velocity (we call it simply  $u$  here but mean the radial velocity within the fixed plane of the LSC) is vanishing at the wall due to the no-slip condition allowing generally negative as well as positive slopes. In summary two quantities are needed to determine the BL thickness: the slope and the level.

In general the temperature level obtained from instantaneous flow fields differs from the arithmetical mean temperature (here zero) and can be negative or positive. In figure 6.11a an example of the negative temperature level  $T_L$  at position  $d_T$  is sketched. It is therefore necessary to determine a level for the case of thermal BLs also since only the mean temperature distribution might lead to a wrong thermal BL thickness. This has also been shown by Zhou *et al.* [169]. To determine the thermal BL thickness we use the global minimum of the temperature field within a certain  $z$ -interval  $I$  as the level value.

For the viscous BL the situation is even more tricky. As negative as well as positive slopes

## 6 BOUNDARY LAYER STRUCTURE ANALYSIS

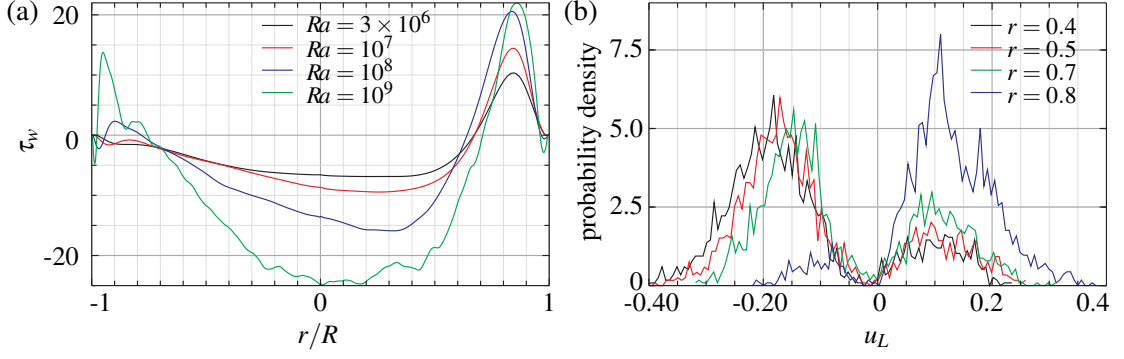


FIGURE 6.12: (a) Time averaged wall shear stress  $\tau_w = \langle \partial_z u \rangle_t$  on the bottom plate along  $l_{LSC}$  for different  $Ra$  and (b) p.d.f. of the velocity level  $u_L$  at different radial positions for  $Ra = 10^7$ ,  $Pr = 0.786$ ,  $\Gamma = 1$ .

might occur, we have to consider positive and negative levels. Thus we need the global maximal as well as global minimal velocity value within  $I$ . The sign of the derivative which determines the slope should then fix the sign of the level quantity.

The length of the interval  $I$  is a free parameter in the definition of the proper temperature/velocity level. We will further analyse what influence the choice of  $I$  has on the resulting boundary layer thickness. If proper slopes and levels are provided a complete statistical analysis of the local boundary layer thickness can be performed.

In order to analyse the boundary layer on the bottom plate and corresponding quantities with special emphasis on the LSC, not all radial positions must be taken into account, since smaller structures that occur in the corners are not part of the LSC itself (see figure 6.4). As the position of the zero time-averaged wall shear stress (i.e. the mean stagnation point) is almost independent of  $Ra$  (as shown in figure 6.12a), we conclude that considering the region  $J = \{r | r \in [-0.7 : 0.5]\}$  is sufficient. An argument for the upper bound can be found in figure 6.12b. There the dependence of the probability density function (p.d.f.) for the maximal value of the radial velocity component in the lower half of the cell on the radial position is presented. It can be seen that mainly negative velocity values, which correspond to the wind velocity, occur for  $r \leq 0.5$ , while for larger  $r$  the positive velocity values, which are part of the smaller vortex in the corner, dominate. A similar argument can be made for the lower bound. During the following analysis we therefore concentrate on p.d.f.s in the region  $l_{LSC} \cap J$ .

### 6.5.2 Determination of proper slopes and levels for the BL extraction

In the following we compare different techniques for determining the thermal ( $\delta_T$ ) and viscous ( $\delta_V$ ) BL thicknesses, respectively. As described above, two main ingredients are necessary: the slope and the level. We focus on each of them separately and then combine them to evaluate the BL thickness.

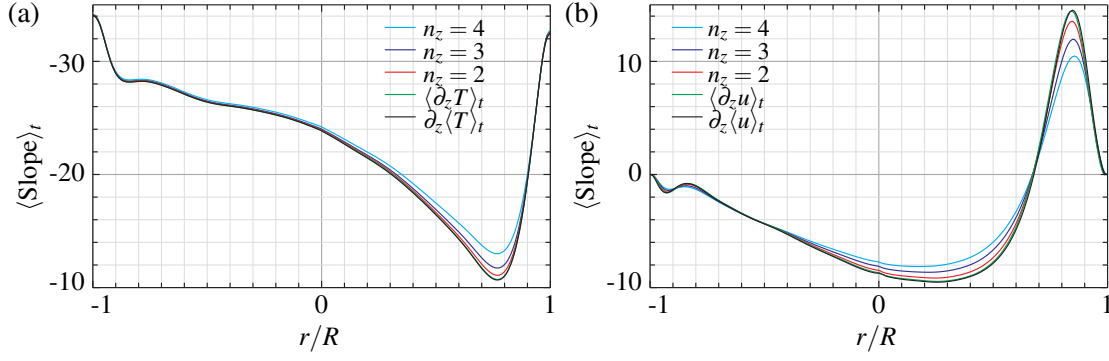


FIGURE 6.13: Different methods to obtain the (time averaged) slope of the (a) temperature field and (b) radial velocity field using linear fitting for the first  $n_z$  nodes and direct derivative  $\langle \partial_z f \rangle_t$  compared to the time averaged field  $\langle \partial_z f \rangle_t$ ,  $f \in \{T, u\}$ ,  $Ra = 10^7$ ,  $Pr = 0.786$ ,  $\Gamma = 1$ .

First we address the question of how the slope can be extracted from a fluctuating instantaneous field. To answer this, we must decide whether the normal gradient at the wall is a good estimate of the slope or an additional fitting is needed. Since  $\langle \partial_z f \rangle_t = \partial_z \langle f \rangle_t$  for a quantity  $f \in \{T, u\}$ , the slopes obtained from time-averaged fields can be used to check various differentiation techniques applied to instantaneous fields while evaluating the BL thickness. On the one hand we simply consider the derivative at the wall  $\langle \partial_z f \rangle_t$  (fitted with a three-point Lagrange polynomial) as in the case of the time averaged fields  $\partial_z \langle f \rangle_t$ . On the other hand we take a number  $n_z$  of points next to the wall and perform a linear regression (with one free parameter as the value at the wall is fixed by the boundary condition). In figure 6.13 the comparison for different  $n_z$  and the derivative is shown for  $Ra = 10^7$ . We conclude that the direct derivative technique, i.e.  $\langle \partial_z f \rangle_t$ , delivers the best agreement with the time averaged field  $\partial_z \langle f \rangle_t$  for both BLs, therefore it is applied for the BL extraction. The fact that fitting with a higher number of points leads to gentler slopes can be explained as follows: with increasing number of points the instantaneous vertical profiles deviate more from the linear ones, therefore their linear fits become gentler.

Besides the slope we also need a proper level and thus, as described above, an interval  $I$  in which it is determined. We know from theory that  $\delta_T = 1/2Nu$  is a good approximation of the mean thermal BL thickness. In addition  $\delta_T/\delta_u \approx 1$  holds for a Prandtl–Blasius BL for  $Pr \approx 1$ . Therefore we choose  $I_n = n(H/2Nu)$  and compare the results obtained for different  $n$ . In addition we consider  $I_\infty = H/2$  as a possible interval. As taking the maximum/minimum and time-averaging do not commute, we do not expect that the averaged results from instantaneous fields coincide with the results from the averaged field. Nevertheless in figure 6.14 in addition to the instantaneous results, also the results obtained for the averaged fields (with  $T_L$  and  $u_L$  within  $I_\infty$ ) are compared. Besides the levels reached, the position at which the maximum/minimum occurs is an interesting quantity. Therefore in figure 6.14e,f the p.d.f.s of the level values and boundary layer thicknesses obtained for different  $I$  are shown for the thermal and viscous cases.

## 6 BOUNDARY LAYER STRUCTURE ANALYSIS

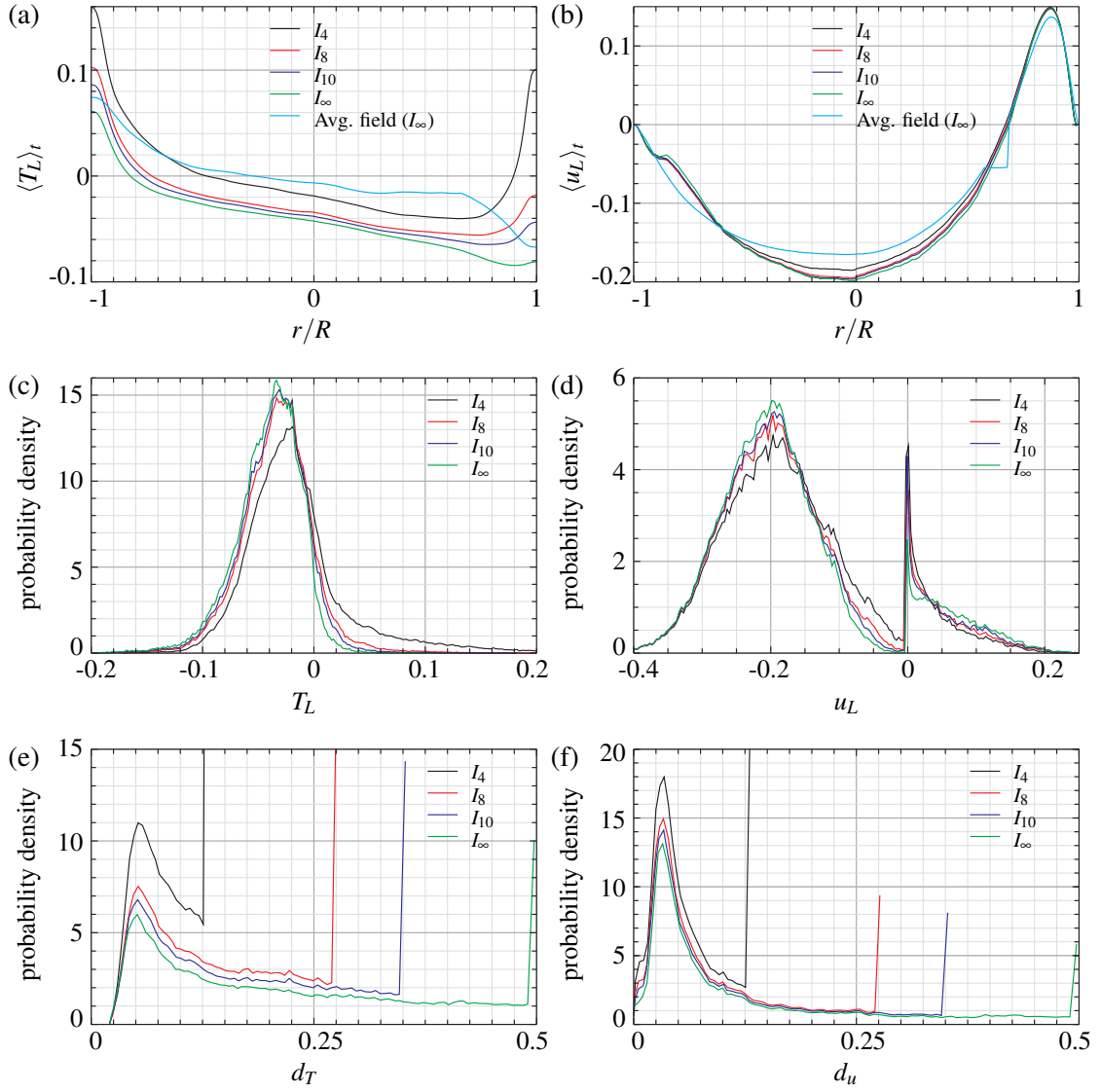


FIGURE 6.14: Evaluation of the temperature and velocity levels from searching within different  $z$ -intervals  $I$ . Time-averaged results for temperature (a) and velocity (b), corresponding p.d.f.s of the temperature (c) and velocity (d) for  $r \in [-0.7, 0.5]$  and p.d.f.s for the height  $d$  at which the level is reached for the temperature (e) and velocity (f),  $Ra = 10^7$ ,  $Pr = 0.786$ ,  $\Gamma = 1$ .

We observe that the thermal BL analysis is much more sensitive to the size of the interval  $I$ . Since we want to develop one criterion for both types of BL, we derive it for the thermal BL and afterwards apply it to the viscous BL, as well. Negative temperature levels  $T_L$  sketched in figure 6.11a are typical for instantaneous temperature profiles. Indeed figure 6.14a reflects that for larger intervals the time-averaged temperature decreases. Figure 6.14c underlines this since with increasing size of  $I$  the p.d.f. sets the weight to negative velocity values instead of positive

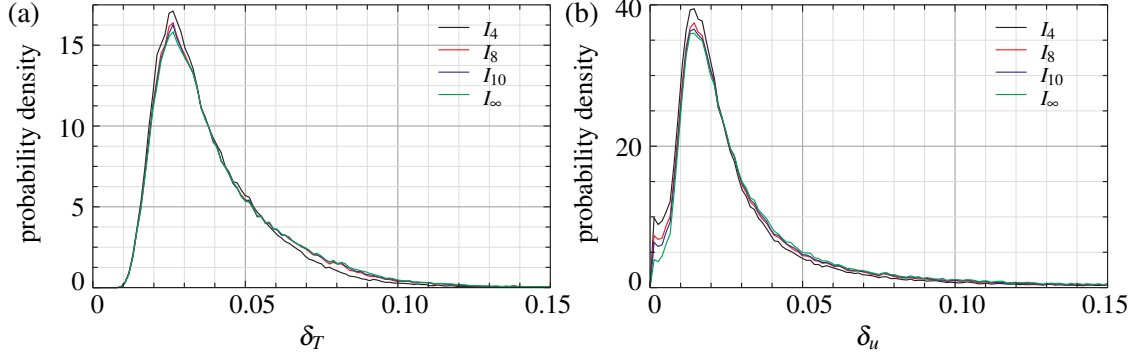


FIGURE 6.15: P.d.f.s of the obtained BL thicknesses of the (a) thermal BL and (b) viscous BL from searching within different  $z$ -intervals  $I$  for  $r \in J$ ,  $Ra = 10^7$ ,  $Pr = 0.786$ ,  $\Gamma = 1$ .

ones. This can be justified from figure 6.14e where additionally to the peaks at  $d_T \approx 0.025$  a second peak at the upper bound of each considered interval is seen. This is due to events for which the global minimum occurs at the upper boundary. Since these peaks get less important for larger  $I$  for more events, the global minimum is found within the interval. Since we are interested in the level to define the BL thickness the first peak at  $d_T \approx 0.025$  is the relevant one. If in the bulk at larger heights  $z$  a cold plume causes negative temperature values which in turn cause a lower  $T_L$ , this indeed should have minor influence on the BL thickness. Thus we decided that  $I_4$  is the proper interval to evaluate the BL thicknesses as the main peak is already within this interval and it stretches not too deeply into the bulk region.

From figure 6.14d it is concluded that the velocity levels show a strong splitting due to the sign of the velocity. Since we are interested in the wind velocity of the LSC, the negative velocity values are of most interest to us. The peak in the p.d.f. close to zero (but on the positive side) is a result of the velocity fluctuations close to the wall [170]. Even if the peak is quite high this case can be neglected due to the small histogram bin size and therefore small probability.

### 6.5.3 Resulting BL thicknesses

In figure 6.15 the BL thicknesses based on the obtained slopes and levels are presented. The fact that the p.d.f.s for different  $I$  are similar underlines that the choice of  $I$  (of course within proper bounds) has no major influence on the p.d.f. (and thus also not on the mean values) of the BL thickness. The p.d.f. found for  $\delta_u$  shows a similar behaviour as already reported by Zhou & Xia [173] who conducted quasi-two-dimensional experiments and obtained (spatially averaged) BL profiles using particle image velocimetry (PIV). The p.d.f. rises strongly for small boundary layer thicknesses, reaches its maximum and descends much more slowly for larger BL thicknesses. The p.d.f. for the thermal BL behaves in a similar way but is wider and shifted to larger BL thicknesses. This will be discussed in detail in the next section.

## 6 BOUNDARY LAYER STRUCTURE ANALYSIS

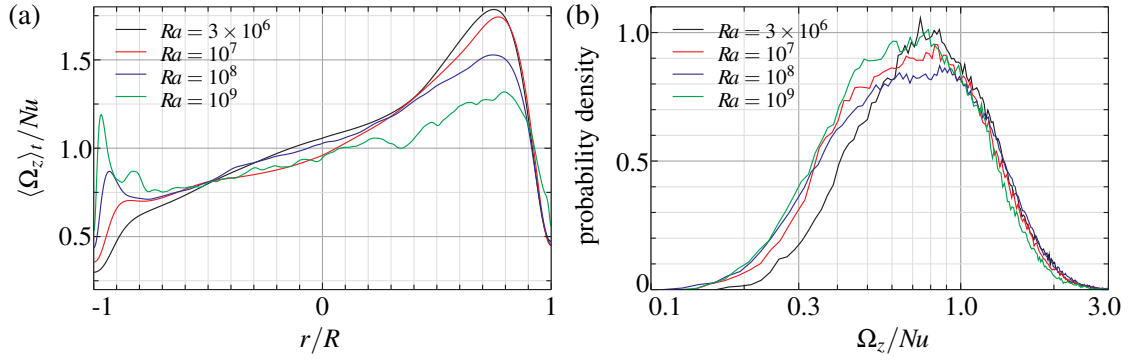


FIGURE 6.16: Local heat flux in units of  $Nu$  on the bottom plate along  $l_{LSC}$  for different  $Ra$ , (a) time-averaged and (b) p.d.f. for  $r \in [-0.7, 0.5]$ ,  $Pr = 0.786$ ,  $\Gamma = 1$ .

### 6.6 Boundary layer characteristics

The analysis of the  $Ra$ -dependence of BL characteristics includes the different quantities involved. Therefore the levels and slopes as well as the resulting BL thicknesses and their ratio are discussed.

#### 6.6.1 Slopes and levels

As mentioned before the slopes of the temperature and wind velocity profiles are worth evaluating not only with respect to the BL thicknesses but because they are meaningful in themselves, as well. In the case of the temperature field the slopes at the wall are proportional to the local heat flux orthogonal to the wall. In the case of the bottom plate the slopes are thus proportional to the vertical local heat flux  $\Omega_z$ .

In figure 6.16a the local heat flux along the wind direction is depicted in terms of  $Nu$ . It is observed that the heat flux normalized with  $Nu$  almost collapses for all Rayleigh numbers considered in the interval  $J = \{r | r \in [-0.7, 0.5]\}$ . In particular the maxima of the p.d.f.s of this local heat flux in the interval  $J$  occur for all Rayleigh numbers at 0.8 as shown in figure 6.16b.

Outside  $J$  and close to the vertical wall the heat flux reflects some interesting features due to the secondary rolls as displayed in figure 6.16a. From this we conclude that the vortices in the corners (here close to  $r = 0.8$ ) are also essential drivers of the heat. The comparison of the horizontal normalized heat flux profiles for different  $Ra$  in figure 6.16a also shows that even though the largest  $\Omega_z$  values are reached within this corner region for all the  $Ra$ , it becomes less important for increasing  $Ra$ .

Contrary to this another structure becomes more important for the heat flux with increasing  $Ra$ . It was shown in figure 6.12a that in the remaining corners (here close to  $r = -0.9$ ) a smaller vortex structure develops. Owing to the rising plumes close to the vertical wall, the flow detaches from the bottom plate. For higher  $Ra$  this effect becomes so strong that a separation bubble and

## 6.6 BOUNDARY LAYER CHARACTERISTICS

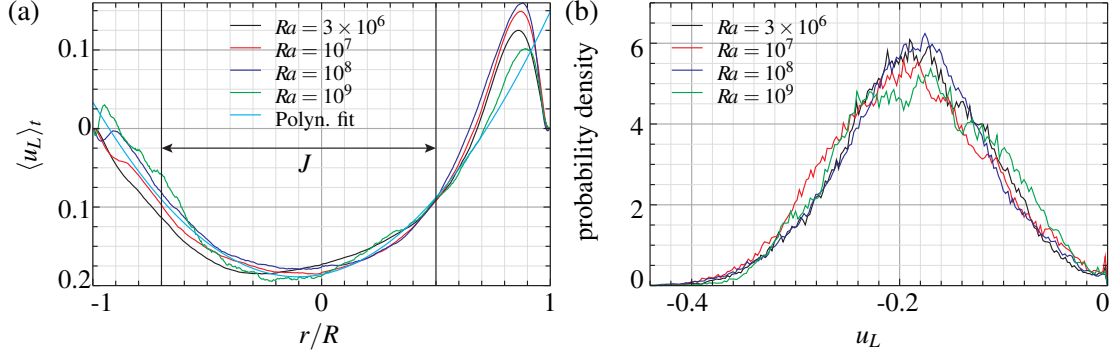


FIGURE 6.17: (a) Time-averaged wind velocity level  $u_L$  along  $l_{LSC}$  for different  $Ra$  with a polynomial fit for  $r \in [-0.7, 0.5]$ ; (b) p.d.f. for the wind velocity level for  $r \in [-0.7, 0.5]$ ,  $Pr = 0.786$ ,  $\Gamma = 1$ .

therefore a vortex structure develops, which induces motion against the direction of the wind close to the bottom plate and thus a positive  $\tau_w$ .

This argument is also supported by the levels presented in figure 6.17a which for larger  $Ra$  reflect positive mean velocities in this corner region close to  $r = -0.9$ . Within  $J$ , where the wind is dominant, the mean velocity levels can be approximated by a parabola for all  $Ra$  considered. In figure 6.17a the fit with a second-order polynomial for  $r \in J$  results in  $u_L(r) = 0.277(r + 0.104)^2 - 0.189$ . This means that the wind along the plate has a varying magnitude and reaches its maximum at  $r = -0.104$ . The existence of a varying wind velocity has been also observed by Zhou *et al.* [170] in two-dimensional DNS and similarly by Kaczorowski *et al.* [70] in DNS in a cube.

The observed  $Ra$ -independence of the dimensionless wind velocity magnitude is also visible in the p.d.f.s (see figure 6.17b). They almost coincide for all investigated  $Ra$  and are symmetric around  $u_L \approx -0.2$ . Similar results were obtained in experiments. For example du Puits *et al.* [103] found a mean velocity magnitude of  $|u_L| \approx 0.18$  in the centre of their cylindrical cell for  $Ra = 1.12 \times 10^{11}$ ,  $Pr = 0.7$  and  $\Gamma = 1.13$ , while Sun *et al.* [140] obtained  $|u_L| \approx 0.1$  in their quasi-two-dimensional experiments for  $Ra = 3.43 \times 10^9$ ,  $Pr = 4.3$  and  $\Gamma = 1.04$ . The deviation of our results from the latter might be an effect of the considerably different Prandtl numbers.

Besides the velocity levels the temperature levels  $T_L$  also reveal an interesting  $Ra$ -dependence. Their time averaged distributions and p.d.f.s are presented in figure 6.18. As shown by [169], the fluctuating temperature level has an effect on the p.d.f. of the thermal BL thickness. We have argued that levels below zero are reached due to a global temperature minimum within the interval  $I$  (recall figure 6.11). From figure 6.18 it is concluded that the radial distribution of the time averaged levels as well as the p.d.f. are shifted to higher levels, i.e. closer to the arithmetic mean temperature zero, with increasing  $Ra$ . Thus for higher  $Ra$  the case of a global temperature minimum which deviates from zero is less probable. If the temperature level would be chosen as

## 6 BOUNDARY LAYER STRUCTURE ANALYSIS

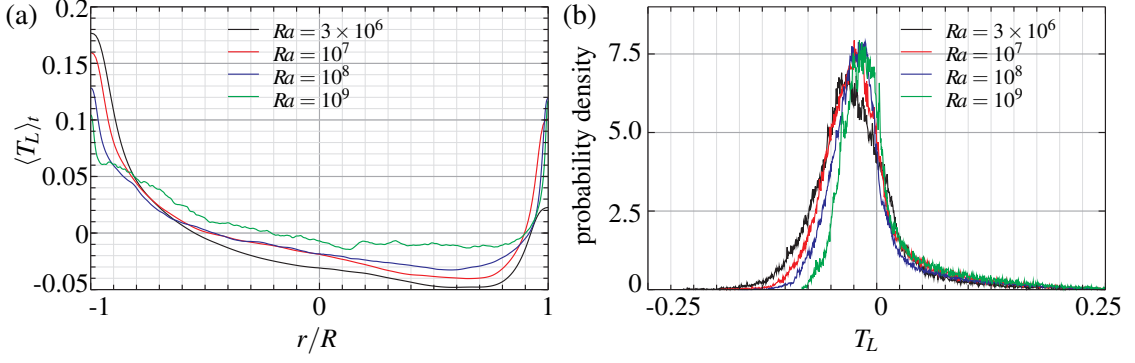


FIGURE 6.18: Temperature level  $T_L$  along  $l_{LSC}$  for different  $Ra$ , (a) time-averaged and (b) p.d.f. for  $r \in [-0.7, 0.5]$ ,  $Pr = 0.786$ ,  $\Gamma = 1$ .

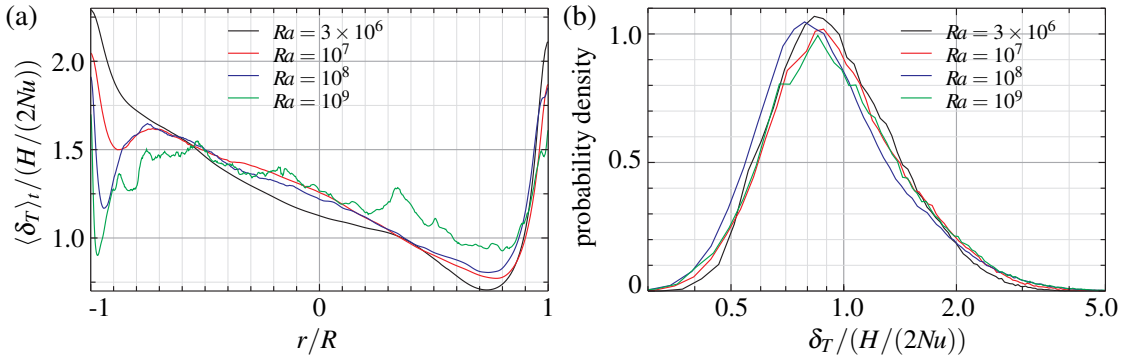


FIGURE 6.19: Thermal boundary layer thickness  $\delta_T$  in units of  $H/2Nu$ , (a) time-averaged and (b) p.d.f. for  $r \in [-0.7, 0.5]$ ,  $Pr = 0.786$ ,  $\Gamma = 1$ .

the arithmetic mean temperature the later obtained BL thicknesses were closer to our results in the case of larger  $Ra$ .

### 6.6.2 Boundary layer thickness

Finally we compare the BL thicknesses for different  $Ra$ , starting with the thermal BL in figure 6.19(a), where the time-averaged BL thickness along  $l_{LSC}$  is presented in units of its approximation  $H/2Nu$ . We observe a nearly linear and  $Ra$ -independent increase of this normalised thermal BL thickness along the wind, i. e. within  $J$ , for decreasing  $r$ . Since the PDF of  $\delta_T/(H/2Nu)$  presented in figure 6.19(b) shows an almost  $Ra$ -independent behaviour the normalisation with  $Nu$  compensates perfectly the decreasing BL thickness with growing  $Ra$ . Thus the found PDF is universal (for the investigated tuples  $(Ra, Pr, \Gamma)$ ) and the mean  $\delta_T$  shows a  $Ra$  scaling

$$\langle \delta_T \rangle_{t,r} \sim 1/Nu \sim Ra^{-0.285 \pm 0.003}. \quad (6.8)$$



## 6.6 BOUNDARY LAYER CHARACTERISTICS

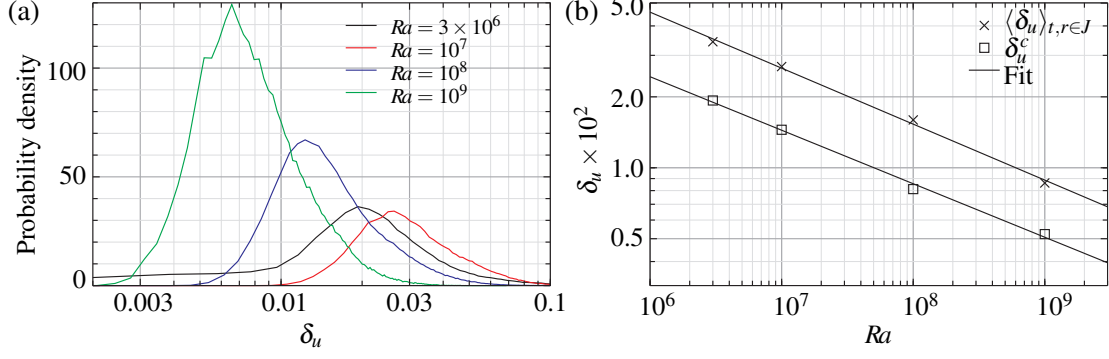


FIGURE 6.20: (a) p.d.f. of viscous boundary layer thickness  $\delta_u$  for  $r \in [-0.7, 0.5]$  and (b) fit of most probable  $\delta_u$  versus  $Ra$ ,  $Pr = 0.786$ ,  $\Gamma = 1$ .

Finally we compare the BL thicknesses for different  $Ra$ , starting with the thermal BL in figure 6.19a, where the time averaged BL thickness along  $l_{LSC}$  is presented in units of  $H/2Nu$ . We observe a nearly linear and  $Ra$ -independent increase of this normalized thermal BL thickness along the wind, i.e. within  $J$ , for decreasing  $r$ . Since the p.d.f. of  $\delta_T/(H/2Nu)$  presented in figure 6.19b shows an almost  $Ra$ -independent behaviour the normalization with  $Nu$  compensates perfectly the decreasing BL thickness with growing  $Ra$ . Thus the p.d.f. found is universal (for the investigated triplets  $(Ra, Pr, \Gamma)$ ) and the mean  $\delta_T$  shows an  $Ra$  scaling

$$\langle \delta_T \rangle_{t,r} \sim 1/Nu \sim Ra^{-0.285 \pm 0.003}. \quad (6.9)$$

As one can see from figure 6.19b, the BL thickness is distributed almost symmetrically around 85% of its approximated value if a logarithmic scale is used.

In the case of the viscous BL the rescaling of the BL thickness with an approximated value is more complicated since no proper value exists. In figure 6.20a the p.d.f. of the viscous BL thickness  $\delta_u$  reflects a Gaussian-like behaviour if scaled logarithmically. If the (not rescaled) p.d.f.s with logarithmic scale are fitted with a Gaussian curve, the most probable BL thickness  $\delta_u^c$  can be evaluated. This  $\delta_u^c$  shows a  $Ra$ -dependence (shown in figure 6.20b)

$$\delta_u^c \sim Ra^{-0.227 \pm 0.010}, \quad (6.10)$$

while  $\langle \delta_u \rangle_{t,r \in J}$  scales as

$$\langle \delta_u \rangle_{t,r \in J} \sim Ra^{-0.238 \pm 0.009} \quad (6.11)$$

and is larger than  $\delta_u^c$  as expected from the p.d.f.

Thus the exponent in the scaling of the viscous BL thickness with  $Ra$  is slightly smaller than that in the scaling of the thermal BL thickness, which lets us conclude that their ratio  $\delta_T/\delta_u$  is slightly decreasing with increasing  $Ra$ . Using the most probable value  $\delta_u^c$  for the rescaling, we

## 6 BOUNDARY LAYER STRUCTURE ANALYSIS

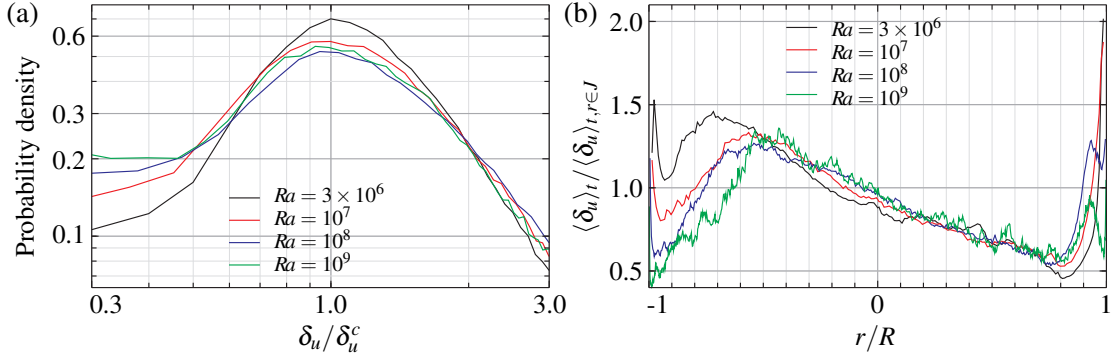


FIGURE 6.21: (a) p.d.f. of viscous boundary layer thickness  $\delta_u$  scaled with the most probable value  $\delta_u^c$  for  $r \in [-0.7, 0.5]$  and (b) time-averaged viscous BL thickness in units of its mean value,  $Pr = 0.786$ ,  $\Gamma = 1$ .

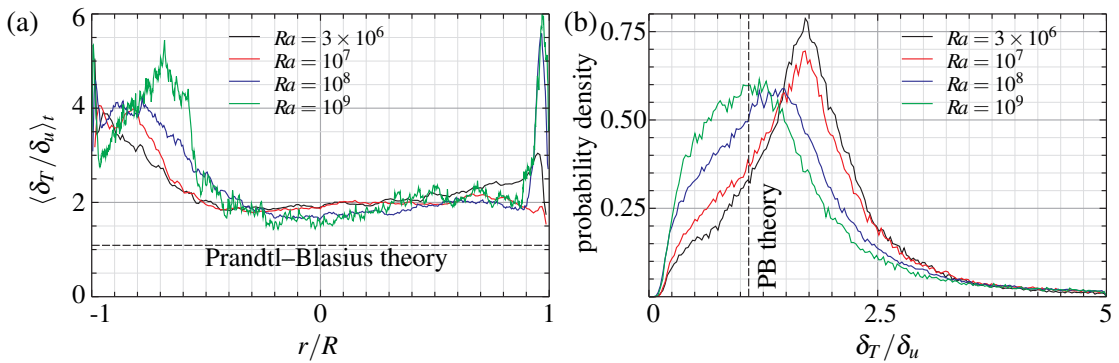


FIGURE 6.22: Ratio  $\delta_T / \delta_u$ , (a) time averaged and (b) p.d.f. for  $r \in [-0.7, 0.5]$ ,  $Pr = 0.786$ ,  $\Gamma = 1$ . The dashed lines correspond to the prediction by Prandtl-Blasius (PB) theory [121].

obtain a similar behaviour for all treated  $Ra$  (see figure 6.21a) as in the case of the thermal BL and as reported by Zhou & Xia [173]. Like in the case of  $\delta_T$  the mean thickness of the viscous BL increases almost linearly along  $l_{LSC}$  (see figure 6.21b).

Besides the individual BL thicknesses also their ratio  $\delta_T / \delta_u$  is of interest. In figure 6.22 the mean ratio  $\delta_T / \delta_u$  over  $l_{LSC}$  and its p.d.f. are shown for different  $Ra$ . We observe that along the plate the ratio remains almost constant within  $J$  but slightly decreases with increasing  $Ra$ . This is exactly what is expected from the previous results. Indeed, the time averaged thermal and viscous BL thicknesses develop almost linearly along the plate, therefore their ratio was expected to be constant within  $J$ . Furthermore, as the individual BL thicknesses scale with  $Ra$  in a different way, an  $Ra$ -dependent ratio is obtained. The p.d.f.s in figure 6.22b reflect that there is a qualitative change from the lower to the higher  $Ra$  cases. This might be due to a change in the dynamics of the systems around  $Ra = 10^8$  as was proposed in the theory by Grossmann & Lohse [51] and supported by the  $Nu$  vs.  $Ra$  dependence presented in figure 6.2.

## 6.7 Comparison with existing theories and models

In the present section the DNS results are first compared to classical BL theories with special focus on the spatial development of the BL thickness and the wind velocity. Further the scalings of integral quantities are compared to theoretical predictions based on different assumptions with respect to the BL theories.

### 6.7.1 Boundary layer theories

Since we have reduced our analysis to a two-dimensional situation with a wind along the flat bottom plate, the obtained results can be compared to the Prandtl–Blasius (PB) theory of laminar BLs [113]. This theory is an approximation of the full governing equation (6.1) applied to the laminar flow parallel to a flat plate of semi-infinite length with a constant wind velocity and no temperature influence on the velocity field. Thus, beside the two-dimensionality several other assumptions are implied. There is first of all the geometry of the flat plate which of course differs from the geometry of a confined Rayleigh–Bénard cell. Studying the influence of the geometry on the development of the BL is far beyond the scope of this paper but it should be mentioned that even for large aspect ratios the large-scale structures have a finite size [8, 59]. The next strong assumption in PB approach is that the temperature is treated as a passive scalar and has no influence on the velocity field. Even though a large effect of buoyancy is expected (due to the occurrence of thermal plumes) a deeper analysis must be left for future studies. In addition the laminarity of the flow is a necessary ingredient of the PB ansatz.

It is well-known that RBC becomes turbulent if a critical  $Ra$  is reached [5], but this does not mean that there are dominant fluctuations in the BL region. To check this we use first of all a theoretical approach [81] for the occurrence of an increasing Tollmien–Schlichting instability within the BL close to a flat plate. The critical shear Reynolds number is estimated as  $Re_s^{\text{crit}} \approx 420$  where  $Re_s = \widehat{U} \widehat{\delta}^* / \widehat{\nu}$ ,  $\widehat{U}$  is the (constant) wind velocity,  $\widehat{\delta}^*$  is the displacement thickness and the hat again marks dimensional quantities. The displacement thickness is connected to our definition of the boundary layer thickness by  $\delta^* \approx \delta_u / 2$ . This can be seen easily by the definition of the displacement thickness [113] applied to an assumed linear profile. Thus  $Re_s$  with our set of references reads  $Re_s = \Gamma^{3/2} Ra^{1/2} Pr^{-1/2} U \delta_u / 2$ . Of course, in the case of RBC the critical  $Re_s$  might be strongly influenced by the geometry and buoyancy but the above relation can be used to estimate the critical  $Re_s$ . We use the most probable viscous BL thickness  $\delta_u^c$  and the largest mean velocity level  $\max_{r \in J} (\langle u_L \rangle_t)$  and thus obtain the scaling (see figure 6.23)

$$Re_s = 0.072 \times Ra^{0.2675} \quad (6.12)$$

based on our DNS data. Extrapolation to higher  $Ra$  tells us therefore that for  $Ra^{\text{crit}} = 1.2 \times 10^{14}$  the critical limit  $Re_s = 420$  is reached. Because all the  $Ra$  covered in our DNS are more than

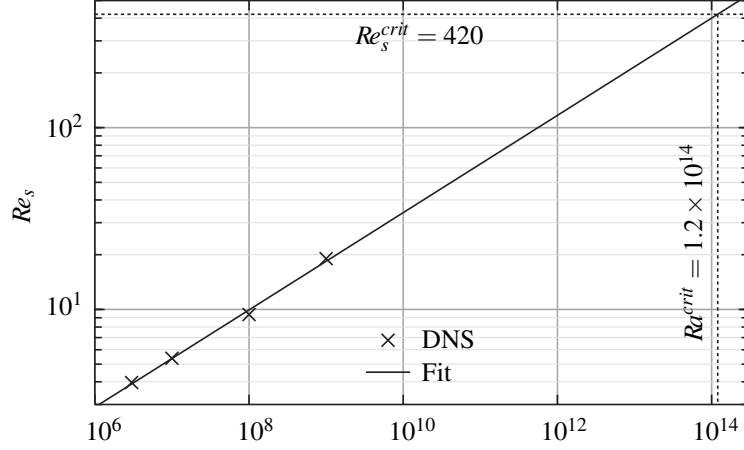


FIGURE 6.23:  $Re_s = \Gamma^{3/2} Ra^{1/2} Pr^{-1/2} U \delta_u / 2$  vs.  $Ra$  and critical  $Ra$  with respect to the Tollmien-Schlichting instability,  $Pr = 0.786$ ,  $\Gamma = 1$ .

five decades smaller than the critical one, we thus conclude that within this estimate our BLs are expected to be predominantly laminar. Note that Sun *et al.* [140] found  $Ra^{crit} = 2 \times 10^{13}$  for quasi-two-dimensional experiments in water.

Even though we are far below  $Ra^{crit}$ , we observe fluctuations in the BL region. We therefore calculate Reynolds stresses [113] and compare the contribution of the fluctuations (turbulent stress) with the total stress, i.e. the sum of the absolutes of laminar and turbulent stresses, and thus the functions

$$\chi_u(r, z) = \frac{|(u_r - \langle u_r \rangle_t)(u_z - \langle u_z \rangle_t)|}{Pr^{1/2} \Gamma^{-3/2} Ra^{-1/2} |\partial_z u_r| + |(u_r - \langle u_r \rangle_t)(u_z - \langle u_z \rangle_t)|} \quad (6.13)$$

$$\chi_T(r, z) = \frac{|(T - \langle T \rangle_t)(u_z - \langle u_z \rangle_t)|}{Pr^{-1/2} \Gamma^{-3/2} Ra^{-1/2} |\partial_z T| + |(T - \langle T \rangle_t)(u_z - \langle u_z \rangle_t)|} \quad (6.14)$$

for the region close to the wall within the LSC plane. Their values vary between zero and one. These limit values correspond to vanishing or infinitely large fluctuations, respectively. We therefore imply a two-dimensional flow with spatially constant mean wind along a plate and thus neglect fluctuations perpendicular to the LSC plane and buoyancy.

The resulting functions  $\chi_u$  and  $\chi_T$  are presented in figure 6.24 in colour together with the mean thicknesses of the viscous BL (case of  $\chi_u$ ) and the thermal BL (case of  $\chi_T$ ) for different  $Ra$ . First of all it is observed that  $\chi_u$  and  $\chi_T$  behave in completely different ways and second that the functions depend weakly on  $Ra$ . Close to the bottom plate the fluctuations are suppressed and the stress is thus dominated by the gradient of wind velocity/temperature. For larger distances from the wall the fluctuations grow and lead to higher  $\chi$ . At the heights of the mean BL thicknesses  $\chi_u$  and  $\chi_T$  grow to 0.5–0.7, which means that the fluctuating contribution is of the same size or even slightly larger than the gradient contribution. Therefore especially for the thermal BL the

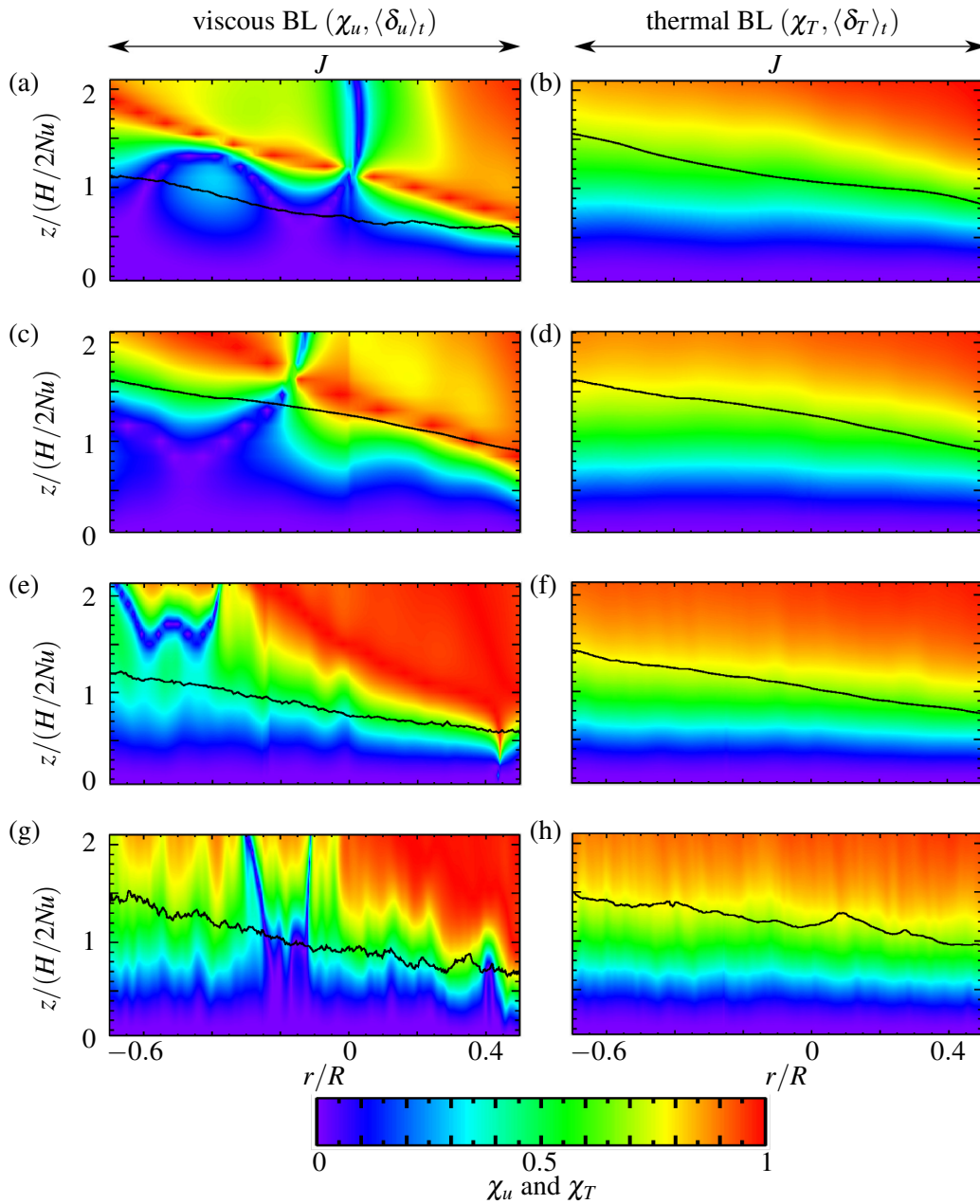


FIGURE 6.24: Relative contributions of fluctuations in the BL region expressed by Reynolds stresses for the viscous ( $\chi_u$ ) (a,c,e,g) and thermal ( $\chi_T$ ) (b,d,f,h) BL (see (6.13),(6.14)). Colour: (a)  $\chi_u$  for  $Ra = 3 \times 10^6$ , (b)  $\chi_T$  for  $Ra = 3 \times 10^6$ , (c)  $\chi_u$  for  $Ra = 10^7$ , (d)  $\chi_T$  for  $Ra = 10^7$ , (e)  $\chi_u$  for  $Ra = 10^8$ , (f)  $\chi_T$  for  $Ra = 10^8$ , (g)  $\chi_u$  for  $Ra = 10^9$ , (h)  $\chi_T$  for  $Ra = 10^9$ , black lines: corresponding mean thicknesses of viscous and thermal BL,  $Pr = 0.786$ ,  $\Gamma = 1$ .

## 6 BOUNDARY LAYER STRUCTURE ANALYSIS

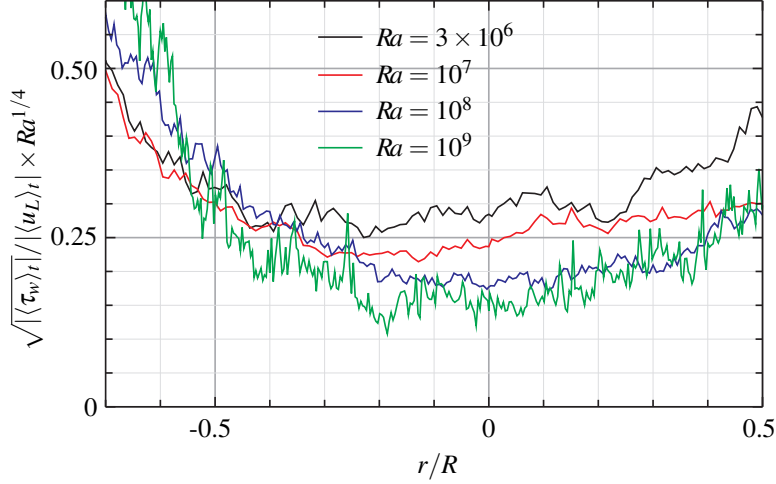


FIGURE 6.25: Ratio  $\sqrt{|\langle \tau_w \rangle_t|} / |\langle u_L \rangle_t|$  (rescaled for clarity with  $Ra^{1/4}$ ) for different  $Ra$ ,  $Pr = 0.786$ ,  $\Gamma = 1$ .

assumption of negligible fluctuations is questionable. This implies that for moderate and large  $Ra$  the influence of these fluctuations, which are not part of the PB theory cannot be neglected and should be investigated in more detail in the future.

Further we observed that the thicknesses of the thermal and the viscous BL increase almost linearly in the direction of the wind as it was already shown in figures 6.19a and 6.21b. Contrary to this PB theory predicts an increase with the square root of the distance along the plate [113]. In fact an almost linear increase is typical for a turbulent BL developing along a flat plate [81] under the assumption of a constant mean wind velocity. But the linear increase is not a sufficient criterion for a turbulent BL. One of the additional requirements is the

$$\frac{d\langle \delta_u \rangle_t}{dx} \sim \frac{\sqrt{|\langle \tau_w \rangle_t|}}{|\langle u_L \rangle_t|}, \quad (6.15)$$

where  $x$  is the wind direction (here radial). It follows directly from an order of magnitude analysis [81]. The right-hand side of (6.15) is evaluated in figure 6.25 and expected to be constant, since the BL thickness is increasing linearly. This is not observed, especially for larger  $Ra$  for which the effects of turbulence should be stronger.

Besides this the BL profiles in the case of a turbulent BL must contain a logarithmic behaviour as was obtained by Hölling & Herwig [65]. On the other hand recent studies by Zhou & Xia [173] show that PB profiles can be obtained if a proper rearranging is performed. To clarify these conflicting results we consider time-averaged local profiles for  $Ra = 10^9$  at  $r = -0.1$ . This choice is motivated by the fact that we expect the strongest influence of fluctuations for our highest  $Ra$  while the position corresponds to the maximal wind magnitude. In figure 6.26 the time averaged temperature (a) and velocity (b) profiles are shown for this position. In addition

## 6.7 COMPARISON WITH EXISTING THEORIES AND MODELS

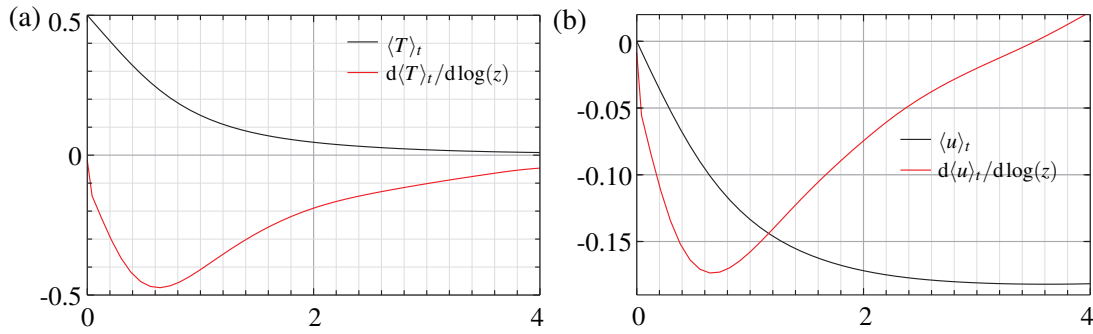


FIGURE 6.26: Local profiles at  $r = -0.1$  of (a) the temperature and (b) the wind velocity in combination with diagnostic functions indicating the occurrence of a logarithmic behaviour if a plateau is present for  $Ra = 10^9$ ,  $Pr = 0.786$ ,  $\Gamma = 1$ .

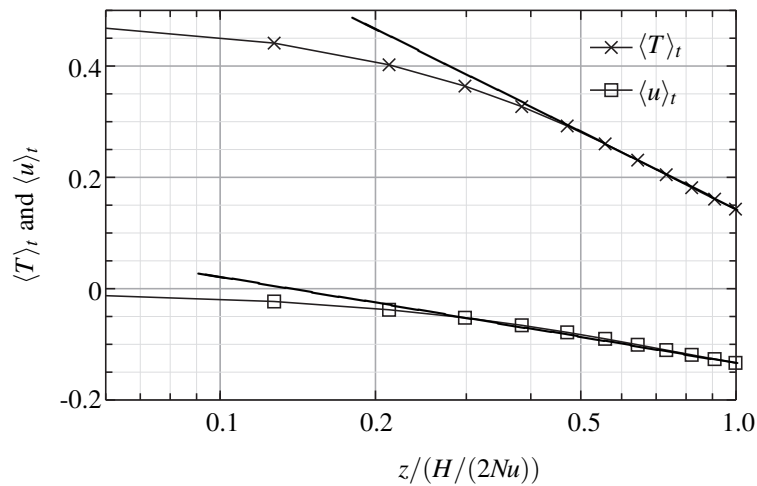


FIGURE 6.27: Local profiles at  $r = -0.1$  of the temperature and the wind velocity with logarithmic spatial scale,  $Ra = 10^9$ ,  $Pr = 0.786$ ,  $\Gamma = 1$ .

diagnostic functions for the occurrence of a logarithmic behaviour are given [see 122]. A plateau of  $df(z)/d\log(z)$  indicates thereby the presence of a logarithmic behaviour. Apparently no plateau is obtained but for both profiles an extremum below  $H/2Nu$  is visible. Figure 6.27 provides another less quantitative presentation of the profiles depicted with a logarithmic length scale. The figure reveals an almost linear behaviour within the upper two-thirds of the BL, which is equivalent to a logarithmic behaviour on a linear scale. Thus we want to emphasize that although in a logarithmic scale the profiles almost coincide with straight lines (figure 6.27) in a certain region, they are essentially non-logarithmic as illustrated by the diagnostic functions in figure 6.26. This together with the invalidity of (6.15) suggests that the linear increase of the BL thicknesses is not simply caused by turbulent BLs.

Another interesting quantity is the ratio of the BL thicknesses  $\delta_T/\delta_u$ , since according to

PB theory it can be approximated by an  $Ra$ -independent (constant) value [121]. As previously shown the thermal BL thickness can be approximated using  $Nu$  and thus knowledge of the ratio allows to approximate the viscous BL thickness. Our results imply that the ratio is almost constant in the direction of the wind and approaches its theoretical value with increasing  $Ra$  (see figure 6.22). This can also be seen from the  $Ra$ -scaling of the BL thicknesses shown in the previous section. From this we obtain the ratio scaling  $\delta_T/\delta_u \sim Ra^{-0.05}$  (which is of course only an approximation because of neglected correlations). Still, for the considered range of  $Ra$  the theoretical value  $\delta_T/\delta_u = Pr^{-0.357+0.022\log_{10}(Pr)} = 1.09$  [121] is almost reached. Similarly the p.d.f.s in figure 6.22b reveal that the theoretical values are approached for higher  $Ra$ . This result is quite surprising since on the one hand the ratio follows the prediction of PB theory to be spatially constant, on the other hand depends on  $Ra$  which is in contradiction to PB theory. Furthermore the  $Ra$ -dependence leads to better agreement with the PB theory for higher  $Ra$ , for which larger effects of the fluctuations are expected. Stevens *et al.* [133] also found a reasonable agreement with PB theory. They obtained about 15% smaller values  $\delta_T/\delta_u$  compared to ours. A possible reason for this discrepancy is that Stevens *et al.* [133] determine  $\delta_u$  in a different way: they use the point of maximum of the quantity  $\vec{u} \cdot \vec{\nabla}^2 \vec{u}$  in the vicinity of the wall instead of the slope criterion.

Besides the fluctuations another BL characteristic might lead to deviations from the classical BL theories. To our knowledge in all discussed models the assumption of a *constant wind* along the plate is made. In figure 6.17a we have shown that the wind is varying strongly along the plate (as also shown by Zhou *et al.* [170] in two-dimensional DNS) and the horizontal component of the mean wind velocity even vanishes at some points. Therefore a further investigation of the influence of such a spatially varying wind on the BL characteristics is needed. We leave this point open for future studies.

### 6.7.2 Scaling of integral quantities

Besides the comparison with PB theory in a direct way we compare integral quantities derived from the DNS data with predictions of Grossmann–Lohse (GL) theory [5, 50] partly based on PB BLs, and the theories by Shraiman & Siggia [128] and Hölling & Herwig [65] which consider turbulent BLs. First of all the Reynolds number  $Re$  obtained is compared to the theories in two different ways. On the one hand it is possible to calculate  $Re$  using the wall shear stress obtained along  $l_{LSC}$  (see figure 6.12a). If we consider the maximal absolute dimensionless wall shear stress  $\tau_w^{\max}$  within the  $r$ -interval  $J$ , we find  $\tau_w^{\max} \sim Ra^\gamma$  with  $\gamma = 0.221$ . In contrast, if we consider the mean wall shear stress  $\langle \tau_w \rangle_r$  within  $J$ , we obtain  $\langle \tau_w \rangle_r \sim Ra^\gamma$  with  $\gamma = 0.206$  (see figure 6.28). The scalings are of course correct only if the above-mentioned set of reference quantities is used. To simplify the comparison we therefore recall dimensional quantities at this point (and again mark them with a hat). Since for the reference velocity  $u_{ref} \sim Ra^{1/2}$ , we



## 6.7 COMPARISON WITH EXISTING THEORIES AND MODELS

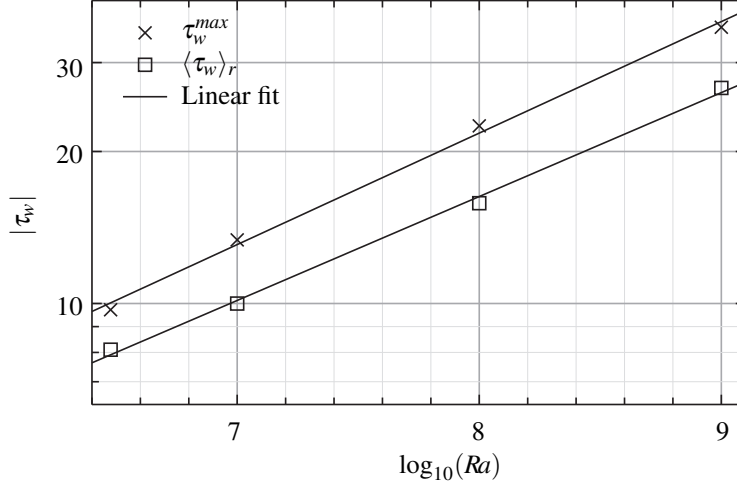


FIGURE 6.28:  $Re$  vs.  $Ra$  scaling obtained from the wall shear stress by using PB theory,  $Pr = 0.786$ ,  $\Gamma = 1$ .

obtain  $\hat{\tau}_w \sim Ra^{\gamma+1/2}$ . From PB theory we obtain that  $Re \sim \hat{\tau}_w^{2/3}$  [121]. Applying the scaling of  $\hat{\tau}_w$  with  $Ra$ , obtained in the DNS, gives us

$$Re \sim \hat{\tau}_w^{2/3} \sim (Ra^{\gamma+1/2})^{2/3} = Ra^{(2\gamma+1)/3} = \begin{cases} Ra^{0.481} \text{ for } \tau_w^{\max}, \\ Ra^{0.471} \text{ for } \langle \tau_w \rangle_r. \end{cases} \quad (6.16)$$

GL theory predicts the scaling depending on different regimes within  $(Ra, Pr)$ -space, in particular for regime  $II_l$   $Re \sim Ra^{2/5}$  and for regime  $IV_l$   $Re \sim Ra^{1/2}$ , where most of the treated pairs  $(Ra, Pr)$  are within  $IV_l$  and for smaller  $Ra$  they are in  $II_l$ . Therefore we find a good agreement.

The velocity levels obtained for different  $Ra$  can be used to compare the  $Re$  versus  $Ra$  scaling with the theories in a more quantitative way. We calculate  $Re$  by means of the height of the cell  $H$ , the mean velocity level  $U = \langle u_L \rangle_{t,r \in J}$  and the (constant) viscosity which reads in our units  $Re = \Gamma^{3/2} Ra^{1/2} Pr^{-1/2} UH$ . By linear fitting  $Re$  versus  $Ra$  the scaling

$$Re = 0.187 \times Ra^{0.496} \quad (6.17)$$

is obtained. The results are shown in figure 6.29a in comparison with predictions from GL theory for the corresponding regimes and with the theory by Shraiman & Siggia [128]. Here for the theory of Grossmann & Lohse [51] no single regimes have been considered but the set of

coupled equations

$$\begin{aligned}
 NuRaPr^{-2} &= c_1Re^2g\left(\sqrt{Re_c/Re}\right)^{-1} + c_2Re^3 \\
 Nu &= c_3Re^{1/2}Pr^{1/2}f\left(2aNuRe_c^{-1/2}g\left(\sqrt{Re_c/Re}\right)\right)^{1/2} \\
 &+ c_4PrRef\left(2aNuRe_c^{-1/2}g\left(\sqrt{Re_c/Re}\right)\right)
 \end{aligned} \tag{6.18}$$

with  $f(x) = (1 + x^4)^{-1/4}$ ,  $g(x) = x(1 + x^4)^{-1/4}$ ,  $a = 0.482$ ,  $c_1 = 8.685$ ,  $c_2 = 1.441$ ,  $c_3 = 0.462$ ,  $c_4 = 0.013$  and  $Re_c = 1.041$  has been solved numerically for  $Re$  and  $Nu$ . Then a linear fitting has been performed to obtain effective scalings for the considered  $Ra$  range. The scaling laws are given in figure 6.29a. In all cases scaling exponents slightly below 1/2 are obtained while the prefactor varies strongly. This might be due to the choice of the reference velocity which is somewhat arbitrary. In the literature different velocities are used which show similar scalings while their absolute values vary [5].

Easier is the comparison for  $Nu$  as the absolute value is not influenced by the choice. As reported in section 6.3 the DNS results are in good agreement with experiments with respect to  $Nu$ . Here, the main focus should be on comparison with three theories based on different assumptions. Besides the GL theory the theories by Shraiman & Siggia [128] (SS-90) and Hölling & Herwig [65] (HH-06) should be considered. Neither theory includes different regimes as the GL theory does. While HH-06 considers the fully turbulent BLs (as they obtained in DNS and experiments in a way similar to figure 6.27), SS-90 predicts turbulent viscous and laminar thermal BLs. The latter is justified by a thermal BL nesting in the viscous one. As shown before, the thermal BL is always thicker than the viscous one for our  $Ra$ ,  $Pr$ ,  $\Gamma$  combination, therefore this assumption seems to be questionable in our case. Shraiman & Siggia [128] predict the validity of their theory for the considered  $Pr$  within  $3 \times 10^7 \lesssim Ra \lesssim 10^{13}$ .

In figure 6.29b a comparison of our DNS data with the three theories is provided. Of course, none of the theories reproduces the DNS results over the whole considered  $Ra$  range exactly. For a small  $Ra$  interval  $10^7 \lesssim Ra \lesssim 10^8$  there is a quite good agreement with Hölling & Herwig [65]. The effective scaling exponent  $\gamma_{eff}$  in the theory by Grossmann & Lohse [51], determined with a linear fit within the complete considered  $Ra$ -interval, is found to agree best with the exponent obtained from our DNS results. Furthermore, only this theory predicts increasing scaling exponents for  $Ra \gtrsim 10^8$  in agreement with the experimental and numerical results presented in figure 6.2.

## 6.8 Conclusions

Direct numerical simulations of Rayleigh–Bénard convection in a cylindrical container with aspect ratio one for  $Pr = 0.786$  and  $Ra = 10^5 - 10^9$  have been performed in order to analyse

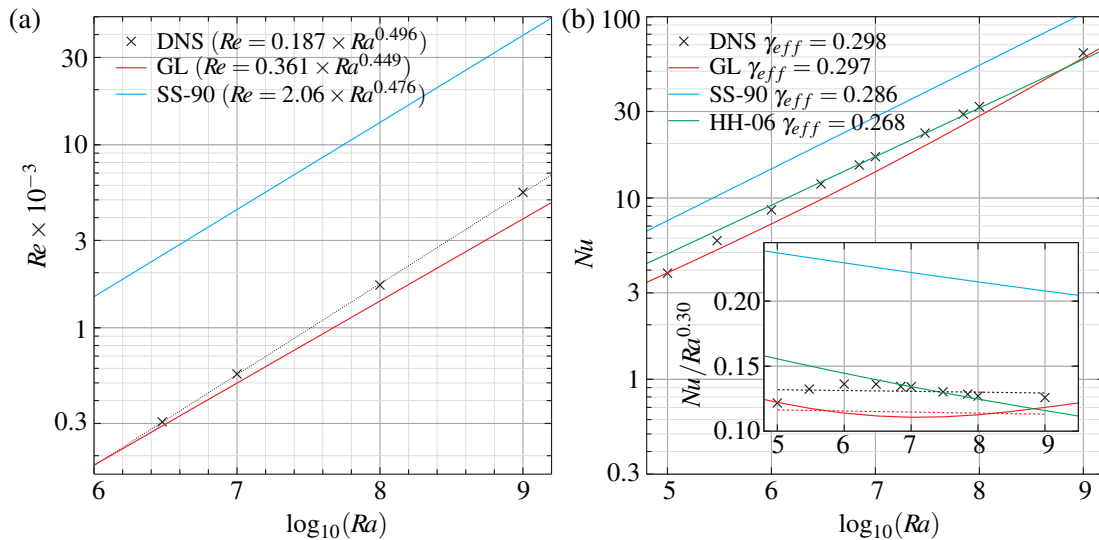


FIGURE 6.29: Scalings from our DNS in comparison with existing theories, (a)  $Re$  versus  $Ra$  scaling and (b)  $Nu$  versus  $Ra$  scaling in comparison with predictions from the theory by Grossmann & Lohse [50] (GL), the theory by Shraiman & Siggia [128] (SS-90) and the theory by Hölling & Herwig [65] (HH-06). Inset of (b): reduced  $Nu$  versus  $Ra$  and fitting to obtain effective scaling exponents  $\gamma_{eff}$ ,  $Pr = 0.786$ ,  $\Gamma = 1$ .

the boundary layers thickness and related quantities. The analysis is restricted to the plane of the large-scale circulation and in particular the viscous and thermal boundary layers in the region close to the bottom plate. Methods to support this analysis are presented and discussed in detail. This includes time averaging over periods without major reorientations and a local and instantaneous determination of the boundary layer thicknesses and the wind velocity. Therefore not only mean values but also probability density functions are analysed.

The results can be summarized as follows: the time-averaged boundary layer thicknesses show a linear increase along the wind direction which occurs for all  $Ra$  considered, while their ratio stays spatially constant and converges slowly with growing  $Ra$  against its theoretical prediction based on Prandtl–Blasius theory. The linear increase of the boundary layer thicknesses is a deviation from Prandtl–Blasius theory and might be explained by domination of fluctuations in the boundary layer region. Nevertheless the evaluation of the diagnostic functions for the presence of the logarithmical BL profiles has not confirmed the presence of fully turbulent BLs for the Rayleigh numbers considered either. In contrast the presence of a spatially varying wind magnitude which is partly dictated by the confined geometry of the convection cell, might be one reason for the linear increase of the BL thickness. This fact is independent of whether fluctuations in the boundary layer region are accounted for. To our knowledge, all boundary layer models considered in the theory of RBC have neglected this fact so far. Nevertheless, the integral quantities  $Nu$  and  $Re$  can be predicted well based on the assumptions of a constant wind.

## 6 BOUNDARY LAYER STRUCTURE ANALYSIS

The authors would like to thank Guenter Ahlers and Joerg Schumacher for fruitful discussions and helpful comments. Furthermore they are grateful to Susanne Horn for updating the DNS code [66] and providing several postprocessing routines and acknowledge support by the Deutsche Forschungsgemeinschaft (DFG) under grant SH405/2-1.

## 7 Spatial resolution requirements

**Citation and credit:** As a conference proceeding for the 3rd International Conference on Turbulence and Interactions 2012 this paper was published in the the book “Turbulence and Interactions: Proceedings of the TI 2012 conference” in 2014. This is the authors’ version of the paper. The original publication is available at [www.springerlink.com](http://www.springerlink.com).

©Springer-Verlag Berlin Heidelberg 2014

**Title:** Numerical investigation of the spatial resolution requirements for turbulent Rayleigh-Bénard convection

**Authors:** Sebastian Wagner, Olga Shishkina & Claus Wagner [157]

**Contribution:** I performed and evaluated the numerical simulations, created all the figures and wrote the first version of the manuscript, which structure is preserved.

### Abstract

The key requirement for setting up a direct numerical simulation (DNS) is a sufficiently fine grid allowing to resolve locally all relevant micro-scales. In case of turbulent Rayleigh-Bénard convection (RBC) this is usually done by fulfilling different analytically derived criteria for the boundary layers and the bulk flow. In order to analyse if these requirements are sufficient, DNS of turbulent RBC in a cylindrical container with aspect ratio unity and Prandtl number  $Pr = 0.786$  have been performed for Rayleigh numbers  $Ra$  up to  $10^9$ . The micro-scales obtained in the DNS as well as their scaling with  $Ra$  are compared with the corresponding theoretical predictions. The analysis reveals that the smallest scales, occurring close to the wall, are about half of the estimated ones. Furthermore, their scaling differs slightly from the estimations while the criterion for the bulk flow fits quite well.

## 7.1 Introduction

The flow driven by the temperature difference between a heated bottom and a cooled top plate, called Rayleigh–Bénard convection (RBC), is a simplified model of many convective flow problems occurring in nature and technology (for recent reviews we suggest [5, 84]). Due to its simplicity, it can be investigated by means of direct numerical simulations (DNS) which is the most accurate ansatz in computational fluid dynamics due to the fact that no turbulence-model is needed. This accuracy is only provided if the computational grid is fine enough to resolve even the smallest scales occurring in the flow.

In the past different attempts to deduce the necessary resolution have been made. In general, two types of investigations exist. On the one hand, grid studies can be performed in which the grid is refined until certain quantities, like the integral vertical heat-flux (called Nusselt number  $Nu$ ), are converged with respect to the grid spacing (e.g. [135]). The general result is that a certain number of grid points within the viscous and thermal boundary layers (BLs) are needed (which results in a very fine mesh close to rigid walls). In addition, a weaker restriction apart from the walls needs to be fulfilled to resolve the motion of the bulk flow. The results on the necessary points in the BLs is collected and published in [121]. To obtain proper computational meshes by performing grid resolution studies is ineffective since a lot of simulations have to be performed while most of them are meaningless due to a lack of spatial resolution. Therefore, on the other hand different attempts have been made to estimate the spatial resolution requirements analytically (see [57, 121]). Based on the insight that different criteria for the BLs and the bulk flow are necessary, Shishkina *et al.* [121] estimated besides a global mesh resolution also the necessary number of nodes to resolve Prandtl-Blasius (laminar) BLs.

In a recent numerical study [155] the BLs close to the horizontal walls showed deviations from Prandtl-Blasius (PB) theory. This leads to the question whether the assumption of laminar BLs can lead to proper estimates on the boundary layer resolution. Therefore, in the present paper a direct comparison of estimated micro-scales with the results from over-resolved DNS is made.

## 7.2 Numerical method

Direct numerical simulations (DNS) have been performed using a fourth-order accurate finite-volume code in cylindrical coordinates  $(r, \phi, z)$ . Some more details and literature on the solver are collected in [155].

We solve the dimensionless conservation laws of momentum, energy and mass in Oberbeck-

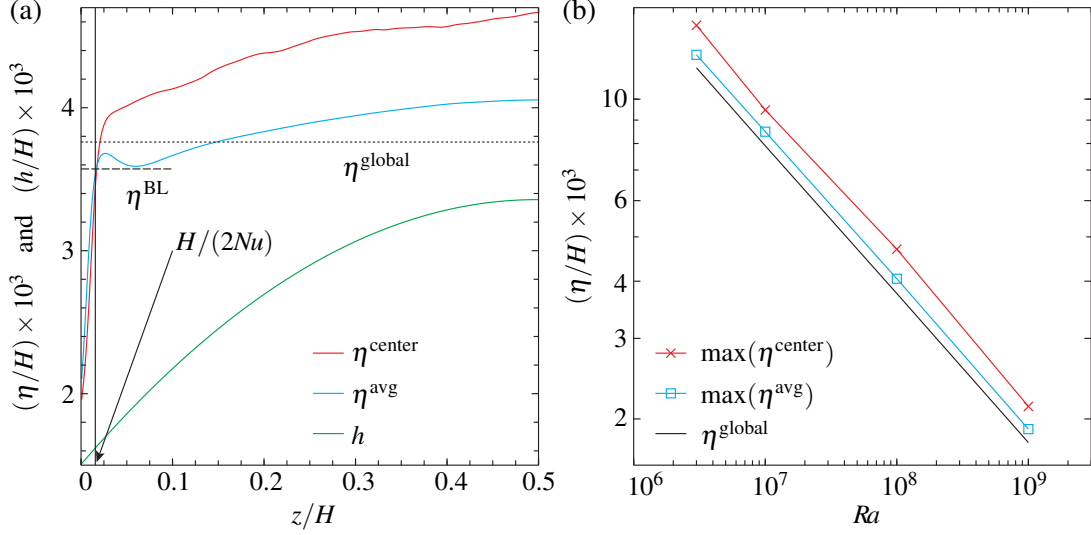


FIGURE 7.1: (a) (—) Mesh spacing  $h$  in vertical direction in comparison with the local micro-scales (—)  $\eta^{\text{center}} = (\nu^3 / \langle \varepsilon \rangle_{t,\phi,r \leq 0.1R})^{1/4}$ , (—)  $\eta^{\text{avg}} = (\nu^3 / \langle \varepsilon \rangle_{t,r,\phi})^{1/4}$  as well as the theoretical estimates (· · ·)  $\eta^{\text{global}} = Pr^{1/2} Ra^{-1/4} (Nu - 1)^{-1/4} H$  and (— —)  $\eta^{\text{BL}} = 2^{-3/2} a^{-1} Nu^{-3/2} Pr^{0.5355 - 0.033 \log(Pr)} H$  (see text) for  $Ra = 10^8$  and (b) their largest values for different  $Ra$ ,  $Pr = 0.786$ ,  $\Gamma = 1$ .

### Boussinesq approximation

$$\partial_t \vec{u} + \vec{u} \cdot \vec{\nabla} \vec{u} = -\vec{\nabla} p + \sqrt{\frac{Pr}{Ra \Gamma^3}} \vec{\nabla}^2 \vec{u} + T \vec{e}_z, \quad (7.1)$$

$$\partial_t T + \vec{u} \cdot \vec{\nabla} T = \sqrt{\frac{1}{Pr Ra \Gamma^3}} \vec{\nabla}^2 T, \quad \vec{\nabla} \cdot \vec{u} = 0, \quad (7.2)$$

in a cylindrical computational domain with aspect ratio  $\Gamma$  (diameter  $D = 2R$  per height  $H$ ) equal to one.<sup>1</sup> Due to non-dimensionalization the characteristic dimensionless Rayleigh number  $Ra = \alpha g H^3 \Delta T / (\nu \kappa) \in [10^6, 10^9]$  and Prandtl number  $Pr = \nu / \kappa = 0.786$  occur. On the cylinder's surface no slip-conditions are prescribed, the vertical wall is adiabatic and on the top and bottom plate the temperature is fixed with  $T_{\text{bottom}} > T_{\text{top}}$ .

For simplicity and computational effectiveness the computational mesh is chosen structured and non-uniform (i.e. the nodes are clustered close to the rigid walls).

Structured grid means that the distribution of nodes in one spatial direction is independent from the other directions. The distribution of the nodes follows a tanh-function [143] and is visualized in figure 7.1a. Since the usual criteria for the mesh-resolution should be investigated and discussed in the present paper, the spatial resolution in the DNS is chosen finer than the one estimated by theory. The numbers of computational nodes in the DNS along different directions with further simulation parameters are collected in table 7.1.

<sup>1</sup> $\partial_t$  denotes the partial derivative with respect to time  $t$ , while  $\vec{e}_z$  is the unit vector in  $z$  direction.

## 7 SPATIAL RESOLUTION REQUIREMENTS

TABLE 7.1: Simulation parameters in the DNS:  $N_i$  number of computational nodes in  $i \in \{r, \phi, z\}$ -direction and smallest and largest mesh-spacing  $h$  in vertical direction,  $Pr = 0.786$ ,  $\Gamma = 1$

$Ra$	$N_r \times N_\phi \times N_z$	$\min(h/H) \times 10^3$	$\max(h/H) \times 10^3$
$3 \times 10^6$	$96 \times 256 \times 192$	4.51	5.60
$10^7$	$96 \times 256 \times 192$	4.51	5.60
$10^8$	$192 \times 512 \times 384$	1.51	3.36
$10^9$	$384 \times 1024 \times 768$	0.65	1.78

### 7.3 Spatial resolution requirements in RBC

In a proper DNS, the smallest scales occurring in a turbulent flow need to be resolved. Apart from the walls, i.e. in case of (at least locally) isotropic turbulence and for  $Pr \leq 1$  the resolution of Kolmogorov scales  $\eta_K$  is required. This means  $h/\eta_K \leq 1$  should be fulfilled, where  $h$  is the mean grid spacing of the computational grid [57, 121].

In case of isotropic turbulence, Kolmogorov defined  $\eta_K = (\nu^3/\varepsilon)^{1/4}$  where  $\nu$  is the kinematic viscosity and  $\varepsilon$  is the kinetic dissipation rate which is given as  $\varepsilon = (\nu/2)\sum_i \sum_j (\partial_{x_j} u_i + \partial_{x_i} u_j)^2$  (see e.g. [101]). Close to the walls, the requirement of isotropy is not longer fulfilled, thus the question of the resolution of this area arises. Assuming that we fulfill  $h/(\nu^3/\varepsilon)^{1/4} \leq 1$  everywhere in the computational domain and there is a wind in  $x$  direction parallel to a rigid wall (with no-slip condition). Further, let  $z$  be the direction orthogonal to the wall and (without loss of generality)  $\partial u_x/\partial z \geq 0$ . Then we obtain at this wall

$$1 \geq h(\nu^3/\varepsilon)^{-1/4} \gtrsim h\sqrt{\nu\partial_z u_x}\nu^{-1} = hu_\tau\nu^{-1} \equiv h^+ \quad (7.3)$$

Here  $h^+$  denotes the grid spacing in wall-units  $\nu/u_\tau$ . The restriction  $h^+ \leq 1$  at the wall (to resolve large velocity gradient in the viscous sub-layer) is well known from the literature [101]. Thus the requirement  $h/(\nu^3/\varepsilon)^{1/4} \leq 1$  lets us fulfill the two criteria  $h/\eta_K \leq 1$  (apart from the wall in case of isotropic turbulence) and  $h^+ \leq 1$  at the wall. We assume that in between these regions the restriction needs to be fulfilled, as well. Therefore, only the requirement  $h/(\nu^3/\varepsilon)^{1/4} \leq 1$  needs to be fulfilled everywhere in the domain. For a simpler notation, we call  $(\nu^3/\varepsilon)^{1/4}$  as *micro-scales*  $\eta$  in the following.

For the sake of simplicity, we focus on  $Pr = 0.786$ . Further we restrict ourselves to time- (and spatial-) averaged dissipation rates to make analytical derivations feasible.

From the conservation law of momentum, it can be derived analytically [121] that

$$\langle \varepsilon \rangle_{t,r,\phi,z} = \frac{\nu^3}{H^4} (Nu - 1) Ra Pr^{-2} \quad (7.4)$$

while the Nusselt number  $Nu \equiv \frac{\langle u_z T - \kappa \partial_z T \rangle_{t,r,\phi}}{\kappa \Delta T / H}$  is the integral heat flux in vertical direction, which



## 7.4 MICRO-SCALES PREDICTED IN DNS

is a function of  $Ra, Pr$  and the geometry of the convection cell. Since  $\langle \varepsilon \rangle_{t,r,\phi,z}$  includes the boundary layers close to the rigid walls in which  $\varepsilon$  is large [79], the question must be answered whether the global micro-scale  $\eta^{\text{global}}$  based on  $\langle \varepsilon \rangle_{t,r,\phi,z}$  can be used to estimate the bulk flow micro-scales.

To estimate the required resolution of kinetic and thermal boundary layers in the vicinity of the rigid walls Shishkina *et al.* [121] derived:

$$\langle \varepsilon \rangle_{t,r,\phi,z=z_0 \in \text{BL}} \gtrsim \frac{64\nu^3 a^4 Nu^6}{H^4} \left( \frac{\delta_\theta}{\delta_u} \right)^6 \quad (7.5)$$

Here  $a \approx 0.482$  is a parameter obtained from experiments and  $\delta_\theta, \delta_u$  are the thicknesses of the thermal and viscous BL, respectively. In the derivation, the boundary layers have been assumed to be of PB type. By this estimation

$$\left( \frac{\delta_\theta}{\delta_u} \right) = Pr^{-0.357+0.022 \log(Pr)} \quad (7.6)$$

can be obtained for  $3 \times 10^{-4} \leq Pr \leq 3$ . Further the necessary number of grid-points within the thermal and viscous BL is estimated by distributing points equidistantly based on  $\langle \varepsilon \rangle_{t,r,\phi,z=z_0 \in \text{BL}}$ . Since in a recent publication [155] the question was addressed, whether the PB theory is the proper description of the boundary layers occurring in turbulent RBC, we further tested whether (7.5) together with (7.6) can be used as a proper estimate  $\eta^{\text{BL}}$  for the BL resolution.

## 7.4 Micro-scales predicted in DNS

Similar as in the analytical derivations we obtain in our DNS time-averaged dissipation rates  $\langle \varepsilon \rangle_t$  as defined above. Due to azimuthal symmetry in the cylindrical convection cell we further analyse  $\phi$ -averaged dissipation rates and concentrate on the lower half of the convection cell (up-down-symmetry). In figure 7.2a the resulting micro-scales

$$\eta^{\text{local}} = (\nu^3 / \langle \varepsilon \rangle_{t,\phi})^{1/4} \quad (7.7)$$

(in units of  $\eta^{\text{global}}$ ) are shown for  $Ra = 10^8$ . As expected from the literature [79]  $\eta$  is largest at the center of the convection cell and decreases strongly near the walls.

In the following, we will concentrate on vertical profiles  $\eta(z)$  since at the horizontal walls thermal BLs exist in addition to the viscous BLs. First it seems worth clarifying, whether a structured grid is suitable for our DNS. Since a viscous BL develops close to the vertical wall, resolving the smallest  $\eta(r)$  for each  $z$  in a structured grid (i.e. the grid spacing  $h$  in  $z$ -direction is independent of  $\phi$  and  $r$ ) is too strict since it requires an extremely fine mesh in the whole domain. However, considering  $|\partial_z \langle u_r \rangle_t|$  and  $|\partial_r \langle u_z \rangle_t|$  (as shown in units of its maximum in figures 7.2b

## 7 SPATIAL RESOLUTION REQUIREMENTS

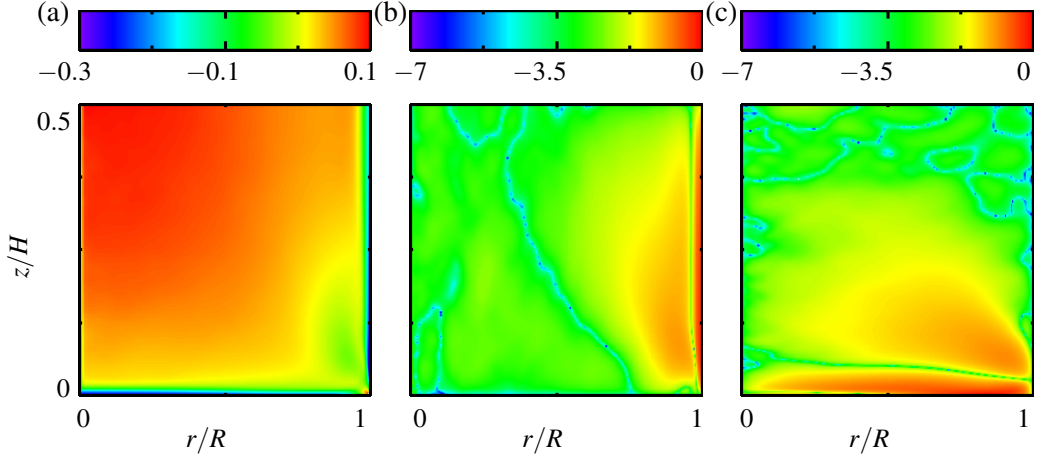


FIGURE 7.2: Spatial distribution of (a) micro-scales in units of their volume average  $\log_{10}(\eta^{\text{local}}/\eta^{\text{global}})$ , (b),(c) single components of gradient tensor in units of their maximum  $\log_{10}(|\partial_r \langle u_z \rangle_t|/\max(|\partial_r \langle u_z \rangle_t|))$  and  $\log_{10}(|\partial_z \langle u_r \rangle_t|/\max(|\partial_z \langle u_r \rangle_t|))$ , respectively, for  $Ra = 10^8$ ,  $Pr = 0.786$ ,  $\Gamma = 1$ .

and 7.2c) we obtain that close to the wall only the components of the gradient orthogonal to the wall contribute significantly to the dissipation rates. Therefore, the boundary layer at the vertical wall mainly requires resolution in  $r$ -direction but not in  $z$ -direction. Nevertheless, in the following not only profiles  $\eta(z)$  at the cell center

$$\eta^{\text{center}} = (\mathbf{v}^3 / \langle \epsilon \rangle_{t, \phi, r \leq 0.1R})^{1/4}, \quad (7.8)$$

but also profiles based on dissipation rates averaged in radial direction

$$\eta^{\text{avg}} = (\mathbf{v}^3 / \langle \epsilon \rangle_{t, r, \phi})^{1/4} \quad (7.9)$$

will be discussed to be on the safe side. The resulting smallest and largest  $\eta$  are collected in figures 7.1b, 7.3a for different  $Ra$  and the corresponding profiles for  $Ra = 10^8$  are depicted in figure 7.1a.

Figure 7.1a reveals that the largest micro-scales (occurring at the convection cell center) are larger than the estimate  $\eta^{\text{global}}$  (as obtained from equation (7.4)). The largest difference is obtained for  $\eta^{\text{center}}$ . Nevertheless,  $\max(\eta^{\text{center}})$  and  $\max(\eta^{\text{avg}})$  reflect the same  $Ra$  dependence as  $\eta^{\text{global}}$  does (see figure 7.1b). Therefore,  $\eta^{\text{global}}$  can be used as an estimate for the micro-scales at the cell center  $\eta^{\text{bulk}}$  if an additional constant prefactor  $c$  is introduced, i.e.  $\eta^{\text{bulk}} = c\eta^{\text{global}}$ . For the case of  $\eta^{\text{center}}$  the prefactor is  $c \approx 1.22$  while for  $\eta^{\text{avg}}$  we obtain  $c \approx 1.07$ . Nevertheless, the lower bound requirement  $\eta^{\text{global}}$  can be used if we want to be on the safe side.

Considering the micro-scales at the wall, i.e. the overall smallest micro-scales, the situation is more complex. Already figure 7.1a reveals that the micro-scales strongly increase in the boundary layer region ( $z \leq H/(2Nu)$ ) and are much smaller than the estimate  $\eta^{\text{BL}}$ . From this

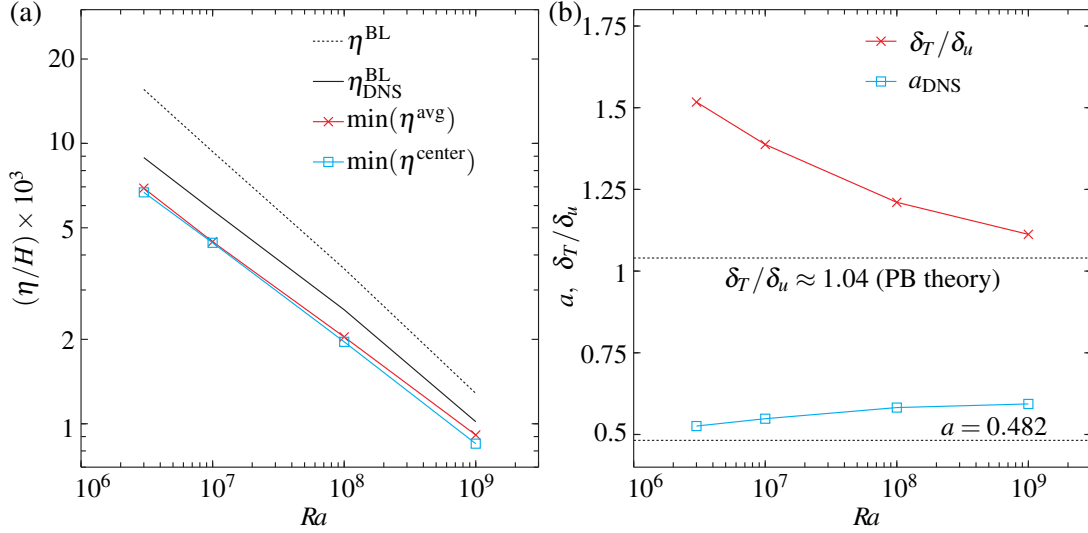


FIGURE 7.3: (a) Comparison of micro-scales (at the wall) (—)  $\eta^{avg}$  (7.9), (—)  $\eta^{center}$  (7.8) with theoretical estimates (7.5) based on  $a = 0.482$  from experiment, (b)  $\delta_\theta/\delta_u$  from theory (7.6) ( $\cdots$ )  $\eta^{BL}$  and  $a$ ,  $\delta_\theta/\delta_u$  from DNS (—)  $\eta_{DNS}^{BL}$ , for different  $Ra$ ,  $Pr = 0.786$ ,  $\Gamma = 1$ .

we conclude that this requirement is not restrictive enough. Recalling equation (7.5) reveals that  $\eta^{BL}$  contains two problematic parameters:  $a$  and  $\delta_\theta/\delta_u$ . While  $a \approx 0.482$  is obtained from experiments,  $\delta_\theta/\delta_u$  is usually predicted by using PB theory (7.6). If we evaluate these two parameters using the DNS results based on [155]) we obtain their tendency with respect to  $Ra$  as depicted in figure 7.3b revealing deviations from the ones given Shishkina et al. In figure 7.3a  $\eta^{BL}$  is compared with the micro-scales at the wall obtained in DNS. Further  $a$  and  $\delta_\theta/\delta_u$  from DNS have been used to evaluate  $\eta_{DNS}^{BL}$  from (7.5). The comparison shows that the deviations of  $\eta^{BL}$  from  $\eta^{center}$  (which is almost equivalent to considering  $\eta^{avg}$ ) can be reduced by using  $\eta_{DNS}^{BL}$ . Even the scaling with  $Ra$  fits better to the DNS results. Nevertheless, even  $\eta_{DNS}^{BL}$  is not restrictive enough. As a proper resolution requirement at the wall we suggest to use  $\eta^{BL}/2$  for the considered  $Ra$ ,  $Pr$ . The number of points is thereby not necessarily increased, since the equidistant distribution of nodes does not fit to the strong increase of the micro-scales within the BLs. A clever distribution of computational nodes (fulfilling  $h \leq \eta^{BL}/2$  at the wall and  $h \leq c\eta^{global}$  at the cell center) is thus required to match  $\eta^{center}$  (or  $\eta^{avg}$ ) as depicted in 7.1(a). For example, if the nodes are distributed as described by  $\eta^{avg}$  the number of points in  $z$ -direction for  $Ra = 10^8$  is 263, which is about 70% of the nodes we used in the simulation.

## 7.5 Conclusions

We compare theoretical estimates on the BL and bulk resolution with the resolution requirements derived from over-resolved DNS of RBC. It was shown that the analytical derivation based on the

## 7 SPATIAL RESOLUTION REQUIREMENTS

volume- (and time-) averaged kinetic dissipation rates leads to a proper estimate for the resolution required at the convection cell center. Considering the boundary layers the theoretically predicted smallest micro-scales in the boundary layers are larger than the ones obtained by analysing the DNS results. For the considered  $Ra$ ,  $Pr$  the estimate for the micro-scales needs to be decreased by a factor of two to guarantee a proper resolution at the wall. Further, the dramatic changes of the micro-scales within the BLs compel us to distribute the computational nodes non-equidistantly close to the walls. Therefore, eventhough the mesh at the walls needs to be finer, the required overall number of nodes in the BLs might be unchanged.

The authors acknowledge support by the Deutsche Forschungsgemeinschaft (DFG) under grant SH405/2-1.

## 8 Falkner-Skan boundary layer structure

**Citation and credit:** This chapter consists of a paper published in the Journal of Fluid Mechanics 730, pages 442–463, September 2013.

It is available online at <http://dx.doi.org/10.1017/jfm.2013.347>. With permission of Oxford University Press the authors' version of the paper is posted here.

©Cambridge University Press 2012

**Title:** Falkner-Skan boundary layer approximation in Rayleigh-Bénard convection

**Authors:** Olga Shishkina, Susanne Horn & Sebastian Wagner [119]

**Contribution:** I performed and analysed the numerical simulations for Prandtl number 0.786, developed the evaluation technique for the determination of the angle of attack from DNS results and applied it to the numerical data. Further, I created the figures 8.3, 8.8, 8.9, 8.10 and wrote parts of the text in section 8.7 of the paper.

### Abstract

To approximate the velocity and temperature within the boundary layers in turbulent thermal convection at moderate Rayleigh numbers, we consider the Falkner–Skan ansatz, which is a generalization of the Prandtl–Blasius one to a non-zero-pressuregradient case. This ansatz takes into account the influence of the angle of attack  $\beta$  of the large-scale circulation of a fluid inside a convection cell against the heated/cooled horizontal plate. With respect to turbulent Rayleigh–Bénard convection, we derive several theoretical estimates, among them the limiting cases of the temperature profiles for all angles  $\beta$ , for infinite and for infinitesimal Prandtl numbers  $Pr$ . Dependences on  $Pr$  and  $\beta$  of the ratio of the thermal to viscous boundary layers are obtained from the numerical solutions of the boundary layers equations. For particular cases of  $\beta$ , accurate approximations are developed as functions on  $Pr$ . The theoretical results are corroborated by our direct numerical simulations for  $Pr = 0.786$  (air) and  $Pr = 4.38$  (water). The angle of attack  $\beta$  is estimated based on the information on the locations within the plane of the large-scale circulation where the time-averaged wall shear stress vanishes. For the fluids

considered it is found that  $\beta \approx 0.7\pi$  and the theoretical predictions based on the Falkner–Skan approximation for this  $\beta$  leads to better agreement with the DNS results, compared with the Prandtl–Blasius approximation for  $\beta = \pi$ .

## 8.1 Introduction

Turbulent thermal convection between two horizontal plates with lower heated and upper cooled flat surfaces has been the subject of numerous experimental and numerical studies. This problem is known as turbulent Rayleigh–Bénard convection (RBC), and for reviews we refer to [5, 32, 84, 129].

In turbulent thermal convection for moderate Rayleigh numbers the thermal boundary layers, which are located close to the heated or cooled horizontal plates, and the viscous boundary layers, which are attached to all rigid walls, can be transitional or even laminar [5]. In this case the mean flow characteristics within the boundary layers are usually approximated using the Prandtl–Blasius ansatz, i.e. under the assumption that the wind of turbulence (or large-scale circulation, LSC) above the viscous boundary layer is horizontal and constant, which leads to a zero pressure derivative with respect to the wind direction.

In contrast, recent direct numerical simulation (DNS) of turbulent RBC in different fluids showed that, first, the time-averaged pressure gradient does not vanish [118]; second, the wind is non-constant along its path; and third, the ratio of the thicknesses of the thermal and viscous boundary layers, although almost constant along the wind, is approximately twice as large as that predicted by the Prandtl–Blasius equations [155]. A non-parallel wind or, in other words, the angle of attack  $\beta$ ,  $\beta < \pi$ , of the large-scale circulation of a fluid inside an RBC cell against the heated/cooled horizontal plate, influences the flow characteristics within the boundary layers.

In the present work, in order to account for the influence of the angle  $\beta \neq \pi$  and, hence, of the non-parallel and non-constant wind, we make use of the Falkner–Skan approximation of the boundary layers in turbulent thermal convection, which can be interpreted as an extension of the Prandtl–Blasius ansatz to a non-zero pressure change along the wind. As we show in the present work, this approach, compared with a Prandtl–Blasius one, leads to more reliable predictions of some integrated quantities related to the thicknesses of the thermal and viscous boundary layers.

Since our theoretical estimates are compared with <sup>1</sup> the numerical data, we start the paper with a short description of the numerical ansatz (section 8.2), then discuss the boundary layer equations (section 8.3) and their own boundary conditions, i.e. the wind at the edge of the viscous boundary layer (section 8.4). After that the solutions of the obtained system of the boundary layer equations as well as their limits for Prandtl numbers  $Pr \ll 1$  and  $Pr \gg 1$  are derived (section 8.5). Finally, the balance between the thicknesses of the thermal and viscous

---

<sup>1</sup>In the original paper the incorrect phrase “corroborated against” was used.

## 8.2 GOVERNING EQUATIONS AND DNS OF TURBULENT RBC

boundary layers is discussed in section 8.6 and a corroboration of the theory with the numerical results, obtained in the DNS of turbulent RBC in water and air, is discussed in section 8.7.

### 8.2 Governing equations and DNS of turbulent RBC

We consider the following system of the governing momentum (8.1), (8.2), (8.3), energy (8.4) and continuity (8.5) equations for the Rayleigh–Bénard problem in Boussinesq approximation:

$$\tilde{u}_t + \tilde{u}\tilde{u}_x + \tilde{v}\tilde{u}_y + \tilde{w}\tilde{u}_z + \tilde{p}_x/\tilde{\rho} = \tilde{\nu}(\tilde{u}_{xx} + \tilde{u}_{yy} + \tilde{u}_{zz}), \quad (8.1)$$

$$\tilde{v}_t + \tilde{u}\tilde{v}_x + \tilde{v}\tilde{v}_y + \tilde{w}\tilde{v}_z + \tilde{p}_y/\tilde{\rho} = \tilde{\nu}(\tilde{v}_{xx} + \tilde{v}_{yy} + \tilde{v}_{zz}) + \tilde{\alpha}\tilde{g}(\tilde{T} - \tilde{T}_{\text{mid}}), \quad (8.2)$$

$$\tilde{w}_t + \tilde{u}\tilde{w}_x + \tilde{v}\tilde{w}_y + \tilde{w}\tilde{w}_z + \tilde{p}_z/\tilde{\rho} = \tilde{\nu}(\tilde{w}_{xx} + \tilde{w}_{yy} + \tilde{w}_{zz}), \quad (8.3)$$

$$\tilde{T}_t + \tilde{u}\tilde{T}_x + \tilde{v}\tilde{T}_y + \tilde{w}\tilde{T}_z = \tilde{\kappa}(\tilde{T}_{xx} + \tilde{T}_{yy} + \tilde{T}_{zz}), \quad (8.4)$$

$$\tilde{u}_x + \tilde{v}_y + \tilde{w}_z = 0, \quad (8.5)$$

where  $\tilde{u}$  and  $\tilde{w}$  are the horizontal components of the velocity along the axes  $\tilde{x}$  and  $\tilde{z}$ , respectively, and  $\tilde{v}$  is the vertical component of the velocity along the axis  $\tilde{y}$ ,  $\tilde{t}$  denotes time and  $\tilde{p}$  the pressure. A variable marked as a subindex denotes the partial derivative with respect to this variable, e.g.  $\tilde{u}_t \equiv \partial\tilde{u}/\partial\tilde{t}$ ,  $\tilde{u}_x \equiv \partial\tilde{u}/\partial\tilde{x}$ , etc. Further,  $\tilde{T}_{\text{mid}}$  is the arithmetic mean of the top temperature  $\tilde{T}_{\text{top}}$  and bottom temperature  $\tilde{T}_{\text{bot}}$ ,  $\tilde{T}_{\text{bot}} > \tilde{T}_{\text{top}}$ ,  $\tilde{\rho}$  denotes the density,  $\tilde{\nu}$  the kinematic viscosity,  $\tilde{\kappa}$  the thermal diffusivity,  $\tilde{\alpha}$  the isobaric thermal expansion coefficient and  $\tilde{g}$  the acceleration due to gravity. The velocity vanishes on the domain's boundary, according to the impermeability and no-slip boundary conditions, while the normal derivative of the temperature on the vertical wall is equal to zero, because of its adiabaticity.

Substituting the factorization  $\tilde{X} = \tilde{X}_{\text{ref}}X$  for each dimensional variable  $\tilde{X}$  in the system (8.1)–(8.5), where  $X$  is a dimensionless variable and  $\tilde{X}_{\text{ref}}$  the corresponding reference value,  $\tilde{x}_{\text{ref}} = \tilde{D}$ ,  $\tilde{u}_{\text{ref}} = (\tilde{\alpha}\tilde{g}\tilde{D}\tilde{\Delta})^{1/2}$ ,  $\tilde{t}_{\text{ref}} = \tilde{x}_{\text{ref}}/\tilde{u}_{\text{ref}}$ ,  $\tilde{T} - \tilde{T}_{\text{mid}} = \tilde{\Delta}T$ ,  $\tilde{\Delta} \equiv \tilde{T}_{\text{bot}} - \tilde{T}_{\text{top}}$ ,  $\tilde{p}_{\text{ref}} = \tilde{u}_{\text{ref}}^2\tilde{\rho}$ ,  $\tilde{D}$  the width of the container and  $\tilde{H}$  its height, we obtain the following system of dimensionless equations:

$$\begin{aligned} u_t + uu_x + vu_y + wu_z + p_x &= \Gamma^{-3/2}Ra^{-1/2}Pr^{1/2}(u_{xx} + u_{yy} + u_{zz}), \\ v_t + uv_x + vv_y + wv_z + p_y &= \Gamma^{-3/2}Ra^{-1/2}Pr^{1/2}(v_{xx} + v_{yy} + v_{zz}) + T, \\ w_t + uw_x + vw_y + ww_z + p_z &= \Gamma^{-3/2}Ra^{-1/2}Pr^{1/2}(w_{xx} + w_{yy} + w_{zz}), \\ T_t + uT_x + vT_y + wT_z &= \Gamma^{-3/2}Ra^{-1/2}Pr^{-1/2}(T_{xx} + T_{yy} + T_{zz}), \\ u_x + v_y + w_z &= 0, \end{aligned} \quad (8.6)$$

Here  $Ra$  and  $Pr$  are the Rayleigh number and Prandtl number,

$$Ra = \tilde{\alpha}\tilde{g}\tilde{\Delta}\tilde{H}^3/(\tilde{\nu}\tilde{\kappa}), \quad Pr = \tilde{\nu}/\tilde{\kappa}, \quad (8.7)$$

TABLE 8.1: DNS parameters for the Prandtl number 0.786 and 4.38: the number of mesh nodes in the direction  $N_i$  ( $i = r; \phi; z$ ), the number of nodes in the thermal and viscous BLs as used in the DNS ( $n_T$  and  $n_u$ ) and as required by theory [121] ( $\check{n}_T$  and  $\check{n}_u$ ), the Nusselt number  $Nu$  with its maximal deviation and the number of dimensionless time units  $\tau$  used for the statistical averaging. The data for  $Pr = 0.786$  are adopted from [155].

$Pr$	$Ra$	$N_r$	$N_\phi$	$N_z$	$n_T$	$\check{n}_T$	$n_u$	$\check{n}_u$	$Nu$	$\tau$
0.786	$10^7$	96	256	192	8	4	8	3	$16.9 \pm 0.2$	3775
	$10^8$	192	512	384	11	5	11	5	$31.9 \pm 0.2$	1240
	$10^9$	384	1024	768	13	7	12	6	$63.1 \pm 0.4$	318
4.380	$10^7$	64	512	128	6	3	9	5	$16.2 \pm 0.5$	200
	$10^8$	192	512	384	9	4	14	6	$32.9 \pm 0.2$	760
	$10^9$	384	512	768	16	6	25	9	$64.7 \pm 0.7$	250

respectively, and  $\Gamma \equiv \tilde{D}/\tilde{H}$  is the aspect ratio. The dimensionless temperature varies between  $T_{\text{bot}} = 0.5$  at the bottom and  $T_{\text{top}} = -0.5$  at the top horizontal walls and satisfies  $\partial T / \partial \mathbf{n} = 0$  on the vertical walls, where  $\mathbf{n}$  is the normal vector. All velocity components are equal to zero on the domain's boundary.

DNS of turbulent RBC in air and water in a cylindrical domain of the aspect ratio  $\Gamma = 1$  are performed using the same finite-volume code as in [123], [66]. The computational grids used in the DNS resolve Kolmogorov and Batchelor scales in the whole domain. According to the conducted *a posteriori* grid resolution analysis, we take up to two times more grid nodes within the thermal and viscous boundary layers than in the theoretical estimates derived in [121] for the minimally required numbers of the nodes,  $N_{th}$  and  $N_v$ , respectively. Further details on the conducted DNS can be found in table 8.1.

Direct numerical simulations of turbulent RBC in air and water in a cylindrical domain of the aspect ratio  $\Gamma = 1$  are performed using the same finite-volume code as in [123] and [66]. The computational grids used in the DNS resolve Kolmogorov and Batchelor scales in the whole domain. According to the *a posteriori* grid resolution analysis conducted, we take up to twice as many grid nodes within the thermal and viscous boundary layers than in the theoretical estimates derived in [121] for the minimally required numbers of the nodes,  $N_{th}$  and  $N_v$ , respectively. Further details on the DNS can be found in table 8.1.

In figure 8.1 we can see temperature patterns, or so-called sheet-like plumes, which develop at the edges of the thermal boundary layers. These snapshots are obtained in the DNS of turbulent RBC for  $Ra = 10^7$ ,  $10^8$  and  $10^9$  and  $Pr = 0.786$  (air) and  $Pr = 4.38$  (water). The direction of the wind can already be visually identified in the instantaneous temperature fields, presented in figure 8.1. The horizontal cross-sections are arranged in such a way that the mean LSC above the viscous boundary layer goes from left to right. Thus, the cold fluid from the top hits the lower hot boundary layer at the left side, the wind blows along the plate and sweeps up material



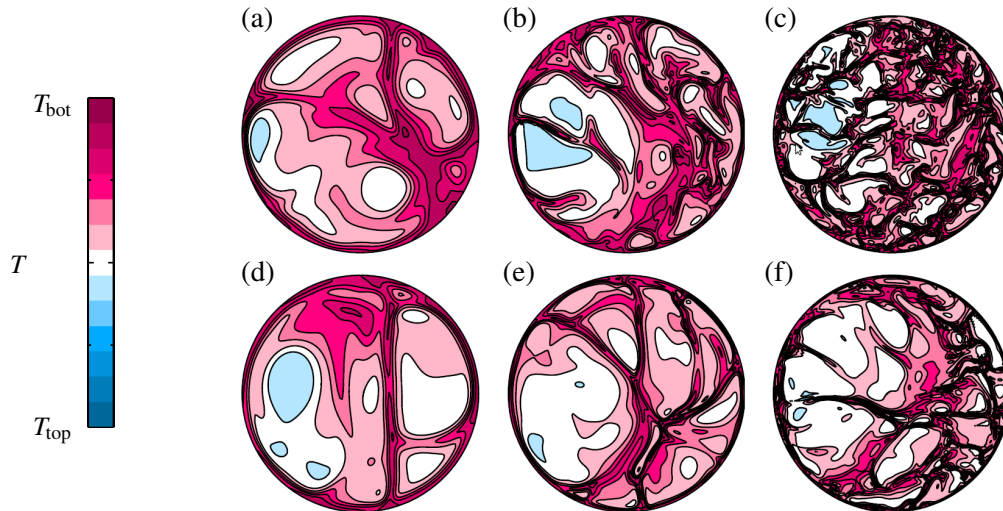


FIGURE 8.1: Instantaneous temperature distribution at the edges of the thermal boundary layers, as obtained in DNS of turbulent RBC for (a, d)  $Ra = 10^7$ , (b, e)  $10^8$  and (c, f)  $10^9$ , for (a, b, c) air,  $Pr = 0.786$ , and (d, e, f) water,  $Pr = 4.38$ . Here the mean wind above the viscous boundary layer goes from left to right.

along its path, resulting in smaller structures on the right side, which then detach as plumes and move upwards.

More qualitatively, the directions of the mean wind are evaluated in the same way as in [155]. For each simulation we first determine the time periods without serious changes of the local wind direction, i.e. without cessations and reversals of the large-scale circulation [44, 70, 158, 162, 166]. The wind direction is extracted in a similar way as in [19], based on the information on the temperature distribution at the vertical wall at the height  $H/2$  from the bottom. Once the time period and the direction of the mean LSC are fixed, we conduct the time averaging of the main flow characteristics in the vertical cross-section, which corresponds to the LSC, and in another vertical cross-section, which is orthogonal to it ( $LSC_{\perp}$ ).

In figure 8.2 we can see distributions of the time-averaged temperature in the LSC and  $LSC_{\perp}$  planes for  $Ra = 10^8$  and both operating fluids considered. The arrows show the directions of the mean velocity vectors. As one can see for both fluids, in the LSC plane there are three relatively large rolls: the LSC itself, which has an anticlockwise direction of rotation, and two secondary rolls, which are located in the upper right and lower left corners and rotate in the clockwise direction. In the plane, orthogonal to LSC ( $LSC_{\perp}$ ) we observe four-roll structures, also for both fluids. Here at a half-height from the bottom the fluid moves from the vertical walls towards the centre.

Note that the mean flow distributions presented in figure 8.2, although they look two-dimensional, are obtained from well-resolved three-dimensional DNS of turbulent RBC in a cylinder. In the following paragraphs we develop and check our theoretical estimates against the numerical

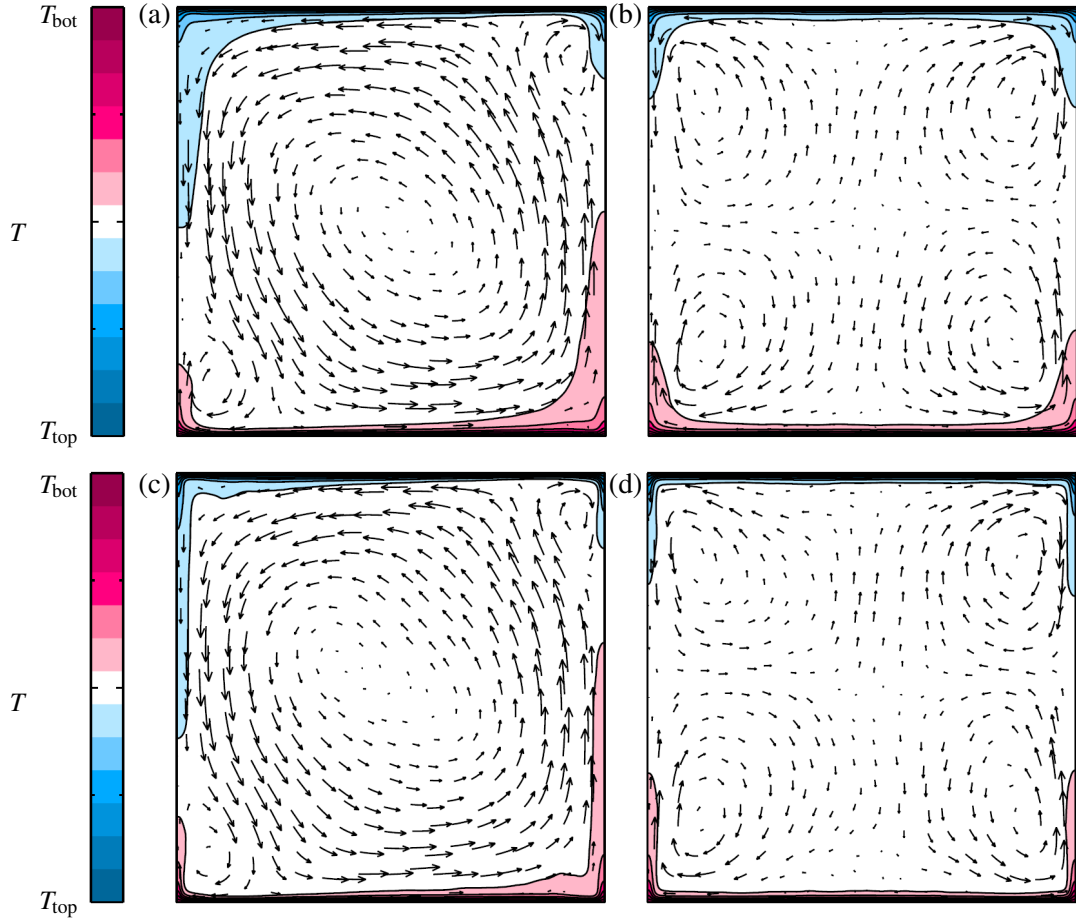


FIGURE 8.2: Distributions of the time-averaged temperature in the vertical planes of (a, c) LSC and (b, d) LSC<sub>⊥</sub>, as obtained by DNS of turbulent RBC for  $Ra = 10^8$ , for (a, b) air,  $Pr = 0.786$ , and (c, d) water,  $Pr = 4.38$ . The arrows show the mean velocity (wind) vectors.

data obtained in these DNS.

### 8.3 Boundary layer equations

In this section we develop the boundary layer equations whose solutions approximate the temperature and velocity fields within the laminar viscous boundary layers in Rayleigh–Bénard convection. Here we admit a non-zero pressure gradient along the horizontal isothermal wall considered.

Without restriction of generality we assume that the coordinate system  $(\tilde{x}, \tilde{y}, \tilde{z})$  is chosen in such a way that at the edge of the viscous boundary layer the horizontal  $\tilde{z}$ -component of the wind is negligible, compared to its other horizontal component along the  $\tilde{x}$ -axis. Thus, taking  $\tilde{w} \equiv 0$  in (8.1)–(8.5) and assuming that the flow is laminar within the viscous boundary layer and, hence, the time dependences of the flow components are negligible, one obtains the following

system of equation for the steady and two-dimensional boundary-layer flow:

$$\widetilde{u}\widetilde{u}_{\widetilde{x}} + \widetilde{v}\widetilde{u}_{\widetilde{y}} + \widetilde{p}_{\widetilde{x}}/\widetilde{\rho} = \widetilde{v}\widetilde{u}_{\widetilde{x}\widetilde{x}} + \widetilde{v}\widetilde{u}_{\widetilde{y}\widetilde{y}}, \quad (8.8)$$

$$\widetilde{u}\widetilde{v}_{\widetilde{x}} + \widetilde{v}\widetilde{v}_{\widetilde{y}} + \widetilde{p}_{\widetilde{y}}/\widetilde{\rho} = \widetilde{v}\widetilde{v}_{\widetilde{x}\widetilde{x}} + \widetilde{v}\widetilde{v}_{\widetilde{y}\widetilde{y}} + \widetilde{\alpha}\widetilde{g}(\widetilde{T} - \widetilde{T}_{\text{mid}}), \quad (8.9)$$

$$\widetilde{u}\widetilde{T}_{\widetilde{x}} + \widetilde{v}\widetilde{T}_{\widetilde{y}} = \widetilde{\kappa}\widetilde{T}_{\widetilde{x}\widetilde{x}} + \widetilde{\kappa}\widetilde{T}_{\widetilde{y}\widetilde{y}}, \quad (8.10)$$

$$\widetilde{u}_{\widetilde{x}} + \widetilde{v}_{\widetilde{y}} = 0. \quad (8.11)$$

Following Prandtl's ansatz [112], we estimate separately the order of magnitude of each component in the above equations. The viscous boundary layer is thin and, hence,  $\widetilde{\delta}_u(\widetilde{x}) \ll \widetilde{x}$ , where  $\widetilde{\delta}_u$  is the thickness of the viscous boundary layer. For the representative length  $\widetilde{L}$  in the horizontal direction we have  $\widetilde{x} \sim \widetilde{L}$ ,  $\widetilde{y} \sim \widetilde{\delta}_u$ . Assuming that  $\partial a/\partial b \sim a/b$  for any  $a$  and  $b$  and that  $\widetilde{u} \sim \widetilde{U}$ , where  $\widetilde{U}$  is the horizontal component of the wind velocity above the boundary layer, from the continuity equation (8.11) we obtain that  $\widetilde{v} \sim \widetilde{U}\widetilde{\delta}_u/\widetilde{L}$ .

Further, the orders of magnitude of the first components  $\widetilde{*}_{\widetilde{x}\widetilde{x}}$  in the right-hand sides of (8.8)–(8.10) are much smaller than those of the second ones  $\widetilde{*}_{\widetilde{y}\widetilde{y}}$ , and therefore they are negligible. Assuming that the rest components in the momentum equation (8.8) are of the same order, one obtains that the order of magnitude of the pressure is  $\widetilde{p} \sim \widetilde{\rho}\widetilde{U}^2$  and that  $\widetilde{\delta}_u/\widetilde{L} \sim Re^{-1/2}$ ,  $Re \equiv \widetilde{L}\widetilde{U}/\widetilde{\nu}$ ,  $Re \gg 1$ .

In (8.9), the orders of magnitude of the components  $\widetilde{u}\widetilde{v}_{\widetilde{x}} \sim \widetilde{v}\widetilde{v}_{\widetilde{y}} \sim \widetilde{\delta}_u\widetilde{U}^2/\widetilde{L}^2$  and  $\widetilde{v}\widetilde{v}_{\widetilde{y}\widetilde{y}} \sim \widetilde{v}\widetilde{U}/(\widetilde{L}\widetilde{\delta}_u)$  are much smaller than the order of magnitude of the component  $\widetilde{p}_{\widetilde{y}}/\widetilde{\rho} \sim \widetilde{U}^2/\widetilde{\delta}_u$  if  $Re \gg 1$ . For the buoyancy term one obtains:  $\widetilde{\alpha}\widetilde{g}(\widetilde{T} - \widetilde{T}_{\text{mid}}) \sim \widetilde{\alpha}\widetilde{g}\widetilde{\Delta}$ . As it was shown in [155], in turbulent Rayleigh–Bénard convection the wind velocity  $\widetilde{U}$  is of the same order of magnitude as the free-fall velocity  $\sqrt{\widetilde{\alpha}\widetilde{g}\widetilde{\Delta}\widetilde{L}}$ ; therefore in (8.9) the buoyancy term, being of order  $\sim \widetilde{\alpha}\widetilde{g}\widetilde{\Delta}$ , is also negligible compared to the pressure term  $\widetilde{p}_{\widetilde{y}}/\widetilde{\rho} \sim \widetilde{\alpha}\widetilde{g}\widetilde{\Delta}(\widetilde{L}/\widetilde{\delta}_u)$ . (Note that this boundary layer model differs from the [137] model for a very slow wind  $\widetilde{U} \ll \sqrt{\widetilde{\alpha}\widetilde{g}\widetilde{\Delta}\widetilde{L}}$  above the viscous boundary layer, where the buoyancy cannot be neglected.)

Thus instead of the equations (8.8)–(8.10), one can consider the following system of equations within the boundary layer:

$$\widetilde{u}\widetilde{u}_{\widetilde{x}} + \widetilde{v}\widetilde{u}_{\widetilde{y}} = \widetilde{v}\widetilde{u}_{\widetilde{y}\widetilde{y}} - \widetilde{p}_{\widetilde{x}}/\widetilde{\rho}, \quad (8.12)$$

$$0 = -\widetilde{p}_{\widetilde{y}}/\widetilde{\rho}, \quad (8.13)$$

$$\widetilde{u}\widetilde{T}_{\widetilde{x}} + \widetilde{v}\widetilde{T}_{\widetilde{y}} = \widetilde{\kappa}\widetilde{T}_{\widetilde{y}\widetilde{y}}, \quad (8.14)$$

respectively. Relations (8.12)–(8.14) are known as Prandtl [102] and Pohlhausen [99]<sup>2</sup> equations, respectively. With respect to Rayleigh–Bénard convection, (8.12) is often considered with neglected pressure term  $\widetilde{p}_{\widetilde{x}}/\widetilde{\rho}$ , as in the case of a parallel flow over a flat plate [14]. Following

<sup>2</sup>By mistake in the original paper the wrong reference ‘‘Pohlhausen [100]’’ was used.

## 8 FALKNER-SKAN BOUNDARY LAYER STRUCTURE

tradition, throughout the paper we call the reference case (8.12)–(8.14) with zero pressure term  $\tilde{p}_x/\tilde{\rho}$  the Prandtl–Blasius one.

Since the flow considered is two-dimensional and incompressible, let us further introduce the streamfunction  $\tilde{\Psi}$ , which satisfies  $\tilde{u} = \tilde{\Psi}_{\tilde{y}}$  and  $\tilde{v} = -\tilde{\Psi}_{\tilde{x}}$ . One can rewrite the equations (8.12) and (8.14) in terms of the streamfunction  $\tilde{\Psi}$  as follows:

$$\tilde{\Psi}_{\tilde{y}}\tilde{\Psi}_{\tilde{y}\tilde{x}} - \tilde{\Psi}_{\tilde{x}}\tilde{\Psi}_{\tilde{y}\tilde{y}} = \tilde{v}\tilde{\Psi}_{\tilde{y}\tilde{y}\tilde{y}} - \tilde{p}_x/\tilde{\rho}, \quad (8.15)$$

$$\tilde{\Psi}_{\tilde{y}}\tilde{T}_{\tilde{x}} - \tilde{\Psi}_{\tilde{x}}\tilde{T}_{\tilde{y}} = \tilde{\kappa}\tilde{T}_{\tilde{y}\tilde{y}}. \quad (8.16)$$

Similarity solutions of these equations are sought with respect to a certain similarity variable  $\xi$ , assuming that  $\tilde{\Psi}$  and  $\xi$  are representable in the following forms:

$$\tilde{\Psi} = \tilde{v}\Psi(\xi)g(x), \quad (8.17)$$

$$\xi = yf(x), \quad (8.18)$$

where

$$x \equiv \tilde{x}/\tilde{L}, \quad y \equiv \tilde{y}/\tilde{L} \quad (8.19)$$

and the horizontal component of the velocity (wind) at the edge of the viscous boundary layer is independent of the vertical coordinate  $\tilde{y}$ , i.e.  $\tilde{U} = \tilde{U}(\tilde{x})$ . Here  $\Psi$ ,  $g$  and  $f$  are dimensionless functions and  $\tilde{L}$  is a representative length in the horizontal direction.

### 8.3.1 Energy equation

Using relations (8.17), (8.18) and representing the temperature as

$$\tilde{T} = \tilde{T}_{\text{bot}} - \Theta\tilde{\Delta}/2, \quad (8.20)$$

where  $\Theta = \Theta(\xi)$  is dimensionless temperature, from (8.16) we obtain the following energy equation:

$$\tilde{\kappa}f^2\Theta_{\xi\xi} + \tilde{v}fg_x\Psi\Theta_{\xi} = 0. \quad (8.21)$$

Here and in the following,  $g_x$  and  $f_x$  denote the derivatives with respect to  $x$  (8.19) of the functions  $g$  and  $f$ , respectively. Since a non-trivial solution is sought,  $f \neq 0$ , for the existence of a similarity solution the requirement

$$g_x/f = a, \quad a = \text{const.}, \quad (8.22)$$

must be fulfilled. Putting  $a = 1$ , we finish with the following energy boundary layer equation:

$$\Theta_{\xi\xi\xi} + Pr\Psi\Theta_{\xi} = 0. \quad (8.23)$$

### 8.3.2 Momentum equation

Under assumptions (8.17), (8.18) the momentum equation (8.15) reads as

$$\frac{\tilde{v}^2}{\tilde{L}^3} (fg(fg)_x(\Psi_{\xi})^2 - f^2gg_x\Psi\Psi_{\xi\xi}) = \frac{\tilde{v}^2}{\tilde{L}^3} f^3g\Psi_{\xi\xi\xi} - \frac{\tilde{p}_{\bar{x}}}{\tilde{\rho}}. \quad (8.24)$$

Again, since a non-trivial solution is sought,  $f \neq 0$ ,  $g \neq 0$ , we obtain

$$\frac{(fg)_x}{f^2} (\Psi_{\xi})^2 - \frac{g_x}{f} \Psi\Psi_{\xi\xi} = \Psi_{\xi\xi\xi} - \frac{\tilde{p}_{\bar{x}}}{\tilde{\rho}} \frac{\tilde{L}^3}{f^3g\tilde{v}^2}. \quad (8.25)$$

At the edge of the viscous boundary layer the viscous effects become less important, which, together with the independence of the horizontal component of the wind from the vertical coordinate, leads to the following approximation of the pressure term:

$$\tilde{U}\tilde{U}_{\bar{x}} = -\frac{\tilde{p}_{\bar{x}}}{\tilde{\rho}} \quad \implies \quad -\frac{\tilde{p}_{\bar{x}}}{\tilde{\rho}} \frac{\tilde{L}^3}{f^3g\tilde{v}^2} = \frac{(\tilde{U}^2)_{\bar{x}} \tilde{L}^3}{2f^3g\tilde{v}^2}. \quad (8.26)$$

Since the pressure gradient remains unchanged in the vertical  $y$ -direction within the boundary layer (see (8.13)), from this and (8.25) we obtain

$$\frac{(fg)_x}{f^2} (\Psi_{\xi})^2 - \frac{g_x}{f} \Psi\Psi_{\xi\xi} = \Psi_{\xi\xi\xi} + \frac{(\tilde{U}^2)_{\bar{x}} \tilde{L}^3}{2f^3g\tilde{v}^2}. \quad (8.27)$$

For the existence of a similarity solution, all the coefficients in this equation must be constant and the free term might be a function of  $\xi$  or a constant. This together with (8.22) leads to the requirement

$$\frac{gg_{xx}}{(g_x)^2} = c, \quad c = const. \quad (8.28)$$

Depending on the constant  $c$ , the function  $g$  can take the form

$$g(x) = \begin{cases} B \exp(bx), & c = 1, \\ B(x+d)^n, & c \neq 1, n = (1-c)^{-1}, \end{cases} \quad (8.29)$$

with certain constants  $B$ ,  $b$  and  $d$ . Without loss of generality one may further assume that  $d = 0$ .

Equation (8.27) can then be rewritten as

$$(c+1)(\Psi_\xi)^2 - \Psi\Psi_{\xi\xi} = \Psi_{\xi\xi\xi} + \frac{(\tilde{U}^2)_{\tilde{x}} \tilde{L}^3}{2(g_x)^3 g \tilde{v}^2}. \quad (8.30)$$

## 8.4 Wind at the edge of the viscous boundary layer

According to the two possible representations of function  $g$  (8.29), in this section we consider two different types of wind, which admit similarity solutions of the boundary layer equations.

### 8.4.1 Wind as an exponential function

Let us consider the first case, i.e.  $c = 1$  and  $g(x) = B \exp(bx)$ . Together with (8.17) and (8.18) and relation (8.22), the streamfunction

$$\tilde{\Psi} = \tilde{v}\Psi(\xi)B \exp(bx) \quad (8.31)$$

and the similarity variable

$$\xi = ybB \exp(bx) \quad (8.32)$$

are obtained. Substituting into the differential equation (8.30), it turns out that a similarity solution can be obtained if the wind  $\tilde{U}$  has the form

$$\tilde{U} = \tilde{U}_0 \exp(kx) \quad (8.33)$$

and the relations

$$B = \sqrt{\frac{2}{k}} \sqrt{\frac{\tilde{L}\tilde{U}_0}{\tilde{v}}}, \quad b = \frac{k}{2} \quad (8.34)$$

are satisfied. The momentum boundary layer equation (8.30) takes then the following form:

$$\Psi_{\xi\xi\xi} + \Psi\Psi_{\xi\xi} + 2 - 2(\Psi_\xi)^2 = 0. \quad (8.35)$$

Taking  $\xi = 1$  and  $y = \tilde{\delta}_u/\tilde{L}$ , where  $\tilde{\delta}_u$  is the viscous boundary layer thickness, one finds from (8.32) that  $\tilde{\delta}_u$  evolves in the horizontal direction  $\tilde{x}$  as

$$\tilde{\delta}_u \sim \sqrt{\frac{\tilde{v}\tilde{L}}{\tilde{U}_0}} \exp(-kx/2). \quad (8.36)$$

## 8.4 WIND AT THE EDGE OF THE VISCOUS BOUNDARY LAYER

Therefore, for the local Reynolds number  $Re = \tilde{L}\tilde{U}/\tilde{\nu}$ , based on the wind  $\tilde{U}$  (8.33), we obtain

$$\delta_u \equiv \tilde{\delta}_u/\tilde{L} \sim Re^{-1/2}. \quad (8.37)$$

Note that, according to the above model and relations (8.33) and (8.36), the boundary layer thickness should decrease (increase) along  $x$  if the wind magnitude increases (decreases) with growing  $x$ . In contrast, our DNS of turbulent Rayleigh–Bénard convection [155] showed that near the horizontal plate, after the stagnation point, the boundary layer thickness grows together with the wind magnitude (see also [26]). Therefore the next possible similarity solution for a wind, which can be represented as a power function, seems to be more relevant with respect to Rayleigh–Bénard convection.

### 8.4.2 Wind as a power function

In the second case, for  $g = Bx^n$ , the streamfunction  $\tilde{\Psi}$  and the similarity variable  $\xi$  are given by

$$\tilde{\Psi} = \tilde{\nu}\Psi Bx^n, \quad (8.38)$$

$$\xi = yBnx^{n-1}. \quad (8.39)$$

If the wind  $\tilde{U}$  has the form

$$\tilde{U} = \tilde{U}_0x^m, \quad (8.40)$$

and the relations

$$B = \sqrt{\frac{2}{m+1}} \sqrt{\frac{\tilde{L}\tilde{U}_0}{\tilde{\nu}}}, \quad n = \frac{m+1}{2} \quad (8.41)$$

are satisfied, then from this and (8.30) we obtain the Falkner & Skan [42] equation

$$\Psi_{\xi\xi\xi} + \Psi\Psi_{\xi\xi} + \frac{2m}{m+1}(1 - (\Psi_{\xi})^2) = 0. \quad (8.42)$$

Further, (8.39) reveals for  $\xi = C = \text{const.}$  and  $y = \tilde{\delta}_u$  that

$$\tilde{\delta}_u = C \sqrt{\frac{2}{m+1}} x^{1-m} \sqrt{\frac{\tilde{\nu}\tilde{L}}{\tilde{U}_0}}. \quad (8.43)$$

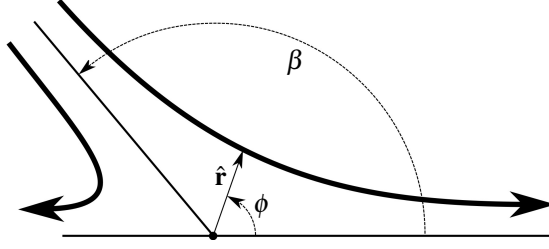


FIGURE 8.3: Sketch of the power-function wind and the corresponding polar coordinate system  $(r, \phi)$ , where  $\hat{r}$  being the radial unit vector and  $\beta$  the corner angle, as defined in (8.47).

Hence, for the dimensionless boundary layer thickness  $\delta_u$  and Reynolds number based on the wind  $\tilde{U}$  (8.40), the following relation holds:

$$\delta_u \equiv \frac{\tilde{\delta}_u}{\tilde{L}} \sim \sqrt{\frac{x}{Re}}. \quad (8.44)$$

Note, the relation (8.44) holds for the Prandtl–Blasius boundary layer ( $m = 0$ ) as well as for general Falkner–Skan boundary layers and is one of the main assumptions in the [50] theory on scaling in thermal convection for the case of non-turbulent boundary layers (see also [51, 55, 134]).

Note that the relation (8.44) holds for the Prandtl–Blasius boundary layer ( $m = 0$ ) as well as for general Falkner–Skan boundary layers, and is one of the main assumptions in the Grossmann & Lohse [50] theory on scaling in thermal convection for the case of non-turbulent boundary layers; see also [51, 55, 134].

### 8.4.3 Appearance of the power-function wind in the core flow

Following Falkner & Skan [42], one can show that the wind  $\tilde{U}$  (8.40) might appear in a corner flow along the sides of the corners. Indeed, let us consider a core flow whose velocity components in polar coordinates  $(r, \phi)$  are determined by

$$\tilde{U}_r = \tilde{U}_0 r^m \cos((m+1)\phi), \quad (8.45)$$

$$\tilde{U}_\phi = -\tilde{U}_0 r^m \sin((m+1)\phi). \quad (8.46)$$

The velocity component  $\tilde{U}_\phi$  of such a flow vanishes if  $\phi = j\pi/(m+1)$ ,  $j = 0, 1, 2, \dots$  A sketch of this flow and the corresponding polar coordinate system are presented in figure 8.3 and the streamfunctions of the flow (8.45), (8.46) for different  $m$  are presented in figure 8.4.

One can see that this flow can be interpreted as a flow along the sides of a corner, whose size is equal to

$$\beta = \pi/(m+1). \quad (8.47)$$



## 8.5 SOLUTIONS OF THE BOUNDARY LAYER EQUATIONS AND THEIR LIMITS

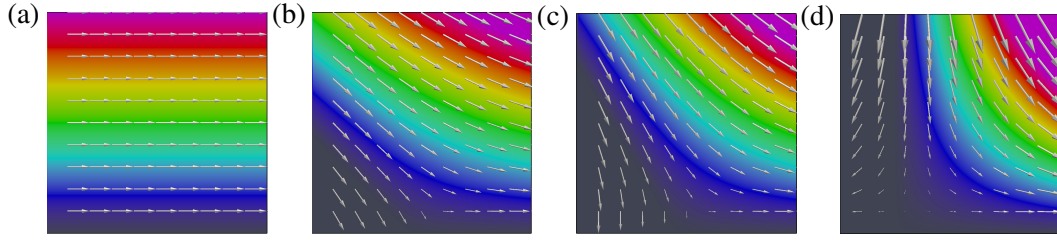


FIGURE 8.4: Streamfunctions (colours) for flows inside corners of the size  $\beta = \pi/(m+1)$  for (a)  $m = 0$  (Prandtl–Blasius flow), (b)  $m = 1/3$ , (c)  $m = 1/2$  and (d)  $m = 1$  (stagnation-point flow). The arrows show the velocity vectors with the components  $\tilde{U}_r$  (8.45) and  $\tilde{U}_\phi$  (8.46).

On the surfaces of the corner, e.g. when  $\phi = 0$ , the velocity varies as a power function on the distance  $r$  along the surface. Thus, in a Cartesian coordinate system for  $\phi = 0$  the horizontal velocity can be presented as a power function on the coordinate  $x$ .

Comparing the LSC of the fluid in the core region, obtained in the DNS of turbulent RBC (figure 8.2a,c) with the streamlines in figure 8.4, one concludes that the wind in turbulent RBC, which slides off from the secondary rolls and then flows along the lower horizontal wall with pitch angle  $\beta$ ,  $\beta \in [\frac{\pi}{2}, \frac{3\pi}{4}]$ , is similar to a flow inside a corner of size  $\beta$ . This together with the relation (8.47) makes it clear that the wind can be approximated by a power function of the form (8.45), (8.46) with  $m \in [1/3; 1]$ .

## 8.5 Solutions of the boundary layer equations and their limits

### 8.5.1 Horizontal velocity and temperature profiles

Vertical profiles of the temperature and horizontal velocity near the horizontal plates are primary flow characteristics and their investigation is a part of any RBC study [3, 33, 47, 56, 104, 111, 122, 135, 136, 140, 145, 149, 173]. They are usually compared against the predictions for laminar boundary layers, based on the Prandtl–Blasius ansatz, which is a particular case of the more general Falkner–Skan approach.

Therefore, in this section we study the temperature and velocity profiles, which one can obtain within the general Falkner–Skan approximation. Further, we derive the limits of the temperature profiles for the general Falkner–Skan approximation and prove that these limits are the same for the Prandtl–Blasius approximation and the general Falkner–Skan approximation.

Based on the results of the previous section, let us consider the following system of the momentum (Falkner–Skan)

Based on the results of the previous section, let us consider the following system of boundary layer equations with respect to Rayleigh–Bénard convection: the momentum (Falkner–Skan) is

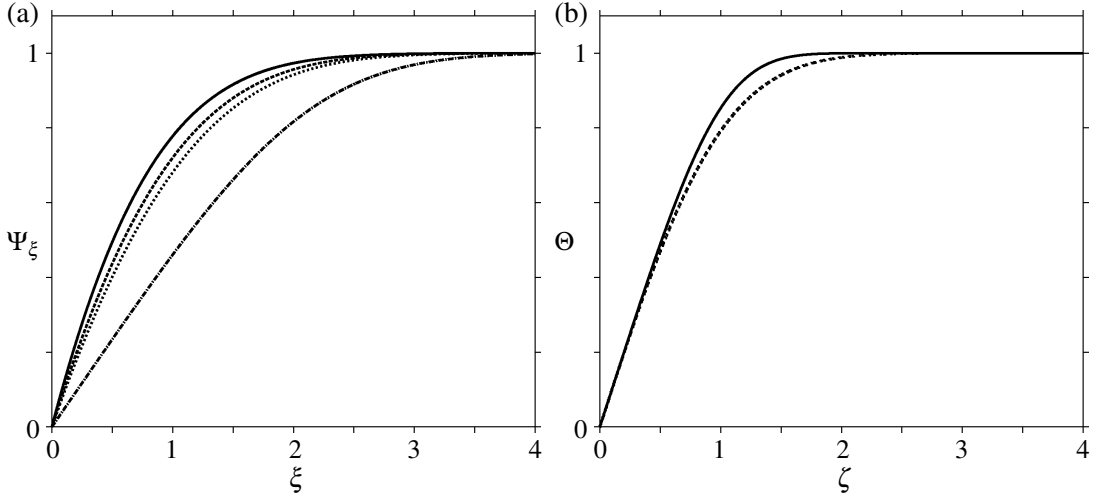


FIGURE 8.5: (a) Solutions of the Falkner-Skan equation for  $m = 0$  (Prandtl-Blasius flow, ---),  $m = 1/3$  ( $\cdots$ ),  $m = 1/2$  (- -) and  $m = 1$  (stagnation-point flow, —). (b) Limiting cases  $\Theta(\zeta) = \int_0^\zeta \exp(-B\chi^\omega) d\chi$  for the rescaled temperature profiles for all values of  $m$ :  $Pr \ll 1$  ( $\omega = 2$ ,  $B = \pi/4$ , - -) and  $Pr \gg 1$  ( $\omega = 3$ ,  $B = \Gamma^3(4/3) \approx 0.712$ , —).

given by

$$\begin{aligned} \Psi_\xi \xi \xi \xi + \Psi \Psi_\xi \xi \xi + \frac{2m}{m+1} (1 - (\Psi_\xi)^2) &= 0, \\ \Psi(0) = 0, \quad \Psi_\xi(0) = 0, \quad \Psi_\xi(\infty) = 1, \end{aligned} \quad (8.48)$$

and energy by

$$\begin{aligned} \Theta_{\xi\xi} + Pr \Psi \Theta_\xi &= 0, \\ \Theta(0) = 0, \quad \Theta(\infty) = 1. \end{aligned} \quad (8.49)$$

One can solve these equations numerically [42, 160]. The solution of the momentum equation (8.48) depends only on  $m$ , while that of the energy equation (8.49) also depends on Prandtl number. In figure 8.5a the profiles of  $\Psi_\xi$  (horizontal velocity component) are presented for different values of  $m$  associated with a core flow in a corner  $\beta = \pi/(m+1)$ . Therefore the cases  $m = 0$ ,  $m = 1/3$ ,  $m = 1/2$  and  $m = 1$  correspond, respectively, to a Prandtl-Blasius flow over a horizontal plate, flows in corners  $3\pi/4$  and  $2\pi/3$  and a stagnation-point flow in a right-angle corner. In figure 8.6a,b,c the temperature profiles are presented for particular cases  $m = 0$  and  $m = 1$ , for Prandtl numbers 0.1, 1 and 10.

Although the solution of the energy boundary layer (8.49) depends strongly on  $m$  and  $Pr$ , the rescaled temperature profiles with respect to a similarity variable  $\zeta = \xi \Theta_\xi(0)$  demonstrates only a weak dependence on  $m$  (see figure 8.6d,e,f). The choice of the similarity variable  $\zeta$  provides the temperature derivative (with respect to  $\zeta$ ) equal to 1 at the plate,  $\Theta_\zeta(0) = 1$ . In order to

## 8.5 SOLUTIONS OF THE BOUNDARY LAYER EQUATIONS AND THEIR LIMITS

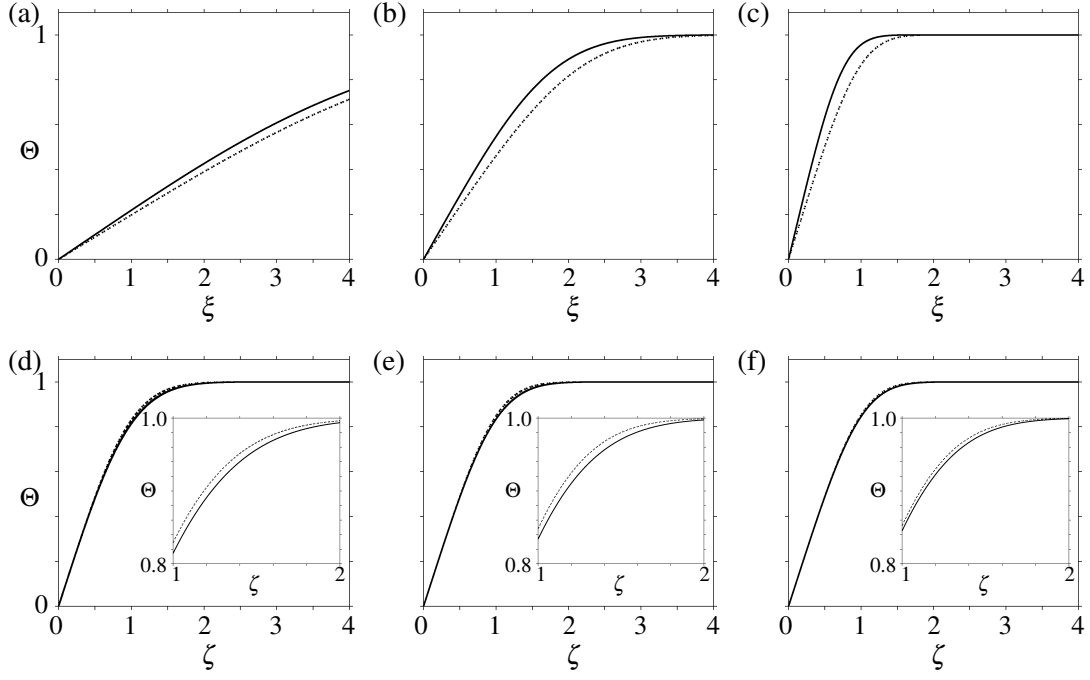


FIGURE 8.6: (a,b,c) Temperature profiles with respect to the similarity variable  $\xi$  and (d,e,f) rescaled temperature profiles with respect to the similarity variable  $\zeta = \xi \Theta_{\xi}(0)$ , (a,d) for  $Pr = 0.1$ , (b,e)  $Pr = 1$ , (c,f)  $Pr = 10$ , and  $m = 0$  (Prandtl–Blasius flow, - -),  $m = 1$  (stagnation-point flow, —).

understand the reasons for such a conjunction of the rescaled profiles for a Prandtl–Blasius approximation ( $m = 0$ ) and stagnation-point approximation ( $m = 1$ ) for a fixed Prandtl number, we further derive the limiting cases of the rescaled temperature profiles for  $Pr \ll 1$  and  $Pr \gg 1$ .

### 8.5.2 Limiting cases of the temperature profiles for all $m$

Case  $Pr \ll 1$

If the Prandtl number is much smaller than one, the thickness of the viscous boundary layer  $\tilde{\delta}_u$  is smaller than that of the thermal boundary layer  $\tilde{\delta}_\theta$ . Therefore, for infinitely small Prandtl numbers, in most of the thermal boundary layer, the horizontal component of the velocity is equal to the wind (8.40). Due to the continuity equation the corresponding vertical component of the velocity is equal to

$$\tilde{V} = -m\tilde{U}_0 \frac{\tilde{x}^{m-1}\tilde{y}}{\tilde{L}^m} \quad (8.50)$$

and the thermal boundary layer (8.14) is reduced to

$$\tilde{U}\tilde{T}_{\tilde{x}} + \tilde{V}\tilde{T}_{\tilde{y}} = \tilde{\kappa}\tilde{T}_{\tilde{y}\tilde{y}}. \quad (8.51)$$

With the similarity variable

$$\zeta = \tilde{y} \sqrt{\frac{(1+m)\tilde{U}(x)}{\pi \tilde{\kappa} \tilde{x}}} = \sqrt{\frac{\tilde{U}_0(1+m)}{\pi \tilde{\kappa} \tilde{L}^m}} \tilde{y} \tilde{x}^{(m-1)/2} \quad (8.52)$$

for the function  $\Theta$ , defined by (8.20), one obtains the following equation

$$\Theta_{\zeta\zeta} + \frac{\pi}{2} \zeta \Theta_{\zeta} = 0, \quad (8.53)$$

with the solution

$$\Theta(\zeta) = \int_0^{\zeta} \exp\left(-\frac{\pi}{4} \chi^2\right) d\chi. \quad (8.54)$$

This function is presented in figure 8.5b with a dashed line. The choice of the similarity variable  $\zeta$  (8.52) provides the solution (8.54) with the boundary conditions

$$\Theta(0) = 0, \quad \Theta_{\zeta}(0) = 1, \quad \Theta(\infty) = 1. \quad (8.55)$$

From the definition of the similarity variable  $\zeta$  (8.52) one further obtains the scaling of the thermal boundary layer thickness:

$$\tilde{\delta}_{\theta} \sim \sqrt{\frac{\tilde{\kappa} \tilde{x}}{\tilde{U}(x)}} = \sqrt{\frac{\tilde{x}/\tilde{L}}{RePr}} \tilde{L} \quad \Longrightarrow \quad \delta_{\theta} \equiv \frac{\tilde{\delta}_{\theta}}{\tilde{L}} \sim Re^{-1/2} Pr^{-1/2} \left(\frac{\tilde{x}}{\tilde{L}}\right)^{1/2} \quad (8.56)$$

with local Reynolds number  $Re = \tilde{L}\tilde{U}/\tilde{\nu}$ .

Case  $Pr \gg 1$

For Prandtl numbers much larger than one, the thickness of the thermal boundary layer  $\tilde{\delta}_{\theta}$  is smaller than that of the viscous boundary layer  $\tilde{\delta}_u$ . For very large Prandtl numbers, in the thermal boundary layer the horizontal component of the velocity is a linear function of the vertical coordinate. At the edge of the viscous boundary layer (outside the thermal boundary layer) the horizontal component of the velocity is approximately equal to the wind  $\tilde{U}$ , so the horizontal component of the velocity within the thermal boundary layer can be approximated as

$$\tilde{u} = \frac{\tilde{y}}{\tilde{\delta}_u} \tilde{U}. \quad (8.57)$$

## 8.5 SOLUTIONS OF THE BOUNDARY LAYER EQUATIONS AND THEIR LIMITS

Substituting the wind  $\tilde{U}$  (8.40) and the thickness of the viscous boundary layer (8.43) into this relation, one obtains the horizontal velocity within the thermal boundary layer:

$$\tilde{u} = \frac{1}{C} \sqrt{\frac{\tilde{U}_0^3(m+1)\tilde{L}}{2\tilde{v}}} \left(\frac{\tilde{y}}{\tilde{L}}\right) \left(\frac{\tilde{x}}{\tilde{L}}\right)^{(3m-1)/2}. \quad (8.58)$$

Because of the continuity equation, the vertical component of the velocity is equal to

$$\tilde{v} = -\frac{3m-1}{4C} \sqrt{\frac{\tilde{U}_0^3(m+1)\tilde{L}}{2\tilde{v}}} \left(\frac{\tilde{y}}{\tilde{L}}\right)^2 \left(\frac{\tilde{x}}{\tilde{L}}\right)^{(3m-3)/2}. \quad (8.59)$$

Then in the considered case one obtains the following energy boundary layer equation:

$$\tilde{u}\tilde{T}_{\tilde{x}} + \tilde{v}\tilde{T}_{\tilde{y}} = \tilde{\kappa}\tilde{T}_{\tilde{y}\tilde{y}}. \quad (8.60)$$

Introducing the similarity variable  $\zeta$ ,

$$\zeta = \frac{1}{\Gamma(4/3)C^{1/3}} \left(\frac{\tilde{U}_0(m+1)}{2\tilde{L}^m}\right)^{1/2} \left(\frac{1}{6\tilde{\kappa}}\right)^{1/3} \left(\frac{1}{\tilde{v}}\right)^{1/6} \tilde{y}\tilde{x}^{(m-1)/2}, \quad (8.61)$$

where  $\Gamma$  is the gamma function, one obtains from (8.60) the ordinary differential equation

$$\Theta_{\zeta\zeta} + 3\Gamma^3(4/3)\zeta^2\Theta_{\zeta} = 0 \quad (8.62)$$

for the dimensionless temperature  $\Theta$ . This equation has a solution

$$\Theta(\zeta) = \int_0^{\zeta} \exp(-\Gamma^3(4/3)\chi^3)d\chi, \quad (8.63)$$

which satisfies the boundary conditions (8.55). This function is presented in figure 8.5b with a continuous line.

From the definition of the similarity variable  $\zeta$  (8.61) one further obtains

$$\tilde{\delta}_{\theta} \sim \tilde{\kappa}^{1/3}\tilde{v}^{1/6} \sqrt{\frac{\tilde{x}}{\tilde{U}(x)}} = \sqrt{\frac{\tilde{x}/\tilde{L}}{Re}} Pr^{-1/3}\tilde{L}, \quad (8.64)$$

and hence

$$\delta_{\theta} \equiv \frac{\tilde{\delta}_{\theta}}{\tilde{L}} \sim Re^{-1/2} Pr^{-1/3} \left(\frac{\tilde{x}}{\tilde{L}}\right)^{1/2} \quad (8.65)$$

with the local Reynolds number  $Re = \tilde{L}\tilde{U}/\tilde{v}$ .

One can sum up the results (8.56) and (8.65) as follows. For very small and very large Prandtl

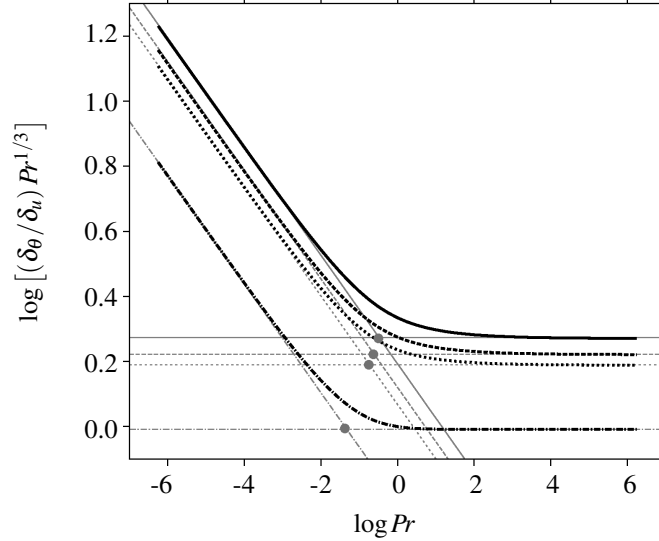


FIGURE 8.7: The dependence of the ratio  $\delta_\theta/\delta_u$  of the thermal and viscous boundary layer thicknesses on Prandtl number for  $m = 0$  (Prandtl–Blasius flow, ---),  $m = 1/3$  ( $\cdots$ ),  $m = 1/2$  (- -) and  $m = 1$  (stagnation-point flow, —). Critical Prandtl number  $Pr^* \approx 0.27m + 0.05$  (grey dots) for the regime change of  $\delta_\theta/\delta_u$  from  $\sim Pr^{-1/2}$  to  $\sim Pr^{-1/3}$ .

numbers the thickness of the thermal boundary layer scales as

$$\delta_\theta \equiv \frac{\tilde{\delta}_\theta}{\tilde{L}} \sim \begin{cases} Re^{-1/2} Pr^{-1/2} \left(\tilde{x}/\tilde{L}\right)^{1/2}, & Pr \ll 1, \\ Re^{-1/2} Pr^{-1/3} \left(\tilde{x}/\tilde{L}\right)^{1/2}, & Pr \gg 1. \end{cases} \quad (8.66)$$

Since the thickness of the viscous boundary layer scales as in (8.44) and is independent of Prandtl number, the ratio of the thermal and viscous boundary layers scales with the Prandtl number as follows:

$$\delta_\theta/\delta_u \sim \begin{cases} Pr^{-1/2}, & Pr \ll 1, \\ Pr^{-1/3}, & Pr \gg 1, \end{cases} \quad (8.67)$$

for all possible  $m$ . This means that the ratio  $\delta_\theta/\delta_u$  is independent from the Reynolds number as well as from the horizontal coordinate  $\tilde{x}$ .

## 8.6 Ratio of the thermal and viscous boundary layers

One can solve the system (8.48), (8.49) numerically for all possible values of  $m$  and  $Pr$  and then evaluate the thicknesses of the viscous ( $\tilde{\delta}_u$ ) and thermal ( $\tilde{\delta}_\theta$ ) boundary layers, based on the slope method. The ratio of the thicknesses with respect to the similarity variable  $\xi$  is equal to the ratio of the thicknesses in physical space [121].

## 8.6 RATIO OF THE THERMAL AND VISCOUS BOUNDARY LAYERS

In figure 8.7 the dependence of the ratio  $\delta_\theta/\delta_u$ , normalized with  $Pr^{-1/3}$ , is presented for some particular values of  $m$ . As derived in the previous section, for all  $m$ , the ratio scales as  $\sim Pr^{-1/2}$  for small and as  $\sim Pr^{-1/3}$  for large Prandtl numbers. For the Prandtl–Blasius flow ( $m = 0$ ), the ratio can be approximated as

$$\left. \frac{\delta_\theta}{\delta_u} \right|_{m=0} \approx \begin{cases} 0.589Pr^{-1/2}, & Pr < 3 \times 10^{-4}, \\ Pr^{-0.357+0.022\log Pr}, & 3 \times 10^{-4} \leq Pr \leq 3, \\ 0.982Pr^{-1/3}, & 3 < Pr, \end{cases} \quad (8.68)$$

as shown in [121]. Here and below  $\log \equiv \log_{10}$  is the logarithm to base 10. For  $m = 1/3$ ,  $m = 1/2$  and  $m = 1$  (stagnation-point flow) one can take, respectively, the following approximations:

$$\left. \frac{\delta_\theta}{\delta_u} \right|_{m=1/3} \approx \begin{cases} 1.170Pr^{-1/2}, & Pr < 10^{-3}, \\ 1.736Pr^{-0.393+0.017\log Pr}, & 10^{-3} \leq Pr \leq 10^2, \\ 1.550Pr^{-1/3}, & 10^2 < Pr, \end{cases} \quad (8.69)$$

$$\left. \frac{\delta_\theta}{\delta_u} \right|_{m=1/2} \approx \begin{cases} 1.318Pr^{-1/2}, & Pr < 10^{-3}, \\ 1.902Pr^{-0.395+0.017\log Pr}, & 10^{-3} \leq Pr \leq 10^2, \\ 1.675Pr^{-1/3}, & 10^2 < Pr, \end{cases} \quad (8.70)$$

and

$$\left. \frac{\delta_\theta}{\delta_u} \right|_{m=1} \approx \begin{cases} 1.561Pr^{-1/2}, & Pr < 10^{-3}, \\ 2.183Pr^{-0.400+0.017\log Pr}, & 10^{-3} \leq Pr \leq 10^3, \\ 1.879Pr^{-1/3}, & 10^3 < Pr. \end{cases} \quad (8.71)$$

Figure 8.7 reveals that for a fixed  $Pr$  the ratio  $\delta_\theta/\delta_u$  is larger for larger  $m$ . Let  $Pr^*$  be the critical Prandtl number, i.e. the Prandtl number at which the asymptotes for the regimes  $\sim Pr^{-1/2}$  for small  $Pr$  and  $\sim Pr^{-1/3}$  for large  $Pr$  intersect. The numerically evaluated approximation of the critical Prandtl numbers  $Pr^*$ , which are marked in figure 8.7 with grey dots, is as follows:

$$Pr^* \approx 0.27m + 0.05. \quad (8.72)$$

Thus, one obtains  $Pr^* \approx 0.046$  for  $m = 0$ ,  $Pr^* \approx 0.185$  for  $m = 1/3$ ,  $Pr^* \approx 0.229$  for  $m = 1/2$  and  $Pr^* \approx 0.325$  for  $m = 1$ .

It is well known that in the case of Prandtl–Blasius flow ( $m = 0$ ) the viscous and the thermal boundary layers have the same thickness for  $Pr = 1$ . For larger  $m$  the Prandtl number should also be larger in order to provide equal thicknesses of the boundary layers. In particular, from (8.69)–(8.71) one obtains that  $\delta_\theta/\delta_u = 1$  for  $Pr = 4.24$  if  $m = 1/3$ , for  $Pr = 5.35$  if  $m = 1/2$  or

for  $Pr = 7.59$  if  $m = 1$ .

For the operating fluids air ( $Pr = 0.786$ ) and water ( $Pr = 4.38$ ), which we study in our DNS of turbulent RBC, from (8.68)–(8.71) one obtains the following estimates of the ratio of the thermal and viscous boundary layer thicknesses, depending on the pitch angle  $\beta$  of the wind:

$$\left. \frac{\delta_\theta}{\delta_u} \right|_{Pr=0.786} \approx \begin{cases} 1.08, & \beta = \pi & (m = 0), \\ 1.88, & \beta = 3\pi/4 & (m = 1/3), \\ 2.06, & \beta = 2\pi/3 & (m = 1/2), \\ 2.37, & \beta = \pi/2 & (m = 1), \end{cases} \quad (8.73)$$

and

$$\left. \frac{\delta_\theta}{\delta_u} \right|_{Pr=4.38} \approx \begin{cases} 0.60, & \beta = \pi & (m = 0), \\ 0.98, & \beta = 3\pi/4 & (m = 1/3), \\ 1.07, & \beta = 2\pi/3 & (m = 1/2), \\ 1.23, & \beta = \pi/2 & (m = 1), \end{cases} \quad (8.74)$$

respectively.

## 8.7 Theory versus the DNS results

The value of  $m$  and the thicknesses of the thermal ( $\tilde{\delta}_\theta$ ) and viscous ( $\tilde{\delta}_u$ ) boundary layers are extracted from our DNS as follows. First, the temperature distributions on the vertical wall are used to determine the instantaneous orientation of the LSC in a similar way as was done by Brown & Ahlers [19] and Wagner *et al.* [155]. Further, time periods without serious reorientations of the LSC are detected, which last up to 682 time units. Note that each time unit equals  $(\tilde{H}/(2\tilde{\alpha}\tilde{g}\tilde{\Delta}))^{1/2}$ . During these periods the angle corresponding to the LSC plane does not change more than  $0.06\pi$ . In the analysis of the DNS data the mean orientation during this time periods is chosen to fix the LSC plane (see figure 8.2a,c). Within this plane the instantaneous flow fields, which are recorded with a sampling rate of three per time unit, are analysed and the local instantaneous thicknesses of the viscous and thermal boundary layers close to the heated bottom plate are determined by applying the slope method, in a similar way to how it is done in the above theory.

In order to estimate the angle  $\beta$  at which the large-scale circulation attacks the heated/cooled plates, we first find locations within the plane of the large-scale circulation where the time-averaged wall shear stress is equal to zero. Here  $\eta_h$  and  $\eta_v$  are the distances from the bottom left corner to the next locations at, respectively, the bottom or left vertical wall, where the wall shear stress  $\tau_w$  is equal to zero (see the sketch in figure 8.8). The values of  $\beta$  and  $m$  can be then



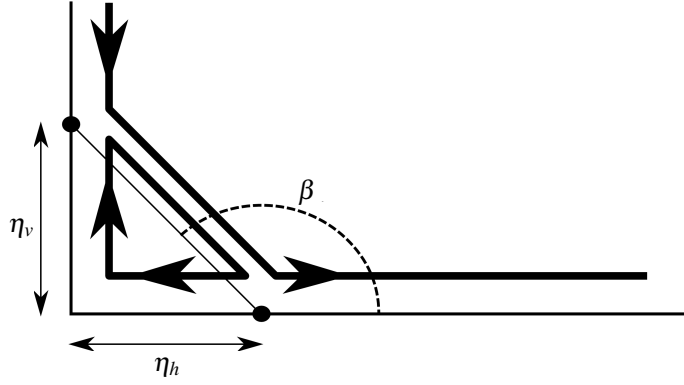


FIGURE 8.8: Sketch of the large-scale circulation (wind) and secondary roll within the plane of the large-scale circulation. Dots mark the locations, where the wall shear stress is equal to zero. The distances from the left bottom corner to the these locations are denoted as  $\eta_v$  and  $\eta_h$ . The angle  $\beta$ , at which the wind attacks the horizontal plate, is determined by (8.75).

estimated as follows:

$$\beta = \pi - \arctan(\eta_v/\eta_h), \quad (8.75)$$

$$m = \pi/\beta - 1. \quad (8.76)$$

In figure 8.9 the time-averaged wall shear stresses at the bottom and left vertical wall from figure 8.8 in the plane of the large-scale circulation are presented for water and air and different Rayleigh numbers. One can see that locations  $\eta_v$  and  $\eta_h$  depend only weakly (and non-monotonically) on the Rayleigh number and Prandtl number, at least for the considered range of  $Ra$  and  $Pr$ . Thus, for the operating fluids air and water, we obtained

$$\beta = \begin{cases} 0.695\pi \pm 0.015\pi & \text{(air),} \\ 0.705\pi \pm 0.025\pi & \text{(water);} \end{cases} \quad (8.77)$$

$$m = \begin{cases} 0.44 \pm 0.02 & \text{(air),} \\ 0.42 \pm 0.05 & \text{(water).} \end{cases} \quad (8.78)$$

In figure 8.10 the ratios  $\langle \delta_\theta / \delta_u \rangle_t$  of the thermal and viscous boundary layer thicknesses are presented as functions of the radial position  $r$  (see figure 8.2a,c), as they were obtained in the DNS of turbulent RBC of air and water for different Rayleigh numbers, together with their theoretical estimates (8.73) and (8.74). Here  $\langle \dots \rangle_t$  denotes the time averaging. The lowest and highest horizontal grey lines in figure 8.10a,b represent the estimates (8.73) and (8.74) for  $m = 0$  (Prandtl–Blasius flow) and  $m = 1$  (stagnation-point flow), respectively.

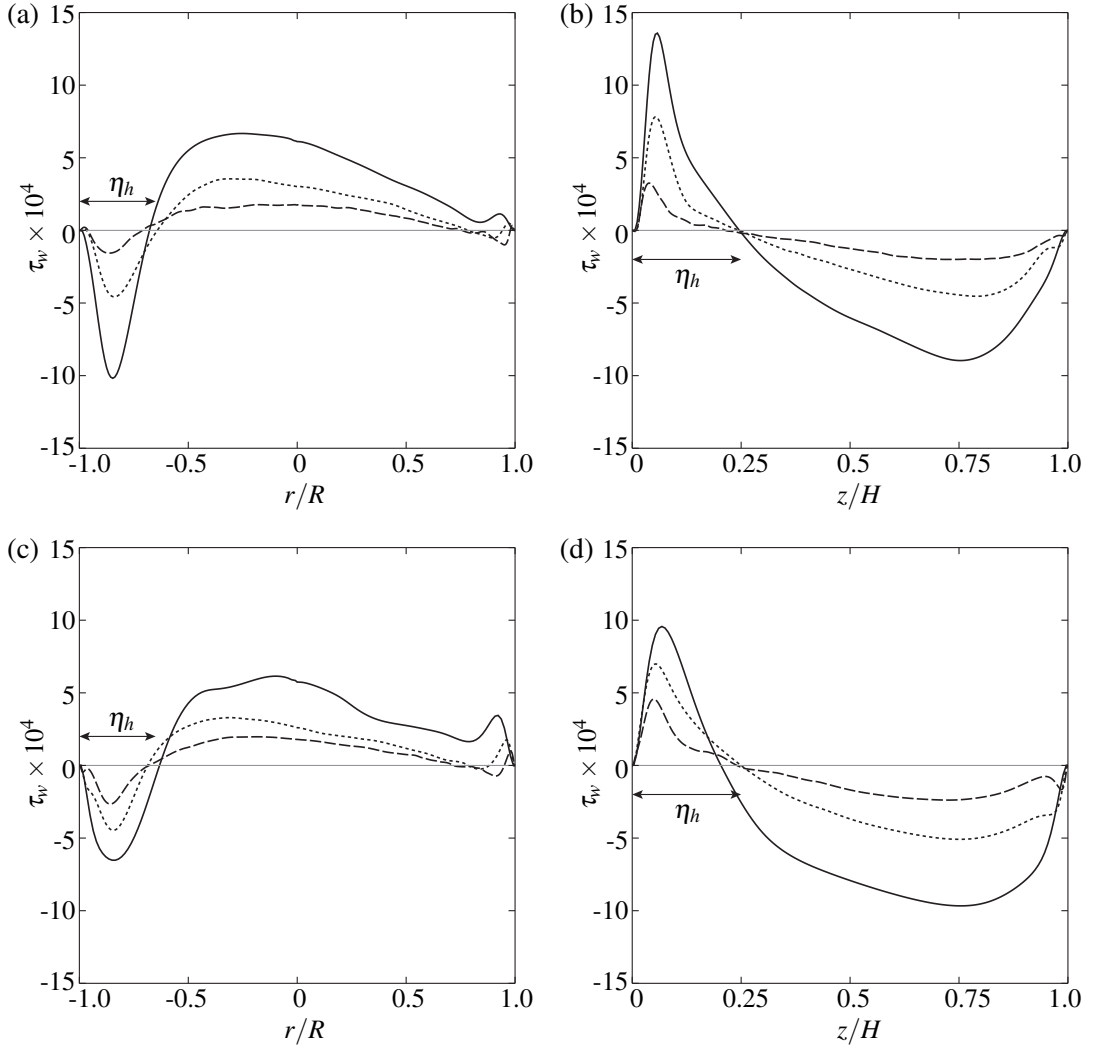


FIGURE 8.9: Time-averaged wall shear stress at the bottom plate (*a,c*) and left vertical wall (*b,d*) in the plane of the large-scale circulation, as obtained in the DNS for air (*a,b*) and water (*c,d*), for  $Ra = 10^7$  (—),  $Ra = 10^8$  (···) and  $Ra = 10^9$  (- - -) with the distances  $\eta_v$  and  $\eta_h$ , as in figure 8.8.

As one can see in figure 8.10, the ratio of the time-averaged thicknesses of the thermal and viscous boundary layers remains almost constant along the path of the wind (apart from the secondary rolls) and depends only weakly on the Rayleigh number. Since the wind is a non-horizontal flow and the angle  $\beta$  between its direction and the horizontal plate belongs to the interval  $[\frac{\pi}{2}, \frac{3\pi}{4}]$ , the predictions of the ratios  $\delta_\theta/\delta_u$  with the approximations (8.73) and (8.74) for  $m \in [1/3; 1]$  are found to be more reliable than those for  $m = 0$  (Prandtl–Blasius flow).

For higher Rayleigh numbers the difference between  $\langle \delta_\theta/\delta_u \rangle_t$ , evaluated from the DNS data, and the previously described Falkner–Skán approximation of  $\langle \delta_\theta/\delta_u \rangle_t$  for the Rayleigh–Bénard boundary layers becomes more visible, which is explained by the increasing influence of the

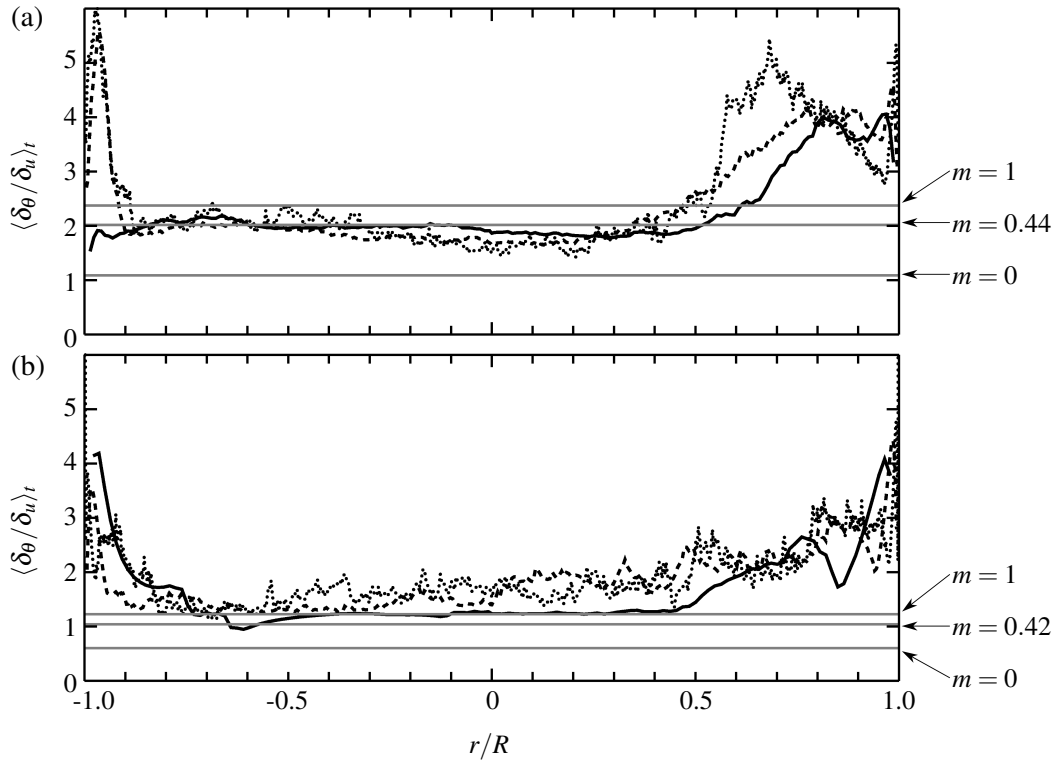


FIGURE 8.10: Ratio  $\langle \delta_\theta / \delta_u \rangle_t$  of the thermal and viscous boundary layer thicknesses for (a) air,  $Pr = 0.786$ , and (b) water,  $Pr = 4.38$ , as obtained in DNS for  $Ra = 10^9$  ( $\cdots$ ),  $Ra = 10^8$  ( $---$ ),  $Ra = 10^7$  ( $\rightarrow$ ), together with the theoretical predictions for  $m = 0$  (Prandtl–Blasius flow),  $m = 1$  (stagnation-point flow) and (a)  $m = 0.44$  and (b)  $m = 0.42$ , as estimated from the DNS data, according to (8.75), (8.76) and (8.78).

fluctuations in the boundary layers and, hence, a stronger deviation of the real flows from this stationary two-dimensional model. Another observation is that for smaller Prandtl numbers the Falkner–Skan approximation provides more accurate predictions compared to the large Prandtl number case, in which, in particular, for very large  $Pr$  the existence of the wind itself becomes questionable [67, 114].

## 8.8 Conclusions

The non-zero pressure gradient in the Rayleigh–Bénard convection cell influences the velocity of the large-scale circulation and all boundary layer characteristics. Therefore, in the present work we considered a system of the boundary layer momentum and energy equations (8.12)–(8.14), which takes into account the presence of the non-zero pressure gradient. It was shown that for the existence of the similarity solution of this system an exponential (8.33) or power-function (8.40) wind above the viscous boundary layer is required.

The power-function wind (8.40), in contrast to the exponential one (8.33), leads to a simulta-

neous increase of the thickness of the viscous boundary layers and the magnitude of the LSC along its path, which is very similar to the situation we observed in our DNS. Therefore the case of the power-function wind was investigated in detail, which led to the Falkner–Skan boundary layer (8.48) and (8.49) to describe the Rayleigh–Bénard boundary layers. These equations and their similarity solutions depend not only on the Prandtl number but also on the angle  $\beta$  (8.47) at which the large-scale circulation (see figure 8.8) attacks the horizontal plate.

For the normalized temperature profiles, which satisfy (8.55) and can be obtained under the assumption of a power-function wind above the viscous boundary layer, a general result was derived. For all angles  $\beta$  and all Prandtl numbers, the temperature profiles are bounded by

$$\Theta(\zeta) = \int_0^\zeta \exp(-B\chi^\omega) d\chi \quad \text{with} \quad B = \begin{cases} \Gamma^3(4/3) \approx 0.712, & \omega = 3, Pr \gg 1, m \\ \pi/4, & \omega = 2, Pr \ll 1. \end{cases} \quad (8.79)$$

These limits are also valid for the particular case of Prandtl–Blasius boundary layers.

For all  $\beta$ , it was shown that the ratio of the thermal and viscous boundary layer thicknesses scales as  $\delta_\theta/\delta_u \sim Pr^{-1/2}$  if  $Pr \ll 1$  and  $\delta_\theta/\delta_u \sim Pr^{-1/3}$  if  $Pr \gg 1$ . The asymptotes for these regimes intersect at the critical Prandtl number  $Pr^*$ , which grows together with decreasing  $\beta$  and can be approximated by (8.72). For certain particular angles  $\beta$  of the wind attack, formulae (8.68)–(8.71) to approximate  $\delta_\theta/\delta_u$  as functions on  $Pr$  were derived based on the numerical solutions of the boundary layer equations.

Using our DNS data for air and water we estimated the angle  $\beta$ , based on the information of the locations within the plane of the large-scale circulation where the time-averaged wall shear stress vanishes, obtaining that  $\beta = 0.695\pi \pm 0.015\pi$  for air and  $\beta = 0.705\pi \pm 0.025\pi$  for water. The theoretical predictions obtained in the present work demonstrated a good agreement with the DNS results for turbulent RBC with the Rayleigh and Prandtl numbers considered.

From the fact that the Falkner–Skan ansatz for  $\beta \neq \pi$  represents the DNS data in a better way than the Prandtl–Blasius one for  $\beta = \pi$ , we conclude that the angle  $\beta$  of the wind attack may also influence the constants in the scaling laws of the Reynolds and Nusselt numbers with the Rayleigh and Prandtl numbers in turbulent RBC with laminar-like boundary layers. In this case a parameter such as  $m$ , which determines the angle  $\beta$  (8.47) and influences the pressure gradient within the viscous boundary layer and the wind (8.40) above the boundary layer, will be involved in the scaling theory, representing the details on the global flow structure.

Further, since the geometry of the container influences the global flow structure and, hence, the angle  $\beta$  at which the wind meets the boundary layer, the Falkner–Skan approximation will lead to an improvement of the models that account for the influence of the regular wall roughness and isothermal obstacles inside the convection cells [125]. The Falkner–Skan ansatz will also be useful for a better understanding of mixed convection flows [9, 126], which are even

## 8.8 CONCLUSIONS

more sensitive to the angle of the wind attack, and especially of forced convection flows [72], which are driven by imposed pressure gradients. These and many other issues related to the applicability of the Falkner–Skan ansatz in turbulent thermal convection should be investigated in the future.

The authors are grateful to Professor S. Grossmann and all participants of the International Conference on Rayleigh–Bénard Turbulence, held in December 2012 in Hong Kong, for very useful discussions on different aspects concerning this work. The authors also acknowledge financial support of the Deutsche Forschungsgemeinschaft (DFG) under the grants SH405/2-1 and SH405/3-1.



## 9 Further evaluation of the Falkner-Skan ansatz

**Citation and credit:** This chapter consists of a paper published in *Physical Review E* 89, article number 033014, March 2014. The authors' version of the paper is posted here with permission of the American Physical Society (APS).

©American Physical Society 2014

**Title:** Influence of the angle between the wind and the isothermal surfaces on the boundary layer structures in turbulent thermal convection

**Authors:** Olga Shishkina, Sebastian Wagner & Susanne Horn [127]

**Contribution:** I performed and evaluated the numerical simulations for  $Pr = 0.1$  and  $1$ , developed the analysis technique for a co-moving frame of reference and extended the boundary layer extraction technique [155] to Prandtl numbers much larger or smaller than one. Further I created figures 9.1, 9.3, 9.4, 9.5, 9.6 and wrote part of the text in section 9.3.

### Abstract

We derive the asymptotes for the ratio of the thermal to viscous boundary layer thicknesses for infinite and infinitesimal Prandtl numbers  $Pr$  as functions of the angle  $\beta$  between the large-scale circulation and an isothermal heated or cooled surface for the case of turbulent thermal convection with laminar-like boundary layers. For this purpose, we apply the Falkner–Skan ansatz, which is a generalization of the Prandtl–Blasius one to a non-horizontal free-stream flow above the viscous boundary layer. Based on our direct numerical simulations (DNS) of turbulent Rayleigh–Bénard convection for  $Pr = 0.1, 1$  and  $10$  and moderate Rayleigh numbers up to  $10^8$  we evaluate the value of  $\beta$  that is found to be around  $0.7\pi$  for all investigated cases. Our theoretical predictions for the boundary layer thicknesses for this  $\beta$  and the considered  $Pr$  are in good agreement with the DNS results.

## 9.1 Introduction

In turbulent thermal convection of fluids confined between a heated lower and a cooled upper horizontal plate, i.e. in Rayleigh–Bénard convection (RBC), thermal boundary layers (BLs) occur at the plates and viscous BLs at all rigid walls. For moderate Rayleigh numbers  $Ra = \tilde{\alpha}\tilde{g}\tilde{\Delta}\tilde{H}^3/(\tilde{\kappa}\tilde{\nu})$  ( $\tilde{\alpha}$  denotes the isobaric thermal expansion coefficient,  $\tilde{g}$  the acceleration due to gravity,  $\tilde{\Delta}$  the temperature difference between the plates,  $\tilde{H}$  their vertical distance,  $\tilde{\nu}$  the kinematic viscosity and  $\tilde{\kappa}$  the thermal diffusivity), these BLs can be transitional or even laminar [5, 32, 41, 50, 84].

To approximate mean flow characteristics within the top and bottom BLs in this case, it is usually assumed that the wind of turbulence, or the so-called large-scale circulation (LSC) above the viscous BL is horizontal and constant, which corresponds to a zero pressure gradient. In contrast to this, recent direct numerical simulations (DNS) of turbulent RBC in different fluids showed that the wind is non-constant along its path [70, 125, 155] and the time-averaged pressure gradient does not vanish [118].

In [119] we have shown that the Prandtl and Pohlhausen BL equations admit similarity solutions if the wind above the viscous BL follows either an exponential behavior or a power function. In the case of an exponential wind, the BL thickness decreases with the wind magnitude, whereas in the case of a power-function wind, the BL thickness increases with it. Based on our DNS of RBC in air and water, with Prandtl numbers  $Pr = \tilde{\nu}/\tilde{\kappa} = 0.786$  and 4.38, respectively, revealing that after the stagnation point the BL thickness grows with the wind magnitude, we concluded that in RBC only the wind obeying a power-law is relevant. This leads to the Falkner–Skan (FS)[42] momentum and Pohlhausen energy equations.

These equations account for a non-parallel wind or, in other words, for an angle  $\beta$ ,  $\beta < \pi$ , between the LSC and the heated and cooled plate, and can be interpreted as an extension of the Prandtl–Blasius (PB) ansatz [102] to the case of a non-zero pressure gradient along the wind. In [119] we have evaluated the FS equations and the viscous BL thickness for four particular values of  $\beta$ :  $\pi$ ,  $3\pi/4$ ,  $2\pi/3$  and  $\pi/2$ . A comparison of the numerical solutions of the FS BL equations with our DNS data of water and air has shown that the FS approach leads to more accurate predictions of the BL thicknesses than the PB ansatz.

Here we give this idea more precision and derive several theoretical estimates. In section 9.2 we present the numerical solution for the whole spectra of angles  $\beta$ . We now provide exact relations for the ratio of the thermal to viscous BL thicknesses in the limiting cases of  $Pr \ll 1$  and  $Pr \gg 1$  and also obtain the critical Prandtl number  $Pr^*$  for which the transition between these two regimes occurs.

Furthermore, we verify the FS approximation against DNS data for the generic Prandtl numbers 0.1, 1.0 and 10.0, see figure 9.1, thus spanning three orders of magnitude in  $Pr$ . The BL properties for those Prandtl numbers are analyzed in section 9.3 in a more sophisticated way,



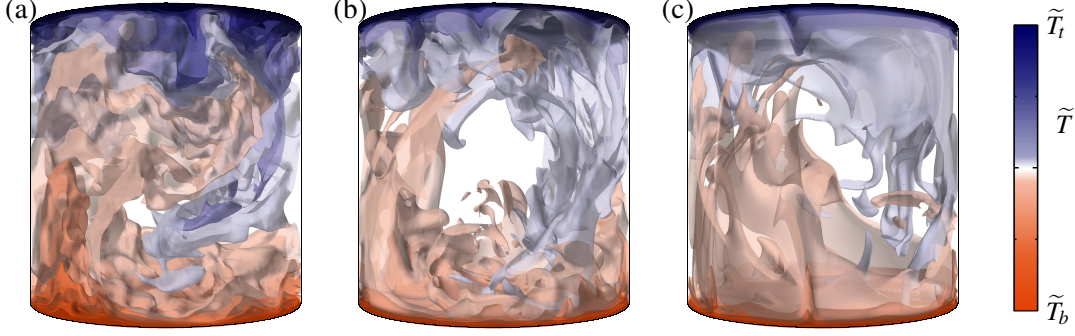


FIGURE 9.1: Instantaneous temperature fields obtained by DNS for  $Ra = 10^8$  and (a)  $Pr = 0.1$ , (b)  $Pr = 1$  and (c)  $Pr = 10$  and presented with 10 isosurfaces for  $\tilde{T} \in [\tilde{T}_t, \tilde{T}_b]$ .

however, than in [119]. Instead of considering stationary LSC-planes, we extract instantaneous LSC-planes, hence, the potential movement of the direction of the LSC is taken into account as well.

Finally, in section 9.4 the mesh resolution requirements for the BLs in DNS are discussed. By employing the FS approximation instead of the PB one, the earlier estimates given in [121] are updated and improved.

## 9.2 Falkner-Skan-Pohlhausen boundary layers

Following Prandtl [102] and Pohlhausen [99]<sup>1</sup> and assuming that the wind and the free-fall velocity magnitudes are similar, from the full system of the 3D governing equations for RBC in Boussinesq approximation,

$$\tilde{u}_t + \tilde{u} \cdot \nabla \tilde{u} + \tilde{\rho}^{-1} \nabla \tilde{p} = \tilde{\nu} \nabla^2 \tilde{u} + \tilde{\alpha} \tilde{g} (\tilde{T} - \tilde{T}_{\text{mid}}) \hat{y}, \quad (9.1)$$

$$\tilde{T}_t + \tilde{u} \cdot \nabla \tilde{T} = \tilde{\kappa} \nabla^2 \tilde{T}, \quad \nabla \cdot \tilde{u} = 0, \quad (9.2)$$

one obtains the following Prandtl (9.3) and Pohlhausen (9.4) equations [112] for laminar BLs:

$$\tilde{u} \tilde{u}_{\tilde{x}} + \tilde{v} \tilde{u}_{\tilde{y}} = \tilde{\nu} \tilde{u}_{\tilde{y}\tilde{y}} - \tilde{p}_{\tilde{x}} / \tilde{\rho}, \quad 0 = -\tilde{p}_{\tilde{y}} / \tilde{\rho}, \quad (9.3)$$

$$\tilde{u} \tilde{T}_{\tilde{x}} + \tilde{v} \tilde{T}_{\tilde{y}} = \tilde{\kappa} \tilde{T}_{\tilde{y}\tilde{y}}. \quad (9.4)$$

Here  $\tilde{u} \equiv (\tilde{u}, \tilde{v}, \tilde{w})^T$  is the velocity vector-function in the coordinate system  $\tilde{x} = (\tilde{x}, \tilde{y}, \tilde{z})$ ,  $\tilde{y}$  is the vertical direction,  $\tilde{x}$  and  $\tilde{z}$  are horizontal directions and  $\tilde{x}$  is along the wind,  $\hat{y} \equiv (0, 1, 0)^T$ , and  $\tilde{T}$  denotes the temperature,  $\tilde{p}$  the pressure,  $\tilde{T}_{\text{mid}}$  the arithmetic mean of the top ( $\tilde{T}_t$ ) and bottom ( $\tilde{T}_b$ ) temperatures,  $\tilde{T}_t < \tilde{T}_b$ ,  $\tilde{\rho}$  the density, and any variable marked as a subindex denotes the partial derivative with respect to this variable, e.g.  $\tilde{u}_{\tilde{t}} \equiv \partial \tilde{u} / \partial \tilde{t}$ ,  $\tilde{u}_{\tilde{x}} \equiv \partial \tilde{u} / \partial \tilde{x}$ ,  $\tilde{u}_{\tilde{x}\tilde{x}} \equiv \partial^2 \tilde{u} / \partial \tilde{x}^2$ .

<sup>1</sup>By mistake in the original paper the wrong reference ‘‘Pohlhausen [100]’’ was used.

The vertical and horizontal walls of the container are assumed to be, respectively, adiabatic or isothermal and all of them are impermeable (no-slip boundary conditions). Note, that the Prandtl–Pohlhausen BL model (9.3), (9.4) differs from that by Stewartson [137] for a very slow wind  $\tilde{U}$  above the viscous BL,  $\tilde{U}^2 \ll \tilde{\alpha} \tilde{g} \tilde{\Delta} \tilde{L}$ , with  $\tilde{L}$  being a representative length along the wind, where the buoyancy cannot be neglected. Since the considered BL flow is 2D and incompressible, (9.3), (9.4) can be rewritten in terms of the streamfunction  $\tilde{\Psi}$ , which satisfies  $\tilde{u} = \tilde{\Psi}_{\tilde{y}}$  and  $\tilde{v} = -\tilde{\Psi}_{\tilde{x}}$ . If a similarity solution is sought under the assumption that  $\tilde{\Psi}$  and the similarity variable  $\xi$  are representable in the forms

$$\tilde{\Psi} = \tilde{v} \Psi(\xi) g(x), \quad \xi = y f(x), \quad (9.5)$$

and for the wind at the edge of the viscous BL holds  $\tilde{U} = \tilde{U}(\tilde{x})$ , then the similarity solution exists only if  $g_x/f$  is constant and  $g$  is either exponential or a power function of  $x$  [119]. Here  $x \equiv \tilde{x}/\tilde{L}$  and  $y \equiv \tilde{y}/\tilde{L}$  are the dimensionless spatial coordinates and the functions  $g$  and  $f$  depend on  $x$  alone. The case in which  $g$  is exponential describes a decreasing BL thickness along the wind, while if  $g$  is a power function, the BL thickness increases. The latter case is in good agreement with DNS results of turbulent RBC [155], which showed that near the horizontal plate, after the stagnation point, the BL thickness grows together with the wind magnitude. Thus, we consider only this case in the following. It leads to a BL of FS type [42], which develops for a corner flow with angle  $\beta$  along the corners' sides (cf. figure 9.4a). In this case the core flow (or wind) above the BL and the pressure term within the BL equal, respectively,

$$\tilde{U} = \tilde{U}_0 x^{-1+\pi/\beta}, \quad (9.6)$$

$$-\tilde{p}_{\tilde{x}}/\tilde{\rho} = (\pi/\beta - 1) x^{-3+2\pi/\beta} \tilde{U}_0^2/\tilde{L}, \quad (9.7)$$

where  $\tilde{U}_0$  is a constant velocity magnitude. If the wind is parallel to the horizontal plate, i.e.  $\beta = \pi$ , the FS BL is reduced to the PB one.

Thus, one obtains the following system of the dimensionless BL equations for the momentum (FS)

$$\Psi_{\xi\xi\xi} + \Psi\Psi_{\xi\xi} + (2 - \gamma) (1 - (\Psi_{\xi})^2) = 0, \quad (9.8)$$

$$\Psi(0) = 0, \quad \Psi_{\xi}(0) = 0, \quad \Psi_{\xi}(\infty) = 1, \quad (9.9)$$

and the energy

$$\Theta_{\xi\xi} + Pr\Psi\Theta_{\xi} = 0, \quad (9.10)$$

$$\Theta(0) = 0, \quad \Theta(\infty) = 1. \quad (9.11)$$

## 9.2 FALKNER-SKAN-POHLHAUSEN BOUNDARY LAYERS

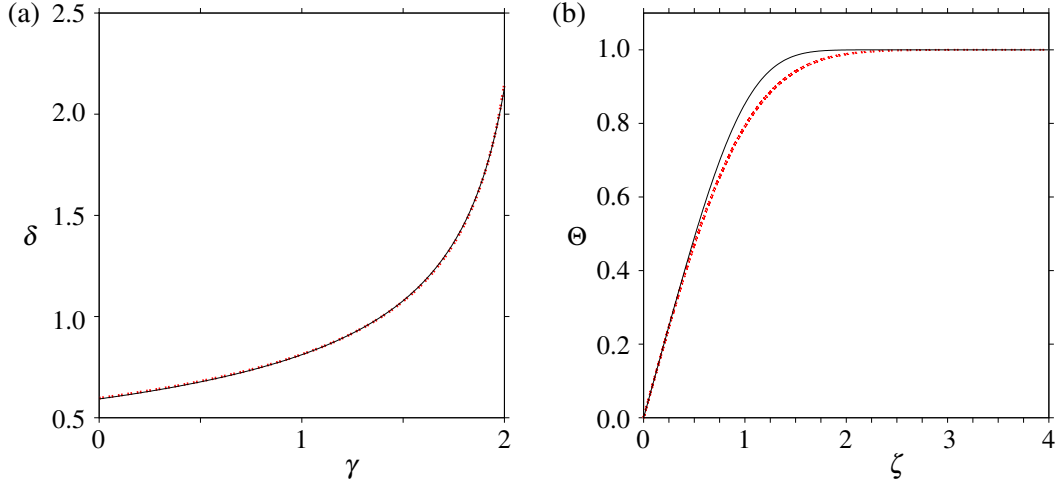


FIGURE 9.2: (a) Dependence on  $\gamma$  (9.15) of the viscous BL thickness  $\delta$  with respect to the similarity variable  $\xi$  (9.12), as obtained from the numerical solutions of (9.8) and (9.9) (—), and its approximation  $\delta_{appr}$  (9.19) (..). (b) Limiting cases  $Pr \ll 1$  (..) and  $Pr \gg 1$  (—) of the rescaled temperature profiles (9.23) and (9.24) in the FS ansatz, for any angle  $\beta$ .

For the similarity variable  $\xi$ , the stream function  $\Psi$  and the dimensionless temperature  $\Theta$  the following expressions hold

$$\xi \equiv \gamma^{-1/2} Re_0^{1/2} y x^{-1+1/\gamma}, \quad (9.12)$$

$$\Psi \equiv \gamma^{-1/2} Re_0^{-1/2} x^{-1/\gamma} \tilde{v}^{-1} \tilde{\Psi}, \quad (9.13)$$

$$\Theta \equiv 2(\tilde{T}_b - \tilde{T})/\tilde{\Delta}. \quad (9.14)$$

Here,  $Re_0 \equiv \tilde{L}\tilde{U}_0/\tilde{v}$  is the Reynolds number based on the wind magnitude and

$$\gamma \equiv 2\beta/\pi. \quad (9.15)$$

With respect to the similarity variable  $\xi$ , the thickness of the viscous BL equals

$$\delta = \left( \Psi_\xi \Big|_{\xi=0} \right)^{-1} \quad (9.16)$$

and can be determined by solutions of the system (9.8) and (9.9).  $\delta$  depends on  $\gamma$  and, hence, on the angle  $\beta$ . Taking  $\xi = \delta$ ,  $y = \tilde{\delta}_u/\tilde{L}$ , where  $\tilde{\delta}_u$  is the thickness of the viscous BL in physical space, from (9.12) one obtains

$$\tilde{\delta}_u/\tilde{L} = \delta \gamma^{1/2} Re_0^{-1/2} x^{1-1/\gamma}. \quad (9.17)$$

From (9.6), (9.15), and (9.16) it follows that

$$\tilde{\delta}_u/\tilde{L} \sim \sqrt{x/Re}, \quad (9.18)$$

## 9 FURTHER EVALUATION OF THE FALKNER-SKAN ANSATZ

where the Reynolds number  $Re$  is based on the wind  $\tilde{U}$  (9.6). Relation (9.18) holds for general Falkner–Skán BLs and thus also for the special case of Prandtl–Blasius BLs, i.e.  $\gamma = 2$ . The proportionality of the relative thickness of the boundary layer and the inverse square-root of the Reynolds number, commonly known as Prandtl–formula, is one of the basic assumptions in the Grossmann–Lohse (GL) theory [50, 51, 134], for the case of non-turbulent BLs. The latter theory estimates the dependence of the mean heat flux, expressed by the Nusselt number, on  $Ra$  and  $Pr$ . Since the more general case of the Prandtl–formula (9.18) still holds for arbitrary  $\gamma$ , the scaling exponents in the theoretical estimates should remain unchanged, while considering Falkner–Skán BLs instead of Prandtl–Blasius BLs. Nevertheless, further estimates, which are based on the balance between the thermal and viscous BLs, may change when applying Falkner–Skán BLs, as we will elaborate below.

The dependence of the viscous BL  $\delta$  on  $\gamma$  is obtained by solving numerically the system of FS equations (9.8) and (9.9) for  $0 \leq \gamma \leq 2$ , i.e. for all angles  $0 \leq \beta \leq \pi$  (see e.g. [160], section 14.2). The result is presented in figure 9.2. It can be well approximated by

$$\delta \approx \delta_{appr} \equiv C_1(C_2 - \gamma)^{-1/2} \quad (9.19)$$

with  $C_1 \approx 0.88$ ,  $C_2 \approx 2.17$ .

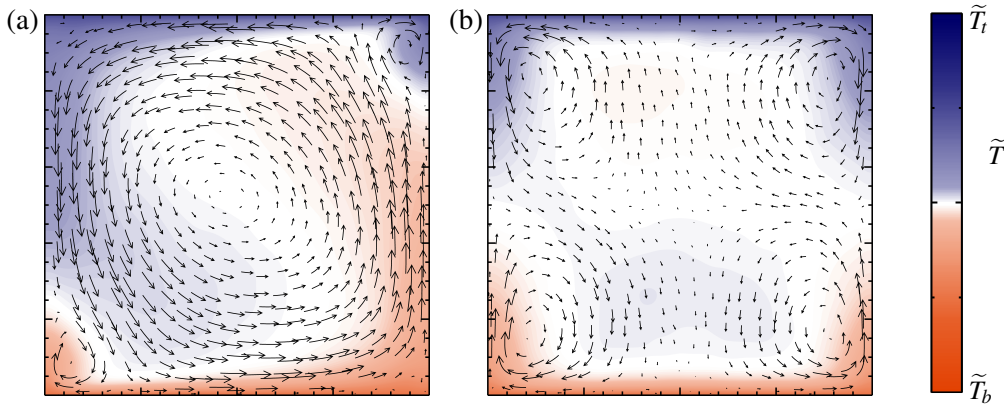


FIGURE 9.3: Time-averaged temperature field with superposed velocity vectors in the vertical (a) LSC-plane and (b) LSC<sub>⊥</sub>-plane, as obtained in DNS of turbulent RBC for  $Ra = 10^7$  and  $Pr = 0.1$  (see table 9.1 for the DNS details).

The temperature distributions within the BLs, i.e. the solution of the energy equations (9.10) and (9.11) does not only depend on  $\gamma$ , but also on  $Pr$ . Using special similarity variables  $\zeta$  as in Shishkina *et al.* [119], one obtains the temperature profiles for the limiting cases  $Pr \ll 1$  and  $Pr \gg 1$  which satisfy the boundary conditions

$$\Theta|_{\zeta=0} = 0, \quad \Theta_{\zeta}|_{\zeta=0} = 1, \quad \Theta|_{\zeta=\infty} = 1. \quad (9.20)$$

## 9.2 FALKNER-SKAN-POHLHAUSEN BOUNDARY LAYERS

Thus, for the similarity variable

$$\zeta = C_3(Pr)\gamma^{-1/2}Re_0^{1/2}yx^{-1+1/\gamma} \quad (9.21)$$

with

$$C_3(Pr) = \begin{cases} 2^{1/2}\pi^{-1/2}Pr^{1/2}, & Pr \ll 1, \\ 6^{-1/3}[\Gamma(4/3)]^{-1}\delta^{-1/3}Pr^{1/3}, & Pr \gg 1, \end{cases}$$

the limiting energy BL equations

$$\begin{aligned} \Theta_{\zeta\zeta} + (\pi/2)\zeta\Theta_{\zeta} &= 0, & Pr \ll 1, \\ \Theta_{\zeta\zeta} + 3\Gamma^3(4/3)\zeta^2\Theta_{\zeta} &= 0, & Pr \gg 1, \end{aligned} \quad (9.22)$$

have the following solution

$$\Theta(\zeta) = \int_0^{\zeta} \exp(-B\chi^{\omega}) d\chi, \quad (9.23)$$

with  $B$  and  $\omega$  being constants defined as follows:

$$\begin{aligned} \omega = 2, \quad B = \pi/4, & & Pr \ll 1, \\ \omega = 3, \quad B = \Gamma^3(4/3) \approx 0.71, & & Pr \gg 1. \end{aligned} \quad (9.24)$$

and  $\Gamma$  being the gamma function. The limiting profiles (9.23), (9.24) are independent of the angle  $\beta$ , i.e. they are the same as in the PB case for all  $\beta$  (see figure 9.2b). Further, for the thermal BL thickness  $\tilde{\delta}_{\theta}$  in physical space, from (9.20), (9.21) one obtains

$$\tilde{\delta}_{\theta}/\tilde{L} = C_3^{-1}\gamma^{1/2}Re_0^{-1/2}x^{1-1/\gamma}. \quad (9.25)$$

The relations (9.17) and (9.25) give the ratio of the thermal to viscous BLs in the limiting cases  $Pr \ll 1$  and  $Pr \gg 1$ , which depends only on the angle  $\beta$  and Prandtl number as

$$\begin{aligned} \tilde{\delta}_{\theta}/\tilde{\delta}_u &= [C_3(Pr)\delta]^{-1} \\ &= \begin{cases} 2^{-1/2}\pi^{1/2}Pr^{-1/2}\delta^{-1}, & Pr \ll 1, \\ 6^{1/3}\Gamma(4/3)Pr^{-1/3}\delta^{-2/3}, & Pr \gg 1. \end{cases} \end{aligned} \quad (9.26)$$

Inserting the approximation (9.19),  $\delta_{appr}$ , into the ratio (9.26), yields

$$\tilde{\delta}_{\theta}/\tilde{\delta}_u \approx C_4(Pr)(C_2 - \gamma)^{1/\omega}Pr^{-1/\omega} \quad (9.27)$$

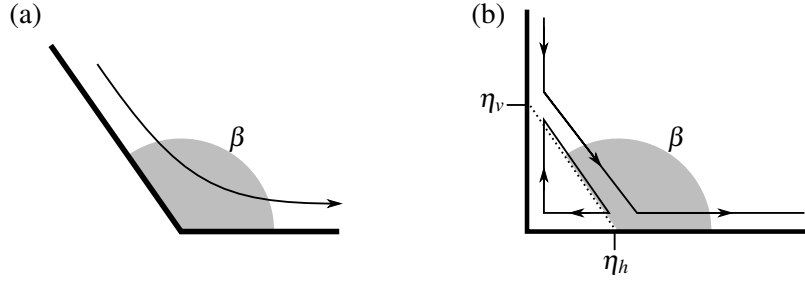


FIGURE 9.4: (a) Sketch of the corner flow with opening angle  $\beta$  in the FS sense. (b) Sketch of the LSC and secondary roll within the LSC-plane near the bottom left corner of figure 9.3a. Here  $\eta_v$  and  $\eta_h$  are the distances from the corner to the locations, where the wall shear stress equals zero, and  $\beta$  is the angle at which the LSC attacks the heated bottom plate.

with

$$\begin{aligned} \omega = 2, \quad C_4 \approx 1.43, \quad Pr \ll 1, \\ \omega = 3, \quad C_4 \approx 1.77, \quad Pr \gg 1. \end{aligned} \quad (9.28)$$

The derived asymptotes (9.27) and (9.28) are in excellent agreement with numerical results for some particular values of  $\beta$ , reported in [119].

The change of the regime from  $Pr^{-1/2}$  ( $Pr \ll 1$ ) to  $Pr^{-1/3}$  ( $Pr \gg 1$ ) in (9.26) corresponds to the critical Prandtl number  $Pr^*$ , where the two asymptotes intersect. From (9.26–9.28) we obtain that  $Pr^*$  can be approximated as follows:

$$Pr^* \approx 0.596 - 0.275\gamma, \quad (9.29)$$

which leads to  $Pr^* \approx 0.046$  for the PB flow [121] and  $Pr^* \approx 0.321$  for the stagnation-point flow.

For any particular  $\gamma$  and not extremely small or large  $Pr$  an approximation of  $\tilde{\delta}_\theta/\tilde{\delta}_u$  can be obtained by applying a least square fit to the numerical solutions of the equations (9.8) – (9.11) for the chosen  $\gamma$  and all possible  $Pr$ .

### 9.3 Wind in turbulent Rayleigh-Bénard convection

In the following, the results of the previous section are verified against DNS of turbulent RBC in a cylindrical domain with a diameter-to-height aspect ratio of 1 for the Prandtl numbers  $Pr = 0.1, 1$  and  $10$  and  $Ra$  up to  $10^8$ . The DNS were conducted using the same finite-volume code as in [67, 123]. The DNS details can be found in table 9.1.

In the case of turbulent RBC for large enough  $Ra$  an LSC of fluid develops (see figure 9.3). Within the vertical LSC-plane one obtains a large roll (LSC, wind) and two secondary rolls in the corners (figure 9.3a), while in the vertical LSC $_{\perp}$ -plane, which is orthogonal to the LSC-plane, a four-roll structure develops (figure. 9.3b). From a large amount of instantaneous flow fields

### 9.3 WIND IN TURBULENT RAYLEIGH-BÉNARD CONVECTION

TABLE 9.1: DNS parameters for different  $Pr$  and  $Ra$ : the number of mesh nodes in  $N_i$ -direction ( $i = r; \phi; z$ ) and in the thermal and viscous BLs as used in the DNS ( $n_T$  and  $n_u$ ) and as estimated in [121] ( $\check{n}_T$  and  $\check{n}_u$ ); Nusselt number  $Nu$  with its maximal deviation and the number of dimensionless time units  $\tau$  used for the statistical averaging.

$Pr$	$Ra$	$N_r$	$N_\phi$	$N_z$	$n_T$	$\check{n}_T$	$n_u$	$\check{n}_u$	$Nu$	$\tau$
0.1	$10^6$	48	256	96	8	7	4	3	$7.34 \pm 0.10$	295
	$10^7$	96	256	192	9	9	4	4	$13.61 \pm 0.08$	506
	$10^8$	192	512	384	13	13	6	5	$26.37 \pm 0.64$	68
1	$10^6$	48	256	96	7	2	7	2	$8.60 \pm 0.09$	1231
	$10^7$	96	256	192	8	3	8	3	$16.99 \pm 0.16$	1082
	$10^8$	192	512	384	11	4	11	4	$32.60 \pm 0.46$	228
10	$10^6$	36	128	72	6	2	3	2	$8.05 \pm 0.03$	3860
	$10^7$	64	512	128	5	3	4	3	$16.43 \pm 0.06$	525
	$10^8$	192	512	384	9	4	11	4	$32.50 \pm 0.29$	184

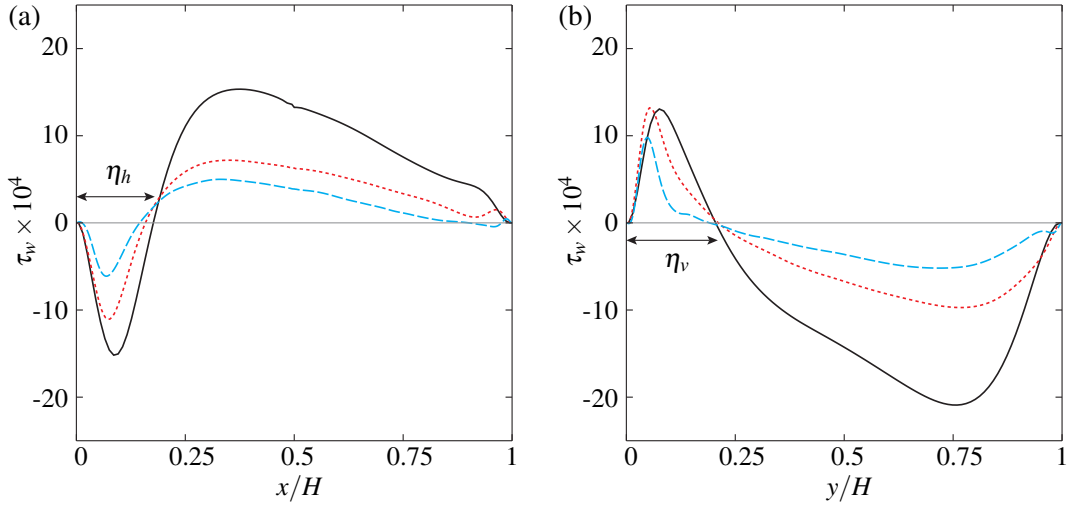


FIGURE 9.5: Dimensionless time-averaged wall shear stress (a) at the bottom,  $\tau_w = \frac{\tilde{H}^2}{Ra\kappa} \langle \frac{\partial \tilde{v}}{\partial x} \rangle_{\tilde{t}}$ , and (b) left vertical wall in the LSC-plane,  $\tau_w = \frac{\tilde{H}^2}{Ra\kappa} \langle \frac{\partial \tilde{u}}{\partial y} \rangle_{\tilde{t}}$ , as obtained in the DNS for  $Pr = 1$  and  $10^6$  (—),  $10^7$  (··) and  $Ra = 10^8$  (- -) with  $\eta_v$  and  $\eta_h$  as in figure 9.4b.

obtained in our DNS and sampled with a frequency of three per time-unit, we extract the wind direction. For this purpose we make use of the temperature distribution at the vertical wall at the height  $\tilde{H}/2$  from the bottom [19, 155]. Figure 9.4b sketches out the LSC and the secondary roll within the LSC-plane near the bottom left corner of figure 9.3a. There  $\beta$  can be understood as the angle between the wind and the heated bottom plate. The value of  $\beta$  is determined by the locations, where the wall shear stress at the vertical and horizontal walls at the sides of the corner is equal to zero (see figure 9.5). Our DNS of turbulent RBC for different  $Ra$  and  $Pr$  show

that  $\beta$  varies around  $0.7\pi$ ,

$$\beta = \begin{cases} 0.69\pi \pm 0.02\pi, & Pr = 0.1, \\ 0.71\pi \pm 0.02\pi, & Pr = 1, \\ 0.71\pi \pm 0.03\pi, & Pr = 10, \end{cases} \quad (9.30)$$

and is similar to the angles obtained earlier for  $Pr = 0.786$  and  $4.38$  and  $Ra$  between  $10^7$  and  $10^9$  [119].

Thus, for  $\gamma = 1.4$ , which corresponds to  $\beta = 0.7\pi$ , we obtain

$$\frac{\tilde{\delta}_\theta}{\tilde{\delta}_u} \approx \begin{cases} 1.25Pr^{-1/2}, & Pr < 10^{-4}, \\ 1.75Pr^{-0.395+0.017\log Pr}, & 10^{-4} \leq Pr \leq 10^3, \\ 1.62Pr^{-1/3}, & 10^3 < Pr, \end{cases} \quad (9.31)$$

where  $\log \equiv \log_{10}$  is the logarithm to base ten. The estimate (9.31) gives  $\tilde{\delta}_\theta/\tilde{\delta}_u \approx 4.52$  ( $Pr = 0.1$ ),  $\tilde{\delta}_\theta/\tilde{\delta}_u \approx 1.75$  ( $Pr = 1$ ) and  $\tilde{\delta}_\theta/\tilde{\delta}_u \approx 0.73$  ( $Pr = 10$ ).

We compare these predictions with the ratios  $\langle \tilde{\delta}_\theta/\tilde{\delta}_u \rangle_{\bar{t}}$  along the wind near the bottom plate, obtained in our DNS. (Here  $\langle \dots \rangle_{\bar{t}}$  denotes the time averaging.) Similar to Shi *et al.* [118], we consider the instantaneous LSC plane and evaluate the viscous and thermal BL thicknesses by using the slope method [155]. The wind velocity is determined as the maximum of the radial velocity considered at heights smaller than  $2\tilde{H}/Nu(\tilde{\delta}_\theta/\tilde{\delta}_u)^{-1}$ , where  $\tilde{\delta}_\theta/\tilde{\delta}_u$  is estimated within the PB ansatz (i.e.  $\beta = \pi$ ).

Note that in [155] the maximum considered height for evaluating the wind magnitude was  $2\tilde{H}/Nu$ , since there  $Pr$  was close to one and, consequently,  $\tilde{\delta}_\theta/\tilde{\delta}_u$  was approximately one as well.

The resulting ratios  $\langle \tilde{\delta}_\theta/\tilde{\delta}_u \rangle_{\bar{t}}$  are presented in figure 9.6 in dependence of the horizontal position  $x/H$ , for different  $Pr$  and  $Ra$ , together with the estimates (horizontal lines) for  $\beta = \pi$  (Prandtl–Blasius flow),  $\beta = \pi/2$  (stagnation-point flow) [119] and  $\beta = 0.7\pi$  (9.31). As one can see, the ratios remain almost constant along the path of the wind. The prediction for  $\beta = 0.7\pi$  represents the DNS results generally better than the classical PB ansatz ( $\beta = \pi$ ) [119].

However, one of the key assumptions of the developed approach is a strong enough wind, i.e. buoyancy can be neglected within the BLs (cf. [119]). Hence, for small Prandtl numbers, the agreement with the theory is better for larger Rayleigh numbers, when the wind dominates over the small-scale fluctuations. This is evident from figure 9.6a for  $Pr = 0.1$ . For  $Ra = 10^6$  and  $10^7$  the strong small-scale fluctuations lead to a small over-prediction of the ratio  $\langle \tilde{\delta}_\theta/\tilde{\delta}_u \rangle_{\bar{t}}$ , whereas for  $Ra = 10^8$  a fair agreement is found. For larger Prandtl numbers, as in the case of  $Pr = 10$  displayed in figure 9.6c, the wind itself is not strong enough, hence the ratio  $\langle \tilde{\delta}_\theta/\tilde{\delta}_u \rangle_{\bar{t}}$  is slightly under-predicted.



## 9.4 CONSEQUENCES FOR THE GRID RESOLUTION IN DNS

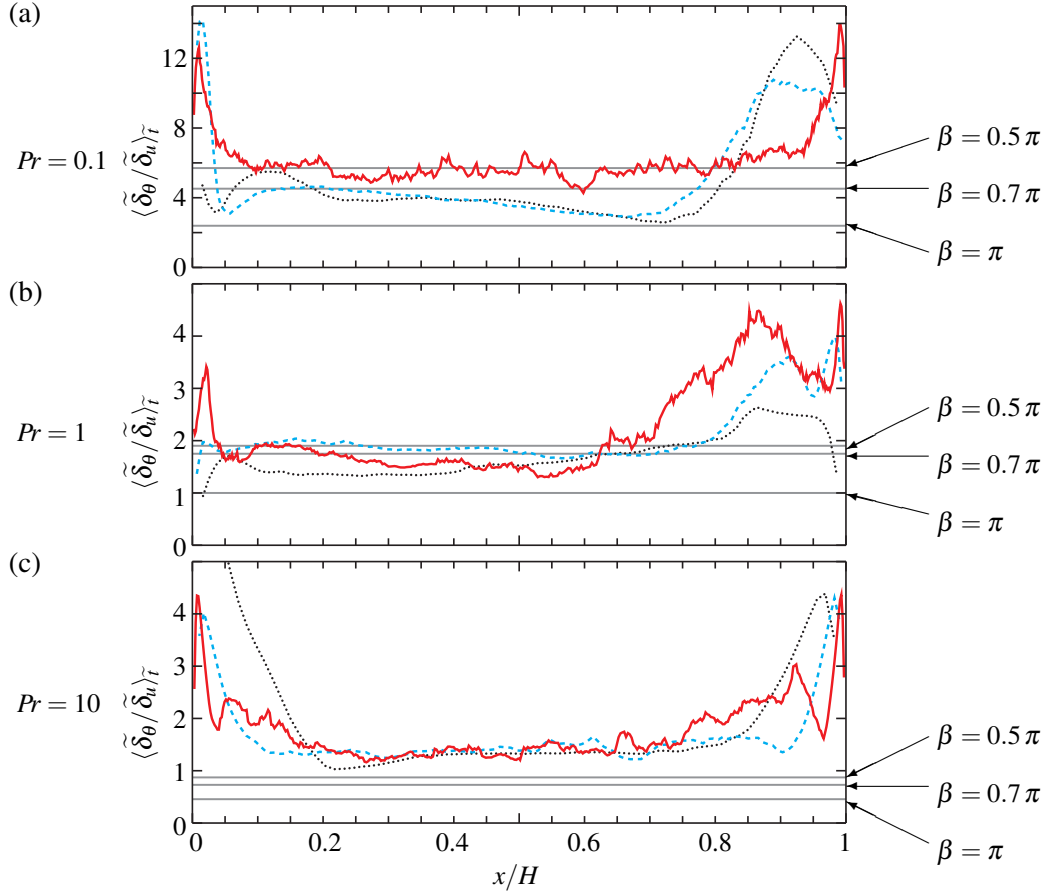


FIGURE 9.6: Ratio  $\langle \tilde{\delta}_\theta / \tilde{\delta}_u \rangle_{\tilde{t}}$  of the thermal and viscous BL thicknesses for (a)  $Pr = 0.1$ , (b)  $Pr = 1$ , (c)  $Pr = 10$ , as obtained in the DNS for  $Ra = 10^8$  (—),  $Ra = 10^7$  (- -) and  $Ra = 10^6$  (· ·) together with the predictions [119] (gray horizontal lines) for  $\beta = \pi$  (Prandtl–Blasius flow),  $\beta = \pi/2$  (stagnation-point flow) and estimate (9.31) for  $\beta = 0.7\pi$ .

Nonetheless, the prediction given by eq. (9.31) is always in a better agreement with the DNS data than the PB one.

## 9.4 Consequences for the grid resolution in DNS

In this section we discuss shortly the influence of wind angle on the required grid resolution in DNS of turbulent thermal convection.

It is the well established criterion [121] that in DNS the (local) mesh size  $\tilde{h}$  must not be larger than the (local) Kolmogorov  $\tilde{\eta}_K(\tilde{x}, \tilde{t})$  [73] and Batchelor  $\tilde{\eta}_B$  [10] scales:

$$\tilde{\eta}_K(\tilde{x}, \tilde{t}) = \left( \tilde{v}^3 / \tilde{\varepsilon}_u(\tilde{x}, \tilde{t}) \right)^{1/4}, \quad (9.32)$$

$$\tilde{\eta}_B(\tilde{x}, \tilde{t}) = \left( \tilde{v} \tilde{\kappa}^2 / \tilde{\varepsilon}_u(\tilde{x}, \tilde{t}) \right)^{1/4} = \tilde{\eta}_K(\tilde{x}, \tilde{t}) Pr^{-1/2}, \quad (9.33)$$

which are defined with the kinetic energy dissipation rate

$$\tilde{\epsilon}_u(\tilde{x}, \tilde{t}) \equiv \frac{\tilde{v}}{2} \sum_i \sum_j \left( \frac{\partial \tilde{u}_i(\tilde{x}, \tilde{t})}{\partial \tilde{x}_j} + \frac{\partial \tilde{u}_j(\tilde{x}, \tilde{t})}{\partial \tilde{x}_i} \right)^2, \quad (9.34)$$

where  $(\tilde{x}_1, \tilde{x}_2, \tilde{x}_3) \equiv (\tilde{x}, \tilde{y}, \tilde{z})$ . In a horizontal plane  $A$  within the viscous BL the energy dissipation rate  $\tilde{\epsilon}_u|_{A \in BL}$  can be approximated as

$$\tilde{\epsilon}_u|_{A \in BL} \approx \tilde{v} \left( \tilde{U} / \tilde{\delta}_u \right)^2. \quad (9.35)$$

From this and (9.17), (9.19) and (9.32) we obtain the following estimate for  $\tilde{\eta}_K|_{A \in BL}$ :

$$\frac{\tilde{\eta}_K|_{A \in BL}}{\tilde{L}} \approx \left( \frac{\gamma}{C_2 - \gamma} \frac{C_{1x}^2}{Re^3} \right)^{1/4}, \quad (9.36)$$

where  $Re \equiv \tilde{L}\tilde{U}/\tilde{v}$  is the Reynolds number based on the wind (9.6).

Therefore, for similar Reynolds numbers, near the isothermal plate, the required mesh size  $\tilde{h}_{st.p.}$  for the stagnation point flow ( $\gamma = \gamma_{st.p.} \equiv 1$ ) is related to the mesh size  $\tilde{h}_{PB}$  for the PB flow ( $\gamma = \gamma_{PB} \equiv 2$ ) by

$$\frac{\tilde{h}_{PB}}{\tilde{h}_{st.p.}} \approx \left( \frac{\gamma_{PB}}{C_2 - \gamma_{PB}} \frac{C_2 - \gamma_{st.p.}}{\gamma_{st.p.}} \right)^{1/4} \approx 1.93. \quad (9.37)$$

This means that in DNS of turbulent thermal convection, in which the wind is not everywhere parallel to the isothermal plate (like in RBC), an up to two times finer mesh resolution than in the case of PB BLs is required within the BLs.

## 9.5 Conclusions

To describe laminar boundary layers in thermal convection, we considered a generalization of the Prandtl–Blasius ansatz to the case of a non-horizontal free-stream flow above the viscous boundary layer, i.e., the Falkner–Skan ansatz [119].

The asymptotes for the ratio of the thermal to viscous boundary layer thicknesses for infinite and infinitesimal Prandtl numbers were derived as functions of the angle  $\beta$  between the wind and the isothermal horizontal plate.

DNS of turbulent RBC for  $Pr = 0.1, 1, \text{ and } 10$  and Rayleigh numbers up to  $10^8$  showed that  $\beta \approx 0.7\pi$  for all investigated cases. The predictions for the boundary layer thicknesses for this  $\beta$  and the considered  $Pr$  are found to be in better agreement with the DNS results than the Prandtl–Blasius ones.

Since the developed approach is based on the assumption of a relatively strong wind above

the viscous boundary layer, which is compatible with the free-fall velocity, the agreement of the theoretical estimates and the DNS results is best for relatively large Rayleigh numbers,  $Ra \gtrsim 10^8$ , and small Prandtl numbers,  $Pr \lesssim 1$ . For smaller  $Ra$  and higher  $Pr$  there is an apparent deviation between theory and DNS, because this prerequisite is less valid. Nonetheless, even in those cases the theoretical predictions based on the Falkner–Skan ansatz result in a better agreement than those based on the Prandtl–Blasius ansatz.

It is also expected that in mixed convection with imposed free-stream flows, moderate Rayleigh numbers and Archimedes numbers about one, even better agreement of the theoretical predictions and DNS or experimental results can be obtained. This and measurements [83] of the BL thicknesses along the path of the large-scale circulation near the isothermal surfaces might be the subject of forthcoming studies.

The authors acknowledge financial support of the Deutsche Forschungsgemeinschaft (DFG) under the grants SH405/2, SH405/3 and SFB 963/1, project A6.



# 10 Influence of the shape of the domain

**Citation and credit:** As a conference proceeding for the 18th STAB/DGLR symposium 2012 this paper was published in the the book “New results in numerical and experimental fluid mechanics IX” in 2014. This is the authors’ version of the paper. The original publication is available at [www.springerlink.com](http://www.springerlink.com).

©Springer International Publishing Switzerland 2014

**Title:** Influence of the geometry on Rayleigh-Bénard convection

**Authors:** Sebastian Wagner, Olga Shishkina & Claus Wagner [156]

**Contribution:** I performed and evaluated the numerical simulations, developed the analysis techniques for cuboid domains, created all the figures and wrote the first version of the manuscript, which structure is preserved.

## Abstract

Direct numerical simulations (DNS) of Rayleigh-Bénard convection in a cube and a cylinder with equal diameter and height are performed to investigate the main responses of the system, namely heat flux and motion. Differences in the latter two quantities for the two geometries suggest a transition between different flow states in the cube, which is not observed in the cylinder due to its rotational symmetry. A method is introduced to analyse the flow dynamics in the cube, which relies on the temperature distribution at the lateral walls. It reveals that above a certain Rayleigh number the global flow structure in the cube is organized in a diagonal manner and not longer parallel to the walls, which leads to differences in the heat flux and the kinetic energy in the cylindrical and the cubic sample.

## 10.1 Introduction

Rayleigh-Bénard convection (RBC) as a model system for many convective flow problems occurring in nature and technology is usually studied in terms of the Oberbeck-Boussinesq (OB) approximation [5]. Within this approximation, the flow is determined by the dimensionless temperature gradient, Rayleigh number  $Ra$ , and a fluid parameter, Prandtl number  $Pr$ . Besides the dynamical similarity, forced by equal  $Pr$  and  $Ra$ , flow setups must be geometrically similar to lead to similar solutions.

The geometry is usually parameterised by one (or more) aspect ratios, e.g. diameter/height for a cylinder. In DNS of Rayleigh-Bénard convection in cylindrical samples filled with air the influence of the aspect ratio on the mean heat flux is reported to be small [8], while experiments in rectangular containers filled with water do not show any significant influence [168] at all. From two-dimensional DNS, it is known [97, 98] that the mean heat flux is significantly influenced by changes in the global flow structure occurring for small aspect ratios. In addition, a theoretical attempt [53] exists trying to explain the influence of the aspect ratio. The latter is based on differences between the boundary layers attached to the vertical and horizontal walls. These differences are discussed for different flow structures (called “plate filling” and “laterally restricted”), but the occurrence of this flow structures are not understood and therefore, the applicability of the theory is questionable.

The aspect ratio is of course not sufficient for describing the geometry, since e.g. a cube and a cylinder, both with aspect ratio one, are still not similar geometries. To our knowledge, the only study comparing the flow in different geometries in a direct way deals with a cylindrical and a rectangular convection cell of equal volume and height, i.e. different aspect ratio, for large  $Ra$  [39]. The comparison reveals, that the temperature and velocity fluctuations in the center of the convection cell differ considerably, in particular, regarding the scaling with  $Ra$ . This means, that the influence of the geometry is not negligible at all for high  $Ra$ .

In the present study, the geometry’s influence on the flow within two cavities with equal aspect ratio is investigated. We performed direct numerical simulation (DNS) of the flow in a cube and a cylinder with equal diameter and height (section 10.2). The main integral responses of the system, namely the Nusselt number (vertical heat flux) and the Reynolds number (motion) and their  $Ra$ -dependence, are compared (section 10.3.1). They show a strong influence of the geometry especially, for small  $Ra$ . To understand these differences a method is introduced to analyse the global flow structure and its instantaneous dynamics (section 10.3.2).

## 10.2 Methodology

DNS of RBC are performed in a cube and a cylinder with equal diameter and height. A fourth-order accurate finite volume code in cylindrical [67, 123] and in Cartesian coordinates [69, 120],

respectively, is used to solve the dimensionless governing equations in OB approximation:

$$\partial_t \vec{u} + \vec{u} \cdot \vec{\nabla} \vec{u} = -\vec{\nabla} p + \sqrt{\frac{Pr}{Ra}} \vec{\nabla}^2 \vec{u} + \theta \vec{e}_z, \quad (10.1)$$

$$\partial_t \theta + \vec{u} \cdot \vec{\nabla} \theta = \sqrt{\frac{1}{RaPr}} \vec{\nabla}^2 \theta, \quad \vec{\nabla} \cdot \vec{u} = 0. \quad (10.2)$$

As reference quantities we use the free-fall velocity  $\sqrt{\alpha g \Delta H}$  and the height  $H$  have been used. The temperature is made dimensionless by  $\theta = (T - T_M)/\Delta$  with  $T_M = (T_{\text{bottom}} + T_{\text{top}})/2$  and  $\Delta = T_{\text{bottom}} - T_{\text{top}}$ . The boundary conditions for the considered domains are defined as follows. Top and bottom plates are isothermal with  $T_{\text{bottom}} > T_{\text{top}}$ , while the vertical walls are adiabatic. Further, no-slip and impermeability conditions are set on all walls. All material properties are considered to be constant except of the density in the buoyancy term, which is assumed to depend linearly on the temperature. The fluid is a (heavy) gas, i.e.  $Pr = \nu/\kappa = 0.786$ , and the Rayleigh number  $Ra = \alpha g \Delta H^3 / (\nu \kappa)$  is varied between  $10^5$  and  $10^7$ . Here,  $\nu$  is the kinematic viscosity,  $\kappa$  the thermal diffusivity,  $\alpha$  the isobaric thermal volume-expansion coefficient,  $g$  the gravitational acceleration and  $H$  the height of the convection cell. The resolution of the simulation is chosen according to [121] and [157].

## 10.3 Results

To investigate the influence of the geometry the two main responses of the system, motion and vertical heat flux, and their dependence on  $Ra$  are investigated. A further analysis of the flow structure in the cube is performed and the obtained results are compared to the flow structure in the cylinder.

### 10.3.1 Integral Responses of the System

The two main responses of the system, motion and heat flux from bottom to top, can be expressed by integral quantities, namely, the Reynolds number  $Re$  and the Nusselt number  $Nu$ . The latter is the ratio of the integral vertical heat flux of the system and the heat flux which would occur in a solid body under the same conditions. It reads in dimensionless formulation

$$Nu = \left\langle \sqrt{Pr Ra} u_z \theta - \frac{\partial \theta}{\partial z} \right\rangle_{A_z, t}, \quad (10.3)$$

where  $A_z$  is the area of the cross-section orthogonal to the  $z$ -direction.

For natural convection the definition of the Reynolds number  $Re$  is more complex, since the choice of the characteristic velocity and length are rather arbitrary. For convenience, we choose the height  $H$  as reference length and calculate a reference velocity from the volume- and

## 10 INFLUENCE OF THE SHAPE OF THE DOMAIN

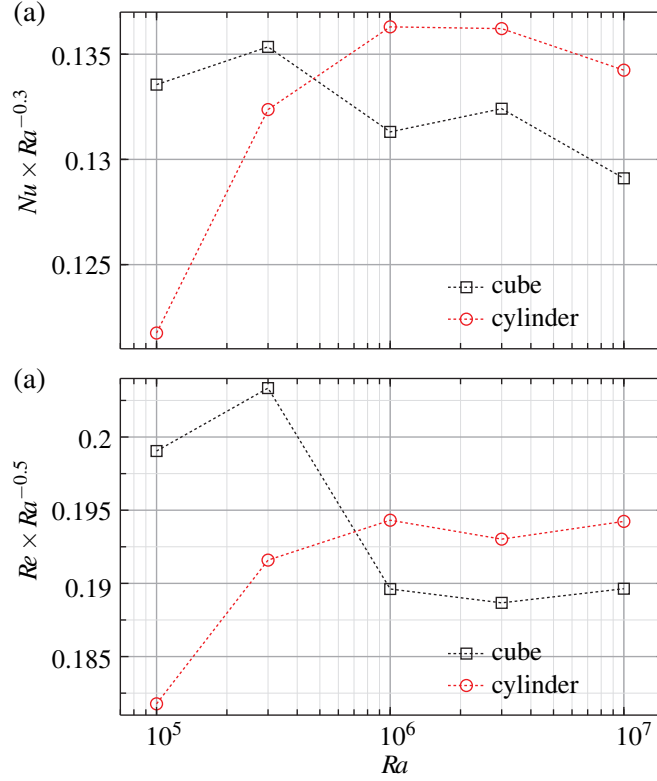


FIGURE 10.1:  $Ra$ -dependence of (a) the reduced Nusselt number  $NuRa^{-0.3}$  and (b) the reduced Reynolds number  $ReRa^{-0.5}$  for cube and cylinder (with equal diameter and height) and  $Pr = 0.786$ .

time-averaged kinetic energy of the flow, i.e.

$$Re = \sqrt{\frac{Ra}{Pr}} \sqrt{\langle \vec{u}^2 \rangle_{V,t}}. \quad (10.4)$$

For both quantities,  $Nu$  and  $Re$ , a large variety of results from DNS and measurements exist to which good agreement is found [71, 155]. Further, there are different theories to describe their dependence on  $Ra$  and  $Pr$ , among which the theory by Grossmann & Lohse [50] should be mentioned here. However, none of the theories sufficiently consider the geometry of the sample.

The comparison of  $Nu$  and  $Re$  obtained in the cube and in the cylinder in our DNS are shown in figure 10.1. For clarity, both quantities are reduced by a certain power of  $Ra$ . Deviations between the cube and the cylinder case up to 10% for  $Nu$  and even up to 60% for  $Re$  are found. For small  $Ra$ , the cube case is characterised by larger  $Nu$  and  $Re$ , while for larger  $Ra$  it is vice versa. Nevertheless, the scaling with  $Ra$  is found to be similar for large  $Ra$ . This tendency is also correct for even larger  $Ra$  as it is pointed out in [71]. Further, there is no universal scaling law  $Nu \sim Ra^\alpha$  with constant  $\alpha$  (and for  $Re$  as well) (cf. [155]). This is explained in theory [50] by a change between different regimes. Nevertheless, the steep drop in  $Re$  and  $Nu$  for the cube for  $Ra \approx 10^6$  must be studied in more detail. To do so, in the next subsection the flow structure in



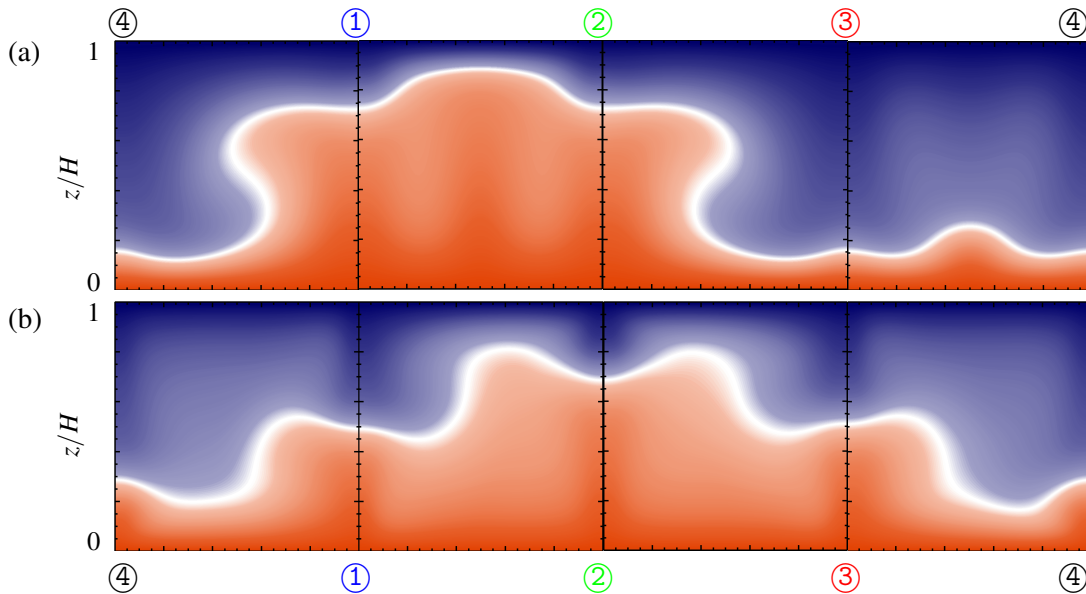


FIGURE 10.2: Time-averaged temperature distribution (red warm, blue cold, white arithmetic mean temperature) on the vertical walls of the cube for (a)  $Ra = 10^5$ , (b)  $Ra = 10^6$  and  $Pr = 0.786$ . The circled numbers mark the corners for the instantaneous analysis.

the cube is further analysed.

### 10.3.2 Flow Structure

As it has been shown previously [155], the structure of the global flow in a cylindrical sample with aspect ratio one is not much influenced by an increase in  $Ra$ . Further, the transition from a stationary equilibrium to an instationary one takes place between  $Ra = 10^5$  and  $Ra = 3 \times 10^5$ . This leads to a steep increase in the reduced Nusselt and Reynolds number (cf. figure 10.1). The latter is also obtained for the cubic sample, but for  $Ra$  around  $10^6$ , both quantities decrease.

To analyse this drop, a method already used for the cylinder [155] is adopted to the cube. When warm fluid is rising close to the vertical wall, this leaves a temperature footprint on the wall, as shown in figure 10.2 for the time-averaged temperature. If the height  $z_0$ , at which the arithmetic mean temperature (of top and bottom plate) is reached, is located close to the top plate, warm fluid is moving upward close to this wall, and if it is located close to the bottom plate, cold fluid is moving downwards. This information is available in instantaneous temperature fields as well. The latter are saved for the whole domain four times per dimensionless time unit  $H/\sqrt{\alpha g \Delta H}$ . For all corners (①:  $x = 0, y = 0$ ), (②:  $x = 0, y = H$ ), (③:  $x = H, y = H$ ), (④:  $x = H, y = 0$ ) the height  $z_0$  is identified in the instantaneous temperature fields. The four time-series  $z_0(t)$  reflect the global flow structure in the cube and its development in time. The time-series, for the  $Ra$ -interval in which the drop in  $Nu$  and  $Re$  appears, are displayed in figure 10.3b,d,f.<sup>1</sup>

<sup>1</sup>It should be noted that for symmetry reasons the corners can be interchanged by rotating and mirroring the domain. This has been done to simplify the comparison between the different  $Ra$ .

## 10 INFLUENCE OF THE SHAPE OF THE DOMAIN

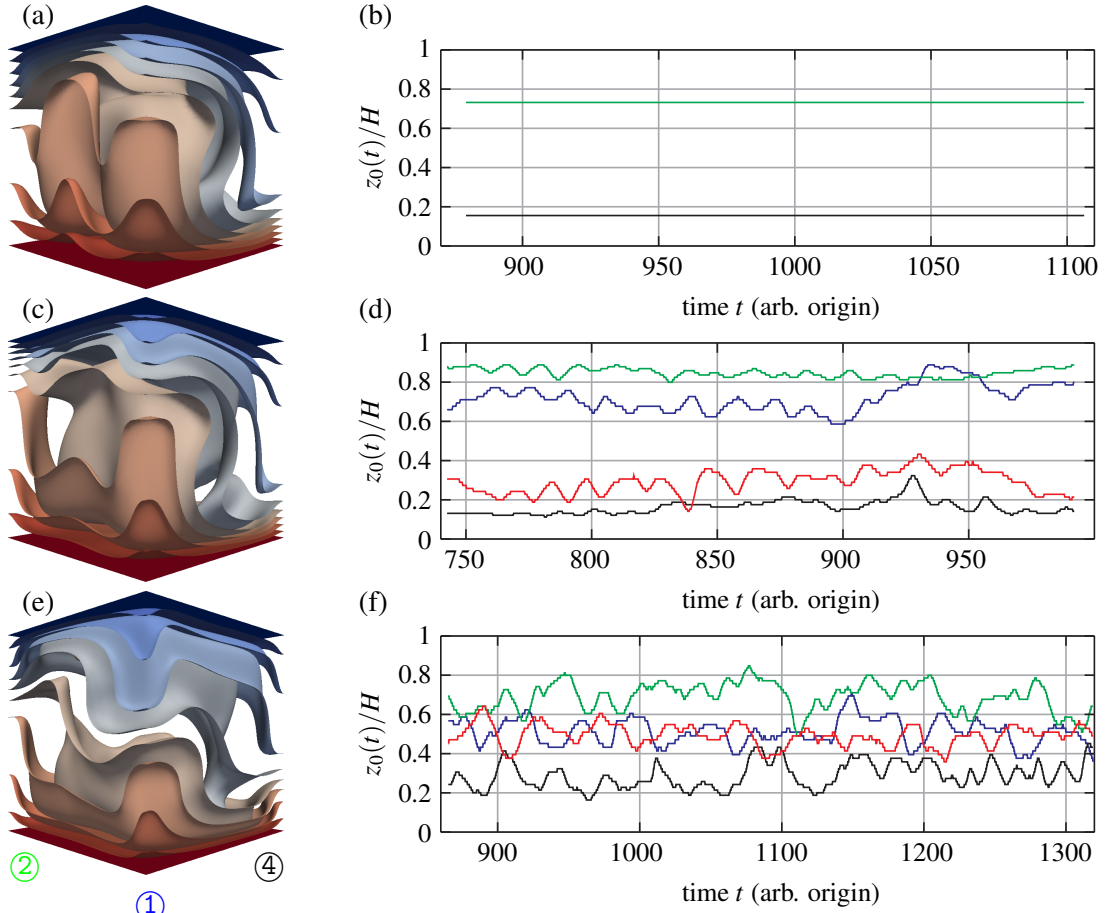


FIGURE 10.3: Isosurfaces of the time-averaged temperature (red warm, blue cold) and corresponding time-histories of the height  $z_0$  as defined in the text (blue: corner ①, green: corner ②, red: corner ③, black: corner ④), for (a),(b)  $Ra = 10^5$ , (c),(d)  $Ra = 3 \times 10^5$  and (e),(f)  $Ra = 10^6$ ,  $Pr = 0.786$ . Note that in figure 10.3b the blue and red lines are not visible because they collapse with the green and black line, respectively.

Additionally, the corresponding isosurfaces of the time-averaged temperature are presented in figure 10.3a,c,e. Both reveal a change in the global flow structure from a flow approximately parallel to the vertical walls ( $Ra = 10^5$ ) to a flow which is organised in a diagonal manner ( $Ra = 10^6$ ). As a consequence, the flow for  $Ra = 10^5$  is rising at the corners ① and ② and between them as figure 10.2a and figure 10.3a reveal. The other limit is reached for  $Ra = 10^6$  for which the warm fluid rises in the corner ② and cold fluid is moving downward in the corner ④ (cf. figure 10.2b and figure 10.3e). In between, for  $Ra = 3 \times 10^5$ , the global flow structure is oriented already slightly diagonal but still shows a large component in direction parallel to the walls.

Of course, this information is not only visible in the temperature field but also, in more detail in the time-averaged velocity field. In figure 10.4, the time-averaged velocity field in the vertical slice at the height of the averaged thickness of the thermal boundary layer  $z_{\text{slice}}/H = (2Nu)^{-1}$

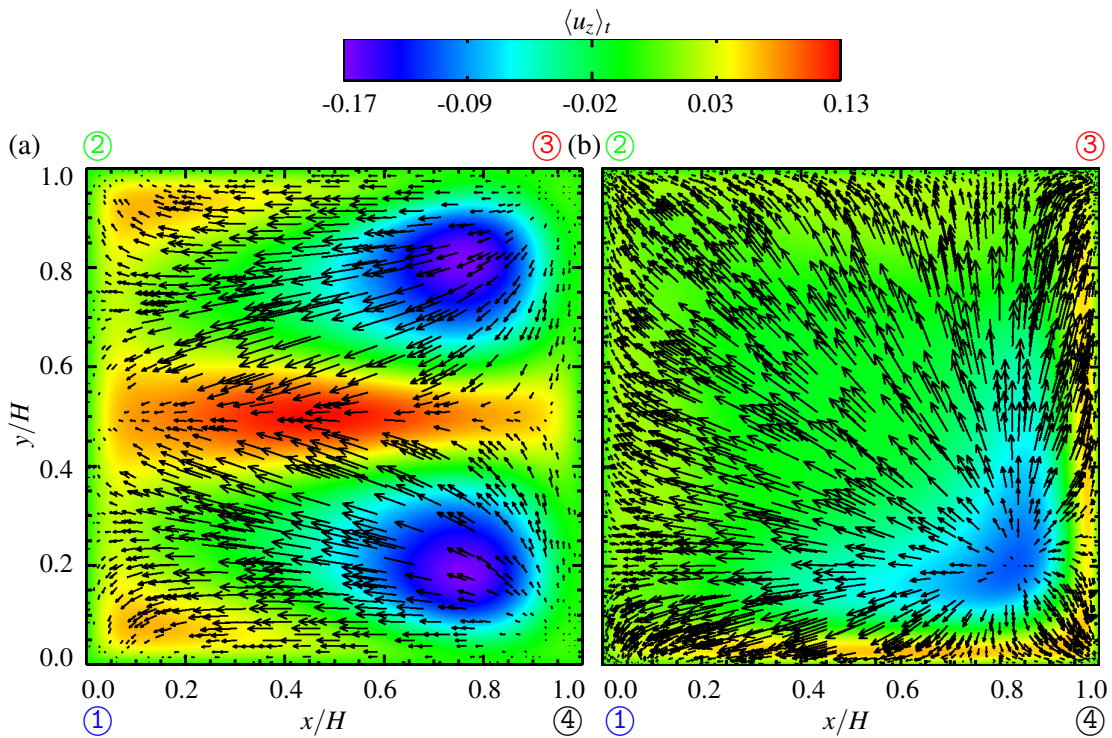


FIGURE 10.4: Horizontal slice at height  $z_{\text{slice}}/H = (2Nu)^{-1}$  of the time-averaged vertical velocity (colour coded) with superimposed velocity vectors within this plane for (a)  $Ra = 10^5$  and (b)  $Ra = 10^6$ ,  $Pr = 0.786$ .

close to the bottom plate is depicted. In colour the magnitude of the vertical velocity is shown, while the superimposed vector-field displays the velocity components within the slice. It becomes obvious that the flow fields are more complicated than it seems from the temperature distribution. For  $Ra = 10^5$ , the flow is mainly pointing from the right to the left (cf. figure 10.4a), while for  $Ra = 10^6$  it is spreading over the whole area but has a dominant diagonal component. This means that the length corresponding to the large scale flow for the diagonal flow is rather  $\sqrt{2}H$  (diagonal of the bottom plate) than simply  $H$ . This leads to an *effective aspect ratio* larger than one, while for the flow parallel to the walls it is one.

The results for a cylindrical sample [8] reveal that  $Nu$  for  $Ra \in [10^7, 10^9]$  is decreasing when the aspect ratio is increased above one. In an experimental study [168] using water (i.e.  $5.18 \leq Pr \leq 7.03$ )  $Nu$  is found to be independent of the aspect ratio larger than one. Since the dependence on the aspect ratio seems to be more pronounced for smaller  $Pr$ , as two-dimensional simulations suggest [97], it can be suggested that the difference in  $Nu$  might be connected to this change in the effective aspect ratio. If in addition, boundary layers of Prandtl-Blasius type are assumed, as is often done for RBC in the considered  $Ra$ -range,  $Nu$  and  $Re$  are related by  $Nu^2 \sim Re$  [121], which makes the drop of  $Re$  reasonable.

For the physical mechanism behind the decrease in  $Re$ , we find the following possible explanation: When the global flow is changing to a diagonal structure, the warm fluid rises in the

corner of the cube. There, the fluid is slowed down by the action of viscous forces present in the boundary layers at two sidewalls.<sup>2</sup> Contrary, for the cylindrical sample and for the global flow in the cube with a structure parallel to the walls, the warm fluid is rising mainly close to one wall, which might lead to a higher  $Re$ . To separate the effect of different effective aspect ratios from the influence of corner effects, further simulations are required.

## 10.4 Summary

DNS of RBC have been performed in a cylindrical container with equal height and diameter and in a cubic container, for  $Pr = 0.786$  and  $Ra \in [10^5, 10^7]$ . The main responses of the system, motion and heat flux, expressed by  $Nu$  and  $Re$  have been evaluated and compared. Large differences between the two geometries in absolute values as well as in their scaling with  $Ra$  have been found. Most interesting is a drop of  $Nu$  and  $Re$  around  $Ra = 10^6$  in case of the cube. While both quantities are larger for the cube for  $Ra = 10^5$ , it is vice versa for  $Ra = 10^7$ . This drop seems to correspond to a change in the global flow structure in the cube, which does not occur in case of the cylinder. The main feature of the cubic geometry in the contrast to the cylindrical one is the presence of two characteristic lengths, namely the side length and the length of the diagonal of the plates. While for smaller  $Ra$  the flow is organized parallel to the vertical walls, it is organized in a diagonal manner for larger  $Ra$ .

It is further found that the scaling of  $Nu$  and  $Re$  is similar for larger  $Ra$ , eventhough the absolute values differ. This remaining difference might be caused by the arbitrary choice of geometries, and in particular the choice of the cube's aspect ratio. For large  $Ra$  rather the diagonal of the cube's bottom plate is characteristic for the flow. Thus, for future studies a comparison of a cylinder and a box-shaped container, with equal effective aspect ratio based on this characteristic length, seems reasonable.

The authors would like to thank Matthias Kaczorowski and Tomasz Czarnota for updating the computational code in Cartesian coordinates and acknowledge support by the Deutsche Forschungsgemeinschaft (DFG) under grant SH405/3-1.

---

<sup>2</sup>In the original paper it was argued here, that "This means that the viscous boundary layers close to two walls are dissipating kinetic energy of the rising fluid." This argument was not completely correct, as in the Oberbeck-Boussinesq approximation the process of dissipation of kinetic energy and its regain as thermal energy is not fully covered. This goes back to one of the basic assumptions of the Oberbeck–Boussinesq approximation, namely that of a small Eckert number [113].

# 11 Aspect-ratio dependency for box-shaped containers

**Citation and credit:** This chapter consists of a paper published in *Physics of Fluids* 25, 085110, 8 August 2013. This is an author-prepared version of the article, which is posted here by permission of AIP Publishing LLC and is available online at <http://dx.doi.org/10.1063/1.4819141>.  
©2013 AIP Publishing LLC

**Title:** Aspect-ratio dependency of Rayleigh–Bénard convection in box-shaped containers

**Authors:** Sebastian Wagner & Olga Shishkina [152]

**Contribution:** I performed and evaluated the numerical simulations, developed the analysis techniques for box-shaped containers, prepared all the figures and wrote the first version of the manuscript, which structure is preserved.

**Note:** Some preliminary results published in this paper were submitted as a conference proceeding [153] for the conference “Direct and large-eddy simulation (DLES) 9” in April 2013. It was accepted after revision for publication in the book “Direct and large-eddy simulation IX” of the Springer series “ERCOFTAC” in September 2013.

## Abstract

We report on a numerical study of the aspect-ratio dependency of Rayleigh–Bénard convection, using direct numerical simulations. The investigated domains have equal height and width while the aspect ratio  $\Gamma$  of depth per height is varied between 1/10 and 1. The Rayleigh numbers  $Ra$  for this study variate between  $10^5$  and  $10^9$ , while the Prandtl number is  $Pr = 0.786$ . The main focus of the study concerns the dependency of the Nusselt number  $Nu$  and the Reynolds number  $Re$  on  $Ra$  and  $\Gamma$ . It turns out that due to  $\Gamma$ , differences to the cubic case (i.e.,  $\Gamma = 1$ ) in  $Nu$  of up to 55% and in  $Re$  of up to 97% occur, which decrease for increasing  $Ra$ . In particular for small  $\Gamma$  sudden drops in the  $Ra$ -scaling of  $Nu$  and  $Re$  appear for  $Ra \approx 10^6$ . Further analysis reveals that these correspond to the onset of unsteady motion accompanied by changes in the global

flow structure. The latter is investigated by statistical analysis of the heat flux distribution on the bottom and top plates and a decomposition of the instantaneous flow fields into two-dimensional modes. For  $Ra$  slightly above the onset of unsteady motion (i.e.,  $Ra \approx 10^6$ ) for all considered  $\Gamma \leq 1/3$  a four-roll structure is present, which corresponds to thermal plumes moving vertically through the domain's center. For  $Ra \geq 10^7$ , also for small  $\Gamma$ , a single-roll structure is dominant, in agreement with two-dimensional simulations and experiments at larger  $Ra$  and  $Pr$ .

## 11.1 Introduction

A fluid confined between a heated bottom and cooled top plate at rest reacts on the temperature gradient parallel to gravitational acceleration by the onset of motion and the occurrence of an increased heat flux in comparison to a solid body, if this temperature gradient is large enough. This phenomenon is known as Rayleigh-Bénard convection (RBC). As a model system for many convective flow problems occurring in nature and technology, RBC has been studied for more than a century [5, 32, 84]. In the last decade the scaling of motion, i.e. Reynolds number  $Re$ , and heat flux, i.e. Nusselt number  $Nu$ , with the two non-dimensional parameters Rayleigh number  $Ra$  and Prandtl number  $Pr$  has been investigated extensively in experiments, numerical simulations and theory. The influence of the geometry as an additional parameter is thereby less good understood.

Generally the geometry can be expressed by an aspect ratio as the ratio of the container's horizontal extend and its height. The studies of this aspect ratio's influence can be separated in two parts: for aspect ratios (much) larger than one and those smaller than one. From experiments with water it was obtained that for the large aspect ratio case  $Nu$  slightly decreases with increasing aspect ratio until a saturation takes place at about aspect ratio five [5, 46]. In Direct Numerical Simulations (DNS) of convection in air a non-monotonic dependency was found [8]. It is connected to the existence of multiple horizontally aligned convection rolls. The number of rolls is thereby determined by the aspect ratio and influences  $Nu$ . For small aspect ratio the situation is similar, but here the rolls are vertically stacked. The number of rolls influences  $Nu$ . States with different amount of rolls can coexist and the way of their mixing depends on  $Ra$  [159, 163]. In particular two-dimensional (2D) simulations reveal, that the change between the different states happens quite rapidly [97, 98]. Theoretical approaches modeling the influence of the aspect ratio are quite limited [34, 53] and none of the theories describing the scaling of  $Nu$  with  $Ra$  and  $Pr$  includes the aspect ratio or any further description of the geometry, so far [50, 65, 128].

In case of  $Re$  the geometry influence is even less studied. For the two-dimensional steady case, an increase of  $Re$  with the aspect ratio is obtained, while the scaling of  $Re$  with  $Ra$  is unchanged [34].

In the present study we investigate RBC by means of three-dimensional (3D) DNS for  $Pr = 0.786$  and  $Ra$  between  $10^5$  and  $10^9$ . To exclude the effect of multiple convection rolls,

we leave the height and width of the container equal, while the depth is decreased. The latter configuration, i.e. a box with equal height and width but a rather short depth, is motivated by a series of experimental studies using e.g. two-dimensional particle image velocimetry [167, 172, 174]. The flow in such a domain is thereby assumed to be quasi two-dimensional, which justifies the two-dimensional measurements. The nearby walls confine the large-scale flow and thus suppress horizontal reorientations, which occur for example in cylindrical domains [19]. This advantage simplifies also the analysis of the numerical data. Since DNS are feasible only for rather small  $Ra$ , due to high computational effort [121], a larger influence of the nearby walls than in the experiments at higher  $Ra$  is expected, which might lead to a strong geometry dependency. Instead of using such a quasi two-dimensional domain, it would be possible to perform 2D DNS. Since for small  $Pr$  differences between 2D and 3D DNS results exist even for integral quantities like  $Nu$  and  $Re$  [114], 3D DNS are required in particular for quantitative studies.

Besides the scaling of  $Nu$  and  $Re$  with  $Ra$  and the aspect ratio, we analyze the geometry's influence on the global flow structure by means of a mode decomposition. The latter one has been already applied to 2D DNS in order to study flow reversals [28, 29]. Special emphasis is set on aspect ratio (depth/height) one fourth, since it was used in many above mentioned experiments.

The paper is organized as follows. In section 11.2 we describe the numerical method and give the simulation parameters. The integral system responses, i.e.  $Nu$  and  $Re$  and their dependences on  $Ra$  and the aspect ratio of the domain are discussed in section 11.3 together with a statistical analysis of related local quantities like the distribution of kinetic energy and local heat flux in section 11.4. To understand the aspect ratio dependence of  $Nu$  and  $Re$  we analyze in section 11.5 the dynamics of the flow and the global flow structure. This is accompanied by a comparison with results obtained in a cylinder with equal diameter and height and an outlook to larger  $Ra$  up to  $10^9$  in section 11.6. The paper is closed by a summary in section 11.7.

## 11.2 Numerical Method and Simulation Parameters

A fourth order accurate finite volume method [120] working in box-shaped domains is used to solve the equations describing the conservation of mass, momentum and energy in Oberbeck-Boussinesq approximation. They read in non-dimensional form

$$\begin{aligned} \frac{\partial \vec{u}}{\partial t} + \vec{u} \cdot \vec{\nabla} \vec{u} &= -\vec{\nabla} p + \sqrt{\frac{Pr}{Ra}} \vec{\nabla}^2 \vec{u} + T \vec{e}_z, \\ \frac{\partial T}{\partial t} + \vec{u} \cdot \vec{\nabla} T &= \sqrt{\frac{1}{PrRa}} \vec{\nabla}^2 T, \quad \vec{\nabla} \cdot \vec{u} = 0, \end{aligned}$$

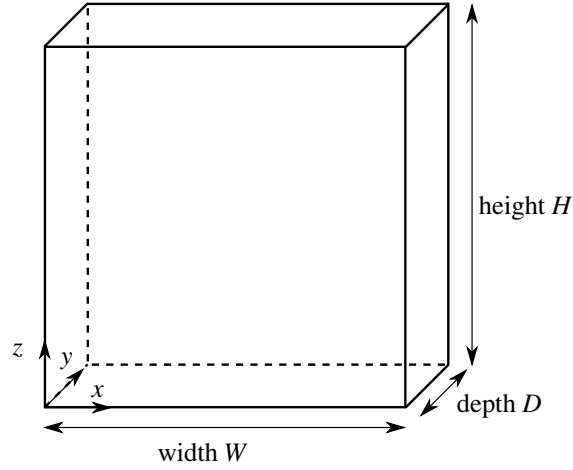


FIGURE 11.1: Sketch of the computational domain with nomenclature and coordinate system.

where  $\vec{u}$  is the velocity,  $p$  is the pressure,  $T$  is the temperature and  $\vec{e}_z$  is the unit vector in vertical direction. The dimensionless parameters characterizing the fluid and the sample are the Rayleigh number  $Ra = \hat{\alpha}\hat{g}\hat{\Delta}\hat{H}^3/(\hat{\nu}\hat{\kappa})$  and the Prandtl number  $Pr = \hat{\nu}/\hat{\kappa}$ . For non-dimensionalization the free-fall velocity  $\sqrt{\hat{\alpha}\hat{\Delta}\hat{g}\hat{H}}$  and the height of the container  $\hat{H}$  are used, while their ratio is the reference for time, i.e.  $\hat{t}_{\text{ref}} = \sqrt{\hat{H}/(\hat{\alpha}\hat{g}\hat{\Delta})}$ . The temperature is made dimensionless by  $T = (\hat{T} - \hat{T}_M)/\hat{\Delta}$  with  $\hat{\Delta} = \hat{T}_{\text{bottom}} - \hat{T}_{\text{top}}$  and  $\hat{T}_M = (\hat{T}_{\text{bottom}} + \hat{T}_{\text{top}})/2$ . Here, the hat denotes dimensional quantities and  $\hat{\nu}$  is the kinematic viscosity,  $\hat{\kappa}$  the thermal diffusivity,  $\hat{\alpha}$  the isobaric thermal expansion coefficient and  $\hat{g}$  the gravitational acceleration. The simulations are initialized by a fluid at rest and a linear temperature gradient superposed by a small disturbance to accelerate the onset of convection.

No-slip and impermeability conditions are set on all walls, the vertical walls are adiabatic and the bottom and top plates isothermal with  $\hat{T}_{\text{bottom}} > \hat{T}_{\text{top}}$ . The width  $\hat{W}$  of the domain is chosen equal to the height  $\hat{H}$  and the aspect ratio ratio  $\Gamma = \text{depth}/\text{height} = \hat{D}/\hat{H}$  is varied between 1/10 and 1 (cf. figure 11.1).

The Rayleigh number is varied between  $10^5$  and  $10^9$ , while the Prandtl number is kept constant at  $Pr = 0.786$ . In the appendix in table 11.1 these and further simulation parameter like the spatial resolution are collected. The latter has been chosen according to Shishkina *et al.* [121] to fulfill the resolution requirements for a DNS. Since this estimate for the resolution inhibits assumptions on the boundary layer structure, the spatial resolution close to the walls has been further increased and was checked a posteriori by using time-averaged kinetic dissipation rates.

Besides time-averaged fields also instantaneous fields have been collected with a sampling frequency of four per time-unit. This allows a posteriori analysis of the flow fields [155]. In particular for small  $Ra$  up to  $Ra \approx 10^7$ , the sampling rate is large enough to resolve even Kolmogorov time-scales  $\hat{\eta}_t = (\hat{\nu}/\hat{\epsilon}_u)^{1/2}$ , with the kinetic dissipation rate  $\hat{\epsilon}_u$ . For the latter the



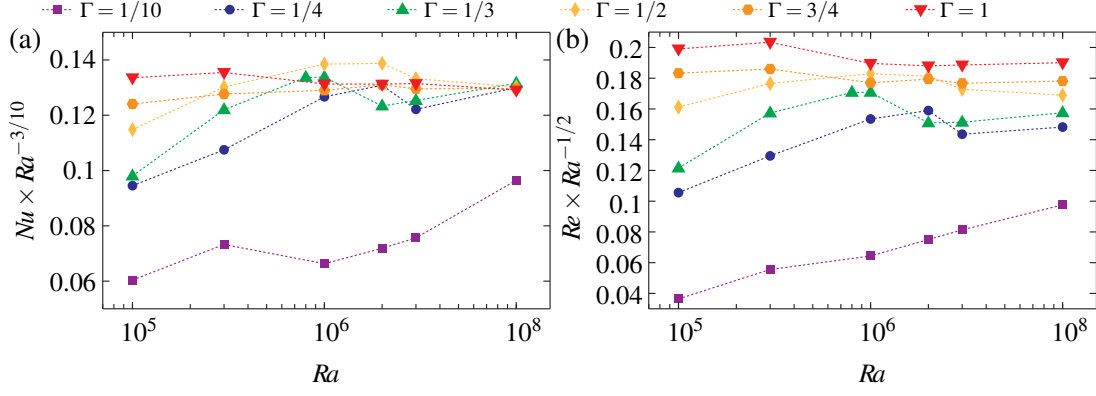


FIGURE 11.2: Reduced  $Nu$  vs.  $Ra$  (a) and reduced  $Re$  vs.  $Ra$  (b) for different  $\Gamma = \text{depth/height}$ ,  $Pr = 0.786$ .

analytical relation  $\langle \hat{\varepsilon}_u \rangle_{t,x,y,z} = \hat{H}^{-4} \hat{v}^3 (Nu - 1) Ra Pr^{-2}$  holds, where  $\langle \cdot \rangle_\phi$  denotes an average with respect to  $\phi$  and  $Nu$  is the dimensionless heat flux as defined in the next section. Thus it follows for the ratio of  $\hat{\eta}_t$  and the time unit  $\hat{t}_{\text{ref}}$ , that  $\hat{\eta}_t / \hat{t}_{\text{ref}} = \sqrt{Pr / (Nu - 1)} \gtrsim 1/4$  for  $Ra \leq 10^7$  and  $Pr = 0.786$ . For larger  $Ra$  this sampling is still sufficient, since the main interest of the analysis lies in large-scale properties which take place on time-scales much larger than  $\hat{\eta}_t$ .

### 11.3 Main system responses

Motion and increased heat flux characterize thermal convection. The motion can be expressed by the Reynolds number  $Re = \sqrt{Ra/Pr} U$  based on the height of the container and on the velocity  $U = \sqrt{\langle \bar{u}^2 \rangle_{x,y,z,t}}$ . Of course other choices of the velocity are possible. This particular choice has on the one hand the advantage, that it does not require analysis of the flow structure, while on the other hand the comparison with experiments is difficult, since the velocity magnitude can be hardly measured in the whole domain at an instant. In the next section we will compare this choice of the velocity with two other possibilities.

The dimensionless heat flux is set in relation to the heat flux of a solid body with the same thermal diffusivity  $\hat{\kappa}$  by the Nusselt number  $Nu = \langle \sqrt{Ra Pr} u_z T - \partial_z T \rangle_{x,y,t}$ . Here  $\partial_z$  denotes the partial derivative with respect to  $z$ . For the chosen set of boundary conditions it can be derived analytically that  $Nu$  is independent of  $z$  for infinitely long averaging time. Thus the deviation of  $Nu$  in vertical direction can be used as a measure for statistical convergence of the results. The largest deviation from the mean value  $\langle Nu \rangle_z$  is given for all unsteady simulations in table 11.1 (in the appendix) together with  $Nu$  and  $Re$  and the averaging time for the unsteady simulations.

The scalings of these quantities with  $Ra$  and the influence of the aspect ratio  $\Gamma$  are studied in the following. To highlight the differences in the scaling of  $Re$  and  $Nu$  with  $Ra$ , they are presented in a reduced form, i.e.  $Nu Ra^{-3/10}$  and  $Re Ra^{-1/2}$ , respectively.

Figure 11.2, which shows the  $Ra$ -scaling for different  $\Gamma$ , reveals the following: First, for the

## 11 ASPECT-RATIO DEPENDENCY FOR BOX-SHAPED CONTAINERS

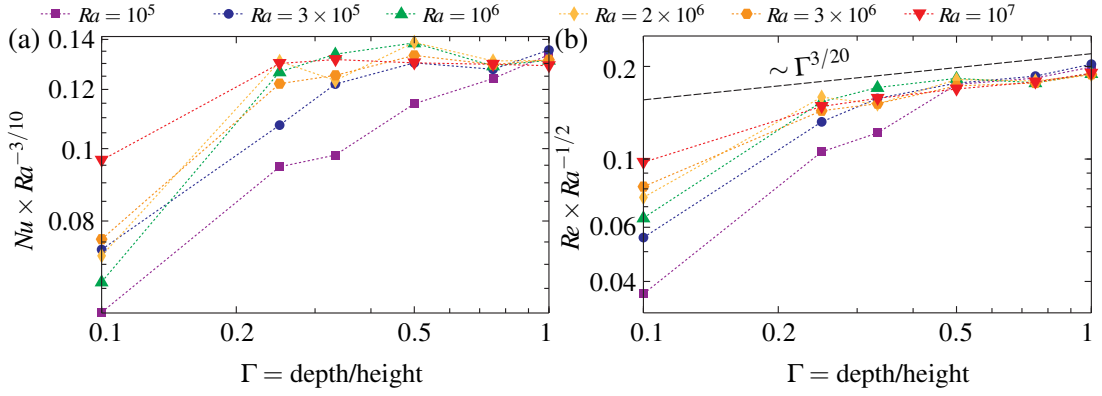


FIGURE 11.3: Reduced  $Nu$  vs.  $\Gamma$  (a) and reduced  $Re$  vs.  $\Gamma$  (b) for different  $Ra$  on a double logarithmic scale,  $Pr = 0.786$ .

constant  $Ra$  differences to the case  $\Gamma = 1$  in  $Nu$  of up to 55% and in  $Re$  of up to 96% are obtained. These large differences occur for small  $Ra$  and decrease with increasing  $Ra$ . For  $Ra = 10^7$   $Nu$  becomes  $\Gamma$ -independent if  $\Gamma \geq 1/4$ . For  $Re$  the differences remain even for large  $Ra$  but the scaling with  $Ra$  becomes similar for all  $\Gamma \geq 1/4$ . In between those two extreme cases, for  $Ra$  around  $10^6$ , a non-monotonic  $\Gamma$ -dependence is found for  $Nu$  and  $Re$ . It is accompanied by sudden drops in  $Nu$  and  $Re$  for certain  $Ra$ . Such drops seem to be special for this box-shaped domains, as they are for example not present in cylindrical domains with equal diameter and height [155]. Since the drops take place within a third of a decade, they differ from the changes in the scaling obtained in cylindrical domains. The latter are due to changes between different flow regimes [50] and take place over several decades in  $Ra$  (see also section 11.6). The rapid changes in  $Nu$  are known from 2D DNS with small aspect ratio and are explained by changes in the flow structures, which take place at certain  $Ra$  [97, 98]. There the flow organizes in a set of vertically stacked rolls, which number depends on  $Ra$  and the aspect ratio. Vertically stacked rolls are not expected for the present three-dimensional domains, but similar changes between different flow states might cause the rapid changes in  $Nu$  and  $Re$ . Therefore the global flow structures and related flow characteristics are studied in the next sections.

To understand the  $\Gamma$ -influence in more detail and to figure out, whether a fundamental scaling law with  $\Gamma$  exists, in figure 11.3 the reduced  $Nu$  and  $Re$  are plotted against  $\Gamma$  on a double logarithmic scale. In case of  $Re$  a  $Ra$ -independent  $\Gamma$ -dependence is found as soon as a critical aspect ratio  $\Gamma_C$  is reached. Thereby  $\Gamma_C$  grows with decreasing  $Ra$ , e.g.  $\Gamma_C \approx 1/4$  for  $Ra = 10^7$ , while  $\Gamma_C \approx 1/2$  for  $Ra = 10^5$ . Above  $\Gamma_C$  the reduced  $Re$  collapse for all  $Ra$  and shows a weak  $\Gamma$  dependence of about  $Re \sim \Gamma^{3/20}$  (indicated by a dashed line in figure 11.3(b)).

For  $Nu$  the situation is more complicated (c.f. figure 11.3(a)). Similar to the case of  $Re$  the differences between the graphs for different  $Ra$  become quite small above a critical  $\Gamma'_C$ . This  $\Gamma'_C$  seems to be slightly larger than  $\Gamma_C$  in case of  $Re$ . Nevertheless the graphs for different  $Ra$  agree

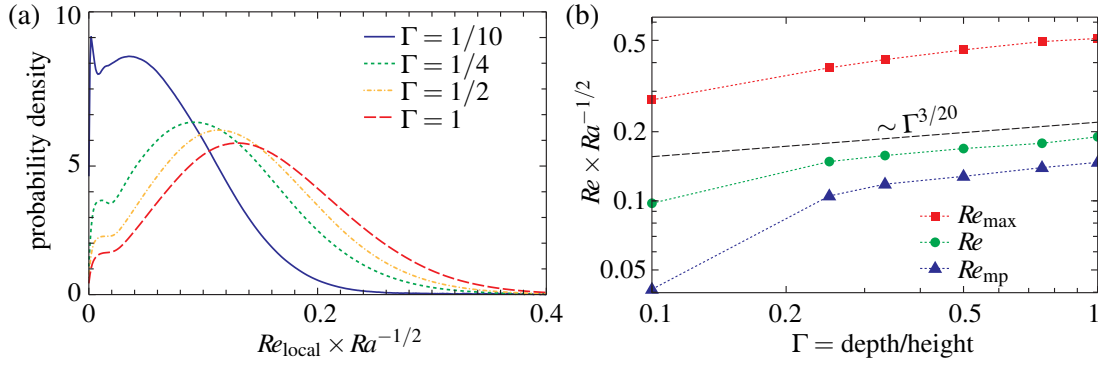


FIGURE 11.4: (a) Time-averaged probability density function of  $Re_{local}$  for different  $\Gamma$  and (b)  $\Gamma$ -scaling of the Reynolds number based on different velocities as defined in the text,  $Ra = 10^7$ ,  $Pr = 0.786$ .

not as good as in case of  $Re$ , which might be connected to the fact  $\Gamma'_C > \Gamma_C$ . Roughly one might conclude that above  $\Gamma'_C$   $Nu$  depends only weakly on  $\Gamma$ .

## 11.4 Statistical analysis

In order to highlight further the differences but also similarities of different aspect ratio cases, we perform a statistical analysis of some quantities, which are closely related to  $Nu$  and  $Re$ . Thereby we use a large amount of instantaneous flow fields as described in section 11.2.

For detailed information about the velocity field, i.e.  $Re$ , we evaluate the local instantaneous velocity magnitude in the whole domain, which can be expressed as a local Reynolds number  $Re_{local} = \sqrt{Ra/Pr} |\vec{u}|$ . The time-averaged probability density functions (p.d.f.) of the latter quantity for different  $\Gamma$  and  $Ra = 10^7$  are depicted in figure 11.4(a). For all different  $\Gamma$  the structure of the p.d.f. is thereby similar: it consists of two parts, a strongly  $\Gamma$ -dependent part for low velocities which we relate to the processes in the viscous boundary layer (BL) and for larger velocities a part with a Gaussian shape, which is associated with the bulk flow. This second part is for  $\Gamma \geq 1/4$  only weakly  $\Gamma$ -dependent. With increasing  $\Gamma$  the tails of this part of the distribution are slightly shifted to larger velocities. This is in good agreement with the tendency that was observed for  $Re$  in figure 11.3(b). In particular if the most probable  $Re_{local}$ , called  $Re_{mp}$ , is compared to  $Re$  the similarities become obvious as shown in figure 11.4(b). Note that in the case of  $\Gamma = 1/10$  the local maximum of the Gaussian-like part is considered and not the peak close to  $Re_{local} = 0$ . For completeness also the Reynolds number based on the maximal vertical velocity  $Re_{max} = \sqrt{Ra/Pr} \langle \max(|u_z|) \rangle_t$  is added to this graph. We find that  $Re_{max} \approx 2.7Re$  and  $Re_{mp} \approx 0.76Re$  for  $\Gamma \geq 1/4$ . As already observed in figure 11.3(b), a scaling of about  $Re \sim \Gamma^{3/20}$  is obtained. This is a quite weak dependence, which is surprising. Since  $Re$  is calculated as a volume-integral, it includes also the viscous BLs with rather small velocity magnitudes. In a

domain with smaller  $\Gamma$  the contribution of the BLs to the total volume is expected to be larger in comparison with a larger  $\Gamma$  (for fixed  $Ra$  and  $Pr$ ). For geometrical reasons this would lead to a stronger  $\Gamma$ -dependence, which is not obtained. Since also  $Re_{\max}$  scales in a similar way, the reason for this cannot only be a decreased BL thickness for small  $\Gamma$ , which would be related to a larger  $Re_{\max}$  as a characteristic velocity of the large scale flow. This issue is further addressed in section 11.4 by an analysis of the global flow structure.

To quantify the variability of the turbulence in dependence of the aspect ratio  $\Gamma$ , we consider profiles of the velocity and temperature fluctuations in  $y$  direction, as depicted in figure 11.5. Several observations can be made: First, the difference between  $\Gamma = 1/10$  and larger  $\Gamma$ , as discussed above, is also visible in the fluctuations of  $T$ ,  $u_x$ ,  $u_z$ . While for  $\Gamma \geq 1/4$  the mentioned fluctuations are very similar in the bulk region  $0.3 \leq y/D \leq 0.5$ , the case  $\Gamma = 1/10$  shows larger temperature and smaller velocity fluctuations. Further, in the case of  $u_z$  the profiles of the fluctuations have a local maximum in the vicinity of the wall at  $y = 0$  only for  $\Gamma \geq 1/4$ . The distance from the wall of the local maximum is considered as the thickness of the viscous BL. Thus the non-existence of the maximum in case of  $\Gamma = 1/10$  can be interpreted as a merging of the BLs attached to the walls at  $y = 0$  and  $y = D$ . The temperature fluctuations reflect a similar effect, since they are much more homogeneous for  $\Gamma = 1/10$  than for larger  $\Gamma$ . The strongest influence of the aspect ratio can be observed for the fluctuations of  $u_y$ . There an decreased aspect ratio leads to smaller fluctuations in the bulk region and thus a suppression of the turbulent motion as a three-dimensional phenomenon. The suppression of motion in  $y$ -direction can be also interpreted as a change in the global flow structure to a quasi 2D one for small  $\Gamma$ . This issue is discussed in the next section.

Before that, we study the  $\Gamma$ -dependence of  $Nu$  by a statistical analysis similar to the one for  $Re_{\text{local}}$ . We evaluate the local heat flux on the bottom and top plates  $\Omega_z = -\partial_z T$  from instantaneous flow fields and depict the results as time-averaged p.d.f.s for  $Ra = 10^7$  (cf. figure 11.6). First of all the similarity of all the p.d.f.s except of the one for  $\Gamma = 1/10$  becomes obvious. This is in good agreement with the fact that  $Nu$ , i.e. the first moment of the p.d.f., is almost  $\Gamma$ -independent for  $\Gamma \geq 1/4$  as shown in figure 11.2(a). In particular those p.d.f.s collapse at two points ( $\Omega_z \approx 7$  and  $\Omega_z \approx 22$ ). This is also correct for the other investigated  $\Gamma$ , which are omitted in the plot for clarity. Furthermore, the spread of the p.d.f.-tails is larger for small  $\Gamma$ , which means, that for small  $\Gamma$  extremely low/high heat fluxes are more probable compared to the larger  $\Gamma$  cases. This might be again connected to the global flow structure, since large  $\Omega_z$  appear where hot/cold plumes penetrate the top/bottom boundary layers. The localization of regions where the appearance of such plumes is very probable depends on the global flow structure, which might depend on  $\Gamma$ .

To investigate, where large  $\Omega_z$  appear at the plates, we extract the positions at the top/bottom plates, where the maxima of the instantaneous  $\Omega_z$  are achieved. These positions for the whole time series are depicted in figure 11.7 as a two-dimensional histogram. Black means a high

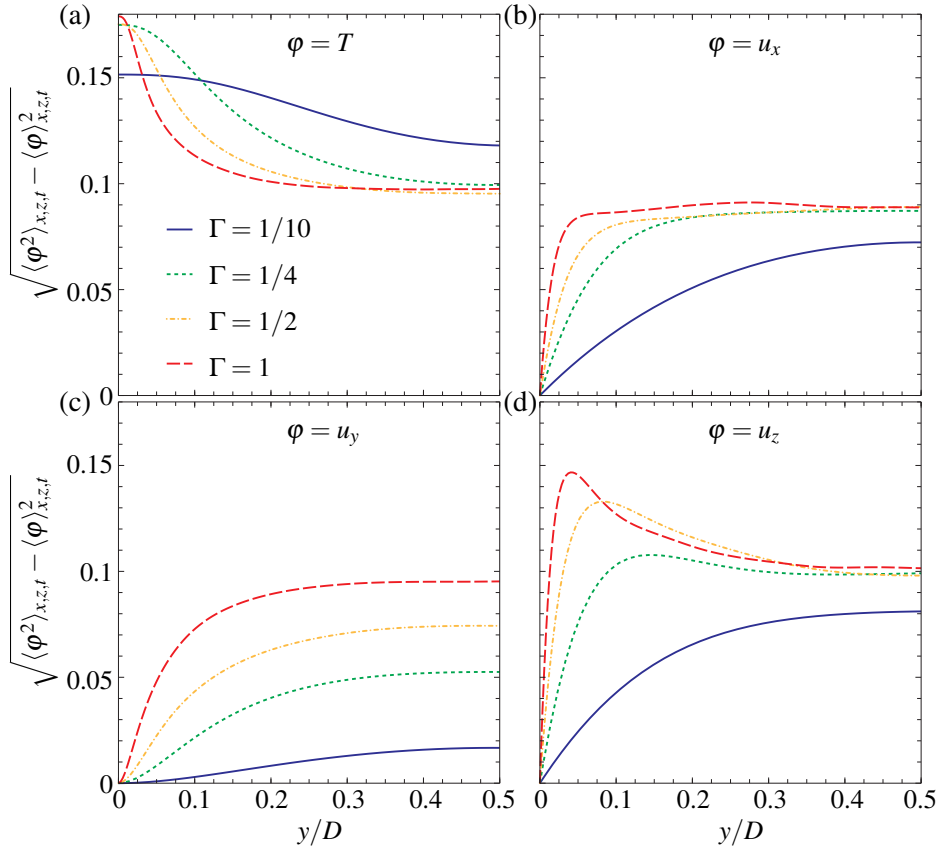


FIGURE 11.5: Horizontal fluctuation profiles of (a) the temperature  $T$  and (b),(c),(d) the velocity components  $u_x$ ,  $u_y$ ,  $u_z$ , respectively, in dependence of the aspect ratio  $\Gamma$  for  $Ra = 10^7$ ,  $Pr = 0.786$ .

probability and white a low one. For symmetry reasons the results for the whole plates are collapsed on one fourth of the plate (c.f. the axis labeling). Note that the histograms look noisy since the very fine computational meshes are used for binning. From figures 11.7(a),(b) it becomes obvious that for small  $\Gamma$  the largest  $\Omega_z$  occurs mainly at the center of the plate, i.e. the upper right corner in the plots. For large  $\Gamma$ , it occurs apart from the center and rather close to the lateral walls, i.e. close to the lower and left edges of figures 11.7(c),(d).

In the following we want to discuss shortly, why larger  $\Omega_z$  are obtained for thermal plume movement through the center of the domain (case I, figure 11.8(a)) compared to the plumes movement along the vertical walls (case II, figure 11.8(b)). In the former case, the plumes hit the horizontal wall almost at a right angle. If the plumes move along the sidewall (case II) they detach due to secondary roll structures appearing in the corners. See also the experimental visualizations by Xi *et al.* [161]. Due to the solid walls the plumes are decelerated when approaching the plate. How deep the cold plume can penetrate the warm boundary layer depends on the vertical component of the plumes' momentum. Since the driving of the plumes is

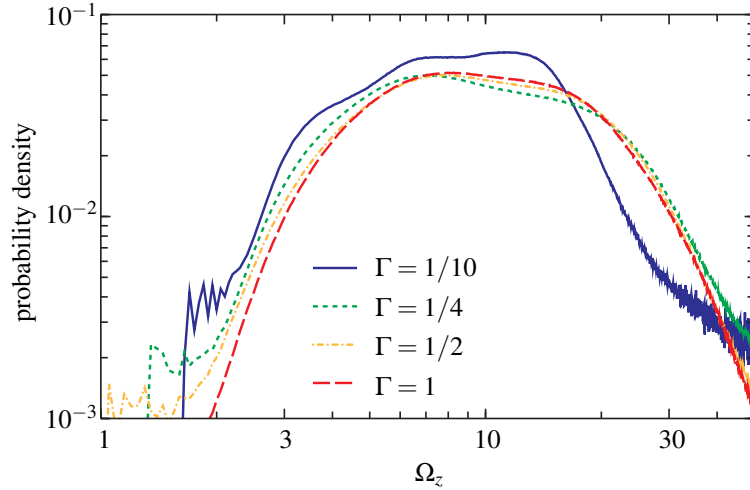


FIGURE 11.6: Time-averaged probability density function of the local instantaneous heat flux on the bottom and top plates  $\Omega_z$  for different  $\Gamma$  and  $Ra = 10^7$ ,  $Pr = 0.786$ .

determined by  $Ra$ , which is kept constant in this argumentation, we can assume that the size of the vertical component of the momentum depends only on the angle between the plume-velocity and the horizontal plate. In case I it is by the above argumentation larger than in case II, and therefore a larger  $\Omega_z$  is more probable if the plumes move through the domain's center.

Since for  $\Gamma \geq 1/4$  the first moment of the p.d.f.s, i.e.  $Nu$ , is independent of  $\Gamma$ , the large  $\Omega_z$  occurring for small  $\Gamma$  need to be accompanied by smaller ones, which thus leads to a larger spreading of the p.d.f.-tails in this case.

For all  $\Gamma$  it is observed that the largest  $\Omega_z$  does not occur closer than about  $H/10$  to the sidewall. This fits also to the argumentation, stating that if plumes fall/rise close to the vertical walls, they detach from the wall and cannot reach the bottom plate close to it. This is obtained also in cylindrical domains, where the largest mean heat flux at the heating plate is obtained at about  $0.9R$ , where  $R$  is the radius of the domain [155]. Further studies show that apart from the horizontal plates, the largest heat flux is also located close to but directly at the vertical walls [80, 124].

## 11.5 Global flow structure and dynamics

In the the present section we give insight in the global flow structure and the dynamics of the flow. Since in RBC in many cases slow transients exist, e.g. flow reversals or reorientations [19], it is insufficient to study time-averaged flow fields. In particular the mentioned slow processes occur on time-scales which are of the order of the simulated time [139]. Thus an analysis of instantaneous fields is required, which inhibits the information about the slow transients and offers the opportunity to separate them from the faster ones [155]. Here the main focus of the

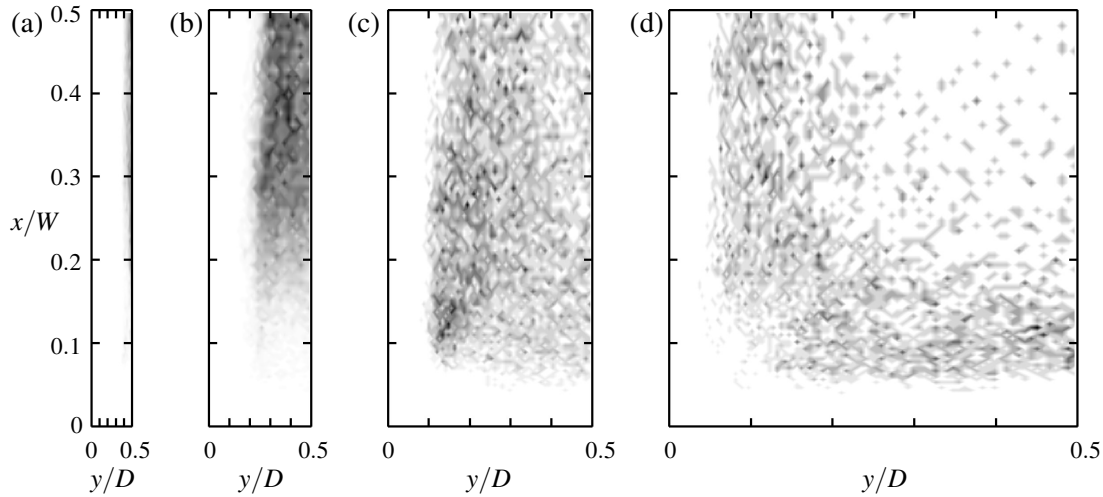


FIGURE 11.7: Histogram of the localization on the bottom/top plate of  $\max(\Omega_z)$  at an instant for (a)  $\Gamma = 1/10$ , (b)  $\Gamma = 1/4$ , (c)  $\Gamma = 1/2$ , (d)  $\Gamma = 1$ . Black corresponds to a large probability and white to small one. For symmetry reasons the plots are reduced to the distribution within one fourth of the bottom plate.  $Ra = 10^7$ ,  $Pr = 0.786$ .

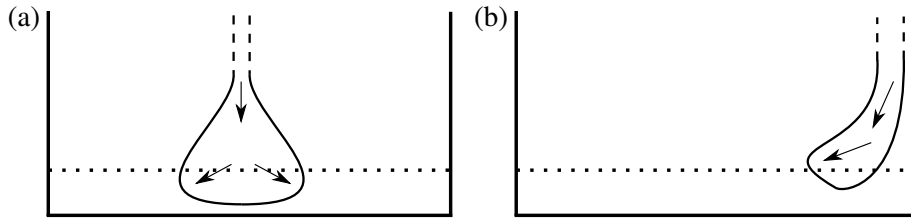


FIGURE 11.8: Sketches of cold thermal plumes arriving at the hot boundary layer (indicated by the horizontal dotted line), which is attached to the heating plate. (a) The thermal plume falls almost vertically in the domain's center, penetrates the boundary layer, which leads to a large local heat flux  $\Omega_z$  at the center of the plate (case I). (b) The thermal plume falls near the vertical wall, detaches to avoid the corner, which leads to a large  $\Omega_z$  close to but not directly at the vertical wall (case II).

study is set on the small  $\Gamma$  cases, to investigate the differences between them and to explain the rapid changes which occur in the  $Ra$ -scalings of  $Nu$  and  $Re$ . Furthermore, for  $Ra = 10^7$  differences between  $\Gamma = 1/10$  and all larger  $\Gamma$  cases are present. This requires further analysis, which is feasible by using instantaneous flow fields. Since the results strongly depend on whether the flow is steady or unsteady, we first discuss the equilibrium state of the flow.

### 11.5.1 Onset of unsteady motion

If a critical  $Ra_C$  is reached, RBC becomes unsteady and for larger  $Ra$  even chaotic or turbulent. The onset of this unsteady motion has been studied widely in larger aspect ratio domains, for which the influence of the side-walls is intentionally kept small. As soon as the aspect ratio becomes smaller, the influence of the sidewalls is increasing and it is expected that larger  $Ra_C$  are

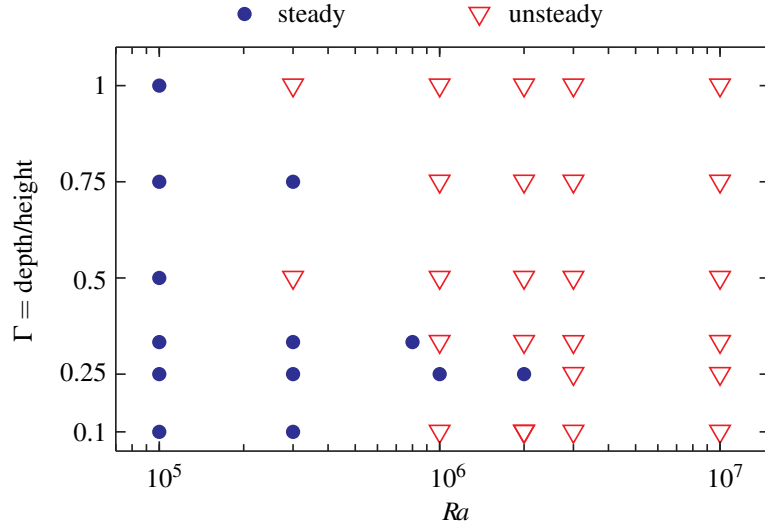


FIGURE 11.9: State of the equilibrium (steady/unsteady) in dependence of  $Ra$  and  $\Gamma$ ,  $Pr = 0.786$ .

required for the onset of unsteady motion, due to a damping of disturbances close to the walls [2, 25, 60, 76]. From a previous study in a cylindrical domain with equal diameter and height we expect the onset of unsteady motion to take place in such a domain between  $Ra = 10^5$  and  $Ra = 3 \times 10^5$  for  $Pr = 0.786$  [155]. Note that besides the geometry of course also  $Pr$  influences this onset. Nevertheless, in case of glycerol ( $Pr = 2547.9$ ) this transition takes place between  $Ra = 10^5$  and  $Ra = 10^6$  as well, which means that the dependence on  $Pr$  is rather weak [67].

To determine, whether the equilibrium is steady or unsteady, time-series of the heat flux entering/leaving the the sample through the bottom/top plate  $Nu^{\text{bottom/top}}(t) = \langle -\partial_z T \rangle_{x,y}|_{z=0/z=1}$  are studied. If for a combination of  $Ra$  and  $\Gamma$  the latter quantities do not vary in time with an amplitude larger than  $10^{-10}$ , the case is called “steady”. In practice this criterion is quite sensitive for our set of parameters, since in unsteady cases amplitudes of order  $10^{-1}$  are obtained. This significant differences might be caused by the relatively large differences between the discussed  $Ra$ . In figure 11.9 the results are collected in a single diagram.

When comparing the sudden drops in the  $Ra$ -scalings of  $Nu$  and  $Re$  (figure 11.2) with figure 11.9, it turns out that up to  $\Gamma = 1/3$  the drops correspond to the transition to time-dependent flow. This was also reported for large aspect ratio experiments, in which modifications in the  $Ra$ -scaling of  $Nu$  appeared due to the onset of time-dependent flow [25]. From the assumption, that the boundary layers are of Prandtl-Blasius-Pohlhausen type, a strong dependence of  $Nu$  and  $Re$  follows [121]. This clarifies that the drops in  $Nu$  and  $Re$  occur simultaneously.

When studying figure 11.9, it becomes obvious that there is no monotonic dependence of  $Ra_C$  and  $\Gamma$ . In particular for  $\Gamma = 1/10$  we obtain  $Ra_C \approx 10^6$  while for  $\Gamma = 1/4$  we find  $Ra_C \approx 3 \times 10^6$ . Apart from these single anomalies, the general tendency is obtained that with decreasing  $\Gamma$  the required  $Ra_C$  increases. As expected from the large aspect ratio studies [2, 60], between an



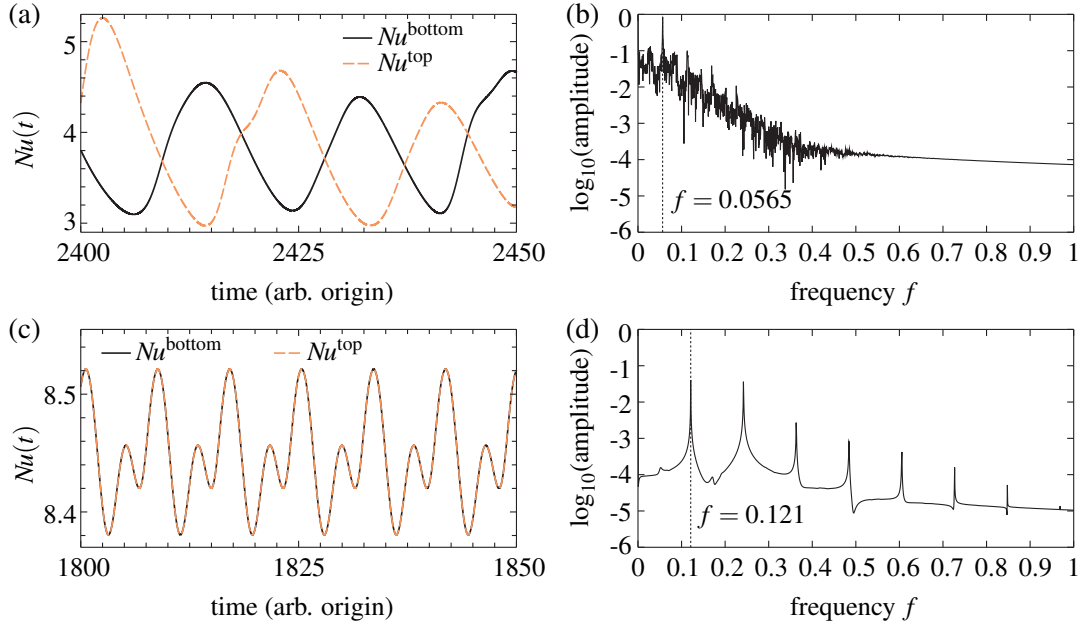


FIGURE 11.10: Time-series  $Nu^{\text{bottom/top}}(t)$  for (a)  $\Gamma = 1/10$  and (c)  $\Gamma = 1/3$  and corresponding time-spectra (b) and (d), respectively.  $Ra = 10^6$ ,  $Pr = 0.786$ .

unsteady equilibrium and a one with a chaotic time-dependence we obtain quasi periodic flows for certain combinations of  $\Gamma$  and  $Ra$ . We did not obtain those periodic flows for all  $\Gamma$ , since only a few  $Ra$  have been studied in the DNS. Therefore the periodic state might appear between two investigated  $Ra$ . Our study does not reveal, whether such quasi periodic states exist for all  $\Gamma$ . In experiments it was found, that the aspect ratio might have influence on this [2].

Since the present study focuses on the aspect ratio dependence of heat flux and motion but not on the transition to turbulence, we leave the investigation of these periodic states, that were found accidentally, beyond the scope of the present work. Nevertheless we want to discuss two particular cases, since they point out the differences between  $\Gamma = 1/10$  and slightly larger  $\Gamma$  cases. In figure 11.10 short intervals of the time-history  $Nu^{\text{bottom/top}}(t)$  for  $Ra = 10^6$  and  $\Gamma = 1/3$  and  $\Gamma = 1/10$  are depicted together with corresponding time-spectra. The time-histories show a significant difference: While for  $\Gamma = 1/3$   $Nu^{\text{bottom/top}}(t)$  oscillate in phase, they do not for  $\Gamma = 1/10$ . As it is quite obvious the time-series for  $\Gamma = 1/10$  is not perfectly periodic, which we ascribe to a slightly too large  $Ra$  for the perfectly periodic case. This aperiodicity is of course also expressed as noise in the spectrum. Besides this difference the spectra show that the dominant frequency is in case of  $\Gamma = 1/10$  only about half of that for  $\Gamma = 1/3$ . The absolute values of the main frequencies are thereby of the order of the turnover frequency  $f_t$ , which can be approximated as  $f_t = \sqrt{Ra/Pr}(Re/L)$ , where  $L$  is the path length corresponding to a turnover and is usually between  $2H$  and  $4H$  [90].

When looking at the flow (cf. the supplementary material [151]) and the instantaneous flow

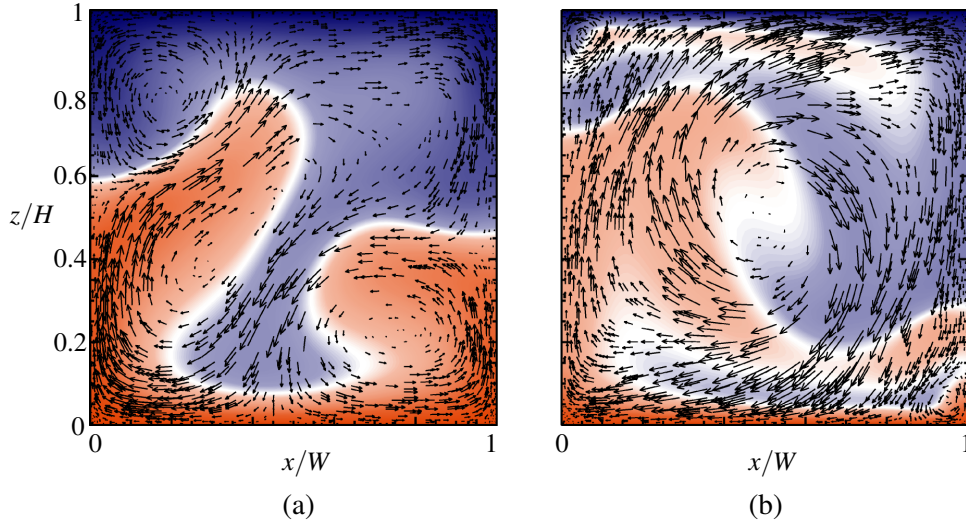
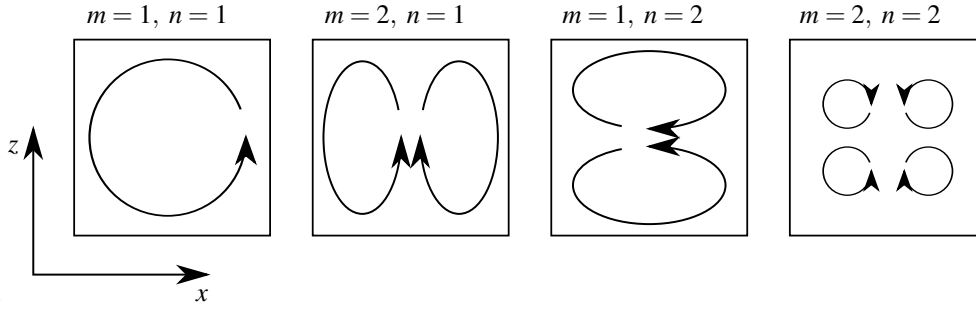
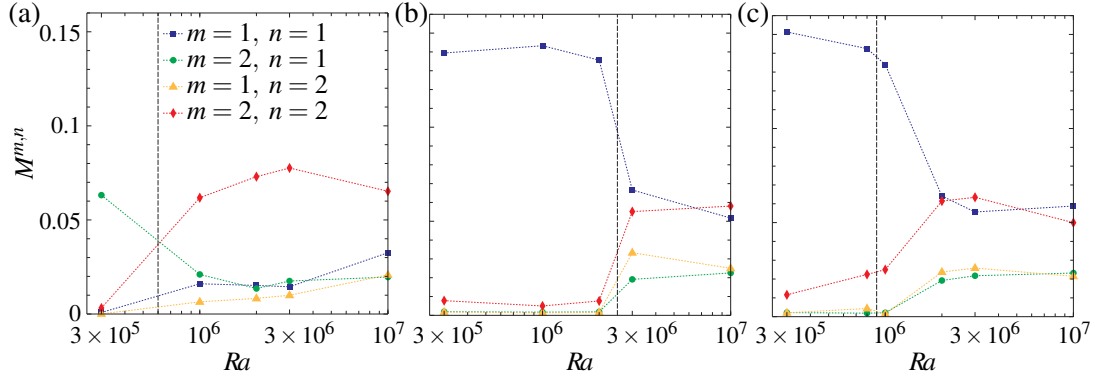


FIGURE 11.11: Vertical slices at half depth of instantaneous temperature fields (red warm, blue cold) with superposed velocity vectors. (a) For  $\Gamma = 1/10$  the dynamics take place in the domain's center where hot and cold plumes rise and fall almost vertically. (b) In contrary the flow for  $\Gamma = 1/3$  consists of a single roll, i.e. warm and cold structures are located close to vertical walls, while the center region is almost not moving and has mean temperature (white),  $Ra = 10^6$ ,  $Pr = 0.786$ .

fields in figure 11.11) it becomes obvious that these two cases have a completely different dynamics caused only by the different  $\Gamma$ . For  $\Gamma = 1/3$  a single convection roll filling the whole box with a superposed horizontal twisting of the bulk region is present. In case of  $\Gamma = 1/10$  the large-scale flow consists of large plume-like structures moving vertically through the center of the domain with alternating vertical direction. This fits quite well to what is presented in figure 11.7. As discussed at the end of section 11.4, the localization of large heat fluxes at the center of the bottom plates for small  $\Gamma$ , corresponds to a global fluid motion through the box center. Those two types of dynamics can be understood as different modes which might be stronger or less strong for different  $Ra$  and  $\Gamma$ . This can be studied in particular for small  $\Gamma$  by a decomposition in several two-dimensional modes, as discussed in the next sub-section.

### 11.5.2 2D mode decomposition

For small aspect ratio  $\Gamma$ , i.e.  $\Gamma \leq 1/3$ , the flow can be considered as quasi two-dimensional [167]. Therefore it is meaningful to use a 2D technique and analyze a vertical slice of the flow field at half depth. We want to investigate in dependence of  $Ra$  and  $\Gamma$  the contributions of a four-roll state (as for  $Ra = 10^6$ ,  $\Gamma = 1/10$ , figure 11.11(a)) and a single-roll state (as for  $Ra = 10^6$ ,  $\Gamma = 1/3$ , figure 11.11(b)). Thus we conduct a decomposition of the flow in several multi-roll states, as it was done to investigate flow reversals in 2D DNS [28, 29]. Therefore, we use the sets of instantaneous flow fields mentioned earlier, and extract the components of the velocity field


 FIGURE 11.12: Sketch of the first four modes  $\vec{v}^{m,n}$  for  $m, n \in \{1, 2\}$  as defined in the text.

 FIGURE 11.13: Contributions of the different modes  $M^{m,n}$  (as defined in the text) in dependence of  $Ra$  for (a)  $\Gamma = 1/10$ , (b)  $\Gamma = 1/4$  and (c)  $\Gamma = 1/3$ . The vertical dashed lines indicate roughly the onset of unsteady motion.  $Pr = 0.786$ .

within the vertical slice at half depth, i.e.  $u_x$  and  $u_z$ . The latter ones are projected on modes

$$v_x^{m,n} = 2 \sin(m\pi x) \cos(n\pi z)$$

$$v_z^{m,n} = -2 \cos(m\pi x) \sin(n\pi z)$$

where we consider for simplicity only  $m, n \in \{1, 2\}$ . In figure 11.12 those four modes are sketched (see also the paper by Chandra & Verma [28]). The projection is done component-wise by a scalar product in the  $L_2$ -space of our two-dimensional sub-domain. Thus we obtain time series  $A_x^{m,n}(t) = \langle u_x(t) v_x^{m,n} \rangle_{x,z}$  and  $A_z^{m,n}(t) = \langle u_z(t) v_z^{m,n} \rangle_{x,z}$ .

Besides the orientation of the flow given by the sign of  $A_x^{m,n}(t)$  and  $A_z^{m,n}(t)$ , they inhibit the contributions of the different modes in a given time-interval. These (scalar) contributions  $M^{m,n}$ , called for simplicity as “modes” in the following, are calculated from the time-series by  $M^{m,n} = \left\langle \sqrt{A_x^{m,n}(t)^2 + A_z^{m,n}(t)^2} \right\rangle_t$ . We expect for the case  $\Gamma = 1/10$  in figure 11.11 the mode  $M^{2,2}$  to be largest, while for  $\Gamma = 1/3$  we suppose that mode  $M^{1,1}$  is dominant.

In figure 11.13 we compare the contributions  $M^{m,n}$  for different  $\Gamma$  in dependence of  $Ra$ . A vertical dashed line indicates roughly the onset of unsteady motion. It turns out, that as soon as  $Ra$  is large enough for unsteady flow, the mode  $M^{2,2}$  gets stronger, which is connected to

plumes moving through the center of the domain, as discussed before. Besides mode  $M^{2,2}$  also the contributions of the two unsymmetric modes  $M^{2,1}$  and  $M^{1,2}$  grow, but they never become dominating. This is contrary to 2D DNS [29], in which for  $Pr = 1$  between  $Ra = 10^6$  and  $Ra = 10^7$  a flow structure similar to mode  $M^{1,2}$  is found. How strong mode  $M^{2,2}$  gets depends on  $\Gamma$  and on the mode distribution for the steady case. While for  $\Gamma = 1/10$  mode  $M^{2,1}$  is the strongest in the steady case (i.e. a mode for which motion through the center-region is already important), in case of  $\Gamma = 1/4$  and  $\Gamma = 1/3$  mode  $M^{1,1}$  dominates in the unsteady flow. If  $Ra$  is increases further above the onset of unsteady flow, the contribution of  $M^{1,1}$  is increasing (c.f. section 11.6 for case  $\Gamma = 1/4$ ). Roughly speaking, for increasing  $\Gamma$  the critical  $Ra$  for the  $M^{1,1}$  dominance decreases. In the limit of large  $Ra$  of about  $10^{10}$  (and larger  $Pr$ ) as in the experiments [167], it can be expected that  $M^{1,1}$  is dominating for all considered  $\Gamma$ .

Looking from this point view, one concludes that for small  $\Gamma$  (and sufficiently large  $Ra$ ) the occurrence of flow reversals [139] becomes more probable, since they are related to the appearance of mode  $M^{2,2}$  in the 2D case [29]. This might explain also the experimental results [147] obtained in similar domains with water at  $Ra \approx 5 \times 10^9$ , where flow reversals are also very probable in case of small aspect ratio. In addition it has been obtained experimentally in a domain with  $\Gamma \approx 3/10$  and  $Pr = 5.7$ , that flow reversals become less probable with increasing  $Ra$  [139]. This agrees quite well with the results obtained here, stating that for  $Ra$  above the onset of unsteady motion the contribution of  $M^{2,2}$  decreases with increasing  $Ra$  (see also section 11.6).

Furthermore, as we have seen in figure 11.11(a) the mode  $M^{2,2}$  is connected to plumes moving across the center of the domain. Thus we can understand that flow reversals, which are sometimes interpreted as slow changes of the flow structure with growing corner vortices [29], might be also interpreted as the occurrence of thermal plumes in the domain's center. This allows to explain, why flow reversals can take place also for free-slip walls, where slow changes of the flow structure are not possible due to missing corner vortices [18].

The occurrence of such plumes, which rise and fall in the center, is especially for small  $\Gamma$  quite reasonable. Due to the fact that the viscous boundary layers attached to all walls fill (in particular for small  $Ra$ ) the region in which three vertical walls are located very closely. Thus, plume motion is "easier" apart from that region, i.e. in the center. For larger  $Ra$  the boundary layers become thinner and the plumes smaller, which then leads to the case of plumes rising closer to the walls. This seems to be the preferred flow structure in all kind of (small aspect ratio) domains for  $Pr$  about one [71, 155].

The fact that the onset of unsteady motion corresponds to a drop in  $Nu$  and a change of the contributions of the different modes agrees also quite well. As reported in the literature, during a flow reversal, i.e. mode  $M^{2,2}$  becomes more important than  $M^{1,1}$ ,  $Nu$  is varying strongly [29]. In addition the global flow structure in general is connected to  $Nu$  [97]. Thus we can conclude that the observed drops in  $Nu$  are not only related to a change to a time-depending flow, but in addition to a change in the global flow structure. We expect that the remaining differences

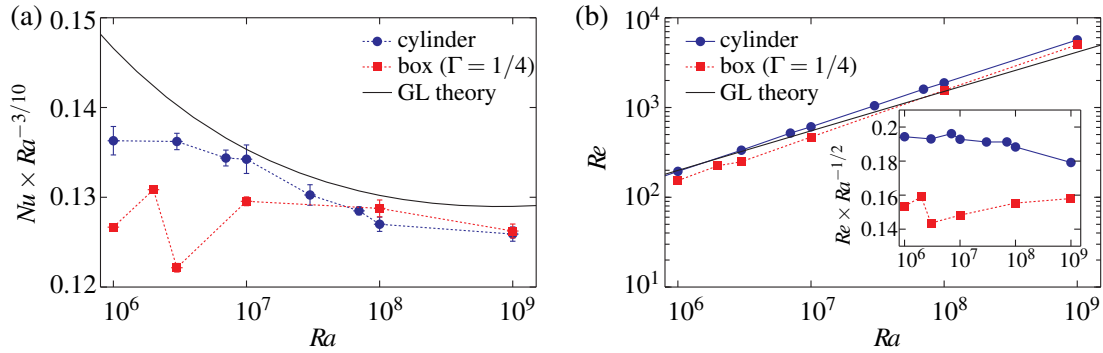


FIGURE 11.14: Comparison between the box with  $\Gamma = 1/4$ , a cylinder with equal diameter and height [155] and the estimate by the Grossmann-Lohse (GL) theory [134] of the  $Ra$ -dependence of (a) the reduced  $Nu$  and (b)  $Re$  and the reduced  $Re$  (inset),  $Pr = 0.786$ .

between  $\Gamma = 1/10$  and larger  $\Gamma$  will decrease as soon as similar global flow structures are present. This means that  $M^{1,1}$  is strong, which is presumably the case for larger  $Ra$ .

## 11.6 Comparison of box and cylinder

To close this study, we want to extend the investigation of  $\Gamma = 1/4$  to higher  $Ra$  up to  $Ra = 10^9$ , since this particular  $\Gamma$  is chosen for quasi 2D experiments.[167] In the following we call this geometry as "box" for simplicity. Further we want to compare the results for this domain, with the results for a cylinder with equal diameter and height [155], since this type of container is widely used [5].

Similar to section 11.3 we start the comparison with the integral quantities defined before. In figure 11.14 the  $Ra$  dependence of  $Nu$  and  $Re$  for the box and the cylinder is depicted for  $Ra$  between  $10^6$  and  $10^9$ . Further the theoretical estimate by the Grossmann-Lohse (GL) theory [134] is added. Note that this theory only allows  $Ra$  and  $Pr$  as parameters and does not include any geometrical properties.

At first it should be mentioned that due to the different axis-scale the drops of  $Nu$  and  $Re$ , which happen at the onset of unsteady motion in the box as discussed before, seem much more pronounced here than in figure 11.2. It is further obtained that up to  $Ra \approx 10^7$ ,  $Nu$  is smaller in the box, while for larger  $Ra$  it is vice versa. For the cylinder the reduced  $Nu$  is decreasing for  $Ra \geq 10^6$ , which is also in good agreement with other DNS and experiments as well as the GL theory [155]. A similar decrease cannot be found in case of the box, eventhough for  $Ra > 10^8$  the reduced  $Nu$  is slightly decreasing. This leads at  $Ra = 10^9$  to very similar  $Nu$  in the box and the cylinder, which suggests that for large  $Ra$  the shape of the container does not have a strong influence on  $Nu$ . A similar result was also found in section 11.3 when comparing different  $\Gamma$ .

The result of  $Nu$  being independent of the geometry for large  $Ra$  cannot be necessarily generalized to other characteristics of the flow. When considering for example the temperature

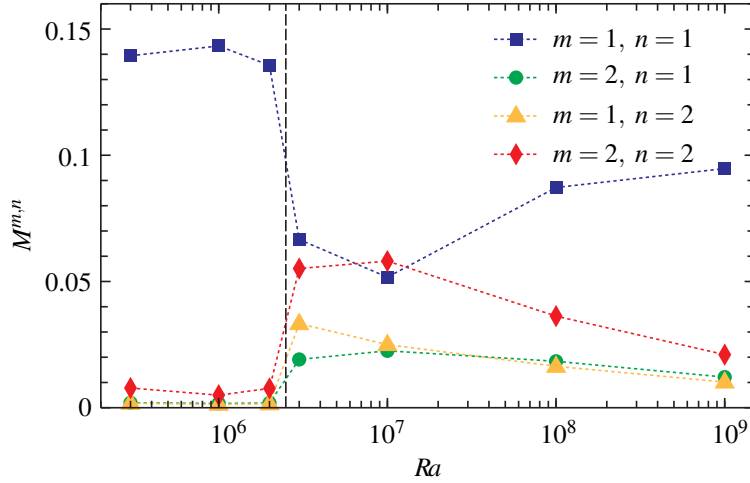


FIGURE 11.15: Contributions of the different modes  $M^{m,n}$  (as defined in the text) in dependence of  $Ra$  for  $\Gamma = 1/4$  up to  $Ra = 10^9$  for  $Pr = 0.786$ .

and velocity fluctuations in the domains center, significant differences between a box-shaped and a cylindrical geometry have been obtained experimentally [39].

But even for integral quantities like  $Re$  differences between box and cylinder remain. While a slight decrease in the reduced  $Re$  is found for the cylinder, it is slowly increasing with  $Ra$  in case of the box. The additional differences in the absolute values might be explained as before (cf. section 11.3): due to a larger volume of the cylinder, the boundary layers (with smaller velocities) have a smaller contribution to the volume integral for calculating  $Re$ . Thus we find already for geometrical reasons larger  $Re$  in the cylinder than in the box. There is also reasonable agreement with the GL theory when comparing  $Re$ . The predicted effective scaling exponent (here  $Re \sim Ra^{4/9}$ ) seems to be slightly smaller than the one for the DNS results. The gauge-freedom of the theory lets us adjust the absolute value of  $Re$  by multiplying it with a constant without changing  $Nu$  or the  $Ra$ -dependence. Thus comparing the absolute values of  $Re$  from the DNS and the theory is not reasonable here.

When considering the contributions of the different modes  $M^{n,m}$  as discussed in the previous section, the expected tendencies are realized. As depicted in figure 11.15, the contribution of the mode  $M^{1,1}$  is increasing with  $Ra$  after the transition to an unsteady flow. In particular for  $Ra$  larger than  $10^8$  the single roll state  $M^{1,1}$  contributes at most, while the contributions of the other modes are decreasing with  $Ra$ .

The occurrence of different modes in dependence of  $Ra$  is one of the major differences between the box and the cylinder. While in the cylinder the global flow structure remains the same between  $Ra = 10^5$  and  $10^9$  for  $Pr \approx 1$  and is similar to mode  $M^{1,1}$  in the azimuthal plane of the LSC [155], it shows around the onset of unsteady motion a complicated mixture of different modes in case of the box.

These different modes might also cause differences in the scaling of  $Nu$  and  $Re$ . Since for similar  $Ra$  also the transition to a bulk dominated flow takes place, the mentioned effects are difficult to separate. Perhaps in case of even larger  $Ra$ , for which it is expected that the global flow structure remains the same also in the box, the differences between cylinder and box become easier to analyse. Due to very high computational effort [121] we leave this point open for future studies.

## 11.7 Summary

DNS of RBC in box-shaped containers have been conducted in order to investigate the influence of the aspect ratio  $\Gamma$  (depth/height) for equal length and height of the box. Main focus of the study has been set on the influence of  $\Gamma$  on  $Nu$  and  $Re$  and the connection to the global flow structure.

It is shown that, in particular for small  $Ra$ , the  $\Gamma$ -influence is strong and leads to a decrease in  $Nu$  of up to 55% and in  $Re$  of even up to 97% in comparison to the cubic case, respectively. With increasing  $Ra$  the  $\Gamma$ -influence decreases leading at  $Ra = 10^7$  to similar  $Nu$  for  $\Gamma \geq 1/4$ . Differences in  $Re$  remain even at large  $Ra$  resulting in a scaling  $Re \sim \Gamma^{3/20}$  for large  $Ra$ .

The study further reveals for small  $\Gamma$  sudden drops in  $Nu(Ra)$  and  $Re(Ra)$ . These drops occur at  $Ra$  slightly above the onset of unsteady motion, which is found to depend strongly and in a non-monotonic way on  $\Gamma$ . A decomposition of instantaneous flow fields into two-dimensional states with different amounts of rolls reveals, that this onset of unsteady motion is accompanied by a change to a four-roll structure which corresponds to a plume-movement through the domains center. For  $Ra$  much larger than the onset of unsteady motion, the flow is in a single roll state even for small  $\Gamma$ , which is in good agreement with experiments at even larger  $Ra$  showing the single roll state [167].

A comparison of the case  $\Gamma = 1/4$  and a cylinder with equal diameter and height, which are both types of domains used frequently in experiments, points out that for  $Ra \lesssim 5 \times 10^7$  a smaller heat flux is obtained for the box, while for larger  $Ra$  both, box and cylinder geometries, lead to similar  $Nu$ . The scaling of the reduced  $Nu$  with  $Ra$  differs significantly in the cylinder and the box, which we ascribe to changes in the global flow structure that occur only in case of the box.

One can conclude, that eventhough RBC flows in the box with small  $\Gamma$  are simpler to analyse and they demonstrate their “quasi two-dimensionality” in experiments at large  $Ra$ , these flows can have much more complicated structures for lower  $Ra$  and show interesting features which should be further investigated.

The authors would like to thank Matthias Kaczorowski and Tomasz Czarnota for updating the numerical code, Daniel Schmeling for proofreading and acknowledge financial support by the German Research Foundation (DFG) under grant SH405/3-1.

## Appendix

 TABLE 11.1: List of simulation parameters:  $Ra$ ,  $\Gamma$  governing parameters,  $N_i$  number of nodes in direction  $i$ ,  $n_T$ ,  $n_u$  number of nodes in the thermal/viscous boundary layer [121],  $\tilde{n}_T$ ,  $\tilde{n}_u$  estimates [121] for the required number of nodes in the boundary layers,  $\tau$  amount of time-units used for averaging in case of unsteady flow,  $Nu$  Nusselt number and deviation in the vertical direction,  $Re$  Reynolds number based on mean kinetic energy,  $Pr = 0.786$ .

$Ra$	$\Gamma$	$N_x \times N_y \times N_z$	$n_T$	$n_u$	$\tilde{n}_T$	$\tilde{n}_u$	$\tau$	$Nu$		$Re$
$10^5$	1/10	$64 \times 32 \times 64$	20	18	2	1	—	1.91		11.52
	1/4	$64 \times 32 \times 64$	14	13	2	2	—	2.99		33.38
	1/3	$64 \times 32 \times 64$	13	13	2	2	—	3.10		38.44
	1/2	$64 \times 64 \times 64$	12	11	2	2	—	3.63		55.29
	3/4	$64 \times 64 \times 64$	11	11	2	2	—	3.92		57.96
	1	$64 \times 64 \times 64$	11	10	2	2	—	4.22		62.96
$3 \times 10^5$	1/10	$96 \times 32 \times 96$	27	26	2	2	—	3.22		30.43
	1/4	$96 \times 32 \times 96$	22	21	2	2	—	4.73		72.36
	1/3	$96 \times 32 \times 96$	21	20	2	2	—	5.36		86.20
	1/2	$96 \times 64 \times 96$	20	19	2	2	400	5.73	$\pm 0.01$	96.69
	3/4	$96 \times 96 \times 96$	20	19	2	2	—	5.61		101.9
	1	$96 \times 96 \times 96$	20	19	2	2	500	5.96	$\pm 0.01$	111.4
$8 \times 10^5$	1/3	$96 \times 32 \times 96$	17	16	3	2	—	7.89		152.8
$10^6$	1/10	$96 \times 32 \times 96$	24	23	2	2	1435	4.18	$\pm 0.02$	64.35
	1/4	$96 \times 32 \times 96$	17	16	3	3	—	7.99		153.5
	1/3	$96 \times 32 \times 96$	16	15	3	3	250	8.44	$\pm 0.01$	170.8
	1/2	$96 \times 64 \times 96$	16	15	3	3	740	8.74	$\pm 0.01$	182.9
	3/4	$96 \times 96 \times 96$	16	15	3	3	754	8.14	$\pm 0.02$	177.0
	1	$96 \times 96 \times 96$	16	15	3	3	458	8.28	$\pm 0.02$	189.6
$2 \times 10^6$	1/10	$96 \times 32 \times 96$	20	19	2	2	2105	5.58	$\pm 0.04$	106.1
	1/4	$96 \times 32 \times 96$	14	14	3	3	—	10.16		224.8
	1/3	$96 \times 32 \times 96$	15	14	3	3	2215	9.58	$\pm 0.02$	213.5
	1/2	$96 \times 64 \times 96$	14	13	3	3	1048	10.78	$\pm 0.02$	256.3
	3/4	$96 \times 96 \times 96$	14	14	3	3	486	10.18	$\pm 0.04$	253.7
	1	$96 \times 96 \times 96$	14	13	3	3	649	10.20	$\pm 0.02$	265.9
$3 \times 10^6$	1/10	$192 \times 64 \times 192$	26	25	2	2	250	6.64	$\pm 0.05$	140.9
	1/4	$192 \times 64 \times 192$	18	17	3	3	486	10.42	$\pm 0.04$	248.7
	1/3	$192 \times 64 \times 192$	18	16	3	3	487	11.00	$\pm 0.03$	262.2
	1/2	$192 \times 128 \times 192$	17	16	3	3	222	11.69	$\pm 0.10$	299.4



## 11.7 SUMMARY

	3/4	192 × 192 × 192	17	16	3	3	133	11.37	±0.06	306.1
	1	192 × 192 × 192	17	16	3	3	264	11.53	±0.04	326.7
10 <sup>7</sup>	1/10	192 × 64 × 192	16	15	3	3	879	12.15	±0.03	308.6
	1/4	192 × 64 × 192	13	12	4	3	1772	16.37	±0.06	468.7
	1/3	192 × 64 × 192	13	12	4	3	888	16.56	±0.08	498.1
	1/2	192 × 128 × 192	13	12	4	3	800	16.40	±0.05	534.2
	3/4	192 × 192 × 192	13	12	4	3	516	16.32	±0.06	563.2
	1	192 × 192 × 192	13	12	4	3	480	16.25	±0.08	601.1
10 <sup>8</sup>	1/4	384 × 128 × 384	15	14	5	5	382	32.34	±0.24	1553
10 <sup>9</sup>	1/4	768 × 256 × 768	11	10	7	6	194	63.27	±0.39	4995

---



# 12 Heat flux increase due to rough heating and cooling plates

**Citation and credit:** This paper was submitted on 16 October 2013 to the Journal of Fluid Mechanics. On 26 February 2014 a revised version of the paper was submitted, which is still under revision.

**Title:** Heat flux enhancement by regular surface roughness in turbulent thermal convection

**Authors:** Sebastian Wagner & Olga Shishkina [154]

**Contribution:** I modified and extended an existing code for the investigation of the influence of surface roughness in three-dimensional domains, performed the simulations and developed analysis techniques. Further, I created all the figures and wrote the main part of the manuscript's first version (except of the abstract and sections 5 and 6), which structure is preserved.

## Abstract

Direct numerical simulations (DNS) of turbulent thermal convection in a boxed-shaped domain with rough heated bottom and cooled top surfaces are conducted for Prandtl number  $Pr = 0.786$  and Rayleigh numbers  $Ra$  between  $10^6$  and  $10^8$ . The surface roughness is introduced by four parallelepipedal obstacles equidistantly distributed attached to the bottom plate, and four obstacles located symmetrically at the top plate. By varying  $Ra$  and the height and length of the obstacles, we investigate the influence of the regular wall roughness on the turbulent heat transport measured by the Nusselt number  $Nu$ . An empirical function to estimate the increase of  $Nu$  due to the roughness is presented, which agrees well with the DNS results. The exponent in the  $Nu$  vs.  $Ra$  scaling changes from about 0.31 for smooth walls to about 0.37 in the studied cases of rough walls. We show that the mean secondary flow in the cavities between the obstacles is related to the wind that develops in the core part of the domain which is always stronger than the secondary flows and can be influenced by the geometry of the regular roughness in such a way that the strengthening (weakening) of one of them leads to the weakening (strengthening) of the

other. Generally, an increase in the roughness height leads to stronger flows both in the cavities and in the bulk region, while an increase of the width of the obstacles strengthens only the large scale circulation of the fluid and weakens the secondary flows. An increase in  $Ra$  always leads to stronger flows, both in the cavities and in the bulk.

## 12.1 Introduction

Turbulent thermal convection is a process occurring widely in nature and technology. Its fundamental mechanisms have been studied for more than a century for the simplified case of a fluid layer heated from below and cooled from above, i.e. Rayleigh–Bénard convection (RBC) (cf. the reviews by Ahlers *et al.* [5], Chillà & Schumacher [32], Lohse & Xia [84]). In classical RBC, smooth heating and cooling plates are considered and in experiments much effort is spent to realise this ideal case, while in most applications roughness plays an important role. On the one hand, rough surfaces reflect realistic configurations, e.g. convection in the atmosphere is influenced by the roughness of the earth’s surface. On the other hand, in many industrial applications surface roughness is used in order to increase the heat transport, e.g. in heating/cooling devices. Thus, the consideration of the roughness of the heating and cooling plates in numerical studies has the following two advantages: It connects the simplified smooth case with more realistic configurations and allows of separating the influence of the roughness from the usual mechanisms of turbulent thermal convection, owing to the existing knowledge about the smooth case.

Most of the studies considering RBC with rough walls are experimental ones, so far: the heat flux and related quantities for a fixed roughness type and varying Rayleigh number  $Ra$  are usually measured. This is mainly due to the fact that changing the roughness configuration requires expensive constructions of multiple heating and cooling plates. There have been different results with respect to the scaling of the integral heat flux, i.e. the Nusselt number  $Nu$ , as a power law  $Nu = \alpha Ra^\beta$  in these experimental studies. In the experiments by Shen *et al.* [117] an increase of the prefactor  $\alpha$  of about 20% was reported, occurring only if the height of the obstacles is larger than the mean thickness of the thermal boundary layer (BL)  $\delta_T$ . In another study, Du & Tong [40] found a stronger increase if the height of the obstacles is increased. A somewhat different result was obtained in the experiments by Roche *et al.* [108], who found an increase of the exponent  $\beta$ . Since the resulting  $\beta$  was about 1/2, this was interpreted as a triggering of the ultimate regime proposed by Kraichnan [74], at  $Ra$  far below that found and explained for the case of smooth plates [55, 62]. Recent experiments performed by Tisserand *et al.* [146] in a cell with smooth cooling and rough heating plate corroborate this increase of  $\beta$  to about 1/2, but their analysis yielded that it is not caused by increased turbulence, i.e. the ultimate regime. A much weaker increase of  $\beta$  was reported by Qiu *et al.* [105]. Ciliberto & Laroche [35] found a difference between periodic roughness and a power-law distributed one. Only in the case of the

power-law distributed roughness was an increase in the exponent  $\beta$  obtained.

This result was supported by Villermaux [150], who developed a model explaining the heat flux enhancement in the case of a wide spectrum of typical roughness length scales. It is based on the assumption that the heat flux is proportional to the total covering area of the surface and describes an increase of the scaling exponent  $\beta$  of up to 10% depending on the surface's fractal dimension. In case the roughness is introduced uniformly by obstacles of the same height, the model predicts that  $\beta$  remains unchanged.

In numerical simulations Stringano *et al.* [138] found, similar to some of the experimental results, a weak increase of the scaling exponent  $\beta$ .

The differences in the results obtained in particular experiments are usually explained by different types of roughness. Here one distinguishes the roughness introduced by a set of roughness elements of different sizes from that introduced by single-sized elements. In the latter case, the uniform distribution of the elements leads to the so-called regular roughness. Another important issue is whether the roughness height is smaller or larger than the typical boundary layer thicknesses. Even in the case of a high regular roughness, the experimental results might differ, and this is usually explained by the different shapes of the roughness elements. Thus, Ciliberto & Laroche [35] used spheres, Shen *et al.* [117] pyramids with square cross-sections, and Roche *et al.* [108] V-shaped grooves. Connected to this is the result by Du & Tong [40] and Stringano *et al.* [138], stating that the edges of the roughness elements are the most active places of plume emission. All these facts lead to the conclusion that the effect of a rough surface on the heat transport cannot be fully explained by a single geometrical characteristic of the roughness, such as the covering area of the rough surface.

A first step in developing a model that takes the geometrical characteristics of the roughness elements into account has been made by Shishkina & Wagner [125] for the case of relatively high and regularly distributed roughness elements. The model decomposes the heat flux from the rough surface into several contributions from separate parts of the roughness elements. These contributions are estimated by applying the Prandtl–Blasius–Pohlhausen theory of laminar BLs. This model is in good agreement with two-dimensional direct numerical simulations (DNS) in which the roughness is realised by rectangular obstacles. Since on the one hand discrepancies between two-dimensional (2D) and three-dimensional (3D) RBC are present in particular for small Prandtl numbers  $Pr$  [114], and on the other hand deviations of the theory of laminar BLs and DNS results have been obtained [e.g. 155], the comparison of the model with 3D DNS and further model advancement are required. Furthermore, as mentioned earlier, parametric studies of different roughness configurations can hardly be done in experiments, but are required, e.g. during the design process of heat exchangers, where the parameter ranges of  $Ra$  and  $Pr$  are fixed while the roughness is optimised.

In the present paper we report on DNS results obtained in a rectangular domain with equal length and height and a depth equal to one-fourth of the height for  $Pr = 0.786$  and  $Ra$  between

$10^6$  and  $10^8$ . The DNS results for this special geometry with smooth plates (also for other aspect ratios depth/height and in comparison with a cylindrical geometry) have been published earlier [152]. The surface roughness in the present DNS is realised by attaching four box-shaped obstacles to the heating as well as the cooling plate. Besides varying  $Ra$ , the height and length of the obstacles are also varied.

In Section 12.2 the numerical method and the general setup are described. The numerical results about the global heat transport are given in Section 12.3 and compared in detail with the predictions of a two-dimensional model in Section 12.4. In Section 12.5 a further analysis of the DNS data with respect to the global flow structures and velocity distributions in the convection cells with rough heated and cooled plates is presented. Finally, the paper is closed by presenting some conclusions in Section 12.6.

## 12.2 Numerical methodology and setup

A fourth order accurate finite-volume code working in Cartesian coordinates [120] has been used to solve the dimensionless equations describing the conservation of mass, momentum and energy in the Oberbeck–Boussinesq approximation, i.e.

$$\frac{\partial \vec{u}}{\partial t} + (\vec{u} \cdot \vec{\nabla}) \vec{u} = -\vec{\nabla} p + \sqrt{\frac{Pr}{Ra}} \vec{\nabla}^2 \vec{u} + T \vec{e}_z, \quad (12.1)$$

$$\frac{\partial T}{\partial t} + (\vec{u} \cdot \vec{\nabla}) T = \sqrt{\frac{1}{PrRa}} \vec{\nabla}^2 T, \quad \vec{\nabla} \cdot \vec{u} = 0. \quad (12.2)$$

Here  $\vec{u}$  denotes the velocity,  $t$  time,  $p$  pressure,  $T$  temperature and  $\vec{e}_z$  is the unit vector in the vertical direction. For nondimensionalisation, the free-fall velocity  $\sqrt{\hat{\alpha} \hat{g} \hat{\Delta} \hat{H}}$  and the height  $\hat{H}$  have been used. Further, the temperature is nondimensionalised as  $T = (\hat{T} - \hat{T}_M) / \hat{\Delta}$ , where dimensional quantities are marked with a hat and  $\hat{T}_M = (\hat{T}_{\text{bottom}} + \hat{T}_{\text{top}}) / 2$  and  $\hat{\Delta} = \hat{T}_{\text{bottom}} - \hat{T}_{\text{top}}$ . As usual for the Oberbeck–Boussinesq approximation, the kinematic viscosity  $\hat{\nu}$ , the thermal diffusivity  $\hat{\kappa}$ , the thermal expansion coefficient  $\hat{\alpha}$ , the gravitational acceleration  $\hat{g}$  and the density  $\hat{\rho}$  are assumed to be constant. To allow buoyant motion, a linear temperature dependence of the density only on the buoyancy term is assumed. Under these conditions, the dynamics of the flow is governed by the Rayleigh number  $Ra = \hat{\alpha} \hat{g} \hat{\Delta} \hat{H}^3 / (\hat{\nu} \hat{\kappa})$  and the Prandtl number  $Pr = \hat{\nu} / \hat{\kappa}$ . The latter we fix to  $Pr = 0.786$  in all our simulations.

The domain's height  $H$  and length  $L$  are chosen equal, while the depth  $D$  is one-fourth of the height. The top and bottom plates are isothermal with  $T_{\text{bottom}} > T_{\text{top}}$ , the vertical sidewalls are adiabatic and on all surfaces the velocity vanishes due to the no-slip condition. To simulate the influence of the surface roughness of the top and bottom plates, four obstacles with height  $h$  and length  $\ell$  are placed equidistantly on each of these plates (see also the sketch in figure 12.1a and the visualisation of the flow in figure 12.2). These obstacles have temperatures  $T_{\text{top}}$ ,  $T_{\text{bottom}}$ ,

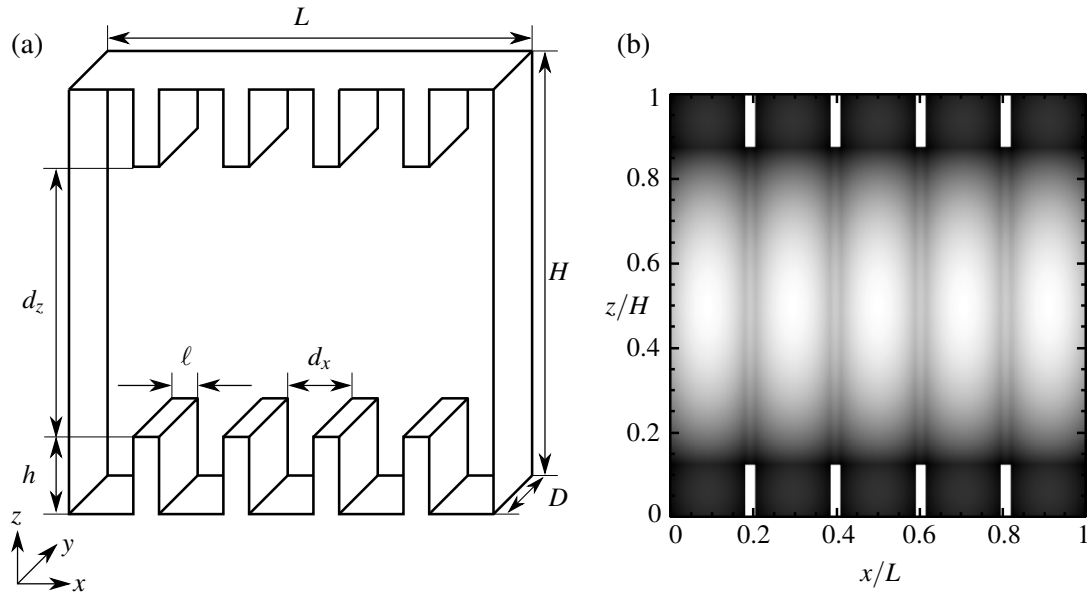


FIGURE 12.1: (a) Sketch of the domain with coordinate system and nomenclature. (b) Distribution of mesh spacing  $\sqrt{\Delta_x \Delta_z}$  (black small, white large) in the  $x$ - $z$ -plane (at arbitrary  $y$ ) for a certain shape of obstacles, where  $\Delta_x$ ,  $\Delta_z$  are the mesh spacings in the  $x$ ,  $z$  direction, respectively.

respectively, as do the surfaces they are attached to.

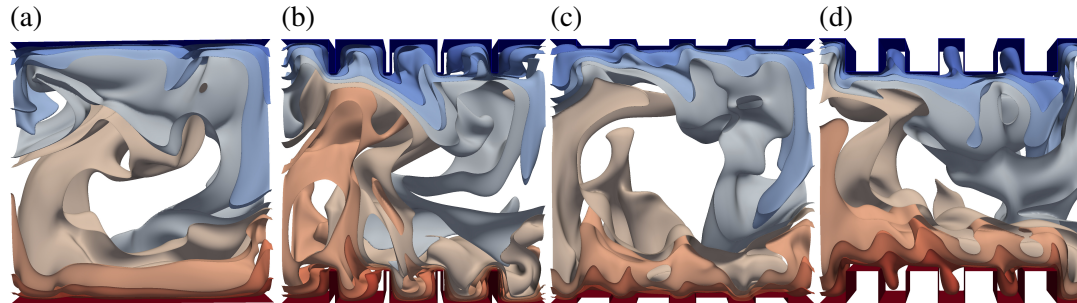


FIGURE 12.2: Instantaneous temperature isosurfaces (red = warm, blue = cold) for smooth plates (a) and rough plates with (b)  $h = 0.125H$ ,  $\ell = 0.025L$ , (c)  $h = 0.025H$ ,  $\ell = 0.125L$  and (d)  $h = 0.125H$ ,  $\ell = 0.125L$  for  $Ra = 10^7$ ,  $Pr = 0.786$ .

To allow effective direct numerical simulations (DNS) in such a complicated domain, the capacitance matrix technique has been used for a non-iterative calculation of the pressure field. For a further decrease of the computational effort, the extend of the obstacles in the  $y$ -direction is restricted to be equal to the domain's depth  $D$ . Thus the non-equidistant mesh-spacing in the  $x$ - and  $z$ -directions is independent of  $y$ , i.e. the  $y$ -direction is regular. This method has been applied previously to the investigation of mixed [9, 126] and forced [72] convection in complicated

domains.

The spatial resolution has been chosen according to Shishkina *et al.* [121]. Considering the boundary layer structure analysis by Wagner *et al.* [155] and the improved boundary layer structure model by Shishkina *et al.* [119, 127], the boundary layer resolution has been further refined. Between the obstacles, the mesh has been chosen fine enough to resolve also any flow separation that might occur at the edges of the obstacles. In figure 12.1b the mesh in the  $x$ - $z$ -plane is visualised for a single roughness configuration. This and further different roughness configurations and the corresponding amounts of computational nodes are given in Table 12.1.

### 12.3 Heat flux enhancement by roughness

The effect of the roughness on the global heat flux is discussed in two ways. First, the influences of different roughness configurations are compared at constant  $Ra$ . A previous numerical study in 2D revealed that the heat flux enhancement by roughness cannot be parametrised only by the covering area, the volume of the obstacles, or similar quantities [125]. It rather depends on more complicated combinations of the height of the obstacles  $h$ , the length  $\ell$ , and  $Ra$ . In the present study we thus vary  $h$  and  $\ell$  independently and similarly to the 2D study (see Table 12.1 for details).

Second, the roughness configuration is fixed, while  $Ra$  is varied. The latter allows a comparison with experimental and numerical results from the literature.

#### 12.3.1 Heat flux for different roughness configurations

As usual in RBC, we consider the heat flux  $\vec{q}$  by convection and conduction in relation to the heat flux for a fluid at rest. In our units, this is  $\vec{q} = \sqrt{RaPr}\vec{u}T - \vec{\nabla}T$ . From equation (12.2) one can derive that for adiabatic vertical sidewalls, the Nusselt number  $Nu(z) = \langle \vec{q} \cdot \vec{e}_z \rangle_{t,A_s}$  is independent of the vertical position  $z$  for  $h \leq z \leq H - h$  and infinite averaging time. Here,  $\langle f \rangle_{t,A_s}$  denotes the average of the quantity  $f$  over time and the horizontal cross-section  $A_s$  of the domain, i.e. the covering area of the smooth bottom plate. Furthermore, the integral heat flux  $Q = A \langle \vec{q} \cdot \vec{n} \rangle_{t,A}$  entering/leaving the fluid through the bottom/top plates, respectively, must be equal to  $NuA_s$ . Here  $\vec{n}$  is the (local) normal vector of the rough surface and  $A = D(L + 8h)$  is the covering area of the rough top or bottom surface. Thus in the following we will only discuss  $Nu = Q/A_s$  and compare it with the Nusselt number of the smooth case  $Nu_s$ .

In figure 12.3a, the heat flux ratio  $Nu/Nu_s$  is plotted against the relative covering area  $A/A_s$ . This means that the height of the obstacles  $h$  is varied for particular values of the length  $\ell$ . (See also the additional abscissa for the corresponding obstacle height at the top of the plots.) We observe that the  $Nu$ -scaling never reaches the line  $Nu/Nu_s = A/A_s$  (the black dotted line in figure 12.3a), which would indicate that  $Nu/Nu_s$  is directly proportional to  $A/A_s$ . Furthermore,



### 12.3 HEAT FLUX ENHANCEMENT BY ROUGHNESS

TABLE 12.1: Simulation parameters in addition to  $Pr = 0.786$ : the Rayleigh number  $Ra$ , the width of the obstacles ( $\ell$ ), height ( $h$ ) and distance ( $d_x$ ) between the roughness elements, the number of computational nodes  $N_i$  in the  $i$ -direction ( $i = x, y, z$ ), the amount of time units  $\tau$  used for averaging and the Nusselt number  $Nu$  with estimated uncertainty, the relative increase of the plates covering area ( $A/A_s$ ) and of the Nusselt number ( $Nu/Nu_s$ ) in comparison with the smooth case.

$Ra$	$\ell/L$	$d_x/L$	$h/H$	$N_x \times N_y \times N_z$	$\tau$	$Nu$	$A/A_s$	$Nu/Nu_s$
$10^6$	0.025	0.18	0.125	$200 \times 64 \times 128$	700	$10.66 \pm 0.03$	2	1.33
	0.125	0.1	0.125	$200 \times 64 \times 128$	700	$9.39 \pm 0.05$	2	1.17
$3 \times 10^6$	0.025	0.18	0.125	$200 \times 64 \times 128$	300	$16.63 \pm 0.09$	2	1.60
	0.025	0.1	0.125	$200 \times 64 \times 128$	300	$15.05 \pm 0.10$	2	1.45
$10^7$	0.025	0.18	0.025	$282 \times 64 \times 192$	300	$18.04 \pm 0.05$	1.2	1.10
			0.05	$282 \times 64 \times 192$	300	$21.17 \pm 0.06$	1.4	1.29
			0.075	$282 \times 64 \times 192$	300	$23.26 \pm 0.08$	1.6	1.42
			0.1	$282 \times 64 \times 192$	300	$25.29 \pm 0.06$	1.8	1.54
			0.125	$282 \times 64 \times 192$	300	$27.00 \pm 0.05$	2	1.65
			0.15	$282 \times 64 \times 224$	300	$28.43 \pm 0.05$	2.2	1.73
			0.2	$282 \times 64 \times 224$	300	$30.61 \pm 0.17$	2.6	1.87
	0.075	0.14	0.025	$280 \times 64 \times 192$	300	$18.13 \pm 0.07$	1.2	1.11
			0.075	$280 \times 64 \times 192$	300	$22.85 \pm 0.13$	1.6	1.39
			0.125	$280 \times 64 \times 192$	300	$25.09 \pm 0.32$	2	1.53
	0.125	0.1	0.2	$280 \times 64 \times 224$	300	$28.34 \pm 0.08$	2.6	1.72
			0.025	$270 \times 64 \times 192$	300	$18.07 \pm 0.14$	1.2	1.10
			0.05	$270 \times 64 \times 192$	300	$21.03 \pm 0.19$	1.4	1.28
			0.075	$270 \times 64 \times 192$	300	$22.35 \pm 0.13$	1.6	1.36
			0.1	$270 \times 64 \times 192$	300	$23.93 \pm 0.10$	1.8	1.46
			0.125	$270 \times 64 \times 192$	300	$24.41 \pm 0.13$	2	1.49
			0.2	$270 \times 64 \times 224$	300	$26.02 \pm 0.13$	2.6	1.59
$3 \times 10^7$	0.025	0.18	0.125	$282 \times 64 \times 224$	300	$39.49 \pm 0.14$	2	1.72
	0.125	0.1	0.125	$282 \times 64 \times 224$	300	$34.78 \pm 0.18$	2	1.51
$10^8$	0.025	0.18	0.125	$398 \times 128 \times 384$	250	$58.65 \pm 0.22$	2	1.81
	0.125	0.1	0.125	$398 \times 128 \times 384$	325	$51.97 \pm 0.19$	2	1.60

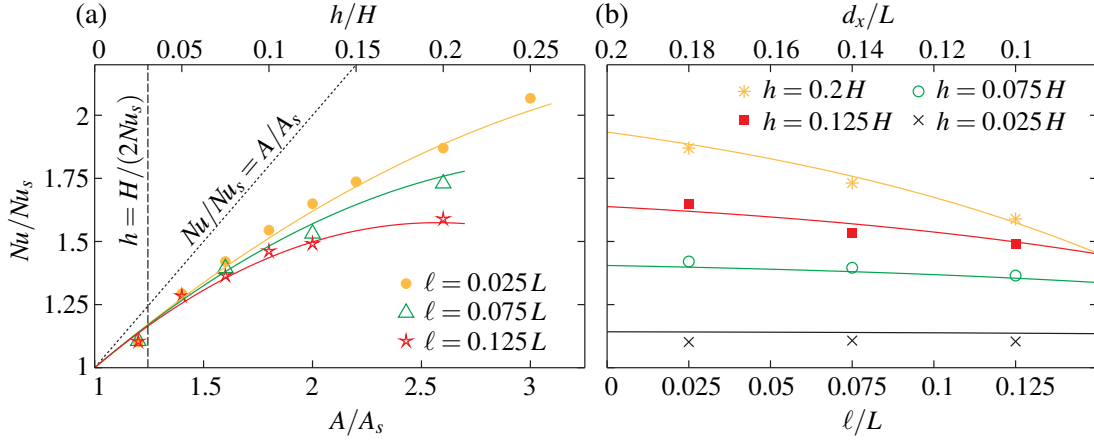


FIGURE 12.3: Influence of the configuration of the obstacles on the relative increase of the Nusselt number from the smooth case,  $Nu/Nu_s$ . The same numerical data for  $Ra = 10^7$  is presented in two different ways: (a) The height of the obstacles  $h$  is varied for different obstacle widths  $\ell$ , which corresponds to an increase of the plates' covering area  $A$  compared to the smooth case  $A_s$ . The black dotted line indicates the case  $Nu/Nu_s = A/A_s$ , while the empirical functions (12.4) for different  $\ell$  are shown as solid lines. A vertical black dashed line indicates the thickness of the thermal boundary layer in the smooth case. (b) For different obstacle heights, the width of the obstacles is varied, which can be also understood as a varying distance  $d_x$  between the obstacles. Solid lines represent (12.4) for different  $h$ .

the larger  $h$  and  $\ell$  get, the stronger is the deviation from this line. This does not mean that  $Nu \geq Nu_s(A/A_s)$  is impossible. For example, in their experiments Du & Tong [40] obtained for  $A/A_s = 1.41$  a relative increase of the heat flux of  $Nu/Nu_s = 1.76$ . The experiments were conducted in a cylindrical container filled with water for  $5 \times 10^8 \lesssim Ra \lesssim 10^{11}$  and with v-shaped grooves in the heating and cooling plates.

The main focus of the present paper is on the influence of regularly distributed obstacles with a height  $h$  larger than the mean thickness of the thermal boundary layer, which can be defined for the smooth case as  $\delta_{T,s} \equiv H/(2Nu_s)$ . Since for  $Ra = 10^7$  we find  $Nu_s = 16.4$  [152] and thus  $\delta_{T,s} \approx 0.03H$ , apart from  $h = 0.025H$  the tips of the obstacles are not hidden in the thermal boundary layer. For clarity we have marked  $\delta_{T,s}$  in figure 12.3a by a vertical black dashed line.

Similarly to Shishkina & Wagner [125] we conclude that the covering area  $A$  is not a universal characteristic for describing the heat flux increase; otherwise all the graphs in figure 12.3a would collapse. Further, figure 12.3 reveals that for small  $A/A_s$  the Nusselt number increases almost linearly with the covering area. For  $A$  larger than a critical value  $A_{\text{crit}}$  (or  $h$  larger than a certain critical height), deviations from this linear dependence become apparent. Thereby  $A_{\text{crit}}$  seems to decrease with increasing  $\ell$ , therefore for large  $A$  the graphs for different  $\ell$  do not collapse. For a fixed covering area and fixed number of obstacles, the largest heat flux enhancement is obtained for small  $\ell$ , i.e. a large distance  $d_x$  between the obstacles. This result is also supported by figure 12.3b, in which for particular values of  $h$  the relative heat flux increase is plotted against

the length of the obstacles  $\ell$ . We observe that especially for large  $h$ , the heat flux decreases with increasing  $\ell$ , while the covering area of the surface remains constant. To achieve a large heat flux, it is thus not sufficient to have a large covering area: there must also be enough space  $d_x$  between the obstacles. For a fixed covering area and increasing obstacle height, larger  $d_x$  is required to obtain the maximum heat flux.

Based on the analysis of the DNS data presented in figure 12.3, we have built an approximation of the relative heat flux deviation due to the regular roughness.

As one can see in figure 12.3a, at least for small obstacle height  $h$ , the relative heat flux increases proportionally to  $h$  and almost independently of the obstacle width  $\ell$ . With further increase in the obstacle height, a certain dependency on the obstacle width  $\ell$  becomes apparent. Therefore, we seek an approximation of the form

$$Nu/Nu_s = 1 + c_1(h/H) + c_2(h/H)^2 f(\ell/L) \quad (12.3)$$

where  $c_1$  and  $c_2$  are constants and the function  $f$  depends only on the obstacle width  $\ell$ . It turns out that the function  $f$  can be well approximated by an exponential function.

The constants  $c_1, c_2$  and the details of the function  $f$  are determined by fitting the DNS data, which leads to the following empirical function describing the heat flux increase by roughness in the considered parameter range

$$\begin{aligned} Nu/Nu_s &\approx 1 + 5.84(h/H) - 5.87 \exp(7.42 \ell/L)(h/H)^2 \\ &= 1 + 0.73r - 0.0917 \exp(7.42 \ell/L)r^2. \end{aligned} \quad (12.4)$$

Here the heat flux increase can be also expressed as a function of the relative increase of the surface area due to the roughness  $r \equiv (A - A_s)/A_s$ . Equation (12.4) is evaluated for the considered  $\ell$  and plotted in figures 12.3a and 12.3b with solid lines. Note that the obtained approximation has an unphysical global maximum outside the considered  $h$ -range. This could be circumvented by a more sophisticated ansatz also valid for even larger  $h$ .

A lower heat flux increase due to roughness, i.e. below the limit  $Nu/Nu_s = A/A_s$ , can be understood as an increased mean thickness of the thermal boundary layer  $\delta_T$  in the rough case compared to the smooth case. For the smooth case we defined above  $\delta_{T,s} \equiv H/(2Nu_s)$ . To get a consistent definition for the rough cases  $\delta_{T,\text{rough}}$ , we have to keep in mind that we used the horizontal cross-section of the domain  $A_s = DL$  for the definition of  $Nu$  and not the actual covering area of the rough surface. Thus, we define

$$\delta_{T,\text{rough}} \equiv (H/(2Nu))(A/A_s), \quad (12.5)$$

so that only for  $Nu/Nu_s = A/A_s$  are the mean thicknesses of the thermal boundary layer in the

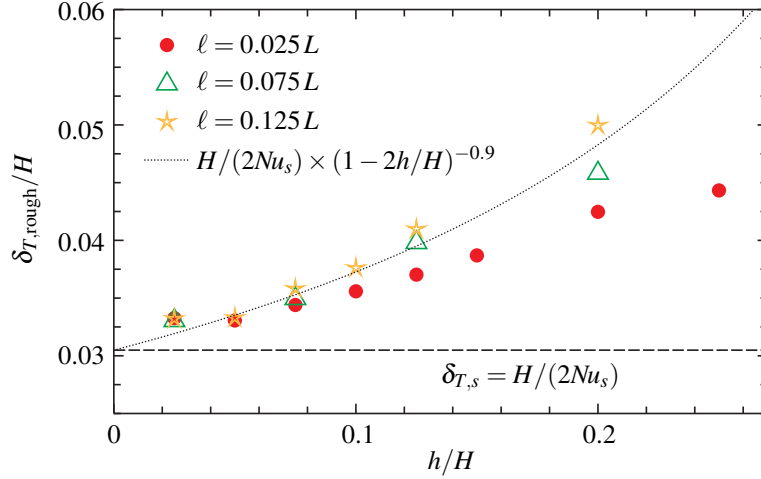


FIGURE 12.4: Comparison of the mean thickness of the thermal boundary layer  $\delta_{T,\text{rough}}$  (for definition, see text) for different roughness configurations and  $Ra = 10^7$ . The black dashed line indicates the smooth case and the black dotted line the limiting approximation (12.6) for extremely wide obstacles.

rough and smooth cases equal. Since we find for all roughness configurations that  $Nu/Nu_s < A/A_s$ , we can deduce that roughness influences the increase of the mean thickness of the thermal boundary layer. Thus,  $\delta_{T,\text{rough}}$  increases for both increasing obstacle height  $h$  and width  $\ell$ .

In figure 12.4, besides the results for  $\delta_{T,\text{rough}}$ , an estimate for wide obstacles is also plotted: for obstacles of width  $\ell = 0.25L$  no space between the obstacles remains. Therefore, the fluid is no longer confined between plates of distance  $H$  but between plates of distance  $H - 2h$ . This leads to an effective Rayleigh number  $Ra_{\text{eff}} = (1 - 2h/H)^3 Ra \leq Ra$ . Thus, when assuming that  $Nu_s \sim Ra^{0.3}$ , which is roughly valid in the considered parameter range [152], we find for the limiting case for extremely wide obstacles with  $\ell = 0.25L$  that  $Nu/Nu_s \approx (Ra_{\text{eff}}/Ra)^{0.3} = (1 - 2h/H)^{0.9}$  and thus

$$\delta_{T,\text{approx}} \approx \delta_{T,s} (1 - 2h/H)^{-0.9}. \quad (12.6)$$

We observed that indeed the DNS results tend to this estimate for growing  $\ell$ . Nevertheless, the estimate does not work as a strict upper bound for the thickness of the thermal BL. The reason for this might be the fact that in the cavities, the relation  $\delta_T = H/(2Nu)$  is only an approximation for the thickness of the thermal boundary layer, and thus it cannot be expected to perfectly represent all the intermediate steps between a smooth plate and obstacles of width  $\ell = 0.25L$ .

To understand the processes leading to the above results in more detail, we decompose the total heat flux entering the container through the heated rough bottom plate  $Q = A \langle \vec{q} \cdot \vec{n} \rangle_{t,A}$  into

### 12.3 HEAT FLUX ENHANCEMENT BY ROUGHNESS

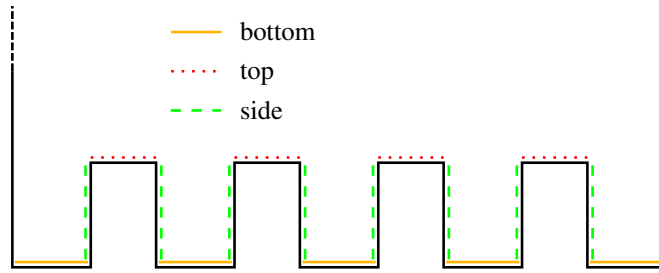


FIGURE 12.5: Two-dimensional sketch and nomenclature for the different contributions to the total heat flux  $Nu$  entering the fluid at the rough bottom plate.

three contributions  $Q_i$ :

$$Q = \sum_i Q_i = Q_{\text{bottom}} + Q_{\text{top}} + Q_{\text{side}}. \quad (12.7)$$

The three contributions correspond to different parts of the rough surface as sketched in figure 12.5.

$Q_{\text{bottom}}$  is the heat flux entering the fluid through the horizontal surfaces between the obstacles, while  $Q_{\text{top}}$  is the contribution from the horizontal surfaces and  $Q_{\text{side}}$  from the vertical surfaces of the obstacles. From these three contributions, we calculate the local Nusselt numbers, defined as

$$Nu_i \equiv \frac{Q_i}{A_i} \quad \text{with} \quad A_i \equiv \begin{cases} 4\ell D, & \text{for } i = \text{top}, \\ 5d_x D, & \text{for } i = \text{bottom}, \\ 8h D, & \text{for } i = \text{side}. \end{cases} \quad (12.8)$$

These  $Nu_i$  can be used to define the thermal boundary layer's local thickness  $\delta_{T,i} \equiv H/(2Nu_i)$ .

Since the heat flux enhancement by an increased covering area of the rough surface can be well understood when considering the integral heat flux contributions  $Q_i$ , we discuss here both  $Q_i$  and  $\delta_{T,i}$ . They are plotted in figure 12.6 against the relative increase of the covering area  $A/A_s$ , for different heights  $h$  and widths  $\ell$  of the obstacles.

We observe that the global heat flux increase over the smooth case is mainly determined by  $Q_{\text{side}}$ , which for small  $h$  increases almost linearly with  $A/A_s$ . Similarly to the case of  $Nu$  in figure 12.3a, deviations from the linear trend are more pronounced for larger  $h$  and  $\ell$  (cf. figure 12.6b,c). These deviations are accompanied by a decrease in  $Q_{\text{bottom}}$  with growing  $\ell$ , while  $Q_{\text{bottom}}$  is almost independent of  $h$ . This can be understood as an effect of the stagnation of warm fluid in the cavities between the heated obstacles. (For the sake of simplicity, we discuss only the heating plate, since the cooling plate leads, by symmetry, to equivalent results.) This warm fluid covers the horizontal surfaces between the obstacles and the lower part of the vertical surfaces of the obstacles. Roughly speaking, figure 12.6 reveals that as soon as  $d_x$  is smaller than

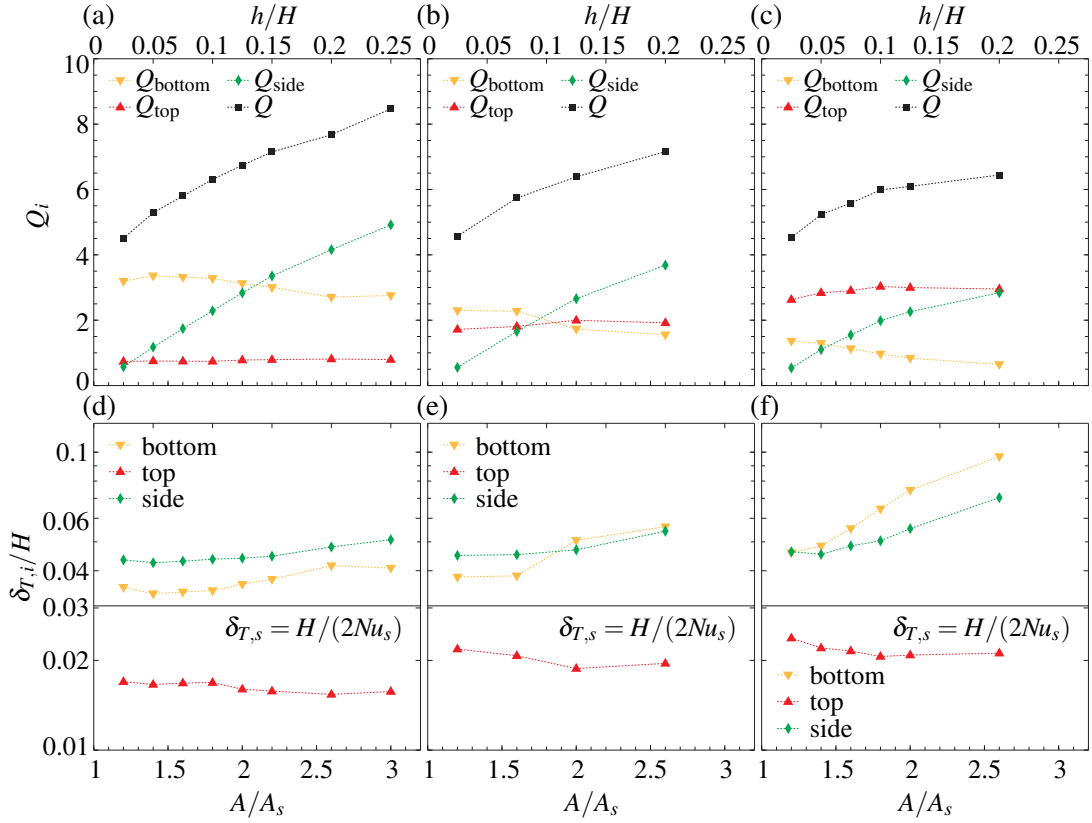


FIGURE 12.6: (a),(b),(c) The different contributions  $Q_i$  to the global heat flux  $Q$  from the top and side surfaces of the obstacles and from the bottom surface between the obstacles. (d),(e),(f) The mean thickness of the thermal boundary layer  $\delta_{T,i}$  at different positions of the rough surface, as defined in the text. For comparison,  $\delta_{T,s}$  for the smooth case is given as a horizontal solid black line. Besides the surface area  $A$  (or the height of the obstacles), also the obstacle width  $\ell$  is varied: (a),(d)  $\ell = 0.025L$ , (b),(e)  $\ell = 0.075L$  and (c),(f)  $\ell = 0.125L$ .  $Ra = 10^7$ ,  $Pr = 0.786$ .

the obstacle height,  $Q_{bottom}$  starts to decrease.

We further consider the thickness of the thermal boundary layer at different parts of the rough surface  $\delta_{T,i}$ . The BL thicknesses  $\delta_{T,bottom}$  and  $\delta_{T,side}$  are larger than those in the case of a smooth heating plate ( $\delta_{T,s}$ ). Only on top of the obstacles is a much smaller thickness  $\delta_{T,top}$  of the thermal boundary layer observed. Since the BL thickness increases along a flat plate [155], it is especially small for slender obstacles (figure 12.6d). For a fixed  $\ell$  and increasing  $h$ , it slightly decreases until a certain threshold is reached, above which  $\delta_{T,top}$  remains almost constant. This threshold is reached when the height of the obstacles and the horizontal distance between them are approximately equal.

From this we can deduce that the increase of the mean thickness of the thermal boundary layer  $\delta_{T,rough}$  (cf. figure 12.4) is mainly caused by the stagnating hot fluid between the obstacles.

Thus we describe the heat flux increase due to roughness (cf. equation (12.4)) in two steps.

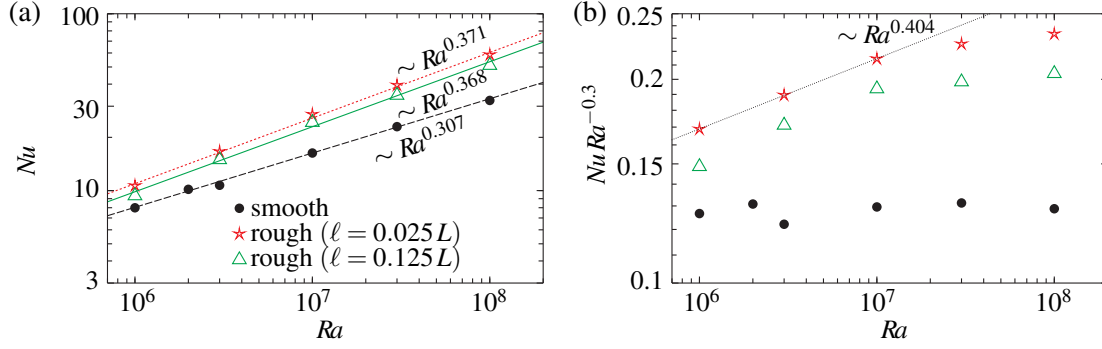


FIGURE 12.7: (a) Comparison of  $Ra$ -scaling of  $Nu$  for the smooth case and rough cases with obstacle widths  $\ell = 0.025L$  and  $\ell = 0.125L$  for obstacle height  $h = 0.125H$  and (b)  $Nu$  reduced by  $Ra^{0.3}$  for a more detailed view. The lines represent linear fits.

First, the contribution from the vertical walls of the obstacles leads to an almost linear and  $\ell$ -independent increase with the obstacle height  $h$ . Second, for large  $h$ , an  $\ell$ -dependent deviation from this trend takes place, which becomes stronger for larger  $\ell$ , i.e. a small distance  $d_x$  between the obstacles. This leads to differences between the heat flux from rough surfaces with equal covering areas as already shown in figure 12.3.

As a consequence, the largest heat flux increase for a fixed number of obstacles and fixed covering area can be achieved for very slender obstacles, i.e. a large distance  $d_x$  between them. In this case, the heat flux in comparison with a smooth plate increases almost linearly with  $h$  even for very large  $h$  and thus the optimal heat flux for a given covering area can be reached.

### 12.3.2 The influence of roughness on the $Ra$ -dependence of the heat flux

Besides the influence of different roughness configurations, we want to compare our results with those from the literature regarding changes in the  $Ra$  dependence of  $Nu$  due to surface roughness. For this comparison, we chose two roughness configurations: rather high and slender obstacles ( $h = 0.125H$ ,  $\ell = 0.025L$ ), and wider obstacles with the same height ( $h = 0.125H$ ,  $\ell = 0.125L$ ). For both configurations, the covering area of the rough plates is twice as big as that of the smooth plates. In Section 12.3.1 we have already obtained for  $Ra = 10^7$  an increase in  $Nu$  of about 65% for the slender obstacles and only about 49% for the wider ones. We vary  $Ra$  between  $10^6$  and  $10^8$  and expect thicknesses of the thermal boundary layers  $\delta_{T,s} \equiv H/(2Nu_s)$  between  $0.015H$  ( $Ra = 10^8$ ) and  $0.065H$  ( $Ra = 10^6$ ). Thus for all considered  $Ra$ , the roughness height  $h$  is at least twice as large as  $\delta_{T,s}$ . Since in the literature a transition from a smooth  $Nu$  vs.  $Ra$  scaling to a rough one for obstacle heights  $h$  of the order of the thickness of the thermal boundary layer  $\delta_{T,s}$  has been reported, we do not expect to find such a transition in the scalings of our numerical results due to larger heights  $h$  considered in our DNS.

In figure 12.7a we compare the  $Ra$ -dependences of the smooth [152] and two rough cases. A

linear fitting reveals, for the smooth case, an average scaling  $Nu_s = 0.116 \times Ra^{0.307}$ , while for the slender obstacles we obtain  $Nu = 0.065 \times Ra^{0.371}$  and for the wider ones  $Nu = 0.061 \times Ra^{0.368}$ . Thus both roughness configurations lead to slightly increased scaling exponents, which is in good agreement with the numerical study by Stringano *et al.* [138], measurements by Qiu *et al.* [105] and the two-dimensional numerical investigation by Shishkina & Wagner [125]. Contrary to the experimental studies by Roche *et al.* [108] and Tisserand *et al.* [146], the scaling exponent is not increased to 0.5. This result is so far interesting, since Tisserand *et al.* [146] used rectangular roughness elements, i.e. rather similar to ours, while Stringano *et al.* [138] considered v-shaped grooves and Qiu *et al.* [105] used square based pyramids. In all these cases a cylindrical domain and larger  $Ra$  were investigated. Thus we conclude that similar results can be obtained even though the roughness configurations are very different. Further, not only the roughness configuration but also  $Ra$  and  $Pr$  determine the changes of the heat flux due to roughness. Understanding the  $Pr$ -dependence goes beyond the scope of the present paper; here we focus only on the  $Ra$ -dependence.

The resulting scaling exponent obtained in our DNS is very similar for both roughness configurations. To get a more detailed view of this, we consider in figure 12.7b  $Nu$  reduced by the scaling in the smooth case, i.e.  $Ra^{0.3}$ . Here it becomes obvious that the power law fits reflect only an average scaling for the considered  $Ra$ -range. For  $Ra \leq 10^7$ , we find an even larger scaling exponent:  $Nu \sim Ra^{0.4}$ —for larger  $Ra$ , the graphs become flatter and, in particular, for wider obstacles, the scaling seems to saturate, with an exponent equal to that of the smooth case, i.e., around 0.3. This means that for a given type of roughness, the influence of that roughness on the scaling exponent becomes weaker with increasing  $Ra$ .

In most of the experiments, which obtained significantly larger exponents, higher  $Ra$  were investigated, e.g. Tisserand *et al.* [146] had  $4 \times 10^{11} \leq Ra \leq 3 \times 10^{15}$ , therefore the above result seems to depend strongly on the roughness configuration (and  $Pr$ ).

So far, we have considered  $Ra$  based on the distance  $H$  between the smooth plates. This choice is somewhat arbitrary, since the consideration of the roughness involves an additional reference length  $d_z$ , which in the case of grooved roughness might be the tip-to-tip distance between the rough top and bottom. Such an interpretation leads to different definitions of  $Nu$  and  $Ra$  as  $Nu_{d_z} = Nu(d_z/H)$  and  $Ra_{d_z} = Ra(d_z/H)^3$  (as long as the aspect ratio influence is weak, which is the case for small  $h$  [168]). Since the height of the obstacles is equal for both our configurations, the tip-to-tip distance  $d_z$  cannot cause a better agreement of the results, but instead a reference length depending on the obstacle width  $\ell$  seems to be a more reasonable choice. Here, we make use of the so-called “equivalent-smooth-wall height”  $H_{esw}$ , which was introduced by Nikuradse [91], and successfully applied to channel and pipe flows with rough walls by Herwig *et al.* [63]. The idea is the following: the height  $H_{esw}$  is chosen in such a way that the volume of the domain with smooth walls and height  $H_{esw}$  is equal to the volume of the domain with rough walls. Thus,



### 12.3 HEAT FLUX ENHANCEMENT BY ROUGHNESS

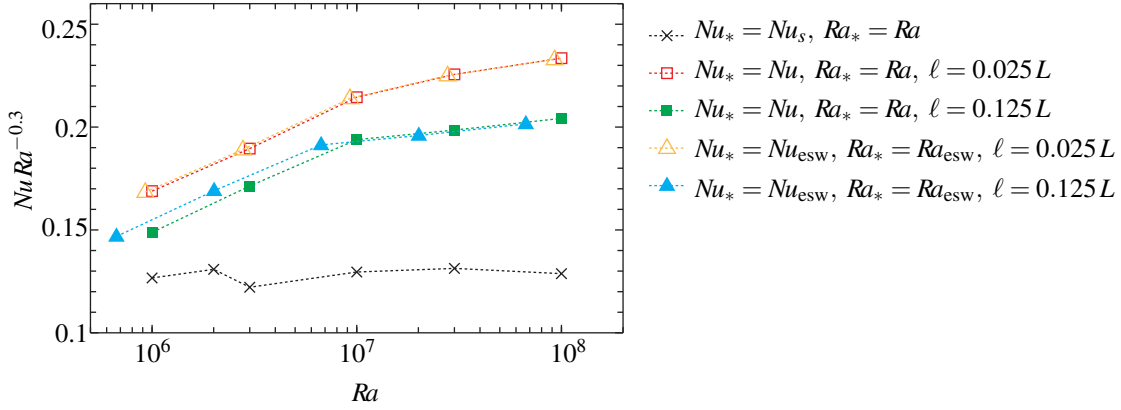


FIGURE 12.8: Comparison of  $Ra$ -scalings for the smooth case and the rough cases with  $\ell = 0.025L$ ,  $h = 0.125H$  and  $\ell = 0.125L$ ,  $h = 0.125H$  for  $Ra$  based on different heights: the usual distance between the smooth plates  $H$  and the “equivalent smooth wall height”  $H_{\text{esw}}$  considered by Herwig *et al.* [63] and Nikuradse [91].

in our case we obtain (cf. figure 12.5)

$$H_{\text{esq}}LD \stackrel{!}{=} HDL - 8\ell hD \implies H_{\text{esw}} = H - 8h\ell/L. \quad (12.9)$$

In figure 12.8, the results from figure 12.7b are plotted together with  $Nu_{\text{esw}} = Nu(H_{\text{esw}}/H)$  against  $Ra_{\text{esw}} = Ra(H_{\text{esw}}/H)^3$ .

It becomes obvious that even though the obstacles are rather high, a different choice of the reference length does not influence the general scaling. This was also pointed out by Du & Tong [40] and Stringano *et al.* [138], who in the case of much smaller roughness elements estimated the influence of the choice to be on the order of the experimental and numerical accuracy, respectively. Therefore it is reasonable to use in our further discussions only the height  $H$  as the reference distance both for rough and smooth walls.

To get further insight into the influence of the roughness on the scaling, we discuss, as in Section 12.3.1, the local thickness of the thermal boundary layer  $\delta_{T,i}$  at different parts of the obstacles. In figure 12.9, the  $Ra$ -scaling of  $\delta_{T,i}$  for the two roughness configurations in comparison to the smooth case is presented. First of all, we observe that on top of the obstacles  $\delta_{T,\text{top}}$  is the smallest and in particular it is smaller than that in the smooth case. Further,  $\delta_{T,\text{bottom}}$  is larger than  $\delta_{T,s}$  in the smooth case. This is in good agreement with the experimental results by Salort *et al.* [109]. Further, for the slender obstacles,  $\delta_{T,\text{top}}$  is smaller than for the wider ones. This is reasonable since the thermal boundary layer thickness increases along the wind path (e.g. Wagner *et al.* [155]) and thus on average  $\delta_{T,\text{top}}$  is expected to be smaller for slender obstacles with less distance along the wind on the obstacle’s top (cf. figure 12.6d,e,f). Similarly,  $\delta_{T,\text{bottom}}$  is larger for the wider obstacles, but here the explanation is different: wider obstacles lead to smaller distances  $d_x$  between the obstacles, which makes it more difficult to wash out the warm

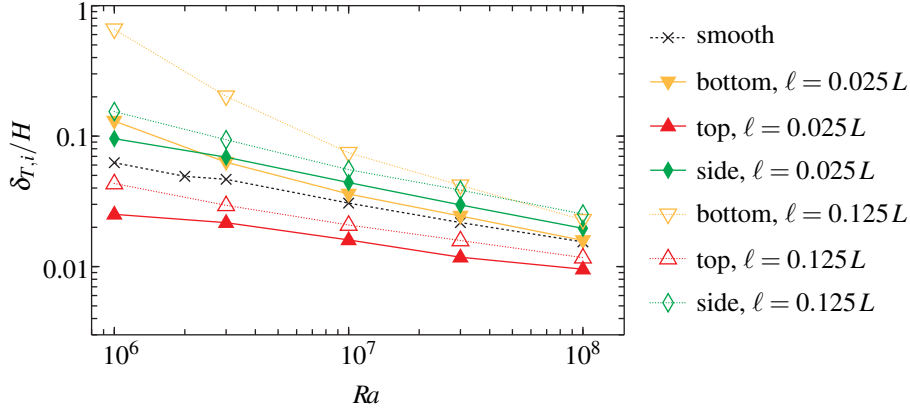


FIGURE 12.9:  $Ra$ -dependence of the thermal boundary layer thickness  $\delta_{T,i}$  at different parts of the rough surfaces (cf. text and figure 12.5) for roughness configurations  $h = 0.125H$ ,  $\ell = 0.025L$  (filled symbols, solid lines) and  $h = 0.125H$ ,  $\ell = 0.125L$  (open symbols, dotted lines) in comparison with the smooth case (crosses, dashed line).

fluid between the wider heated obstacles.

Most interesting for understanding the influence of the roughness on the  $Ra$ -dependence of  $Nu$  is the fact that  $\delta_{T,\text{top}}$  and  $\delta_{T,\text{side}}$  scale similarly to the thermal boundary layer thickness  $\delta_{T,s}$  in the smooth case, and only the scaling of  $\delta_{T,\text{bottom}}$  differs. This allows the interpretation that the ability of the flow to wash the warm fluid out of the cavities between the obstacles increases with increasing  $Ra$ . The reason for this might be the fact that the typical size of the flow structures decreases with increasing  $Ra$ , which makes it possible for the smaller structures to enter the cavities.

Further, for increasing  $Ra$ , the thickness of the boundary layers decreases and thus the core part of the cavities enlarges, which eases the washing-out. Thus, exactly how the roughness influences the  $Ra$ -scaling of  $Nu$  depends on the combination of the size of the typical structures, determined by  $Ra$  and  $Pr$ , and the roughness configuration, i.e. the distance between the obstacles and the shape of the obstacles. Also, of course, the global flow structure, which depends on the geometry of the enclosure [152], might have an influence.

Thus we have found that the  $Ra$ -scaling is similar for slender and wide obstacles (cf. figure 12.7a), which can be explained by the similarity of the two investigated configurations. In the case of an even smaller distance between the obstacles (as in most experimental studies), the influence of the roughness might be much more strongly dependent on  $Ra$ , since, e.g., for small  $Ra$  the warm fluid may completely remain in the cavities. We leave this issue open for future investigations, since the main focus of the present study is on the influence of the roughness configuration for fixed  $Ra$ .

## 12.4 Comparison with theoretical predictions

Here we want to compare the obtained results with the those from the model in Shishkina & Wagner [125] for the heat flux enhancement due to distinct regularly distributed obstacles. The main idea of that model is the decomposition of the total heat flux into the three contributions  $Q_{\text{top}}$ ,  $Q_{\text{bottom}}$ ,  $Q_{\text{side}}$  introduced above, which are modelled separately. The main assumptions of this model are stationary boundary layers, which can be well described by the theory of Prandtl–Blasius and Pohlhausen [see e.g. 121], and obstacles which are much larger than the thermal boundary layer thickness  $H/(2Nu_s)$ . The model is two-dimensional by construction and shows good agreement with DNS results of 2D RBC for  $Pr = 1$  and  $Ra \in \{10^7, 5 \times 10^7, 10^8\}$  and roughness configurations similar to those in the present study.

Due to the fact that the obstacles in the present paper are uniform in the  $y$ -direction, i.e. the additional direction compared to the 2D study, the model can be also verified against our 3D DNS results. For the special case of four obstacles, the estimate for  $Nu$  is

$$Nu = \frac{\sum_i Q_i}{A_s} \approx Nu_s \left( \underbrace{\frac{1}{4} + \frac{3 H_{\text{esw}}}{4 H}}_{\text{bottom \& top}} + \underbrace{\left(\frac{\xi}{2}\right)^{1/4} \frac{8h}{L} \left(\frac{h}{H}\right)^{3/4}}_{\text{side}} \right) \quad (12.10)$$

where  $H_{\text{esw}} = H - 8\ell h/L$  is the “equivalent-smooth-wall height” introduced in Section 12.3.2, and

$$\xi = \begin{cases} bd_x/h, & \text{for } bd_x/h < 1, \\ 1, & \text{otherwise,} \end{cases} \quad (12.11)$$

is the obstacle rarity coefficient with  $0 < \xi \leq 1$  and  $b \approx 0.3$  an empirical parameter.

First of all it should be pointed out that the model does not describe any changes in the  $Ra$  dependence of  $Nu$  due to roughness. This becomes quite obvious when writing the model in a simplified way as  $Nu = G(h, \ell)Nu_s$ , where  $G(h, \ell)$  describes the roughness configuration. Thus, for fixed roughness, the model predicts that  $Nu$  can be obtained from  $Nu_s$  by multiplication by a constant. Thus the 2D model cannot predict the increased scaling exponent due to roughness, which is observed in particular for  $Ra \leq 10^7$ . Since the scaling exponent seems to saturate for very large  $Ra$  to the scaling observed in the smooth case, the model may perform better at that point when considering  $Ra \gg 10^8$ .

In figure 12.10, the heat flux predictions of the model for the horizontal ( $Q_{\text{top}} + Q_{\text{bottom}}$ ) and vertical surfaces ( $Q_{\text{side}}$ ) are compared with the 3D DNS results for  $Ra = 10^7$ .

As depicted in figure 12.10a, the model can not reproduce more than the correct order of magnitude of the deviation from the smooth case (indicated by a horizontal dotted line) when comparing the contributions from the horizontal surfaces. With respect to  $Q_{\text{side}}$  in figure 12.10b,

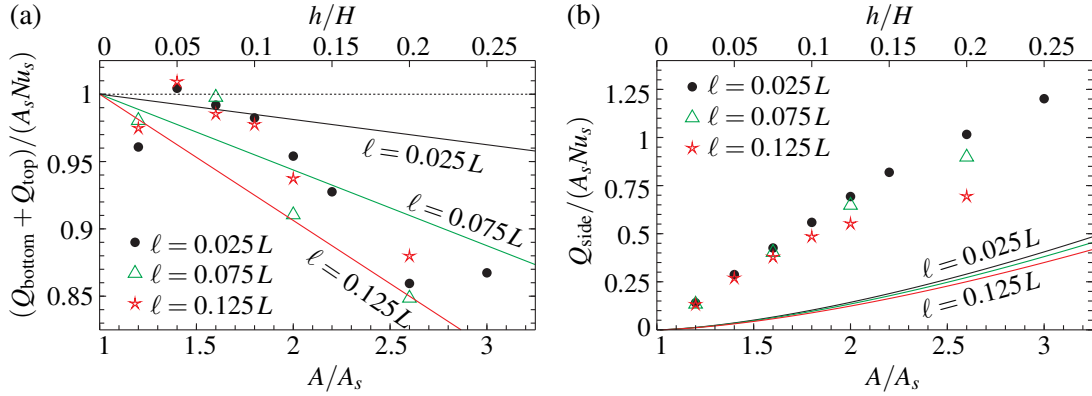


FIGURE 12.10: Comparison of the predictions by Shishkina & Wagner [125] with the DNS results for the heat flux from (a) the horizontal surfaces  $Q_{\text{top}} + Q_{\text{bottom}}$  and (b) the vertical surfaces  $Q_{\text{side}}$  for  $Ra = 10^7$ . The solid lines represent the model predictions for different widths of the obstacles  $\ell$ .

the model strongly underestimates the DNS results, which in total leads then to a strongly underpredicted total heat flux enhancement by the roughness.

The reason for this underestimation might be the assumption of the Pohlhausen theory for infinite vertical heated surfaces [82, 99]<sup>1</sup>, which neglects the occurrence of thermal plumes. The latter are present in particular at the obstacles edges [40, 138]. Furthermore, uplift next to the obstacles' vertical walls is expected to be only caused by buoyancy, i.e. driven by the temperature gradient next to the vertical wall. This estimate might lead to velocities that are far too small, since the flow between the obstacles is also partly driven by the large-scale circulation in the full cell. Further, the global flow structures in the core parts of the convection cells differ in the 2D and 3D cases, which also influences the processes of washing-out of the fluid from the cavities between the isothermal roughness elements. These issues are further discussed in the next section.

## 12.5 Flow structure and velocity statistics

It is well known that in turbulent thermal convection of a fluid with  $Pr \lesssim 1$  and large enough Rayleigh number, a large-scale circulation (wind) of the fluid develops in the bulk, i.e. the core part of the convection cell. This holds for both types of convection cells, with smooth and rough walls (see figure 12.2). The wind direction and its magnitude influence the flows that develop in the cavities between the isothermal roughness elements. In this section we discuss in more detail the wind and the cavity flows and related time-averaged characteristics, and analyse how they are influenced by a particular roughness geometry.

In RBC, the large-scale circulation of the fluid may reverse its direction [139] on time-scales

<sup>1</sup>By mistake in the original paper the wrong reference ‘‘Pohlhausen [100]’’ was used.

## 12.5 FLOW STRUCTURE AND VELOCITY STATISTICS

of the order of the simulated time. If such a process takes place, time-averaged fields are strongly influenced and no longer represent the flow structure. To circumvent this, we consider only time-intervals for averaging without such flow reversals. The latter information is obtained from instantaneous flow fields, saved with a sampling rate of four per time-unit  $(\widehat{H}/(\widehat{\alpha}\widehat{g}\widehat{\Delta}))^{1/2}$ . The instantaneous velocity field at half depth is decomposed into several modes, as described in detail by Wagner & Shishkina [152] and similarly by Chandra & Verma [29]. The time-histories of the contributions of these modes is then used to evaluate the direction of the large scale flow.

In figure 12.11 the time-averaged temperature distributions with superposed velocity vectors are presented for two particular roughness configurations:  $h = 0.125H$  and  $\ell = 0.025L$  or  $\ell = 0.125L$ , as they were obtained in the 2D DNS for  $Pr = 1$ ,  $Ra = 10^8$  [125] and in the present 3D DNS for  $Pr = 0.786$ ,  $Ra = 10^7$ , in the central vertical cross-section. In the two-dimensional case (figure 12.11a,c) one observes an almost circular movement of the fluid, while in the three-dimensional case (figure 12.11b,d) the wind exhibits its three-dimensional spiral structure. Thus in the 3D case the fluid can move along the length of the obstacles, in the direction orthogonal to the cross-sections presented in figure 12.11b,d. Such a fluid movement eases the emission of the thermal plumes from the heated surfaces of the roughness elements, and as a result the wind can remove more heat from these surfaces than in the 2D case.

To analyse the effect of the regular roughness on the large-scale circulation and the flows between the obstacles, we evaluate the time-averaged vertical profiles of the velocity magnitude, which are presented in figure 12.12. Close to the bottom plate, for  $z \leq h$ , the averaging is performed only for the fluid regions, while above the roughness elements, for  $z > h$ , the profiles are averaged over the whole horizontal cross-section. Figure 12.12a,b,c reveals that the wind is always stronger than the mean secondary flow in the cavities between the obstacles. If for a fixed Rayleigh number a certain change of the geometry (the obstacle height or width) leads to a decrease (or increase) in the velocity magnitude of the secondary flow, then in contrary, the magnitude of the wind increases (or decreases).

From the comparison of the profiles for  $Ra = 10^7$  in the cases of slender obstacles (figure 12.12a,  $\ell = 0.025L$ ) and wide obstacles (figure 12.12b,  $\ell = 0.125L$ ), we conclude that the secondary flow is generally stronger if the distance between the roughness elements is large enough, i.e. the obstacles are slender, while the wind close to the upper boundaries of the obstacles is stronger for wide obstacles. This is consistent with the fact that in turbulent thermal convection, the wind accelerates along its path, close to the heated surfaces [70, 155], therefore the presence of wide roughness elements generally leads to a stronger wind above them.

If the Rayleigh number and the height of the regular roughness are fixed and the width of the obstacles is varied, the mean vertical profiles of the velocity magnitude reveal three main regions of the dominance of different tendencies activated by the roughness, as depicted in figure 12.12c. In the first region, within the cavities between the obstacles, the mean flow is stronger for slender obstacles that retain enough space between the roughness elements. The second region, which

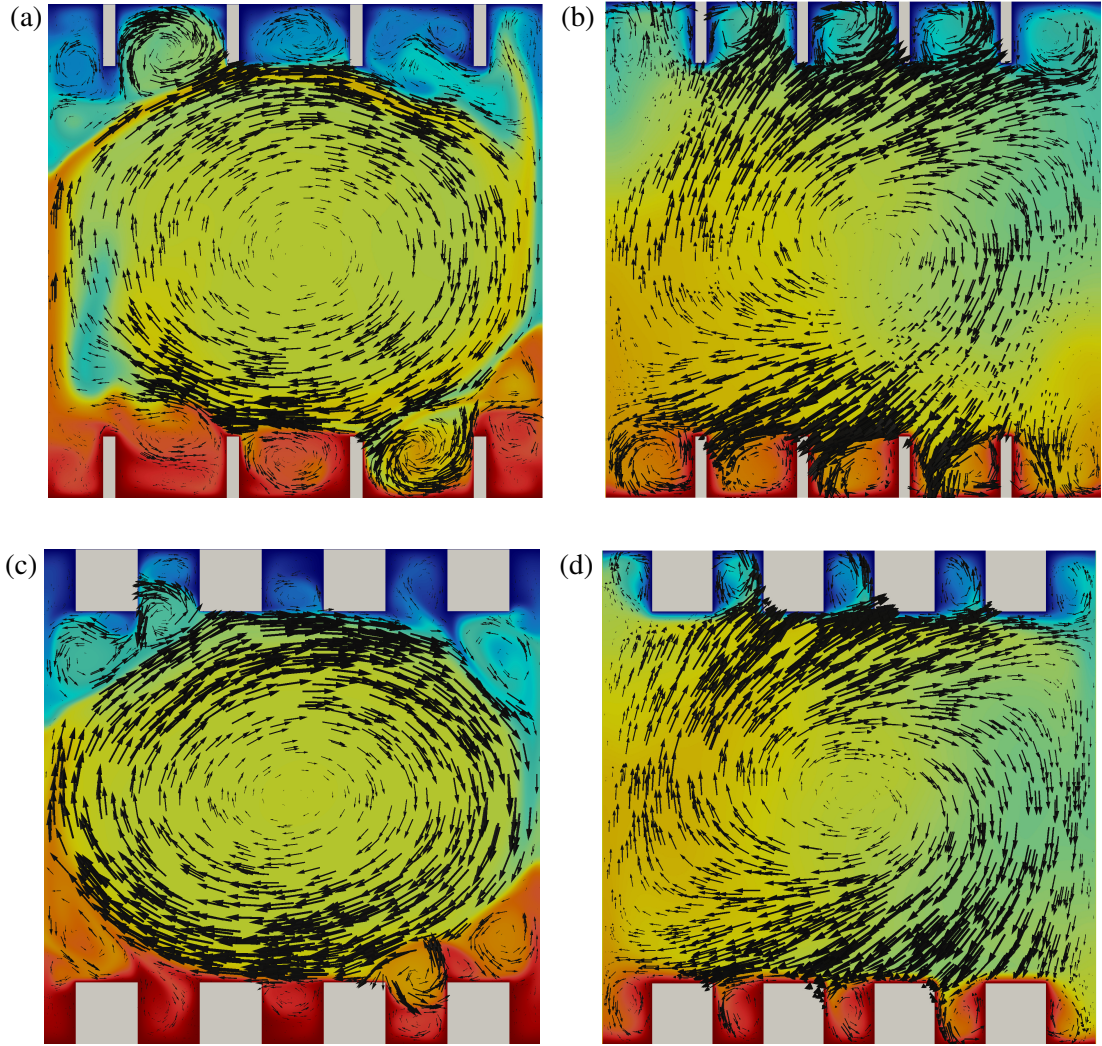


FIGURE 12.11: Time-averaged temperature distributions with superposed randomly distributed velocity vectors for different roughness configurations: (a, b)  $h = 0.125H$ ,  $\ell = 0.025L$ ; (c, d)  $h = 0.125H$ ,  $\ell = 0.125L$  as obtained in (a, c) 2D DNS for  $Ra = 10^8$ ,  $Pr = 1$  [125], and (b, d) 3D DNS for  $Ra = 10^7$ ,  $Pr = 0.786$ , in the vertical slice at a half depth. Colour scale goes from blue ( $\hat{T}_{\text{top}}$ ) to red ( $\hat{T}_{\text{bottom}}$ ) and the length of the vectors represents the magnitude of the in-plane velocity at the arrows' tails.

extends from the upper boundaries of the obstacles to about one-third of the convection cell, the wind is stronger for wider roughness elements. Finally, in the core region of the convection cell, the wind is generally stronger for slender obstacles.

It should be noted that for the nondimensionalisation, the reference velocity  $\sqrt{\hat{\alpha}\hat{g}\hat{\Delta}\hat{H}} \sim \sqrt{Ra}$  has been used. Thus, when comparing the results for different Rayleigh numbers in figure 12.12d, the increase in all regions means that the velocities increase more rapidly than  $\sqrt{Ra}$ .

The above described tendencies are also supported by the analysis of the time-averaged

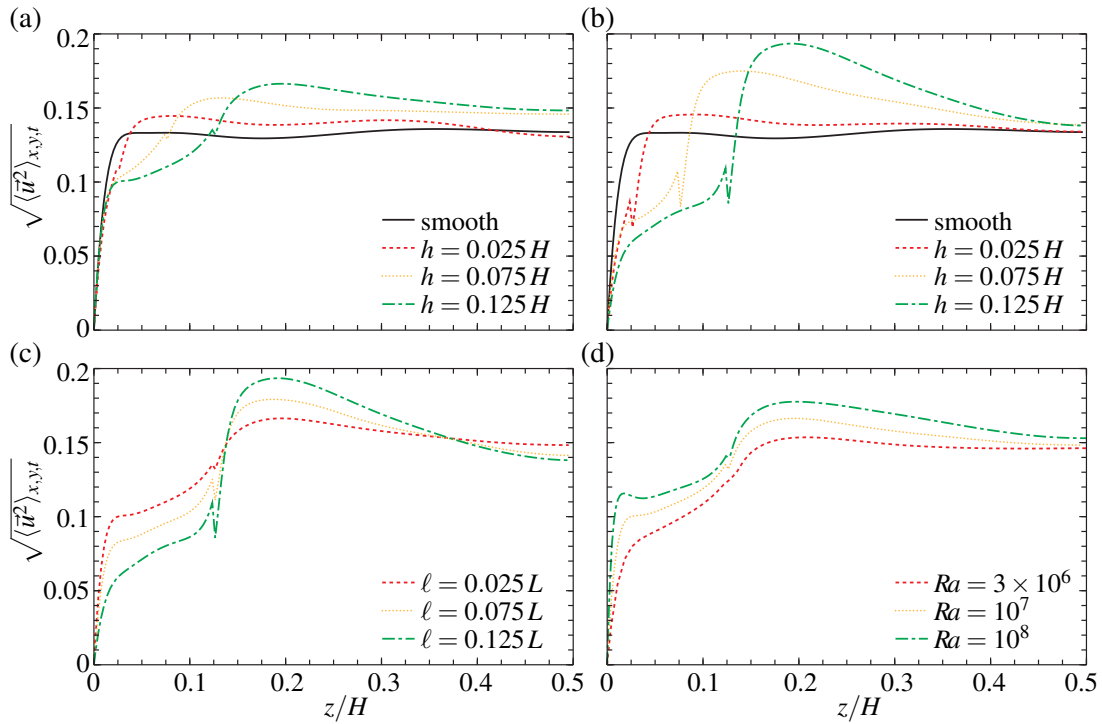


FIGURE 12.12: Vertical profiles of the time and spatially averaged velocity magnitude  $\sqrt{\langle \bar{u}^2 \rangle_{x,y,t}}$ . For  $z \leq h$  the averaging in the  $x$ -direction is performed only over the fluid regions, which leads to discontinuities at  $z = h$ . Profiles for (a)  $\ell = 0.025L$  and (b)  $\ell = 0.125L$  and different  $h$  and (c) for  $h = 0.125H$  and different  $\ell$ , with  $Ra = 10^7$ . (d)  $Ra$ -dependence of the profiles for  $h = 0.025H$  and  $\ell = 0.125L$ .

probability density functions of the local instantaneous velocity magnitude  $|\bar{u}|$ . The probability density functions are evaluated separately for the cavity regions between the obstacles and the remaining core part of the convection cell, as presented in figure 12.13. For a fixed Rayleigh number and fixed width of the roughness elements (figure 12.13a,  $Ra = 10^7$ ,  $\ell = 0.025L$ ) the most probable velocity increases both in the cavity and in the bulk, if the height of the obstacles is increased. In the case of a fixed Rayleigh number and fixed height of the roughness elements and varying obstacle width (figure 12.13b,  $Ra = 10^7$ ,  $h = 0.125H$ ), the tendencies in the cavities and in the bulk are the opposite: with increasing  $l$ , the most probable velocity in the cavities decreases, while that in the bulk increases. As already discussed above, an increase in the obstacle width impedes the development of strong secondary flow structures between the roughness elements but favours the acceleration of the wind above the obstacles. Finally, an increase in the Rayleigh number (figure 12.13c) always leads to an increase in the most probable velocity, both in the cavity and in the bulk regions.

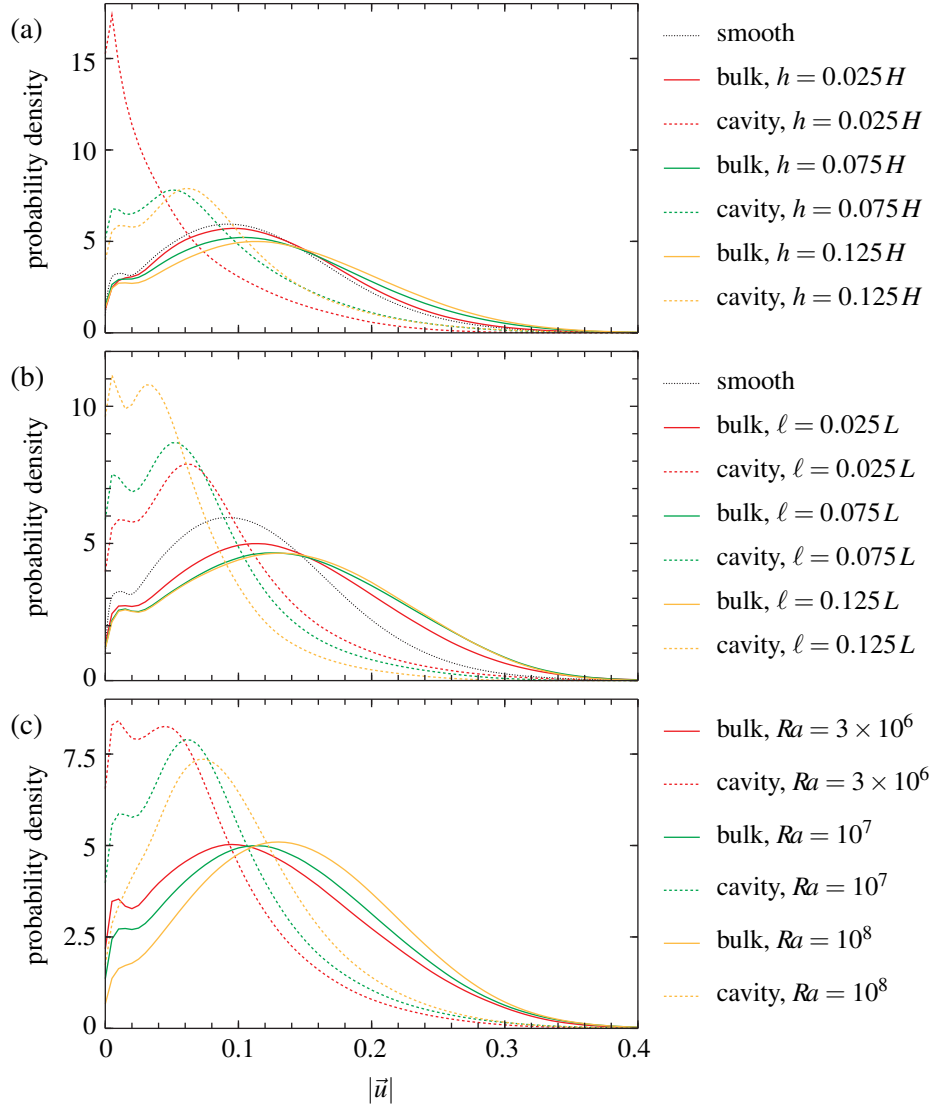


FIGURE 12.13: Probability density function of the velocity magnitude in comparison with the smooth case [152] for (a) different obstacle heights and  $\ell = 0.025L$ ,  $Ra = 10^7$ ; (b)  $h = 0.125H$  and different  $\ell$ ,  $Ra = 10^7$ ; (c)  $h = 0.125H$ ,  $\ell = 0.025L$  and different  $Ra$ . For the rough cases, the PDFs are taken separately for the bulk region, i.e.  $h < z < H - h$  and the cavity region, i.e.  $0 \leq z \leq h$  and  $h - H \leq z \leq H$ .

## 12.6 Conclusions

Direct numerical simulations (DNSs) of the turbulent thermal convection in parallelepipedal domains with rough heated and cooled surfaces were conducted, in which the length, height and depth of the domains are related as 1:1:0.25. In all the simulations, the Prandtl number is equal to  $Pr = 0.786$ , while the Rayleigh number  $Ra$  varies between  $10^6$  and  $10^8$ . The surface roughness is introduced by four box-shaped equidistantly distributed obstacles attached to the



heating bottom plate and four obstacles located symmetrically on the cooled top plate.

The effect of the roughness was investigated in two ways: first, for a fixed Rayleigh number ( $Ra = 10^7$ ) and changing roughness configurations and, second, for fixed roughness types, while varying the Rayleigh number.

As in the 2D study of [125], we obtained that a relative increase in the covering area of the heated/cooled surfaces is not a universal parameter that determines the relative change of the mean heat flux measured by the Nusselt number. Our 3D DNS showed that if the distance between the obstacles is large enough, an almost linear increase of the Nusselt number with the covering area remains longer for slender obstacles, which helps the fluid stagnating between the isothermal obstacles to be washed out from the cavities from time to time. Our DNS results in the considered parameter range are well represented by the empirical function (12.4) presented in this paper to estimate the heat flux increase due to roughness.

The analysis of the local thermal boundary layer thicknesses showed that the thinnest boundary layer develops at the top of the obstacles, and for similar  $Ra$  and  $Pr$  it is always smaller than the BL thickness in the case of a smooth heated/cooled surface. The thickness of the thermal BL at the top of the obstacles is especially small for slender roughness elements. In contrast to the BLs attached to the obstacles' top, the boundary layers near the bottom or vertical sides of the obstacles are always thicker than those in the case of a smooth heated/cooled surface.

For two particular roughness configurations, with slender and wide obstacles but the same covering area of the surfaces ( $\ell = 0.025L, h = 0.125H$  and  $\ell = 0.125L, h = 0.125H$ ), the effect of the roughness on the  $Nu$  vs.  $Ra$  scaling was investigated. It was obtained that the scaling exponent changes from about 0.31 for smooth walls to about 0.37 for both types of rough walls. Again, the strongest effect was observed for the slender roughness elements. A closer look showed that the largest value of the exponent, about 0.40, corresponds to smaller Rayleigh numbers, about  $Ra \approx 10^6$ , while for  $Ra > 10^7$  it reduces and thus the difference between the scaling exponents for  $Ra \approx 10^8$  in the cases of the rough and smooth walls becomes smaller, especially for wide roughness elements. The analysis of the  $Nu$  vs.  $Ra$  scaling with respect to the so-called "equivalent-smooth-wall height"  $H_{esw}$  led to the same result. The thicknesses of the thermal boundary layer at different parts of the roughness elements scale generally in a similar way, both for rough and smooth surfaces. Only near the bottom between the obstacles is the scaling different for small Rayleigh numbers, for which the bottom and two vertical thermal BLs in the cavities between the isothermal obstacles merge, almost fill the cavities, and thus impede the development of a strong enough flow in the cavities.

The 3D DNS results were also compared with the 2D model [125] and agreed well with the 2D DNS for a similar roughness structure. In case of the 3D DNS, large deviations from the 2D model were observed. They are mainly due to a strong underestimation of the heat flux from the vertical walls. The obtained deviation is explained by the essential three-dimensionality of turbulent convective flows, which was not taken into account by the model, and by the fact

that the flows in the cavities between the isothermal obstacles are caused not only by buoyancy but also by the large-scale circulation of the fluid in the core part of the convection cell. For similar configurations of regular roughness, the structure of the large-scale circulation in the two-dimensional and three-dimensional convective flows are also different: in the 3D case the wind exhibits a 3D spiral-like structure, which eases the heat transport from the rough surfaces.

A comparison of the time-averaged vertical profiles of the kinetic energy for different roughness configurations showed that the mean secondary flow in the cavities between the obstacles and the wind, which is always stronger than these secondary flows, are related and can be influenced by the geometry of the regular roughness in such a way that the strengthening (weakening) of one of them leads to the weakening (strengthening) of the other. Thus, wide obstacles impede the flow between them but contribute to the acceleration of the large-scale circulation.

Generally, the growth of the roughness height leads to stronger flows both in the cavities and in the bulk region, while an increase in the obstacle width accelerates only the large scale circulation of the fluid and decelerates the secondary flows between the roughness elements. Any increase in the Rayleigh number leads to stronger flows, both in the cavities and in the bulk.

Further investigations of the influence of regular roughness on the heat and mass transfer in natural convection is needed, in particular issues related to the dependencies on the Prandtl number and the Rayleigh number for large  $Ra$ . The development of a model to predict the heat flux enhancement due to regular wall roughness that takes into account the three-dimensionality of the flows and the influence of the wind on the secondary flows between the obstacles should also be addressed in the future.

The authors acknowledge support by the German Research Foundation (DFG) under grant SH405/3-1.

## Part III

# Conclusions



## 13 Summary

Within seven publications the boundary layers and the global flow structure of turbulent Rayleigh–Bénard convection (RBC) in finite size containers were studied by means of Direct Numerical Simulations (DNSs). As the single publications are closed each by detailed conclusions, only a broad overview connecting the publication’s outcome is given here.

Methods for the extraction of the wind in cylindrical containers and the corresponding boundary layer structure close to the heated bottom plate were introduced and tested (cf. chapter 6). One of the main difficulties of the above mentioned DNS study was, that for the considered Rayleigh numbers in a cylindrical domain the global flow performs azimuthal reorientations and similar transient processes. To separate such transient processes from the remaining dynamics of the flow, knowledge about the instantaneous temperature and velocity field is required. For this purpose, about 80 instantaneous three-dimensional temperature and velocity fields were saved in each turnover of the global flow, which allowed an a posteriori analysis. This idea of saving all the information is applied throughout the whole results part of the thesis. As discussed in section 11.2 this sampling rate is sufficient for resolving the large scale dynamics but is not sufficient for resolving the Kolmogorov time scale for the largest considered Rayleigh numbers. Nevertheless, this technique of saving all the instantaneous information requires enormous amounts of memory. This limits the feasibility of DNS at large Rayleigh numbers in accordance to the large required computational power (cf. chapter 4).

The boundary layer structure obtained in the DNSs for different Rayleigh numbers  $Ra$  was compared to the commonly used theoretical description by Prandtl–Blasius–Pohlhausen (PBP). In the latter theory laminar boundary layers caused by a constant wind, which passes by a semi-infinite flat plate, are considered. The comparison revealed various disagreements in particular with respect to the spatial development of the boundary layer thickness and the ratio of the thicknesses of the thermal and viscous boundary layers. Those disagreements were attributed to violations of the basic assumptions of this theory, namely the neglect of fluctuations, buoyancy and pressure gradients. Perhaps most crucial is the fact that the wind along the bottom plate was found to be not constant but varying in a parabolic way along the plate. A reasonable extension of the PBP approach was therefore the consideration of a pressure gradient, since it does not vanish for flows approaching a flat plate under a certain angle of attack. Such an angle of attack is present in RBC as the flow falls or rises close to the vertical sidewalls and is redirected when approaching the horizontal plates. The boundary layer equations were extended

with respect to such a pressure gradient resulting in a velocity boundary layer equation of the Falkner–Skan (FS) type allowing the solution by a similarity ansatz (cf. chapter 8). The temperature boundary layer equation remained unchanged and was thus of the Pohlhausen type. The angle of attack of the flow approaching the horizontal plates was found to be independent of the Rayleigh number for  $10^6 \leq Ra \leq 10^8$  and the Prandtl number for  $0.1 \leq Pr \leq 10$  (cf. chapter 9). Considering this constant angle of attack, the agreement between DNS and the boundary layer theory was significantly improved with respect to the ratio of the thicknesses of the thermal and viscous boundary layers. Apart from this ratio, for example when considering the temperature profiles in the boundary layer region, the disagreement between DNS and theory was found to be still present. Those remaining discrepancies of the theory manifest the fact that buoyancy and fluctuations remained neglected. Furthermore, in a finite box the flow structure and thus also the pressure gradients are much more complicated than considered in theory.

In the context of DNS an important application of boundary layer theory is the estimation of the required spatial resolution. It was found that the estimates based on the PBP theory [121] strongly underestimate the required boundary layer resolution, which means that the estimates are not restrictive enough (cf. chapter 7). Most crucial for building this estimate is the ratio of the thicknesses of the thermal and viscous boundary layer. Since the improved boundary layer theory was found to be in better agreement with the DNS results with respect to this quantity, it was reasonable to build new estimates based on this theory. As discussed in chapter 9, the consideration of an angle of attack in the boundary layer theory also significantly improves the estimation of the required boundary layer resolution.

To avoid the mentioned transient processes occurring in a cylinder, the containers geometry was changed to a box-shaped one for further studies. This idea was pursued in chapters 10 and 11, in which results for cubic and quasi two-dimensional containers were compared with previous results obtained in a cylinder. In the cubic container, the global flow structure changed for a Rayleigh number of about  $10^6$  from a flow parallel to two opposite sidewalls to a complicated diagonal flow. This change led to drops in the mean heat flux, and in the mean kinetic energy below the corresponding results obtained in a cylinder (cf. chapter 10). In analogy to experiments in water at Rayleigh numbers up to  $10^{12}$  [167], such a diagonal flow can be avoided by considering quasi two-dimensional RBC in a domain of equal height and length but rather small depth. It was therefore studied if the aspect ratio of depth per height influences the flow structure, the mean heat flux and the mean kinetic energy (cf. chapter 11). The global flow structure was analyzed by a decomposition of instantaneous flow fields into predefined two-dimensional modes. This analysis revealed that in the considered Rayleigh number range, a single roll state, i.e. a quasi two-dimensional flow, was present for the aspect ratio of one fourth at sufficiently large  $Ra$ . For lower  $Ra$  and smaller aspect ratio a mixture of different modes was obtained. In particular it was found that a four-roll structure, which was connected to movement through the centre of the box, dominated as soon as the flow was unsteady. Furthermore, the

mean heat flux reached the values for the cylindrical container for high Rayleigh numbers of about  $10^8$ . This allowed the conclusion that quasi two-dimensional RBC can be studied also in DNSs, even though the Rayleigh numbers are some decades smaller than in the corresponding experiments.

Furthermore, RBC was investigated for such a container with additional rough heating and cooling plates (cf. chapter 12). Ordered roughness was introduced by equidistantly spaced obstacles, which have the same temperature as the surface they are attached to. The number of obstacles on each plate was fixed to four and the vertical and horizontal extent of the obstacles as well as the Rayleigh number were varied. These were so far the only three-dimensional DNSs, in which the influence of different roughness configurations was studied. The investigations confirmed experimental results stating that the size of the covering area of the rough surfaces is not sufficient to describe the heat flux increase caused by the roughness. For fixed Rayleigh number of  $10^7$ , an empirical function was given describing this heat flux increase in dependence of the obstacles height and width. It further revealed that for constant covering area, the largest heat flux can be achieved for slender obstacles, i.e. large space between the obstacles. In contrast to some of the experiments it was shown, that for none of the considered configurations the relative heat flux increase was larger than the ratio of the rough and the smooth covering areas. In terms of the Rayleigh number dependence of the heat flux, the study showed, that the roughness causes an increased effective scaling exponent as it was also obtained in some of the experiments. A closer look revealed that for the largest studied Rayleigh numbers the scaling saturates to the one for the smooth plates.





## 14 Outlook

Even though Rayleigh–Bénard convection (RBC) has been investigated for more than a century, there are still many open questions in particular about the turbulent state. Apart from all the questions, which cannot be answered within this thesis e.g. because of the small accessible parameter range, there are open questions, which are directly connected with the presented results.

**Boundary layer analysis** In chapter 6 the wind and the boundary layers close to the heated bottom plate were analysed. For symmetry reasons, it is expected that similar results can be also obtained, when considering the cooled top plate. But, as figures 8.9 and 9.5 indicate, at the vertical sidewall the situation is different due to the corner roll, connected with the redirection of the flow. As proposed by Grossmann & Lohse [53], a different scaling of the viscous boundary layer thickness at the horizontal and the vertical wall with the Rayleigh number, may lead to differences in the heat flux. Therefore, a further study of the viscous boundary layer close to the vertical wall, seems to be reasonable.

Due to the adiabaticity of the vertical sidewall, a thermal boundary layer is not present there. Nevertheless, the presence of the sidewall might be visible in the distribution of the thermal dissipation rates, which can be analyzed by the *dissipation layer* ansatz recently introduced by Petschel *et al.* [96]. The thickness of the dissipation layers is thereby defined similar to the boundary layer thickness as in section 6.5.1; instead of the horizontal velocity and the temperature, the viscous and thermal dissipation rates are considered. The dissipation layers close to the heated plate show quantitative difference to the boundary layers considered in chapter 6, but have also similarities. Most crucial is the fact reported by Petschel *et al.* [96], that the viscous boundary layer can never become thicker than the thermal one, even for very large Prandtl numbers. Contrary, the thickness of the viscous dissipation layer, becomes larger than the thermal one for a Prandtl number of about one. Understanding the relation between these two types of layers and the consequences for the boundary layer theory in particular for different Prandtl numbers is an open question for future research.

**Boundary layer theory** In chapters 8 and 9 the boundary layer theory of Prandtl–Blasius–Pohlhausen was extended to non-vanishing pressure gradients parallel to the heated plate. Even though this led to strongly improved estimates for the ratio of the thermal and viscous boundary

## 14 OUTLOOK

layer thicknesses, in particular for large Prandtl numbers there was still an apparent difference between theory and DNS results. The boundary layer theory is only an approximation of the full set of equations (2.1). Three assumptions seem to be thereby the most questionable: the neglect of buoyancy and fluctuations and the simplification of the geometry. In section 8.3 it was argued that buoyancy can be neglected, as long the large scale flow is much faster than the purely buoyant one, which is correct for Prandtl numbers of order one. Nevertheless, for large Prandtl numbers, this assumption may not longer hold, and the boundary layer structure may approach the limit considered by Stewartson [137]. In between these two extreme cases, a mixture of the model by Stewartson [137] and the model presented here may be a better description of the boundary layers in turbulent RBC, but the existence of a similarity solution, as in the single cases, should be investigated.

A more realistic geometry (e.g. a square box in two-dimensions) should be also considered, which may lead to a more complicated pressure distribution, e.g. as obtained in the DNSs by Shi *et al.* [118]. Without a similarity solution, the boundary layer equations may be difficult to solve analytically, but a numerical solution could clarify the influence of the geometry.

**Quasi two-dimensional RBC** In chapter 11, the influence of the aspect ratio (of depth per height for a box with equal height and length) on the mean heat flux was studied, amongst others. For a Prandtl number of about 0.8 and Rayleigh numbers between  $10^5$  and  $10^7$  a decrease of the heat flux with the aspect ratio was found. Only a few weeks after the publication of this paper ([152]), Huang *et al.* [68] reported on a similar study for Prandtl number 4.3 and Rayleigh numbers up to  $2.5 \times 10^9$ . Their experiments and DNSs revealed a heat flux increase for decreasing aspect ratio, which is contrary to the results presented here. Most interesting is the fact, that they also found changes in the global flow structure and thermal plumes rising and falling in the center of the domain (and not close to the walls as expected). They described, that this change is responsible for the increased heat flux, while in chapter 11 it was argued, that such a global flow structure may cause a decreased mean heat flux. As they used the same numerical method and the spatial resolution was also similar, the disagreement of the results can only be caused by the different Rayleigh and Prandtl numbers. Some recent results, which are not presented here, for Prandtl number 0.8, larger Rayleigh numbers also up to  $10^9$  as in their DNSs, and even smaller aspect ratios still do not show any significant heat flux increase. Therefore the Prandtl number is expected to be the crucial parameter. Perhaps a more sophisticated investigation of the heat transport processes, which take place in the center of the domain for small aspect ratio, can shed more light on this issue.

**Roughness** In chapter 12 the results of the first DNS study of RBC with different roughness configurations were given. Many of the experimental studies in the literature disagree with respect to the heat flux increase, which can be achieved by rough heating and cooling plates

in comparison to smooth ones. One of the reasons commonly given for this disagreement is the fact, that different roughness configurations are used. In the presented DNS study, regular roughness consisting of four obstacles attached to the heating and cooling plates, respectively, was investigated. Even though already there the strong influence of the roughness configurations was found, these results could not fully explain the differences in the results of the experimental studies. Further investigations with roughness configurations, more similar to the ones in the experiments, are required. They are so far difficult to realize, due to the large computational effort, which is required for simulations with a large number of obstacles of complicated shape as in the experiments.

Furthermore, in the experiments with rough plates usually higher Rayleigh numbers are studied than it is feasible in DNSs. Therefore general information is required how roughness configurations from experiments can be scaled to the lower Rayleigh number cases in DNSs. A general idea is, that the ratio of obstacle height to the thickness of the thermal boundary layer must be equal, but this is not fully understood. One way to get a deeper insight is modelling the influence of roughness of the mean heat flux by using the boundary layer theory. An existing model from the literature [125], which works well in case of two-dimensional convection, strongly underpredicts the heat flux increase, which can be obtained in three-dimensional convection (as shown in section 12.4). This model is based on the boundary layer theory by Prandtl–Blasius–Pohlhausen, which was found to be a not perfect approximation of the boundary layers in RBC (cf. chapter 6). Thus, a new model is required for the three-dimensional case.

## 14 OUTLOOK

# Bibliography

- [1] AHLERS, G. 2009 Turbulent convection. *Physics* **2**, 74.
- [2] AHLERS, G. & BEHRINGER, R. P. 1978 Evolution of turbulence from the Rayleigh–Bénard instability. *Phys. Rev. Lett.* **40**, 712–716.
- [3] AHLERS, G., BODENSCHATZ, E., FUNFSCHILLING, D., GROSSMANN, S., HE, X., LOHSE, D., STEVENS, R.J.A.M. & VERZICCO, R. 2012 Logarithmic temperature profiles in turbulent Rayleigh–Bénard convection. *Phys. Rev. Lett.* **109**, 114501.
- [4] AHLERS, G., BODENSCHATZ, E., FUNFSCHILLING, D. & HOGG, J. 2009 Turbulent Rayleigh–Bénard convection for a Prandtl number of 0.67. *J. Fluid Mech.* **641**, 157–167.
- [5] AHLERS, G., GROSSMANN, S. & LOHSE, D. 2009 Heat transfer and large scale dynamics in turbulent Rayleigh–Bénard convection. *Rev. Mod. Phys.* **81**, 503–537.
- [6] AHLERS, G., HE, X., FUNFSCHILLING, D. & BODENSCHATZ, E. 2012 Heat transport by turbulent Rayleigh–Bénard convection for  $Pr \simeq 0.8$  and  $3 \times 10^{12} \lesssim Ra \lesssim 10^{15}$ : Aspect ratio  $\Gamma = 0.50$ . *New J. Phys.* **14**, 103012.
- [7] ARCHIMEDES OF SYRACUSE about 250 BCE *On Floating Bodies*.
- [8] BAILON-CUBA, J., EMRAN, M. S. & SCHUMACHER, J. 2010 Aspect ratio dependence of heat transfer and large-scale flow in turbulent convection. *J. Fluid Mech.* **655**, 152–173.
- [9] BAILON-CUBA, J., SHISHKINA, O., WAGNER, C. & SCHUMACHER, J. 2012 Low-dimensional model of turbulent mixed convection in a complex domain. *Phys. Fluids* **24**, 107101.
- [10] BATCHELOR, G. K. 1959 Small-scale variation of convected quantities like temperature in turbulent fluid. *J. Fluid Mech.* **5**, 113–133.
- [11] BÉNARD, H. 1900 Les tourbillons cellulaires dans une nappe liquide. *Rev. Gén. Sciences Pure Appl.* **11**, 1261–1271, 1309–1328.
- [12] BÉNARD, H. 1901 Les tourbillons cellulaires dans une nappe liquide. – Méthodes optiques d’observation et d’enregistrement. *J. Phys. Théor. Appl.* **10**, 254–266.
- [13] BERCOVICI, D. 2003 The generation of plate tectonics from mantle convection. *Earth Planet. Sci. Lett.* **205**, 107–122.
- [14] BLASIUS, H. 1908 Grenzsichten in Flüssigkeiten mit kleiner Reibung. *Z. Math. Phys.* **56**, 1–37.
- [15] BLOCK, M. J. 1956 Surface tension as the cause of Bénard cells and surface deformation in a liquid film. *Nature* **178**, 650–651.
- [16] BODENSCHATZ, E., PESCH, W. & AHLERS, G. 2000 Recent developments in Rayleigh–Bénard convection. *Annu. Rev. Fluid Mech.* **32**, 709–778.
- [17] BOUSSINESQ, J. 1903 *Théorie Analytique de la Chaleur*. Gauthier-Villars.
- [18] BREUER, M. & HANSEN, U. 2009 Turbulent convection in the zero Reynolds number limit. *Europhys. Lett.* **86**, 24004.
- [19] BROWN, E. & AHLERS, G. 2006 Rotations and cessations of the large-scale circulation in turbulent Rayleigh–Bénard convection. *J. Fluid Mech.* **568**, 351–386.

## BIBLIOGRAPHY

- [20] BROWN, E. & AHLERS, G. 2009 The origin of oscillations of the large-scale circulation of turbulent Rayleigh–Bénard convection. *J. Fluid Mech.* **638**, 383–400.
- [21] BUCKINGHAM, E. 1914 On physically similar systems; illustrations of the use of dimensional equations. *Phys. Rev.* **96**, 345–376.
- [22] BUCKINGHAM, E. 1915 The principle of similitude. *Nature* **4**, 396–397.
- [23] BUELL, J. C. & CATTON, I. 1983 The effect of wall conduction on the stability of a fluid in a right circular cylinder heated from below. *J. Heat Transfer.* **105**, 255–260.
- [24] BUSSE, F. H. 1978 Non-linear properties of thermal convection. *Rep. Prog. Phys.* **41**, 1929–1967.
- [25] BUSSE, F. H. 1985 Transition to turbulence in Rayleigh–Bénard convection. In *Hydrodynamic Instabilities and the Transition to Turbulence* (ed. H. L. Swinney & J. P. Gollub), *Topics in Applied Physics*, vol. 45, pp. 87–137. Springer.
- [26] CALZAVARINI, E., DOERING, C. R., GIBBON, J. D., LOHSE, D., TANABE, A. & TOSCHI, F. 2006 Exponentially growing solutions in homogeneous Rayleigh–Bénard convection. *Phys. Rev. E* **73**, 035301.
- [27] CASTAING, B., GUNARATNE, G., HESLOT, F., KADANOFF, L., LIBCHABER, A., THOMAE, S., WU, X.-Z., ZALESKI, S. & ZANETTI, G. 1989 Scaling of hard thermal turbulence in Rayleigh–Bénard convection. *J. Fluid Mech.* **204**, 1–30.
- [28] CHANDRA, M. & VERMA, M. K. 2011 Dynamics and symmetries of flow reversals in turbulent convection. *Phys. Rev. E* **83**, 067303.
- [29] CHANDRA, M. & VERMA, M. K. 2013 Flow reversals in turbulent convection via vortex reconnections. *Phys. Rev. Lett.* **110**, 114503.
- [30] CHANDRASEKHAR, S. 1981 *Hydrodynamic and Hydromagnetic Stability*. Dover Publications.
- [31] CHAVANNE, X., CHILLÀ, F., CHABAUD, B., CASTAING, B. & HÉBRAL, B. 2001 Turbulent Rayleigh–Bénard convection in gaseous and liquid He. *Phys. Fluids* **13**, 1300–1320.
- [32] CHILLÀ, F. & SCHUMACHER, J. 2012 New perspectives in turbulent Rayleigh–Bénard convection. *Eur. Phys. J. E* **35**, 58.
- [33] CHING, E. S. C. 1997 Heat flux and shear rate in turbulent convection. *Phys. Rev. E* **55**, 1189–1192.
- [34] CHING, E. S. C. & TAM, W. S. 2006 Aspect-ratio dependence of heat transport by turbulent Rayleigh–Bénard convection. *J. Turb.* **7**, N 72.
- [35] CILIBERTO, S. & LAROCHE, C. 1999 Random roughness of boundary increases the turbulent scaling exponents. *Phys. Rev. Lett.* **82**, 3998–4001.
- [36] CIONI, S., CILIBERTO, S. & SOMMERIA, J. 1997 Strongly turbulent Rayleigh–Bénard convection in mercury: Comparison with results at moderate Prandtl number. *J. Fluid Mech.* **335**, 111–140.
- [37] CROSS, M. C. & HOHENBERG, P. C. 1993 Pattern formation outside of equilibrium. *Rev. Mod. Phys.* **65**, 851–1112.
- [38] CUSHMAN-ROISIN, B. & BECKERS, J.-M. 2011 *Introduction to Geophysical Fluid Dynamics*, 2nd edn., *International Geophysics Series*, vol. 101. Elsevier.
- [39] DAYA, Z. A. & ECKE, R. E. 2001 Does turbulent convection feel the shape of the container? *Phys. Rev. Lett.* **87**, 184501.
- [40] DU, Y. B. & TONG, P. 2000 Turbulent thermal convection in a cell with ordered rough boundaries. *J. Fluid Mech.* **407**, 57–84.
- [41] ECKHARDT, B., GROSSMANN, S. & LOHSE, D. 2007 What Rayleigh–Bénard, Taylor–Couette

- and pipe flows have in common. In *Progress in Turbulence II* (ed. M. Oberlack, G. Khujudze, S. Günther, T. Weller, M. Frewer, J. Peinke & S. Barth), *Springer Proceedings in Physics*, vol. 109, pp. 3–10. Springer.
- [42] FALKNER, V. M. & SKAN, S. W. 1931 Some approximate solutions of the boundary layer equations. *Phil. Mag.* **12**, 865–896.
- [43] FERZIGER, J. H. & PERIĆ, M. 2002 *Computational Methods for Fluid Dynamics*, 3rd edn. Springer.
- [44] FUNFSCHILLING, D. & AHLERS, G. 2004 Plume motion and large-scale dynamics in a cylindrical Rayleigh–Bénard cell. *Phys. Rev. Lett.* **92**, 194502.
- [45] FUNFSCHILLING, D., BROWN, E. & AHLERS, G. 2008 Torsional oscillations of the large-scale circulation in turbulent Rayleigh–Bénard convection. *J. Fluid Mech.* **607**, 119–139.
- [46] FUNFSCHILLING, D., BROWN, E., NIKOLAENKO, A. & AHLERS, G. 2005 Heat transport by turbulent Rayleigh–Bénard convection in cylindrical samples with aspect ratio one and larger. *J. Fluid Mech.* **536**, 145–154.
- [47] GAUTHIER, F. & ROCHE, P.-E. 2008 Evidence of a boundary layer instability at very high Rayleigh number. *Europhys. Lett.* **83**, 24005.
- [48] GETLING, A. V. 1998 *Rayleigh–Bénard Convection: Structures and Dynamics, Advanced Series in Nonlinear Dynamics*, vol. 11. World Scientific Publishing.
- [49] GRAY, D. D. & GIORGINI, A. 1976 The validity of the Boussinesq approximation for liquids and gases. *Int. J. Heat Mass Transfer* **19**, 545–551.
- [50] GROSSMANN, S. & LOHSE, D. 2000 Scaling in thermal convection: A unifying view. *J. Fluid Mech.* **407**, 27–56.
- [51] GROSSMANN, S. & LOHSE, D. 2001 Thermal convection for large Prandtl numbers. *Phys. Rev. Lett.* **86**, 3316–3319.
- [52] GROSSMANN, S. & LOHSE, D. 2002 Prandtl and Rayleigh number dependence of the Reynolds number in turbulent thermal convection. *Phys. Rev. E* **66**, 016305.
- [53] GROSSMANN, S. & LOHSE, D. 2003 On geometry effects in Rayleigh–Bénard convection. *J. Fluid Mech.* **486**, 105–114.
- [54] GROSSMANN, S. & LOHSE, D. 2004 Fluctuations in turbulent Rayleigh–Bénard convection: The role of plumes. *Phys. Fluids* **16**, 4462–4472.
- [55] GROSSMANN, S. & LOHSE, D. 2011 Multiple scaling in the ultimate regime of thermal convection. *Phys. Fluids* **23**, 045108.
- [56] GROSSMANN, S. & LOHSE, D. 2012 Logarithmic temperature profiles in the ultimate regime of thermal convection. *Phys. Fluids* **24**, 125103.
- [57] GRÖTZBACH, G. 1983 Spatial resolution requirements for Direct Numerical Simulation of the Rayleigh–Bénard convection. *J. Comp. Phys.* **49**, 241–264.
- [58] HADLEY, G. 1735 Concerning the cause of the general trade winds. *Phil. Trans. Roy. Soc.* **29**, 58–62.
- [59] HARTLEP, T., TILGNER, A. & BUSSE, F. H. 2003 Large scale structures in Rayleigh–Bénard convection at high Rayleigh numbers. *Phys. Rev. Lett.* **91**, 064501.
- [60] HARTLEP, T., TILGNER, A. & BUSSE, F. H. 2005 Transition to turbulent convection in a fluid layer heated from below at moderate aspect ratio. *J. Fluid Mech.* **544**, 309–322.

## BIBLIOGRAPHY

- [61] HE, X., FUNFSCHILLING, D., BODENSCHATZ, E. & AHLERS, G. 2012 Heat transport by turbulent Rayleigh–Bénard convection for  $Pr \simeq 0.8$  and  $4 \times 10^{11} \lesssim Ra \lesssim 2 \times 10^{14}$ : Ultimate-state transition for aspect ratio  $\Gamma = 1.00$ . *New J. Phys.* **14**, 063030.
- [62] HE, X., FUNFSCHILLING, D., NOBACH, H., BODENSCHATZ, E. & AHLERS, G. 2012 Transition to the ultimate state of turbulent Rayleigh–Bénard convection. *Phys. Rev. Lett.* **108**, 024502.
- [63] HERWIG, H., GLOSS, D. & WENTERODT, T. 2008 A new approach to understanding and modelling the influence of wall roughness on friction factors for pipe and channel flows. *J. Fluid Mech.* **613**, 35–53.
- [64] HESLOT, F., CASTAING, B. & LIBCHABER, A. 1987 Transitions to turbulence in helium gas. *Phys. Rev. A* **36**, 5870–5873.
- [65] HÖLLING, M. & HERWIG, H. 2006 Asymptotic analysis of heat transfer in turbulent Rayleigh–Bénard convection. *Int. J. Heat Mass Transfer* **49**, 1129–136.
- [66] HORN, S., SHISHKINA, O. & WAGNER, C. 2011 The influence of non-Oberbeck–Boussinesq effects on rotating turbulent Rayleigh–Bénard convection. *J. Phys.: Conf. Ser.* **318**, 082005.
- [67] HORN, S., SHISHKINA, O. & WAGNER, C. 2013 On non-Oberbeck–Boussinesq effects in three-dimensional Rayleigh–Bénard convection in glycerol. *J. Fluid Mech.* **724**, 175–202.
- [68] HUANG, S.-D., KACZOROWSKI, M., NI, R. & XIA, K.-Q. 2013 Confinement induced heat-transport enhancement in turbulent thermal convection. *Phys. Rev. Lett.* **111**, 104501.
- [69] KACZOROWSKI, M., SHISHKIN, A., SHISHKINA, O. & WAGNER, C. 2006 Development of a numerical procedure for direct simulations of turbulent convection in a closed rectangular cell. In *New Results in Numerical and Experimental Fluid Mechanics VI*, (ed. C. Tropea, S. Jakirlic, H.-J. Heinemann, R. Henke & H. Hönliger), *Notes on Numerical Fluid Mechanics and Multidisciplinary Design*, vol. 96, pp. 381–388. Springer.
- [70] KACZOROWSKI, M., SHISHKINA, O., SHISHKIN, A., WAGNER, C. & XIA, K.-Q. 2011 Analysis of the large-scale circulation and the boundary layers in turbulent Rayleigh–Bénard convection. In *Direct and Large-Eddy Simulation VIII* (ed. H. Kuerten, B. Geurts, V. Armenio & J. Fröhlich), pp. 383–388. Springer.
- [71] KACZOROWSKI, M. & XIA, K.-Q. 2013 Turbulent flow in the bulk of Rayleigh–Bénard convection: Small-scale properties in a cubic cell. *J. Fluid Mech.* **722**, 596–617.
- [72] KOERNER, M., SHISHKINA, O., WAGNER, C. & THESS, A. 2013 Properties of large-scale flow structures in an isothermal ventilated room. *Build. Environ.* **59**, 563–574.
- [73] KOLMOGOROV, A. N. 1941 The local structure of turbulence in incompressible viscous fluid for very large Reynolds numbers. *Dokl. Akad. Nauk. SSSR.* **30**, 299–303.
- [74] KRAICHNAN, R. 1962 Turbulent thermal convection at arbitrary Prandtl number. *Phys. Fluids* **5**, 1374–1389.
- [75] KRISHNAMURTI, R. 1970 On the transition to turbulent convection. Part 1. The transition from two- to three-dimensional flow. *J. Fluid Mech.* **42**, 295–307.
- [76] KRISHNAMURTI, R. 1970 On the transition to turbulent convection. Part 2. The transition to time-dependent flow. *J. Fluid Mech.* **42**, 309–320.
- [77] KRISHNAMURTI, R. 1973 Some further studies on the transition to turbulent convection. *J. Fluid Mech.* **60**, 285–303.
- [78] KÜHN, M., BOSBACH, J. & WAGNER, C. 2009 Experimental parametric study of forced and



- mixed convection in a passenger aircraft cabin mock-up. *Build. Environ.* **44**, 961–970.
- [79] KUNNEN, R. P. J., CLERCX, H. J. H., GEURTS, B. J., VAN BOKHOVEN, L. J. A., AKKERMANS, R. A. D. & VERZICCO, R. 2008 Numerical and experimental investigation of structure-function scaling in turbulent Rayleigh–Bénard convection. *Phys. Rev. E* **77**, 016302.
- [80] LAKKARAJU, R., STEVENS, R. J. A. M., VERZICCO, R., GROSSMANN, S., PROSPERETTI, A., SUN, C. & LOHSE, D. 2012 Spatial distribution of heat flux and fluctuations in turbulent Rayleigh–Bénard convection. *Phys. Rev. E* **86**, 056315.
- [81] LANDAU, L. D. & LIFSCHITZ, E. M. 2007 *Hydrodynamik*, 5th edn., *Lehrbuch der theoretischen Physik*, vol. 6. Harri Deutsch.
- [82] LANDAU, L. D. & LIFSCHITZ, E. M. 1987 *Fluid Mechanics*, 2nd edn., *Course of Theoretical Physics*, vol. 6. Butterworth Heinemann.
- [83] LI, L., SHI, N., DU PUIITS, R., RESAGK, C., SCHUMACHER, J. & THESS, A. 2012 Boundary layer analysis in turbulent Rayleigh–Bénard convection in air: Experiment versus simulation. *Phys. Rev. E* **86**, 026315.
- [84] LOHSE, D. & XIA, K.-Q. 2010 Small-scale properties of turbulent Rayleigh–Bénard convection. *Annu. Rev. Fluid Mech.* **42**, 335–364.
- [85] LORD RAYLEIGH 1916 On convection currents in a horizontal layer of fluid, when the higher temperature is on the under side. *Phil. Mag.* **32**, 529–546.
- [86] MACDONALD, A. M. & WUNSCH, C. 1996 An estimate of global ocean circulation and heat fluxes. *Nature* **382**, 436–439.
- [87] MISHRA, P. K., DE, A. K., VERMA, M. K. & ESWARAN, V. 2011 Dynamics of reorientations and reversals of large-scale flow in Rayleigh–Bénard convection. *J. Fluid Mech.* **668**, 480–499.
- [88] NIEMELA, J. J., SKRBK, L., SREENIVASAN, K. R. & DONNELLY, R. J. 2000 Turbulent convection at very high Rayleigh numbers. *Nature* **404**, 837–841.
- [89] NIEMELA, J. J. & SREENIVASAN, K. R. 2003 Confined turbulent convection. *J. Fluid Mech.* **481**, 355–384.
- [90] NIEMELA, J. J. & SREENIVASAN, K. R. 2003 Rayleigh-number evolution of large-scale coherent motion in turbulent convection. *Europhys. Lett.* **62**, 829–833.
- [91] NIKURADSE, J. 1933 *Strömungsgesetze in rauhen Rohren*, *Forschungsheft*, vol. 361. Verein Deutscher Ingenieure.
- [92] NORMAND, C., POMEAU, Y. & VELARDE, M. G. 1977 Convective instability: A physicist’s approach. *Rev. Mod. Phys.* **49**, 581–624.
- [93] OBERBECK, A. 1879 Über die Wärmeleitung der Flüssigkeiten bei Berücksichtigung der Strömungen in Folge von Temperaturdifferenzen. *Ann. Phys. (Berlin)* **243** (6), 271–292.
- [94] OSTROUMOV, G. A. 1958 Free convection under the conditions of the internal problem. Technical Memorandum 1407. National Advisory Committee for Aeronautics.
- [95] PEARSON, J. R. A. 1958 On convection cells induced by surface tension. *J. Fluid Mech.* **4**, 489–500.
- [96] PETSCHL, K., STELLMACH, S., WILCZEK, M., LÜLFF, J. & HANSEN, U. 2013 Dissipation layers in Rayleigh–Bénard convection: A unifying view. *Phys. Rev. Lett.* **110**, 114502.
- [97] VAN DER POEL, E. P., STEVENS, R. J. A. M. & LOHSE, D. 2011 Connecting flow structures and heat flux in turbulent Rayleigh–Bénard convection. *Phys. Rev. E* **84**, 045303(R).

## BIBLIOGRAPHY

- [98] VAN DER POEL, E. P., STEVENS, R. J. A. M., SUGIYAMA, K. & LOHSE, D. 2012 Flow states in two-dimensional Rayleigh–Bénard convection as a function of aspect ratio and Rayleigh number. *Phys. Fluids* **24**, 085104.
- [99] POHLHAUSEN, E. 1921 Der Wärmeaustausch zwischen festen Körpern und Flüssigkeiten mit kleiner Reibung und kleiner Wärmeleitung. *Z. Angew. Math. Mech.* **1**, 115–121.
- [100] POHLHAUSEN, K. 1921 Zur nährungsweisen Integration der Differentialgleichung der laminaren Grenzschicht. *Z. Angew. Math. Mech.* **1**, 252–268.
- [101] POPE, S. B. 2000 *Turbulent Flows*, 1st edn. Cambridge University Press.
- [102] PRANDTL, L. 1905 Über Flüssigkeitsbewegung bei sehr kleiner Reibung. In *Verhandlungen des III. Int. Math. Kongr., Heidelberg, 1904*, pp. 484–491. Teubner.
- [103] DU PUIITS, R., RESAGK, C. & TRESS, A. 2009 Structure of viscous boundary layers in turbulent Rayleigh–Bénard convection. *Phys. Rev. E* **80**, 036318.
- [104] DU PUIITS, R., RESAGK, C., TILGNER, A., BUSSE, F. H. & TRESS, A. 2007 Structure of thermal boundary layers in turbulent Rayleigh–Bénard convection. *J. Fluid Mech.* **572**, 231–254.
- [105] QIU, X.-L., XIA, K.-Q. & TONG, P. 2005 Experimental study of velocity boundary layer near a rough conducting surface in turbulent natural convection. *J. Turbulence* **30**, 1–13.
- [106] RESAGK, C., DU PUIITS, R., TRESS, A., DALZHANSKY, F. V., GROSSMANN, S., ARAUJO, F. F. & LOHSE, D. 2006 Oscillations of the large scale wind in turbulent thermal convection. *Phys. Fluids* **18**, 095105.
- [107] ROCHE, P.-E., CASTAING, B., CHABAUD, B. & HÉBRAL, B. 2003 Heat transfer in turbulent Rayleigh–Bénard convection below the ultimate regime. *J. Low Temp. Phys.* **134**, 1011–1042.
- [108] ROCHE, P.-E., CASTAING, B., CHABAUD, B. & HERBAL, B. 2001 Observation of the 1/2 power law in Rayleigh–Bénard convection. *Phys. Rev. E* **63**, 045303.
- [109] SALORT, J., LIOT, O., RUSAOUEN, E., SEYCHELLES, F., TISSERAND, J.-C., CREYSSELS, M., CASTAING, B. & CHILLÀ, F. 2014 Thermal boundary layer near roughnesses in turbulent Rayleigh–Bénard convection: Flow structure and multistability. *Phys. Fluids* **26**, 015112.
- [110] SCHEEL, J. D., EMRAN, M. S. & SCHUMACHER, J. 2013 Resolving the fine-scale structure in turbulent Rayleigh–Bénard convection. *New J. Phys.* **15**, 113063.
- [111] SCHEEL, J. D., KIM, E. & WHITE, K. R. 2012 Thermal and viscous boundary layers in turbulent Rayleigh–Bénard convection. *J. Fluid Mech.* **711**, 281–305.
- [112] SCHLICHTING, H. & GERSTEN, K. 2000 *Boundary-Layer Theory*, 8th edn. Springer.
- [113] SCHLICHTING, H. & GERSTEN, K. 2006 *Grenzschicht-Theorie*, 10th edn. Springer.
- [114] SCHMALZL, J., BREUER, M. & HANSEN, U. 2004 On the validity of two-dimensional numerical approaches to time-dependend thermal convection. *Europhys. Lett.* **67**, 390–396.
- [115] SCHMITT, L., RICHTER, K. & FRIEDRICH, R. 1986 Large-eddy simulation of turbulent boundary layer and channel flow at high Reynolds number. In *Direct and Large Eddy Simulation of Turbulence* (ed. U. Schumann & R. Friedrich), pp. 161–176. Vieweg.
- [116] SCHUMANN, U. 1973 Ein Verfahren zur direkten numerischen Simulation turbulenter Strömungen in Platten- und Ringspaltkanälen und über seine Anwendung zur Untersuchung von Turbulenzmodellen. PhD thesis, TH Karlsruhe, KFK 1854.
- [117] SHEN, Y., XIA, K.-Q. & TONG, P. 1996 Turbulent convection over rough surfaces. *Phys. Rev. Lett.* **76**, 908–911.

- [118] SHI, N., EMRAN, M. S. & SCHUMACHER, J. 2012 Boundary layer structure in turbulent Rayleigh–Bénard convection. *J. Fluid Mech.* **706**, 5–33.
- [119] SHISHKINA, O., HORN, S. & WAGNER, S. 2013 Falkner-Skan boundary layer approximation in Rayleigh–Bénard convection. *J. Fluid Mech.* **730**, 442–463.
- [120] SHISHKINA, O., SHISHKIN, A. & WAGNER, C. 2009 Simulation of turbulent thermal convection in complicated domains. *J. Comput. Appl. Math.* **226**, 336–344.
- [121] SHISHKINA, O., STEVENS, R. J. A. M., GROSSMANN, S. & LOHSE, D. 2010 Boundary layer structure in turbulent thermal convection and its consequences for the required numerical resolution. *New J. Phys.* **12**, 075022.
- [122] SHISHKINA, O. & TRESS, A. 2009 Mean temperature profiles in turbulent Rayleigh–Bénard convection of water. *J. Fluid Mech.* **663**, 449–460.
- [123] SHISHKINA, O. & WAGNER, C. 2005 A fourth order accurate finite volume scheme for numerical simulations of turbulent Rayleigh–Bénard convection in cylindrical containers. *C. R. Mecanique* **333**, 17–28.
- [124] SHISHKINA, O. & WAGNER, C. 2007 Local heat fluxes in turbulent Rayleigh–Bénard convection. *Phys. Fluids* **19**, 085107.
- [125] SHISHKINA, O. & WAGNER, C. 2011 Modelling the influence of wall roughness on heat transfer in thermal convection. *J. Fluid Mech.* **686**, 568–582.
- [126] SHISHKINA, O. & WAGNER, C. 2012 A numerical study of turbulent mixed convection in an enclosure with heated rectangular elements. *J. Turbulence* **13**, 1–21.
- [127] SHISHKINA, O., WAGNER, S. & HORN, S. 2014 Influence of the angle between the wind and the isothermal surfaces on the boundary layer structures in turbulent thermal convection. *Phys. Rev. E* **89**, 033014.
- [128] SHRAIMAN, B. & SIGGIA, E. 1990 Heat transport in high-Rayleigh-number convection. *Phys. Rev. A* **42**, 3650–3653.
- [129] SIGGIA, E. 1994 High Rayleigh number convection. *Annu. Rev. Fluid Mech.* **26**, 137–168.
- [130] SPIEGEL, E. A. 1971 Convection in stars, I. basic Boussinesq convection. *Annu. Rev. Astron. Astrophys.* **9**, 323–352.
- [131] STEVENS, B. 2005 Atmospheric moist convection. *Annu. Rev. Earth Planet Sci.* **33**, 605–643.
- [132] STEVENS, R. J. A. M., CLERCX, H. J. H. & LOHSE, D. 2011 Effect of plumes on measuring the large scale circulation in turbulent Rayleigh–Bénard convection. *Phys. Fluids* **23**, 095110.
- [133] STEVENS, R. J. A. M., LOHSE, D. & VERZICCO, R. 2011 Prandtl and Rayleigh number dependence of heat transport in high Rayleigh number thermal convection. *J. Fluid Mech.* **688**, 31–43.
- [134] STEVENS, R. J. A. M., VAN DER POEL, E. P., GROSSMANN, S. & LOHSE, D. 2013 The unifying theory of scaling in thermal convection: The updated prefactors. *J. Fluid Mech.* **730**, 295–308.
- [135] STEVENS, R. J. A. M., VERZICCO, R. & LOHSE, D. 2010 Radial boundary layer structure and Nusselt number in turbulent Rayleigh–Bénard convection. *J. Fluid Mech.* **643**, 495–507.
- [136] STEVENS, R. J. A. M., ZHOU, Q., GROSSMANN, S., VERZICCO, R., XIA, K.-Q. & LOHSE, D. 2012 Thermal boundary layer profiles in turbulent Rayleigh–Bénard convection in a cylindrical sample. *Phys. Rev. E* **85**, 027301.
- [137] STEWARTSON, K. 1958 On the free convection from a horizontal plate. *Z. angew. Math. Phys.* **9**,

## BIBLIOGRAPHY

- 276–282.
- [138] STRINGANO, G., PASCAZIO, G. & VERZICCO, R. 2006 Turbulent thermal convection over grooved plates. *J. Fluid Mech.* **557**, 307–336.
- [139] SUGIYAMA, K., NI, R., STEVENS, R. J. A. M., CHAN, T. S., ZHOU, S.-Q., XI, H.-D., SUN, C., GROSSMANN, S., XIA, K.-Q. & LOHSE, D. 2010 Flow reversals in thermally driven turbulence. *Phys. Rev. Lett.* **105**, 034503.
- [140] SUN, C., CHEUNG, Y.-H. & XIA, K.-Q. 2008 Experimental studies of the viscous boundary layer properties in turbulent Rayleigh–Bénard convection. *J. Fluid Mech.* **605**, 79–113.
- [141] SUN, C., XIA, K.-Q. & TONG, P. 2005 Three-dimensional flow structures and dynamics of turbulent thermal convection in a cylindrical cell. *Phys. Rev. E* **72**, 026302.
- [142] TENNEKES, H. & LUMLEY, J. L. 1972 *A first Course in Turbulence*. MIT Press.
- [143] THOMPSON, J. E., WARSI, Z. U. A. & WAYNE MASTIN, C. 1985 *Numerical Grid Generation: Foundations and Applications*. Elsevier.
- [144] THRELFALL, D. C. 1975 Free convection in low-temperature gaseous helium. *J. Fluid Mech.* **67**, 17–28.
- [145] TILGNER, A., BELMONTE, A. & LIBCHABER, A. 1993 Temperature and velocity profiles of turbulent convection in water. *Phys. Rev. E* **47**, 2253–2257.
- [146] TISSERAND, J. C., CREYSSELS, M., GASTEUIL, Y., PABIOU, H., GIBERT, M., CASTAING, B. & CHILLÀ, F. 2011 Comparison between rough and smooth plates within the same Rayleigh–Bénard cell. *Phys. Fluids* **23**, 015105.
- [147] VASIL’EV, A. Y. & FRICK, P. G. 2011 Reversals of large-scale circulation in turbulent convection in rectangular cavities. *JETP Lett.* **93**, 330–344.
- [148] VEREIN DEUTSCHER INGENIEURE, VDI - GESELLSCHAFT VERFAHRENSTECHNIK UND CHEMIEINGENIEURWESEN (GVC), ed. 2006 *VDI - Wärmeatlas*, 10th edn. Springer.
- [149] VERZICCO, R. 2012 Boundary layer structure in confined turbulent thermal convection. *J. Fluid Mech.* **706**, 1–4.
- [150] VILLERMAUX, E. 1998 Transfer at rough sheared interfaces. *Phys. Rev. Lett.* **81**, 4859–4862.
- [151] WAGNER, S. & SHISHKINA, O. 2013 See supplementary material at <http://dx.doi.org/10.1063/1.4819141> for three-dimensional temperature field movies for  $Ra = 10^6$  and  $\Gamma = 1/10$ ,  $\Gamma = 1/3$ .
- [152] WAGNER, S. & SHISHKINA, O. 2013 Aspect ratio dependency of Rayleigh–Bénard convection in box-shaped containers. *Phys. Fluids* **25**, 085110.
- [153] WAGNER, S. & SHISHKINA, O. 2013 DNS of thermal convection in rectangular domains with different depth. Accepted for publication by Springer.
- [154] WAGNER, S. & SHISHKINA, O. 2013 Heat flux enhancement by regular surface roughness in turbulent thermal convection. *J. Fluid Mech.* Under review.
- [155] WAGNER, S., SHISHKINA, O. & WAGNER, C. 2012 Boundary layers and wind in cylindrical Rayleigh–Bénard cells. *J. Fluid Mech.* **697**, 336–366.
- [156] WAGNER, S., SHISHKINA, O. & WAGNER, C. 2014 Influence of the geometry on Rayleigh–Bénard convection. In *New Results in Numerical and Experimental Fluid Mechanics IX, Contributions to the 18th STAB/DGLR Symposium, Stuttgart, Germany, 2012* (ed. A. Dillmann, G. Heller, E. Krämer, H.-P. Kreplin, W. Nitsche & U. Rist), *Notes on Numerical Fluid Mechanics and*

- Multidisciplinary Design*, vol. 124, pp. 313–321. Springer.
- [157] WAGNER, S., SHISHKINA, O. & WAGNER, C. 2014 Numerical investigation of the spatial resolution requirements for turbulent Rayleigh–Bénard Convection. In *Turbulence and Interactions: Proceedings of the TI 2012 conference* (ed. M. O. Deville, J.-L. Estivalezes, V. Gleize, T.-H. Lê, M. Terracol & S. Vincent), *Notes on Numerical Fluid Mechanics and Multidisciplinary Design*, vol. 125, pp. 181–187. Springer.
- [158] WEISS, S. & AHLERS, G. 2011 The large-scale flow structure in turbulent rotating Rayleigh–Bénard convection. *J. Fluid Mech.* **688**, 461–492.
- [159] WEISS, S. & AHLERS, G. 2011 Turbulent Rayleigh–Bénard convection in a cylindrical container with aspect ratio  $\Gamma = 0.50$  and Prandtl number  $Pr = 4.38$ . *J. Fluid Mech.* **676**, 5–40.
- [160] WILCOX, D. C. 2010 *Basic Fluid Mechanics*, 4th edn. DCW Industries.
- [161] XI, H.-D., LAM, S. & XIA, K.-Q. 2004 From laminar plumes to organized flows: The onset of large-scale circulation in turbulent thermal convection. *J. Fluid. Mech.* **503**, 47–56.
- [162] XI, H.-D. & XIA, K.-Q. 2007 Cessations and reversals of the large-scale circulation in turbulent thermal convection. *Phys. Rev. E* **76**, 036301.
- [163] XI, H.-D. & XIA, K.-Q. 2008 Flow mode transitions in turbulent thermal convection. *Phys. Fluids* **20**, 055104.
- [164] XI, H.-D., ZHOU, Q. & XIA, K.-Q. 2006 Azimuthal motion of the mean wind in turbulent thermal convection. *Phys. Rev. E* **73**, 056312.
- [165] XI, H.-D., ZHOU, S.-Q., ZHOU, Q., CHAN, T. S. & XIA, K.-Q. 2009 Origin of the temperature oscillations in turbulent thermal convection. *Phys. Rev. Lett.* **102**, 044503.
- [166] XIA, K.-Q. 2011 How heat transfer efficiencies in turbulent thermal convection depend on internal flow modes. *J. Fluid Mech.* **676**, 1–4.
- [167] XIA, K.-Q., SUN, C. & ZHOU, S. 2003 Particle image velocimetry measurement of the velocity field in turbulent thermal convection. *Phys. Rev. E* **68**, 066303.
- [168] ZHOU, Q., LIU, B.-F., LI, C.-M. & ZHONG, B.-C. 2012 Aspect ratio dependence of the heat transport by turbulent Rayleigh–Bénard convection in rectangular cells. *J. Fluid Mech* **710**, 260–276.
- [169] ZHOU, Q., STEVENS, R. J. A. M., SUGIYAMA, K., GROSSMANN, S., LOHSE, D. & XIA, K.-Q. 2010 Prandtl–Blasius temperature and velocity boundary-layer profiles in turbulent Rayleigh–Bénard convection. *J. Fluid Mech.* **664**, 297–312.
- [170] ZHOU, Q., SUGIYAMA, K., STEVENS, R. J. A. M., GROSSMANN, S., LOHSE, D. & XIA, K.-Q. 2011 Horizontal structures of velocity and temperature boundary-layers in two-dimensional numerical turbulent Rayleigh–Bénard convection. *Phys. Fluids* **23**, 125104.
- [171] ZHOU, Q., XI, H.-D., ZHOU, S.-Q., SUN, C. & XIA, K.-Q. 2009 Oscillations of the large-scale circulation in turbulent Rayleigh–Bénard convection: The sloshing mode and its relationship with the torsional mode. *J. Fluid Mech.* **630**, 367–390.
- [172] ZHOU, Q. & XIA, K.-Q. 2008 Comparative experimental study of local mixing of active and passive scalars in turbulent thermal convection. *Phys. Rev. E* **77**, 056312.
- [173] ZHOU, Q. & XIA, K.-Q. 2010 Measured instantaneous viscous boundary layer in turbulent Rayleigh–Bénard convection. *Phys. Rev. Lett.* **104**, 104301.
- [174] ZHOU, Q. & XIA, K.-Q. 2013 Thermal boundary layer structure in turbulent Rayleigh–Bénard

## BIBLIOGRAPHY

convection in a rectangular cell. *J. Fluid Mech* **721**, 199–224.

# Curriculum Vitae

## Dipl. Phys. Sebastian Wagner

Geboren am 21. Mai 1984 in Göttingen  
Nationalität: deutsch  
Adresse: Herzberger Landstraße 19, 37085 Göttingen, Deutschland  
Telefon: +49 (0)551 2921096  
e-mail: wagn.seb@gmail.com

## Wissenschaftlicher Werdegang

Juli 2014 Anstellung als wissenschaftlicher Mitarbeiter am Max–Planck–Institut für Dynamik und Selbstorganisation, Göttingen  
August 2012 Anstellung als wissenschaftlicher Mitarbeiter am Institut für Aerodynamik und Strömungstechnik des Deutschen Zentrums für Luft- und Raumfahrt, Göttingen  
Februar 2011 Beginn der Promotion im Rahmen des Promotionsprogramms Prophys der Georg-August University School of Science (GAUSS)  
Dezember 2010 Anstellung als Doktorand am Institut für Aerodynamik und Strömungstechnik des Deutschen Zentrums für Luft- und Raumfahrt, Göttingen  
November 2010 Diplom in Physik, Diplomarbeit: “Potentialtheoretische Modellierung instationärer kompressibler Strömungen mit komplexen Randgeometrien”. Georg-August Universität Göttingen, Note: *sehr gut*  
Juli 2004 Abitur, Otto-Hahn Gymnasium Göttingen, Note: *gut*

## Veröffentlichungen in Zeitschriften

- S. Wagner, O. Shishkina: „Heat flux enhancement by regular surfaces roughness in turbulent thermal convection“, J. Fluid Mech, unter Begutachtung, 2014
- O. Shishkina, S. Wagner, S. Horn: „Influence of the angle between the wind and the isothermal surfaces on the boundary layer structures in turbulent thermal convection“, Phys. Rev. E 89, 033014, 2014
- S. Wagner, O. Shishkina: „Aspect-ratio dependency of Rayleigh–Bénard convection in box-shaped containers“, Phys. Fluids 25, 085110, 2013
- O. Shishkina, S. Horn, S. Wagner: „Falkner-Skan boundary layer approximation in Rayleigh–Bénard convection“, J. Fluid Mech. 730, Seiten 442–463, 2013
- S. Wagner, O. Shishkina, C. Wagner: „Boundary layers and wind in cylindrical Rayleigh–Bénard cells“. J. Fluid Mech. 697, 336–366, 2012

## Veröffentlichungen als begutachtete Buchbeiträge

- S. Wagner, O. Shishkina: „DNS of thermal convection in rectangular domains with different depth“, im Druck, Springer, 2013
- S. Wagner, O. Shishkina, C. Wagner: „Numerical investigation of the spatial resolution requirements for turbulent Rayleigh-Bénard convection“. In: „Turbulence and Interactions: Proceedings of the TI 2012 conference“, Notes on Numerical Fluid Mechanics and Multidisciplinary Design (NNFM), **125**, 181–187, Springer, 2014
- S. Wagner, O. Shishkina, C. Wagner: „Influence of the geometry on Rayleigh-Bénard convection“. In: „New Results in Numerical and Experimental Fluid Mechanics IX“, Notes on Numerical Fluid Mechanics and Multidisciplinary Design (NNFM), **124**, 313–321, Springer, 2014
- S. Wagner, K. Ehrenfried, A. Dillmann: „Numerical simulation of train-tunnel entry using a BEM in time domain“. In: „New Results in Numerical and Experimental Fluid Mechanics VIII“, Notes on Numerical Fluid Mechanics and Multidisciplinary Design (NNFM), **121**, 739–746, Springer, 2013
- S. Wagner, K. Ehrenfried, A. Dillmann: „A simplified model of the wave generation due to train-tunnel entry“, im Druck, Springer, 2010

## Konferenzbeiträge

- 7. European Postgraduate Fluid Dynamics Conference, Ilmenau, 2014 (Poster)
- International Conference on Phase Transitions at Low Temperatures, Pattern Formation and Turbulence, Göttingen, 2014 (Poster)
- Workshop - Methods of characterizing turbulent convection: New perspectives, Münster, 2014 (Vortrag)
- 14. European Turbulence Conference, Lyon (Frankreich), 2013 (Vortrag)
- ERCOFTAC Workshop: Direct and Large-Eddy Simulation 9, Dresden, 2013 (Vortrag)
- International Conference on Rayleigh-Bénard Turbulence, Hong-Kong, 2012, (Vortrag, Poster)
- 18. DGLR-Fach-Symposium der STAB, Stuttgart, 2012 (Vortrag)
- 23. International Congress of Theoretical and Applied Mechanics, Peking (China), 2012 (Vortrag, Poster)
- 3. International Conference on Turbulence and Interactions, La Saline-les-Bains (La Réunion), 2012 (Vortrag)
- 64. Annual Meeting of the APS Division of Fluid Dynamics, Baltimore (USA), 2011 (Vortrag)
- FOR 1182 Workshop: Dynamic of Coherent Structures in Turbulent Flows, Bad Dürkheim, 2011 (Poster)
- 5. European Postgraduate Fluid Dynamics Conference, Göttingen, 2011 (Poster)
- 17. DGLR-Fach-Symposium der STAB, Berlin, 2010 (Vortrag)
- Aerodynamics of Heavy Vehicles 3: Trucks, Buses and Trains, Potsdam, 2010 (Vortrag)



## **Gutachtertätigkeit**

- Gutachter für die Zeitschrift Physical Review Letters
- Gutachter für die Zeitschrift Physical Review E
- Gutachter für die Zeitschrift Journal of Turbulence

## **Lehre**

2011-2013	Übungen beim jährlichen Kurs “Direct Numerical Simulation (DNS) and Large-Eddy Simulation (LES)”, Institut für Aerodynamik und Strömungstechnik des Deutschen Zentrums für Luft- und Raumfahrt, Göttingen
WiSe 2011/12	Übung zum “Vorkurs: Mathematische Methoden der Physik”, Georg-August-Universität Göttingen
SoSe 2011	Übung zur Vorlesung “Mehrdimensionalen Analysis für Physiker”, Georg-August-Universität Göttingen
SoSe 2010	Übung zur Vorlesung “Physik II”, Georg-August-Universität Göttingen
WiSe 2009/10	Übung zur Vorlesung “Thermodynamik und statistische Mechanik”, Georg-August-Universität Göttingen
SoSe 2009	Übung zur Vorlesung “Theoretische Physik III”, Georg-August-Universität Göttingen
WiSe 2008/09	Übung zur Vorlesung “Mathematische Methoden der Physik”, Georg-August-Universität Göttingen

## **Projekte**

- Mitarbeit im Projekt SH405/2-1 „Hochaufgelöste numerische Simulation von turbulenter nicht-Oberbeck-Boussinesq Rayleigh-Bénard Konvektion“ der Deutschen Forschungsgemeinschaft (DFG)
- Mitarbeit im Projekt SH405/3-1 „Der Einfluss der Oberflächenrauigkeit auf den Wärmetransport in turbulenter natürlicher thermischer Konvektion“ der Deutschen Forschungsgemeinschaft (DFG)

---

(Sebastian Wagner)

Göttingen, 21. Juli 2014